# DETECTION AND ASSESSMENT OF WOOD DECAY – GLULAM BEAMS AND WOODEN UTILITY POLES

BY

CHRISTOPHER ADAM SENALIK

DISSERTATION

Submitted in partial fulfillment of the requirements
for the degree of Doctor of Philosophy in Systems and Entrepreneurial Engineering
in the Graduate College of the
University of Illinois at Urbana-Champaign, 2013

Urbana, Illinois

Doctoral Committee:

Professor Henrique Reis, Chair
Associate Professor Emeritus W. Brent Hall
Associate Professor Daniel A. Kuchma
Associate Professor Ramavarapu S. Sreenivas

**ABSTRACT**

This report documents the development of acoustic and ultrasonic inspection methods on wooden glulam beams and utility poles. All beams and poles examined where composed of Douglas-fir. The report begins with a description of the structure of trees, the mechanical behavior of wood subjected to rot, and current utility pole inspection methods. Background regarding inspection methodology on wood structures is provided. Cross-sectional images of the glulam beams and the utility poles used in this study were obtained through the use of computerized axial tomography (CAT or CT) scans. Areas of decay were identified using the CT scan images. Two methods of detecting defects within glulam beams are described: ultrasonic through-transmission and impact-echo. The analysis of the wooden utility poles starts with the development of a two-dimensional, finite difference time domain (FDTD) simulation to model wave propagation through the pole. The simulation is validated against empirical results.

The through-transmission technique used on the glulam beam locates rot through the use of the highest magnitude frequency and area under the power spectrum density curve. A 100 kHz signal was sent through the glulam beam. In areas devoid of decay, the received frequency was approximately 100 kHz. In areas where decay was identified, the frequency of highest magnitude shifted lower towards 85 kHz. Also, the area under the power spectrum density curve of the received signal was greatly diminished in areas of decay.

The impact-echo method used on the glulam beams locates rot through the use of the attenuation rate. An accelerometer was affixed to the surface of the beam. A ball bearing was dropped from 200 mm above the surface next to the accelerometer. The signal was recorded. A spectrogram of the received signal was developed, and the mean rate of attenuation of the frequency range 500 Hz to 20 kHz was calculated. An attenuation rate of 1.17 Nepers per millisecond was found to be the threshold indicative of the presence of rot. Attenuation rates greater than the threshold indicated the presence of rot; lower indicated sound wood. The threshold had an overall error rate of 7.2%.

The report then shifts to developing a two-dimensional, finite difference time domain simulation that can model wave behavior through a wood pole cross-section. The

model incorporates several features that have not been included in previous analyses. These features include: a frequency dispersive model of wave velocity and attenuation, cross-sectional density and geometry information collected directly from CT scans of the utility poles, a perfectly matched layer used to model the behavior or rot, and a center point formulation that allows waves to pass through the center of a cylindrically orthotropic medium. The simulation is validated against the waveform behavior predicted by an analytical model and against experimental data collected from impact through-transmission testing of three actual utility pole specimens.

Defects of various sizes and locations are then simulated in order to identify associated changes in wave behavior. The results of the simulation are used to develop metrics to determine the size, depth, and general location of internal defects within a wooden utility pole. The metrics are then applied to data collected from the wooden utility poles with known internal defects for validation. The predicted defect areas are accurate to within 2.0% of the total cross-sectional area and have a positional accuracy within 17% of the cross-sectional radius.

To Greg and in memory of Rolly

## ACKNOWLEDGEMENTS

When I decided to leave industry and return to academia in order to pursue my Ph.D., there was only one person I considered as my thesis advisor. Dr. Henrique Reis was the individual, and thankfully for me and this project, he accepted the position. Dr. Frank C. Beall has provided invaluable knowledge and insight into the behavior and testing of wood, as well as resources necessary for my research. I am grateful to my other thesis committee members: Dr. W. Brent Hall, Dr. Daniel A. Kuchma, and Dr. Ramavarapu S. Sreenivas. The feedback they have provided has guided me towards the completion of this project.

I owe much to my friends and colleges in the Nondestructive Testing and Evaluation Laboratory. Ben Ervin provided wonderful humor. Jacob Borgerson provided an example of succeeding through adversity. Thomas Suchy provided inspiration to get up early to start the day. Nathan Price provided thoughtful conversation. Bezhad Behnia provided example of how to have a smiling face and good attitude every day regardless of what is happening. Megan McGovern provided intellectual companionship and entertaining camaraderie.

I have appreciated the encouragement of my former employer, Dr. Roland L. Ruhl, and my former co-workers: Dr. Mark G. Strauss, Dwayne G. “Red” Owen, and Mary K. Dooley-Owen. My former roommate and good friend, Josh Yelon, provided priceless programming assistance,

I want to thank Greg Abbott for his support. I would also like to thank him for absolutely everything. In addition, I would like to thank him for anything I forgot. I want to thank him for anything and everything.

This research was made possible by the support of the National Science Foundation under Grant No. CMS 02-01305. I am also very grateful to Dr. Jeffrey J. Morrell of the College of Forestry, Wood Science and Engineering, at the Oregon State University for providing wooden poles. Finally, I would like to thank the Industrial and Enterprise Systems Engineering Department at the University of Illinois at Urbana-Champaign for providing me with both the opportunity to achieve my goal, and also invaluable financial assistance.

**TABLE OF CONTENTS**

## LIST OF FIGURES

## LIST OF TABLES

## CHAPTER 1. INTRODUCTION

The two major forms of bio-deterioration of wood and wood products are decay and insect attack. While many wood structures are routinely inspected for insect attack, such as termite inspection in real estate transactions, inspection for wood decay is rarely performed mainly because of the lack of an effective testing method. Whereas much has been done to preserve wood and wood composites, wood structures such as buildings, wood bridges, utility poles, and others continue to decay, because even the best preservative techniques available today have not been able to truly preserve these materials against the natural process of decay. The process of decay varies with the rot / fungal species, but follows a sequential process of incipient, intermediate, and advanced decay. Incipient decay normally occurs with little visible change to the wood, although the dynamic strength properties can be greatly reduced. The other extreme, i.e., advanced decay, is characterized by wood with no intrinsic strength.

The economic impact of wood decay is also significant. There are millions of dollars in real estate transactions involving wooden structures daily without them being inspected for wood decay. Wooden utility poles also illustrate the potential economic impact of wood decay. There are over 100 million wooden utility poles in the United States [1]. The annual replacement rate due to decay is 0.34% [2]. About a third of the poles replaced due to decay still have useful service life [2]. Assuming an average replacement cost of approximately $2500, a one percent reduction in pole removals from improved inspection techniques saves $8.5 million annually.

Several nondestructive testing methods have been attempted to detect and evaluate the level of wood deterioration caused by decay. These methods include radiation (X-rays and gamma rays, microwave), electrical (low frequency and DC conductance), and acoustic (stress wave methods, sonic and ultrasonic, including acoustic emission and acousto-ultrasonics) [3 - 9]. Radiation methods are affected primarily by density variations and moisture content in the wood. Electrical methods depend on conductivity and dielectric properties, which are specially affected by moisture content below the fiber saturation point. Acoustic methods are largely dependent on mechanical properties (e.g., modulus of elasticity) and density of wood. While the most promising

has been the acousto-ultrasonic approach, all suffer from the inherent variability of wood such as grain angle, density, moisture content variations, and presence of features such as knots, splits, and resin pockets that can mask the presence of decay. While all the past research has contributed to the current state-of-the-art techniques, there is still a strong need to reliably detect and assess decay in wood and wood products.

This report documents the development of acoustic and ultrasonic inspection methods on glulam beams and wooden utility poles. First, a description of the structure of trees, the mechanical behavior of rot, and current utility pole inspection methods is presented. Background regarding inspection methodology on wood structures is provided. Two methods of detecting defects within glulam beams are described: ultrasonic through-transmission and impact-echo.

The report then shifts to developing a simulation that can model wave behavior through a wood pole cross-section. The simulation is validated against theoretical and experimental values. Defects of various sizes are then simulated in order to identify associated changes in wave behavior. The results of the simulation are then used to develop metrics to determine the size, depth, and general location of internal defects within a wooden utility pole. The metrics are then applied to three actual wooden utility poles with known internal defects. The predicted defect areas are accurate to within 2.0% of the total cross-sectional area and have a positional accuracy to within 17% of the cross-sectional radius.

### 1.1. Structure of Trees

Wood has been described as an organic composite material produced by trees. In reality, wood is not a single complex material, but a series of complex materials built of successively diminutive structures ranging in size from angstroms to meters. The macro characteristics of wood are affected by the individual cells. Below is a brief description of the structure of wood from the cellular level up to macroscopic level.

Trees are generally broken into two categories: angiosperms and gymnosperms. Angiosperms are also commonly referred to as deciduous, broadleaf, or hardwood trees. Gymnosperms are commonly referred to as conifers, evergreens, or softwood trees. Hardwood and softwood are the most commonly used terms and are used throughout this

report. Hardwood trees are generally characterized by broad leaves and produce covered seeds within some type of fruiting body other than cones. Hardwood leaves generally change color and are lost during cooler months of the year. Softwood trees are generally characterized by green needles and produce seeds contained within cones. The seeds within the cones do not possess a covering layer as the hardwood seeds do. The needles of a softwood tree are largely kept throughout the year [10 - 12].

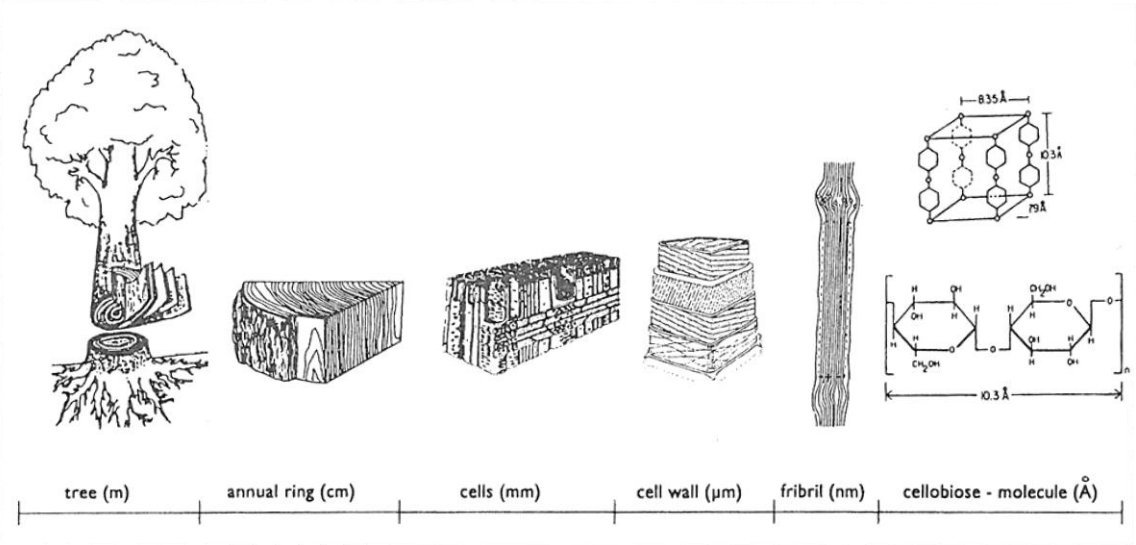


**Figure 1.** Hierarchical structure of wood. Figure adapted from Bucur [13].

It should be noted that the terms hardwood and softwood refer to the structure of the tree. Hardwoods are not necessarily harder or tougher than softwoods. A list of common hardwoods and softwoods and their associated side hardness (the average of the radial and tangential hardness) values are given below in Table 1. Balsa wood may easily be broken by hand, but it a hardwood. The wood examined in this report came from Douglas-fir trees. For this reason, the description below focuses upon the structure of softwoods.

Individual cells of wood are composed of cellulose, hemicellulose, and lignin. Cellulose is a straight chain polymer constructed from glucose; it is a homopolysaccharide (multiple units containing the same type of sugar). Glucose is just one of several sugars that are formed during photosynthesis. Two glucose molecules are used to construct one unit of cellulose, called a cellobiose. Cellulose chains may have between 15000 and 30000 units with approximate dimensions of ten μm ($10^{-6}$ m) in

length and eight angstroms (Å) ($10^{-10}$ m) in diameter [11, 13]. Structures formed using cellulose are ordered and considered crystalline. Hemicellulose is made of several types of sugars in addition to glucose; it is a heteropolysaccharide (multiple units containing the different types of sugar). While cellulose forms long, straight chains composed of thousands of units, hemicellulose is a branching molecule composed of hundreds of units. Hemicellulose is amorphous. Lignin is a complex and amorphous molecule that serves as a binder between cells and gives rigidity to cell walls [11 - 13]. While polysaccharides are hydrophilic, lignin is hydrophobic and aids in the transport of water through cells. The percentages of cellulose, hemicellulose, and lignin vary by tree species. Softwoods generally contain between 40 and 44% cellulose, 20 to 32% hemicelluloses, and 25 to 35% lignin by weight [11, 14].

**Table 1.** Common hardwoods and softwoods and associated side hardness [10]

| **Hardwoods** | | **Softwoods** | |
|---|---|---|---|
| Species | Side Hardness (kN) | Species | Side Hardness (kN) |
| Beech | 5.8 | Larch | 3.7 |
| Oak | 5.6 | Douglas-fir | 2.8 |
| Birch | 5.4 | Pine | 2.6 |
| Ash | 5.1 | Cedar | 2.3 |
| Maple | 4.5 | Spruce | 2.2 |
| Elm | 3.8 | Redwood | 2.0 |

Several chains of cellulose are brought together to form a crystalline structure called a fibril. Several fibrils are then bundled and held together with hemicelluloses. The bundles are called microfibrils. Several microfibrils are then attached to each other with lignin. Layers of microfibrils are used to construct cell walls [11, 12, 14].

The structure of a wood cell is shown in Figure 2. New cell construction begins with a thin membrane layer known as a primary wall. The primary wall (known as the P layer) is unique in that the microfibrils that form its construction are arranged in a random manner. After the primary wall is formed, three secondary walls are formed. The secondary walls are known as the $S_1$, $S_2$, and $S_3$ layers. The microfibrils in the $S_1$ layer are oriented between 50° and 70° to the longitudinal axis of the cell. The microfibrils in the $S_2$ layer are oriented between 10° and 30°. The $S_2$ layer is much

thicker than the $S_1$ and $S_3$ layers. While the $S_1$ and $S_3$ layers are four to six layers of microfibrils thick, the $S_2$ layer can be between 30 and 150 layers of microfibrils thick. The $S_3$ layer is at an orientation of between 60° and 90°. The $S_3$ is the innermost layer and the last to be formed [11, 12, 14].

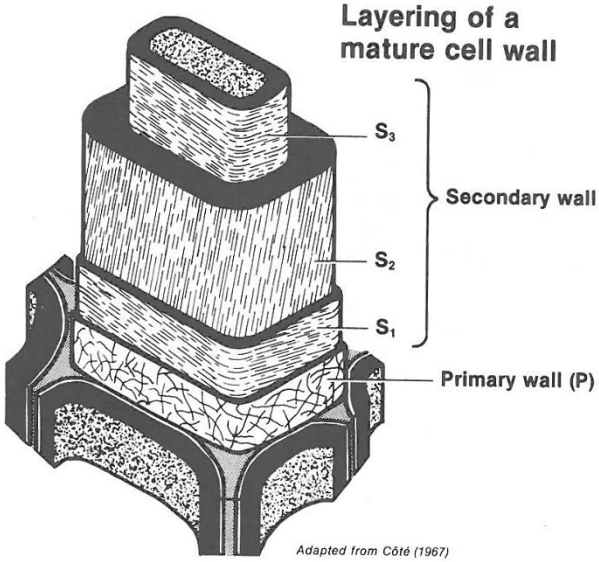


**Figure 2.** Wood cell wall layering. Microfibrils in the primary wall (P) are randomly oriented. Microfibril orientation in the $S_1$, $S_2$, and $S_3$ layers of the secondary wall are 50° to 70°, 10° to 30°, and 60° to 90°, respectively. Figure is extracted from Haygreen [11].

The cells in softwoods are primarily composed of two different types of cells: tracheids and parenchyma. Tracheids are long and slender. Their lengths are typically 100 times greater than their diameters. They serve as mechanical support and fluid transport for the tree. Tracheids compose between 90 and 95% of softwoods by volume. Parenchyma cells are similar in shape to tracheids, but are subdivided along their length. Their primary purpose is food storage for the tree [11, 12, 14].

Figure 3 shows a cross-section of a region of cells from a typical softwood. The cross-sectional face is labeled 1. The radial face is parallel to the region labeled 2. The tangential face is parallel to the region labeled 3. A single annual ring is labeled as 4 and is subdivided into earlywood (cells produced early in the growing season of a year), labeled 5, and latewood (cells produced later in the growing season), labeled 6. The difference in cell size and wall thickness between earlywood and latewood tracheids produces annual rings in trees. Annual ring production is described in greater detail below. Food is carried radially from the outer regions of the tree to the inner regions via

wood rays, labeled 7. If a tree is injured, sap is brought to the sight of the injury via resin ducts, labeled 9. Resin ducts are not cells, but are voids within the cell structure. If a radial ray contains a horizontal resin duct, then it is referred to as a fusiform ray, labeled as 8. The horizontal resin duct within the fusiform ray is labeled as 10. Fluid can move between tracheid cells through a bordered pit, labeled 11. Pits are regions where the cell walls of two adjacent cells are thin and connected. Pits occurring in parenchyma cells are simple pits, labeled 12. If pressure differentials develop between cells, then pits can become aspirated and effectively seals the pit. Pits can become aspirated during the process of a cell transitioning from sapwood to heartwood or during drying. Pit aspiration is partially the reason why preservative chemicals can penetrate the living, outer cells of Douglas-fir (the sapwood), but penetration into the inner, dead cells (the heartwood) is greatly diminished [11, 12, 14].

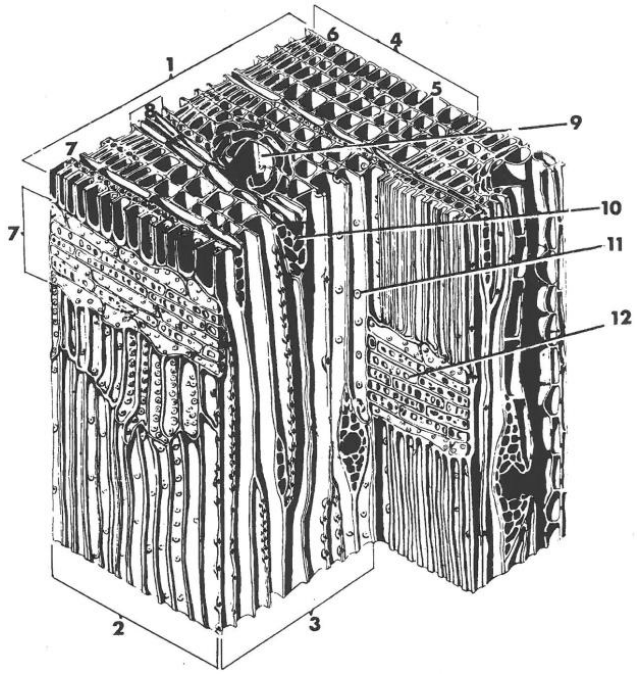


**Figure 3.** Wood structure of a softwood. (1) cross-sectional face, (2) radial face, (3) tangential face, (4) annual ring, (5) earlywood, (6) latewood, (7) wood ray, (8) fusiform ray, (9) vertical resin duct, (10) horizontal resin duct, (11) bordered pit, (12) simple pit. Figure extracted from Foulger [14].

Annual rings are formed by changes in the size and wall thickness of tracheid cells. Figure 4 shows the tracheid cells of both earlywood and latewood. The tracheid cells that are made during the earlywood period are larger and thin walled. Early in the growing season, new cell construction is fast and cells are large (relative to later in the

growing season). As the growing season progresses, the rate of cell production slows and the new cells produced are smaller. The change in new cell construction rate and size is largely affected by changes in available moisture throughout the growing season. It is important to note that the rates at which new cell production and cell development decrease are not equal. As a result, tracheid cells produced later in the growing season are smaller in size, and have greater wall thicknesses than cells produced early in the growing season. Latewood is harder, denser, and stronger than early wood. In some woods, like Douglas-fir and southern pines, the proportion of late wood to early wood is used to judge the strength of the wood [10]. Visually this cycle produces the annular rings seen in the cross-section of a tree.

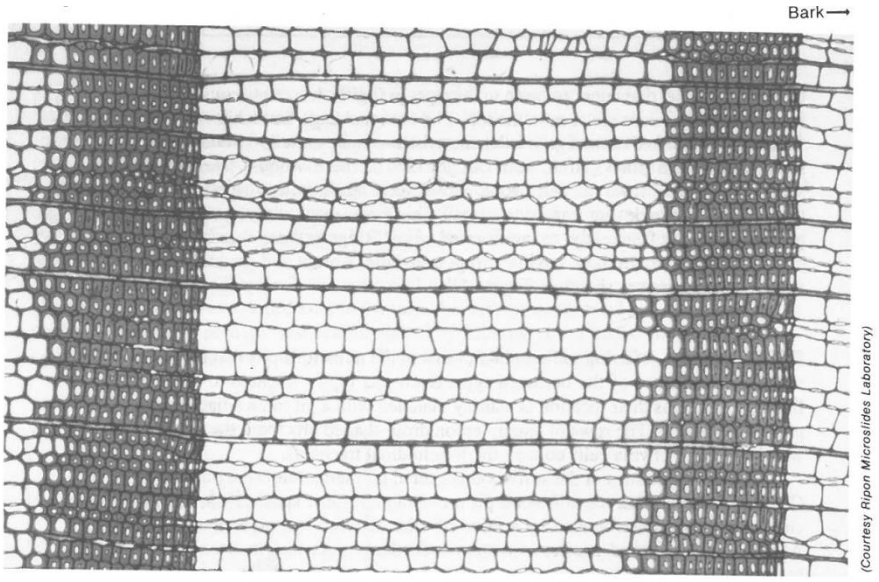


**Figure 4.** Earlywood to latewood transition in a western larch. Note the large, thin walled cells produced early in the growing season (earlywood), and the smaller, thick walled cells produced late in the growing season (latewood). Figure extracted from Haygreen [11].

Figure 5a is a cross-section of red oak. Red oak is a hardwood, but the regions described below are shared by both softwoods and hardwoods. The cross-section of a tree is a composed of a region of bark separated from a region of wood by a thin layer of tissue producing cells. The bark is divided into two regions, the inner bark and the outer bark. The inner bark, marked as region A, is a region of living cells that move sugars produced in the leaves through photosynthesis down to the tree. The inner bark is commonly known as phloem. The outer bark, labeled B, serves as a protective covering

for the tree. The cambium, labeled C, is a layer of cells that produce new tissue. The tissue produced can be either inner bark (phloem) or wood (xylem). The cambium is the thin gray line between the orange-yellow region of inner bark and the pale white-yellow region of sapwood. Wood, also known as xylem, is composed of sapwood, heartwood, and pith. Sapwood, labeled D, is composed of a combination of living and dead cells. The outermost sapwood cells are responsible for moving water and nutrients from the soil up to the leaves. The innermost sapwood cells are responsible for food storage. Heartwood, labeled E, is generally composed of dead cells that serve as mechanical support of the tree. The heartwood in Figure 5a is much darker than the sapwood. This darkening is caused by extractives. Extractives will be explained in greater detail below. The center of the tree has a small region of pith, labeled F, which are cells produced during height growth of the tree. Figure 5b is a cross-section of red pine. Wood rays are labeled as G. Latewood is labeled as H; earlywood is labeled as I. A single annual ring is composed of earlywood and latewood [10].

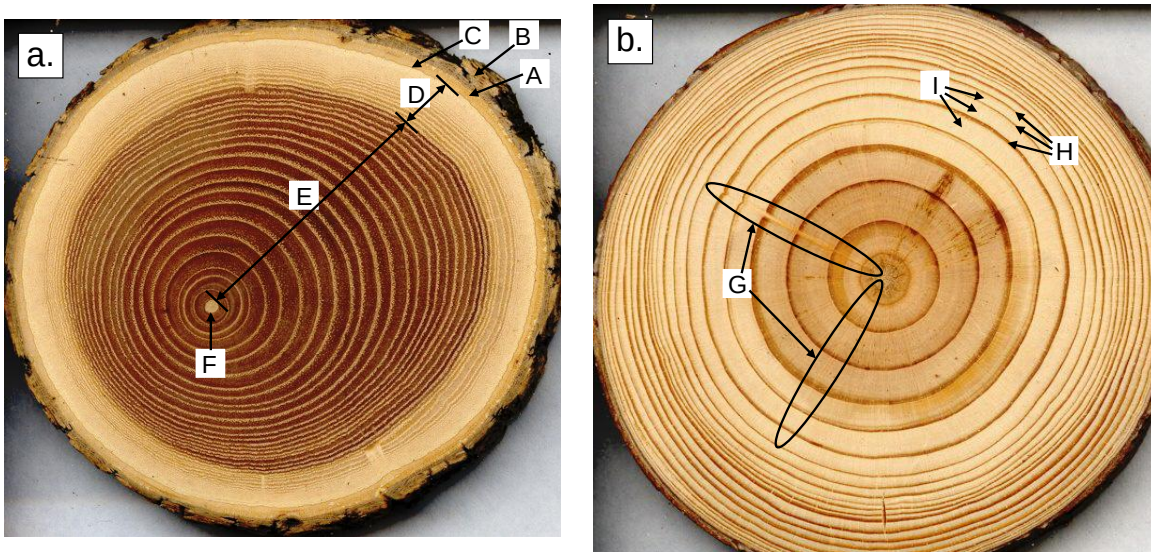


**Figure 5.** Tree cross-sections of **a.** red oak and **b.** red pine. Labels are (A) inner bark (living tissue, phloem), (B) outer bark (dry dead tissue), (C) cambium, (D) sapwood, (E) heartwood, (F) pith, (G) wood rays, (H) latewood, (I) earlywood. Pictures supplied by Dr. Henri D. Grissino-Mayer, University of Tennessee. Figure adapted from Forest Product Laboratory Wood Handbook [10].

Extractives are chemical compounds that form during the transition of wood cells from sapwood to heartwood. Red pine heartwood is clearly lighter than that of red oak.

The difference in shade is caused by the differences in concentrations and / or chemical composition of extractives. Concentrations can range from two to five percent in extractive free species like spruce to as high as 30% by mass in resinous Scots pine [15]. The properties of extractives affect wood qualities and commercial uses, but do not directly affect its mechanical properties. Extractives influence the durability, color, odor, and taste of wood. The extractives of red cedar are the source of the color and odor so coveted by furniture and paneling manufacturers. Bourbon is aged in white oak barrels to impart desirable taste characteristics. Many cookies are flavored with vanillin obtained from wood pulp rather than vanilla beans. Some of these extracts serve as deterrents to sources of decay. The heartwood of redwood, cypress, and cedar are resistant to termites. Research has recently been performed associating extractives with brown rot resistance in larches and Scots pines [16, 17]. Any decay resistance enjoyed by the heartwood does not extend to the surrounding sapwood. Sapwood of all species are susceptible to decay [11].

### 1.2. Brown Rot in Softwoods

Wood rotting fungi are generally put into two different categories: brown rot and white rot. Brown rot is a cellulose attacking rot that predominantly attacks softwoods. Brown rot causes infected wood to become browner in color and shrink. White rot is a cellulose and lignin attacking rot that predominately attacks hardwoods. White rot causes infected wood to become lighter in color but generally retain its original dimensions until advanced stages of decay. Brown rot and white rot do not exclusively infect specific types of wood. Both brown rot and white rot can infect softwood and hardwood [10, 18 - 20]. The rot model used in this report was based upon the work of McGovern [21] involving the effects of brown rot species *Gloeophyllum trabeum* (*G. trabeum*) on yellow southern pine. As a result, this report focuses on the effects of brown rot; white rot is not discussed.

The description below focuses on the characteristics, growth, and mechanical effects brown rot has upon the host wood. The chemical mechanisms through which the mechanical effects are brought about are not described here. Also, the biology of brown rot is discussed only to the point necessary to describe how it brings about the mechanical

changes in the host wood. No description is given of brown rot asexual reproduction processes or microbiology. An in depth discussion of the chemistry of brown rot can be found in [18 - 20, 22 - 26]. A description of the life cycle of brown rot can be found in [18].

There are over 106 varieties of brown rot [18]. The description provided here describes features generally true of many varieties of brown rot. Brown rot behavior is diverse and it is likely there exist varieties that exhibit behaviors other than those described here [19]. At a minimum, the description below is accurate for *G. trabeum* [18]. In nature, brown rot is most often associated with decay of softwood species and structures. As a result, it is frequently stated that brown rot has a greater capacity to decay softwood than hardwood. Laboratory tests have shown that brown rot is equally capable of decaying both softwood and hardwood species [19]. Brown rot is an internal form of decay that is generally reddish in color. Wood infected by brown rot becomes browner in color, as shown in Figure 6a. It often occurs in large structural timbers. Large infected areas are not necessarily uniform. Infected wood shrinks and cracks during the rotting process. Cracks can be either radial or tangential. Severely rotted wood cracks to such an extent that it takes on a cubical appearance, as shown in Figure 6b. At that point, the wood is fragile and can be crumbled into dust when handled as shown in Figure 6c [18, 20].


**Figure 6.** Examples of brown rot, **a.** brown rot in a timber cross-section, **b.** a log showing radial and tangential cracking, **c.** "cubes" of brown rotted wood.

Brown rot spreads when conditions are favorable for growth. Dry wood with a moisture content below 20% is usually safe from fungal attack [3, 18]. Most fungal decay occurs when the moisture content is above 30% [10]. It is also possible for the

wood to be too wet for fungal growth. Water soaked wood may have too little air on the interior to support fungal growth. Generally, the wood must have a moisture content above the fiber saturation point (~30% moisture content), but the cell lumen cannot be saturated. Temperatures of growth range by species, but are generally between 10°C and 35°C. Fungal decay ceases at temperatures below 2°C and above 38°C [10, 20].

The transmission and infection mechanism of brown rot is shown in Figure 7. Brown rot produces fruiting bodies on the surface of the infested wood. Spores from the fruiting body are distributed by the wind or insects. If a spore contacts wood susceptible to fungal attack and favorable growth conditions exist, then the spore will germinate and a new fungal body is produced [10].

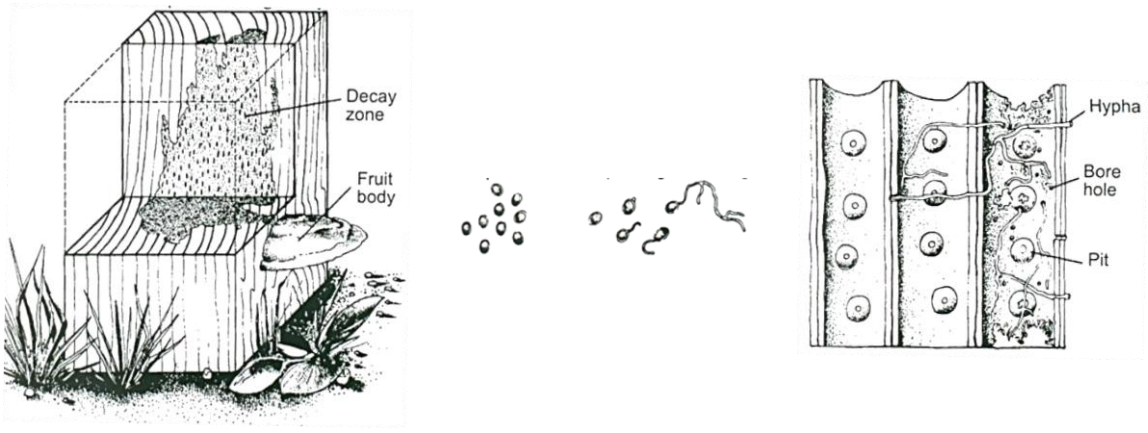


**Figure 7.** Transmission and infection of wood by brown rot: **a.** section of a post showing decay **b.** spores carried by the wind or insects, **c.** spores germinating, **d.** infected wood cells. Figures adapted from Forest Products Laboratory [10].

When a spore germinates, it produces a hypha. A hypha is a filament tube that grows apically. The hyphae are the means by which fungi spread during growth. The mass of hyphae that makes up the fungal body is called the mycelium, shown in Figure 8a. Brown rot grows in cell lumen and moves between cells using two different avenues: through pre-existing pits or through the creation of bore holes [18, 20, 22]. Hyphae easily penetrate the thin pits of cell walls. After penetration, the access point, either pit or bore hole, is widened to allow easier access. Wilcox noted in 1969 that brown rot hyphae almost exclusively used pits rather than bore holes [22]. Eaton indicated brown rot used both methods to spread between cells [18], and Goodell indicated that some brown rot

species prefer pit penetration over bore holes [20]. Hyphae spreading between wood cells via bore holes is shown in Figure 8b.

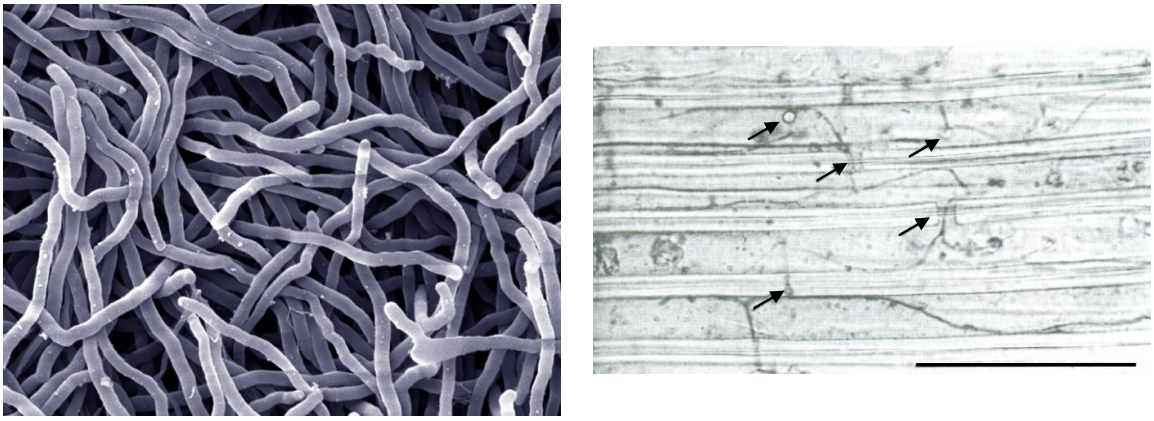

**a.** **b.**

**Figure 8.** Spreading fungus, **a.** Microscopic view of fungus. Individual strands are known as hypha (plural hyphae). The mass of hyphae is called mycelium [27], **b.** hyphae moving between wood cells using bore holes (arrowed). The bar at the bottom right of 8b represents 100 µm. Figure extracted from Eaton [18].

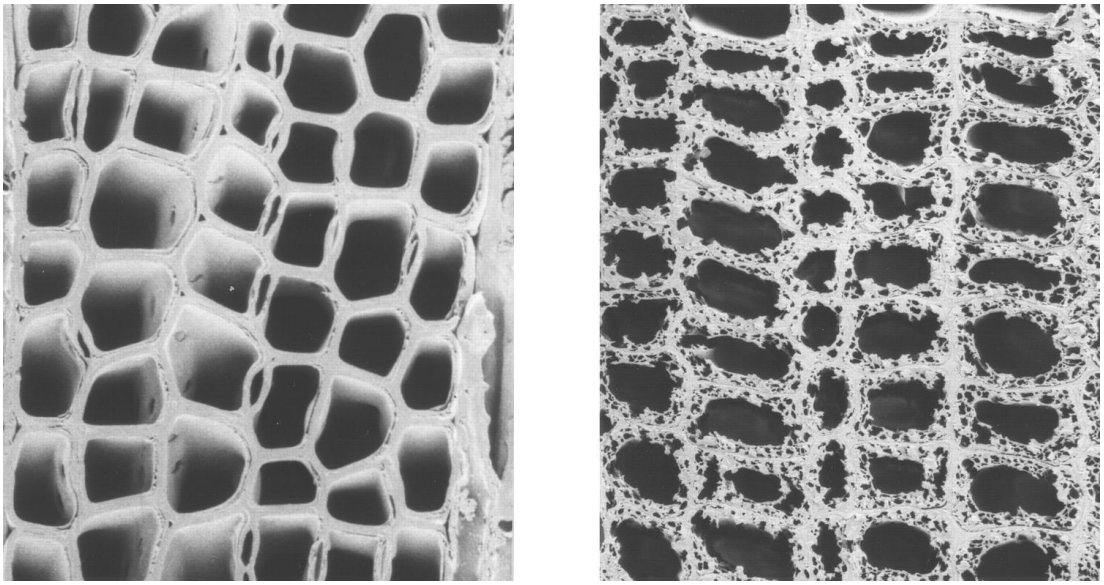

**a.** **b.**

**Figure 9.** Wood cell walls, **a.** sound wood, and **b.** decayed wood. Note the loss of mass in the decayed wall structure; however, the shapes of the original cells are largely maintained by a remaining lignin skeleton. Extracted from Filley [28].

Brown rot hyphae initially move into ray cells and axial parenchyma. Carbohydrates stored in the parenchyma cells provide a readily available energy source

for the fungus. From the ray cells and parenchyma, the brown rot has easy access to deeper regions within the wood in order to spread [20].

Once hyphae invade a cell, the cell degradation process is both rapid and uniform. Brown rot attacks and depolymerizes cellulose chains that make up the microfibrils of the cell. Brown rot also attacks hemicellulose. Brown rot modifies, but does not degrade lignin. Cell wall resistance to brown rot decay has been correlated to lignin content [22]. The $S_3$ and $S_1$ layers of the cell wall have a greater percentage of lignin than the $S_2$ layer. It is this higher lignin content that may explain why brown rot degradation begins in the $S_2$ layer, rather than the $S_3$ layer nearest to the hyphae [18, 20, 22]. Decay of the $S_2$ layer is not limited to regions near the hyphae, indicating that the degrading agent can diffuse through the $S_3$ layer to the $S_2$ layer [20]. As cells decay, cell walls collapse and small splits appear close to the microfibril orientation in the $S_2$ layer [18]. The cracking is exacerbated by the decaying process. Shrinkage of decayed cells due to moisture content loss is considerably greater than in a sound wood cell. The cracking and shrinkage causes the cubical appearance indicative of brown rot decay. Cells in advanced stages of decay are left with a lignin skeleton that maintains the shape of the original cell as shown in Figure 9. Nearly all of the mass loss from brown rot is cause by loss of the cell wall [22].

The depolymerization of the cellulose chains of the $S_2$ layer causes significant strength loss before significant mass loss has occurred. Mass loss is not a good indicator of wood strength. In early stages of rot, mass loss is not a sensitive predictor of strength loss. In some experiments, mass loss was undetectable until the host wood lost 40% of its strength. In later stages of decay, mass loss is misleading, because the conversion of wood mass to mycelium mass is not taken into account [20]. Winandy and Morrell [23] performed mechanical tests on Douglas-fir specimens with increasingly high levels of brown rot decay. A linear relationship was found between weight loss and strength loss. The modulus of rupture (MOR), the work to maximum load (WML) and the modulus of elasticity (MOE) were measured for each specimen. The percentage reduction in each of the properties was three to four time the weight loss estimates. It was found that changes in mechanical properties were a more precise measure of fungal decay. Figure 10a shows

the relationship between percent weight loss and percent loss of MOR for two forms of brown rot.

Curling, et al. [24] expanded upon the work of Winandy [23] by looking at the effects of brown rot on southern pine. The MOR loss rate exceeded the MOE loss rate. Figure 10b shows the percent reduction of each test parameter with respect to days of fungal decay exposure. Note that weight exhibits the smallest change of all of the recorded parameters. A five percent change in weight corresponds to a 40% reduction of MOR, an 80% reduction of WML, and a 20% reduction in MOE. Curling [24] expressed the percentage reduction of each parameter as a ratio of the percent reduction of weight. The ratios were 9:1 for WML, 4:1 for MOR, and 1.5:1 for MOE. It should be noted that when the percentage of weight loss was above 20%, the other three parameters had been reduced by approximately 100% (i.e. no residual strength was left in the wood).

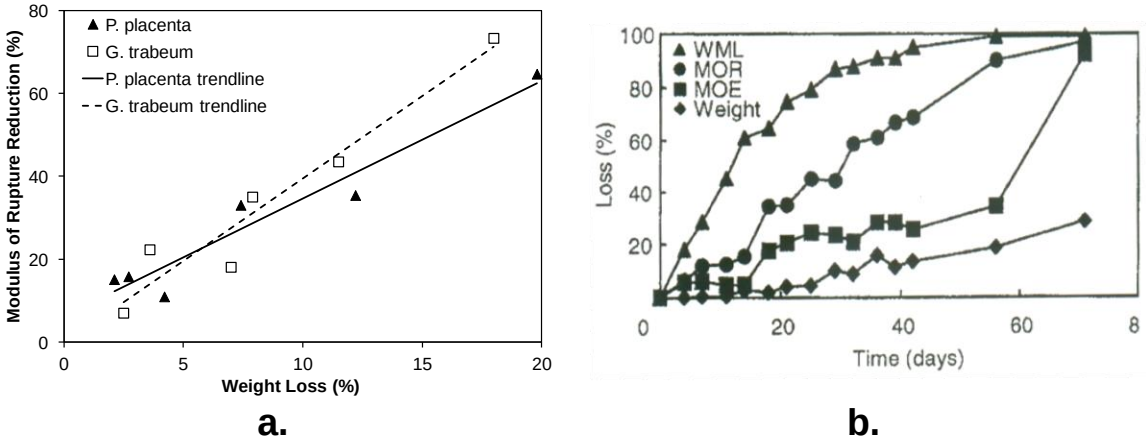


**Figure 10.** Changes to wood properties with weight loss from rot: **a.** Percent weight loss versus percent reduction in modulus of rupture for Douglas-fir exposed to different forms of brown rot. Figure adapted from Winandy [23]. **b.** Percent reduction in work to maximum load (WML), modulus of rupture (MOR), modulus of elasticity (MOE), and weight versus days of southern pine exposure to brown rot. Figure extracted from Curling [24].

Brown rot can drastically and rapidly reduce the mechanical properties of wood. In order to prevent failure of wood structures due to internal decay, inspection and maintenance are required. It is important that the inspection methods used do not compromise the strength of the wood. Nondestructive evaluation (NDE) methods are used to evaluate objects, structures, etc. without causing damage to the inspected specimen, and seem ideally suited for inspection of wood structures.

### 1.3. Current Pole Inspection Methods

Prior to beginning the literature review on nondestructive testing methods, it is informative to know some information about the current methods used to inspect utility poles. The inspection methods described here are from the 1996 Edition of the Wood Pole Maintenance Manual by Morrell [29], and are made in a typical ground test of a utility pole.

The inspector first performs a visual inspection of the general condition of the pole. Loose dirt and debris are cleared from the pole surface. Unusual features such as wide cracks (known as checks), holes, sawdust produced by insects, and damage are examined. If surface rot is suspected, a pick test can be performed by lifting a portion of the wood away from the pole surface with a sharp object. Examples of pick test results are shown in Figure 11. If the lifted portion splinters, then it is likely sound wood. If the lifted portion breaks abruptly, then there is likely surface rot. The pick test is often performed on wood exposed during excavation around the pole.

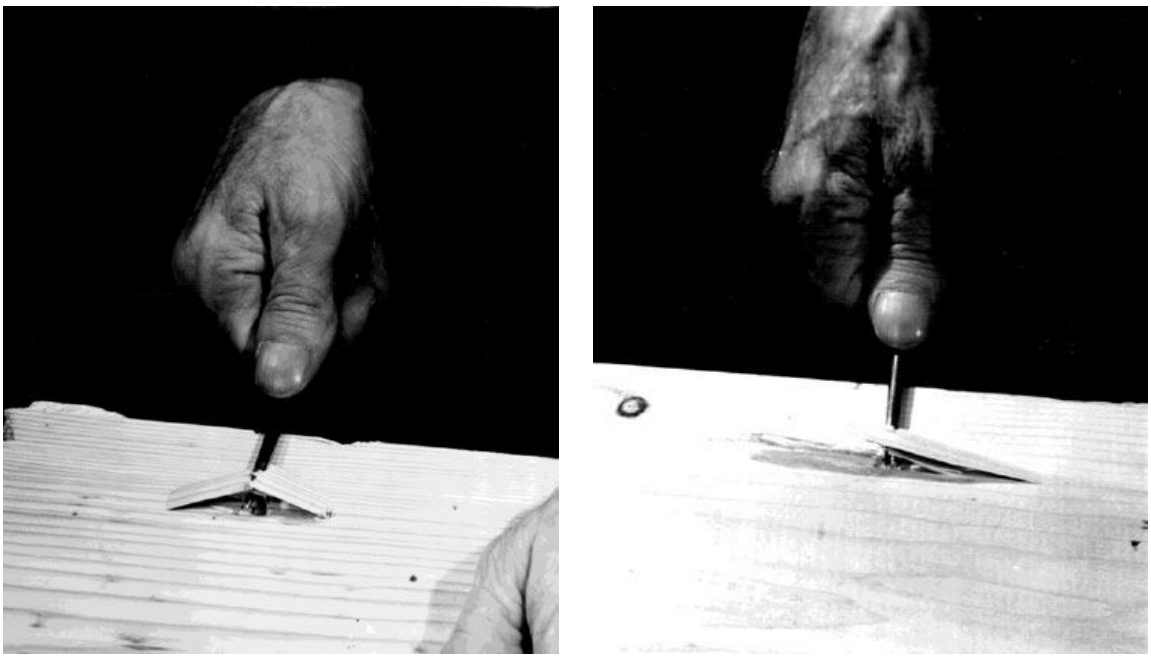

**a.** **b.**

**Figure 11.** Pick test, **a.** an abrupt break indicating surface rot, **b.** splintering indicating sound wood. Figures extracted from Morrell [29].

A sounding test is performed by striking the pole with a blunt object such as a hammer. The inspector determines the likely presence of rot by both the feel of the hammer at impact and the resulting sound of the impact. A sharp, ringing sound is indicative of sound wood. A hollow sound or the damped "thud" are indicative of internal decay. Sounding will reveal advanced decay, but is unlikely to reveal incipient or moderate decay. Also, the effectiveness of sounding is dependent upon the experience of the inspector.

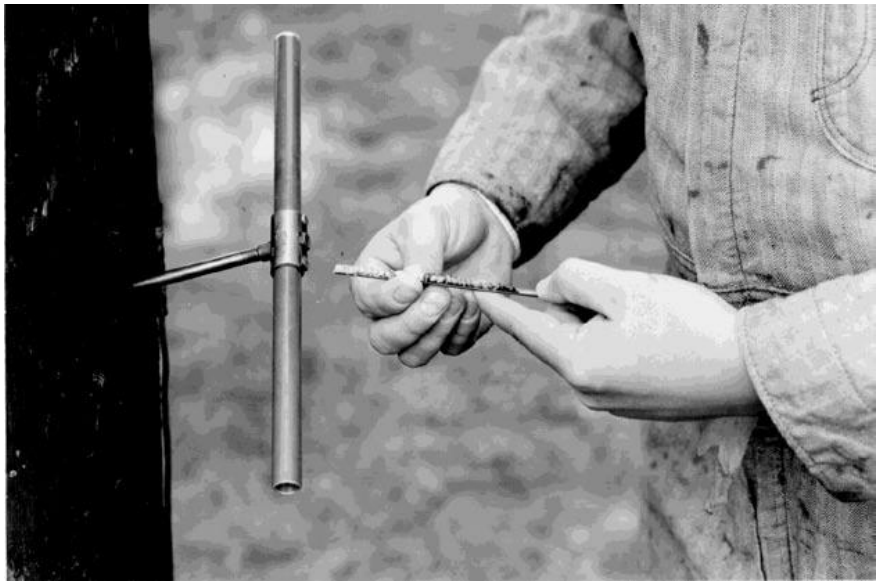

**Figure 12.** Increment borer and extracted core. Figure extracted from Morrell [29]

The inspector can perform a drilling and /or coring test after sounding. Locations that are usually subject to drilling or coring include areas just above the ground level, areas which sounding tests indicate may have internal defects, and areas near large cracks. A core is a thin strip of wood cut across multiple annual rings through the cross-section of the pole. It is obtained by using an increment borer, which is a hollow tube with a sharpened bit on the end. The core is examined for the presence of decay visually and / or through tests designed to determine the presence of fungi. An increment borer and an extracted core are shown in Figure 12.

Sudden decreases in resistance during drilling or coring are indicative of voids or areas of rot. If a defect is detected, then a shell-thickness indicator is used to measure the distance from the surface of the pole to the defect region. A shell thickness indicator is a thin rod approximately the thickness of the corer or drill used to make the hole. It has a slight hook on the end that enables the inspector to determine the location of the edge of the defect, as shown in Figure 13. If a defect is identified after drilling or coring, then additional holes should be drilled around the circumference of the pole to estimate the size of the defect. Once the defect size is estimated, then a decision can be made regarding treatment, reinforcement, or replacement.

Below grade inspection is likely to be required regularly during scheduled pole maintenance. Approximately 460 mm (18 inches) of soil is removed from around the base of the pole. Pole inspection from that point forward is similar to the procedure described above. After the below grade inspection, the pole is often retreated as preservatives within the pole can be lost to the surrounding soil. Holes made during the inspection are treated with preservatives and plugged with preservative treated dowels.

**Figure 13.** Shell-thickness indicator. The hooked end allows the inspector to identify rings and the edge of internal void. Figure extracted from Morrell [29].

## CHAPTER 2. LITERATURE REVIEW

When considering modern advancements in construction materials and the abundance of wood, it is reasonable to ask whether the value of developing new inspection methods for wood is worth the cost and effort. One answer could be that wood is relatively inexpensive, but construction is not.

Gravito [30] listed the energy consumption necessary to produce one ton of typical structural materials. The list is reproduced here as Table 2. The energy consumption is expressed in terms of kilograms of coal. The energy cost to produce one ton of simple concrete, the material closest to wood in terms of cost, is 3250% higher than the energy cost to produce one ton of wood. While it is unlikely that anyone questions the economic value of wood, it is striking how well wood poles and lumber compare with other structural materials.

**Table 2.** Comparative consumption of energy to produce 1 ton of material. Table from Gravito [30]

| Comparative Consumption of Energy | |
|---|---|
| To produce 1 ton | Exhausts (kg EC) |
| Aluminum | 4200 |
| Plastic | 1800 |
| Steel | 1000 |
| Cement | 260 |
| Block of Concrete | 26 |
| Simple Concrete | 26 |
| Wood | 0.8 |

kg EC: Equivalent kilos of Coal
Source: Lenec – National Laboratory of Civil Engineering (Portugal)

The cost of producing a single utility pole from wood (including preservatives) is less than any other material, but fixed costs of transport and installation are present for any pole, regardless of construction material. If wooden poles must be replaced much more often than a pole of another material, then the replacement cost can exceed the material cost. However, in practice, a wooden utility pole with proper preservative treatment and regular maintenance can have a service life exceeding 25 years [30].

Stewart [1] performed an economic analysis on utility pole inspection and replacements. At the time of his analysis in 1990, there were 100 million electric utility

poles in the United States. The analysis (performed assuming conditions within Colorado) showed the cost effectiveness of wooden utility poles over a 50 year lifespan with adjustments for the cost of poles, treatment, installation, inspection, maintenance, retreatment, and replacement. The analysis recommended the continued use of wood poles over any other construction material. One unstated assumption of the analysis was the effectiveness of inspection methods to determine the presence of decay in poles.

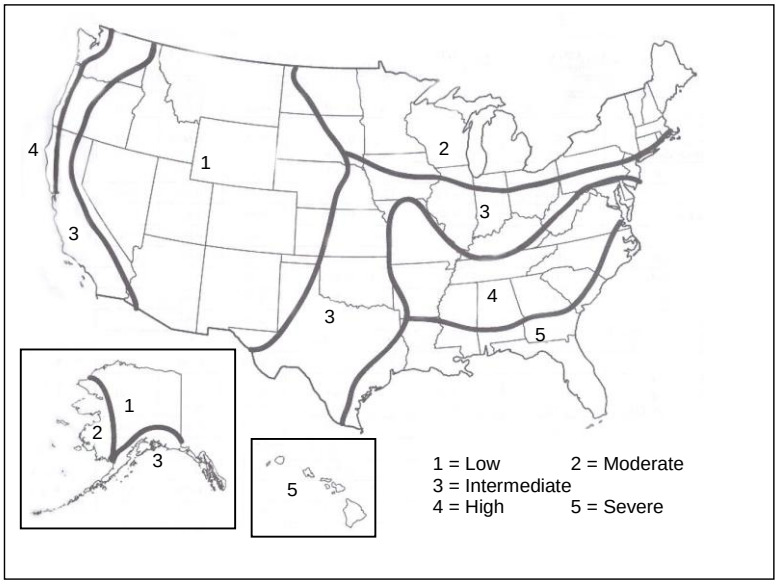


**Figure 14.** Deterioration zones. Figure adapted from Morrell [2].

In 2008, Morrell [2] published a survey of 261 utility companies that combined owned 42 million utility poles. Most respondents believed their poles lasted between 20 and 40 years. An estimated 252,000 poles were purchased each year (a 0.6% annual replacement rate). Wood decay is a common factor that reduces pole strength. In some regions, over half of the pole replacements were due to the presence of decay. The environment in which the pole is placed largely determines the risk of decay. The United States is divided into five deterioration zones as shown in Figure 14. The deterioration zones indicate the relative risk of biological decay from one, the lowest, to five, the highest. The zone of service is a consideration when decisions are made regarding applied preservatives and the inspection timetable. National Electrical Safety Code (NESC) mandates that utility poles maintain two thirds of their required design strength.

In order to comply with the NESC mandate, the utility company must have an inspection technique which accurately identifies the presence of pole decay.

The low cost, abundance, strength, and versatility of wood give it great value. Improvements in wood inspection techniques increase that value. Modern techniques for wood inspection first appeared in the early half of the 20$^{th}$ century. From that time forward, many researchers have explored how wood reacts to a myriad of different probing and examination methods. This section explores the capabilities and limitations of some of those methods.

### 2.1. Overview, Reviews and Status Reports

Numerous overviews have been published which give insight into the state-of-the-art in wood inspection over the last fifty years. A brief list of overviews is provided here for additional historical references. Many of the papers listed are described in greater detail in the subsequent literature review. In 1964, Galligan [31] authored a status report updating the readers to techniques employed at that time. Galligan discusses procedures used to determine: modulus of elasticity, modulus of rupture, density, moisture content, flaws, dimensions, and surface quality. He describes a variety of techniques including static testing, vibrational analysis, nuclear radiation, infrared radiation, electrical resistance, and ultrasound. In 1978, Wilcox [32] provided a summary of how rot changes the mechanical properties of wood. Decay identified through NDE techniques could be correlated to changes in wood density, toughness, compressive strength, and modulus of rupture. In 1981, Szymani [3] and Gerhard [33] authored overviews on grading of lumber using nondestructive evaluation (NDE). Szymani evaluated the feasibility of using various NDE techniques to evaluate lumber at production speed. He examined which techniques were best at identifying particular defects and concluded that ultrasound was the most promising for production speed evaluation if the difficulties of sensor coupling could be overcome. Gerhard [33] examined factors that influence the stress wave speed such as moisture content, knots, temperature, and grain angle. In 1988, Falk [34] provided a primer which described currently used inspection methods such as visual inspection, wood sounding, bending tests, sound velocity, acoustic emission, waveform analysis, microwaves, X-rays, and nuclear magnetic resonance. He also

describes a high correlation between stress wave velocity predictions and modulus of elasticity. In 1994, Ross [35] described nondestructive evaluation (NDE) techniques used to inspect several existing structures including: an eighteenth century mansion, a football stadium, a gymnasium, piers, bridges, a barn, a water cooling tower, wood utility poles, and the USS Constitution. The paper contained detailed summaries of the inspections. In 1996, Morrell [29] authored the Wood Pole Maintenance Manual. The manual describes field methods currently used to inspect wood poles, preservatives, sources and identifiers of biological attacks, and methods of treatment. In 2000, Beall [36] described the properties that were desirable to quantify and the associated inspection methods used to sense the properties. The review covered many properties mentioned above (density, moisture content, mechanical properties) and also included a review of adhesive bonding sensing. In 2002, Beall [37] produced a second overview. It supplemented the 2000 report with additional diagrams useful in describing the testing setups for some of the techniques as well as graphs to describe obtained data. In the same years, Kawamoto [38] examined the advantages and disadvantages of acoustic emission and acousto-ultrasonic techniques. The paper included discussions on sensor types and data processing. A focus was placed upon monitoring and control of kiln drying of wood. In 2003, Bucur [39] summarized several methods of high resolution imaging of wood structures. The review focused upon methods of obtaining tomographic views. A variety of techniques were described including those using X-rays, gamma rays, thermography, microwaves, ultrasonic waves, and nuclear magnetic imaging.

The primary inspection techniques used in this report fall under the umbrella of acoustic and / or ultrasonic inspection methods. The bulk of the literature review is dedicated to discussing these techniques. Other inspection methods are briefly described to give the reader a more complete view of wood inspection. Additional techniques described include: radiographic, chemical, electrical resistance, and thermographic.

### 2.2. Radiographic Inspection Approaches

Radiographic techniques were employed for pole inspections as early as 1938. At that time, the Detroit Edison company had a pole inspection management system that included obtaining radiographs of utility poles. X-ray pole inspection was described by

Stoker [40]. The inspection method entailed exposing a pole to a radiation source while film was placed on the opposite side of the pole. Inspectors were to be 25 feet away during the testing. The required exposure time was not given. Areas of high density would have lower exposure and thus appear brighter on the film. Initially, the round geometry of the pole caused unequal exposure on the film. X-ray paths passing through the edges of the pole traveled through less material than rays passing through the center. This problem was corrected by adding two aluminum wedges in the paths between the source and the edge of the pole. The experimental setup used is shown in Figure 15.

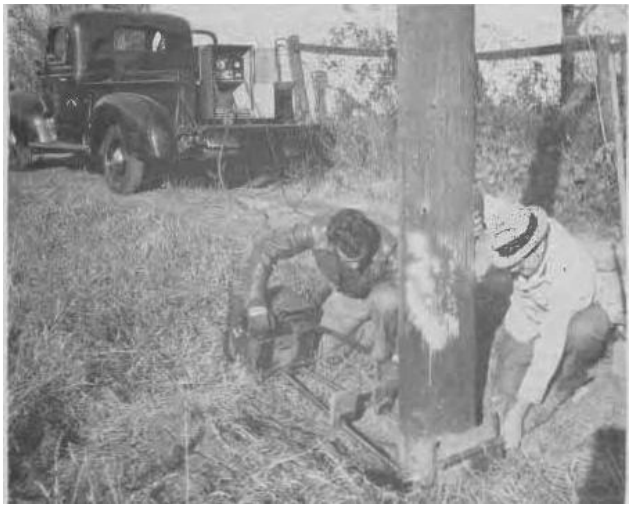

**Figure 15.** Radiographic setup used by Detroit Edison. Figure extracted from Stoker [40].

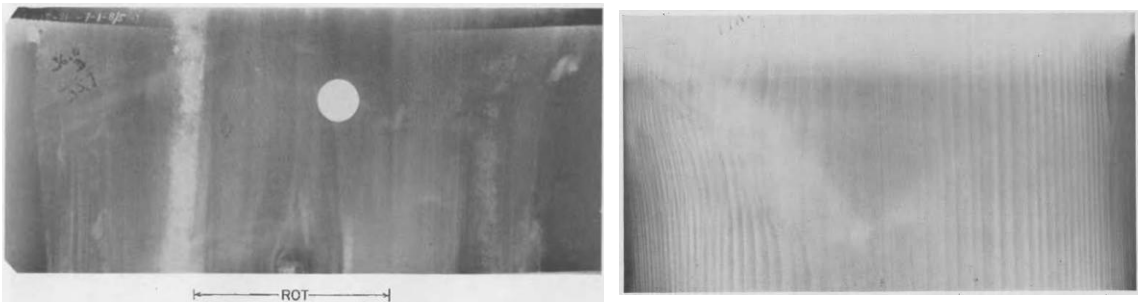


**a.** **b.**

**Figure 16.** Radiograph of utility poles, **a.** northern western cedar with center rot, **b.** southern yellow pine. Note the distinct vertical lines showing the annual rings. Figures extracted from Stoker [40].

The film was developed and checked for features associated with rot. The change in density between latewood and earlywood produced vertical lines along the width of the

radiograph. Loss of distinction between earlywood and latewood was an indicator of rot, though, in practice, it was difficult to definitively identify. The person interpreting the radiographs required specialized training as many features were indistinct. In addition, moisture within rotted regions of the poles add additional mass, potentially masking mass loss from the decay. Moisture content would prove to be a complicating factor for most radiographic techniques. Figure 16a shows a typical radiograph containing rot. Figure 16b shows a sound pine pole with distinct annual rings.

A total of 113 poles were radiographed and then subjected to a measured load to the point of breaking the pole. The break tests were performed to see how well the radiographs predicted strength compromised poles. Based upon the radiographs, 55 poles were condemned and 58 were not. The break tests revealed that ten of the condemned poles were sound, indicating that the use of radiographs had an error rate of approximately 9%.

Eslyn [41] examined decay in silver maples in Iowa. He obtained increment cores from 845 trees and tested them for basidioycetous fungi (brown rot is included in this category). If the fungi were found, then the tree was radiographed. Eslyn developed a thirteen pound thulium X-ray unit. Unlike Stoker's setup which was limited to ground level, Eslyn's unit was strapped to the tree and could be positioned anywhere along its height. Beyond that change, the setup was similar to Stoker: the X-ray unit was on one side of the tree and the film was on the other. Moisture content again masked some mass loss. The exposure time necessary for the radiation source to produce a usable radiograph varied logarithmically by the diameter of the tree. A seven inch pole required under 10 minutes of exposure time; a fifteen inch pole required more than 100 minutes of exposure; a 23 inch pole required over 1,000 minutes of exposure time.

In his overview, Galligan [31] discussed the use of X-rays, beta rays, neutron radiation, and gamma rays as means of determining wood density. It was noted that advancements in film sensitivity were making X-rays a usable field technique while radioactive isotopes had the potential to create lightweight, portable X-ray units. The difficulties presented by the presence of moisture content when using radiation were briefly discussed.

Miller [42] developed a prototype computerized axial tomography unit for use on utility poles. The unit weighed 24 kg (53 lbs), and had a resolution of 1 cm. It was capable of scanning a 30 cm (12 inch) diameter pole with a density of 0.65 g/cm$^3$. The glulam beams examined in Chapter 3 of this report had densities that exceeded this limit. Rather than using film, the device used a semiconductor radiation detector. The source and the detector rotated around the pole while taking measurements. Scanning a pole required approximately eight minutes. A 200 millicurie (200 mCi) americium 241 source was used. The radiation given off during eight minutes would be equivalent to a chest X-ray at one meter (between 50 and 100 microsieverts (μSv)), a dental X-ray at two meters (about 10 μSv), and eating a banana at 23 meters (75 feet) (bananas contain a trace amount of potassium 40, a radioactive isotope, which gives an exposure of approximately 0.01 μSv). The unit is shown in Figure 17.

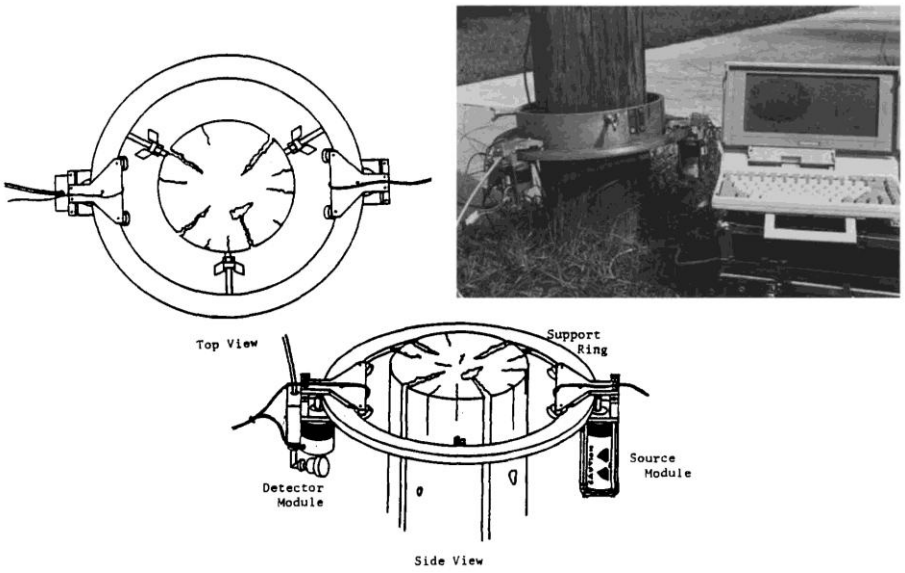


**Figure 17.** Portable radiographic unit. Figures extracted from Miller [42].

The analysis in Miller's paper is lackluster, as images of tested poles are presented without interpretation. The examined poles are not cut to compare the cross-section against the radiographic scan, so the results are not verified. The cross-sectional images produced are shown in Figure 18.

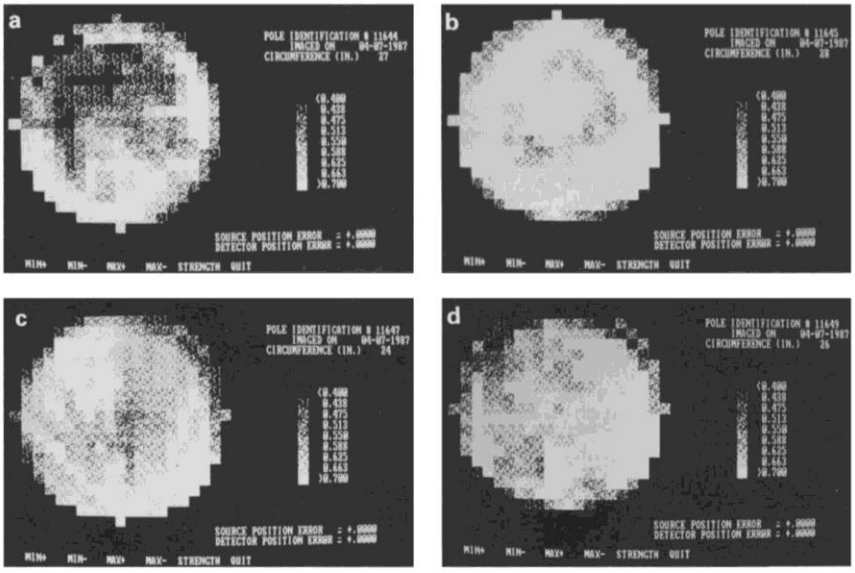


**Figure 18.** Radiographic tomograms of utility poles [42]

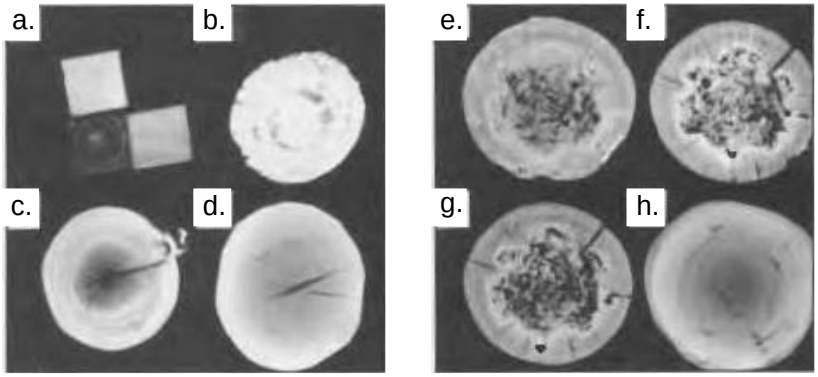


**Figure 19.** Collimated radiographic tomograms of utility poles; **a.** calibration specimens of known densities; **b.** through **d.** are examples presented to show image quality; **e.** through **g.** are scans from a single pole with internal rot at 100 mm below ground line, at ground line, and 100 mm above ground line, respectively; **h.** is a sound pole. Figures adapted from Davis [43].

Davis [43] developed a portable X-ray computerized tomography device that could scan poles up to 450 mm (17.7 inch) in diameter. The device appeared similar to Miller's in operation. The source was on one side, the detector was on the other, and the two rotated automatically around the pole. The device had a density discrimination of five percent and had a density precision within ±50 kg $m^{-3}$. A collimator was used on the source to improve image quality. The unit produced less than 25 µSv per hour at a distance of 2 meters, which is about one third of the radiation exposure from Miller's device. The inspection time required is five minutes. At 53 kg (116 pounds), Davis's

device was over twice the mass of Miller's device. The image quality produced by Davis's device was substantially improved as shown in Figure 19.

Schmoldt [44] examined the possibility of developing software that would automatically interpret CT scans produced from X-rays. The study was an effort to determine the feasibility of using X-rays in production lines to improve lumber output from trees. The problems of log scanning and software speed are not addressed. The software was unable to avoid errors associated with moisture content masking the presence of rot but it was capable of identifying defects such as knots and voids. Schmoldt concluded that even with the limitations, the automated system could increase mill output.

In her summary, Bucur [39] described typical x-ray and gamma ray testing equipment used to generate high resolution cross-sectional images. The test setup she described was substantially similar to both Miller's and Davis's devices. The primary area of improvement was in the amount and speed of data processing. Bucur indicated that nuclear magnetic resonance imaging provided great potential for production line use and was only limited by the current cost of the equipment.

### 2.3. Chemical Inspection Approach

Chemical indicators are binary tests that identify the presence of rot in a wood specimen. Eslyn [45] examined the prevalence of particular fungi by species of wood and location within the North America. Increment cores were taken from poles suspected of internal decay based upon sounding tests. The motivation of the study was to determine the most common types of fungi by wood species and location. The long term goal was to use the information to develop inspection techniques targeted at particular types of rot. He continued his work by infecting southern yellow pine with four different strains of fungi [46]. The paper focused upon identifying colored chemical indicators of rot for use on pole cores. Eslyn found three chemical combinations / procedures that could be used to determine the presence of internal decay: an application of butter yellow and methylene blue followed by bromcresol green and methyl orange, chrome azural-S, and methyl orange and indigo carmine. The chemical treatments were suitable for use in the field. Since chemical inspection methods do not allow the inspector to determine the

size of the internal decay, the techniques were not used in the glulam beam or utility pole analysis.

### 2.4. Thermographic Inspection Approach

In 1964, Galligan [31] reported that studies using infrared radiation were able to identify the presence of knots, but penetration was limited to three eighths of an inch (9.5 mm). In 2001, Wyckhuyse [47] examined infrared thermography as a means of inspecting wood poles. Several methods were attempted to create a heat differential through the pole. The heat source temperature was kept between 80°C and 100°C in order to prevent thermal damage to the wood. The theory was that the increased moisture content of rot would change the heat characteristics of rotten wood and make it visible to infrared inspection. In practice, the low thermal conductivity of wood prevented a heat differential from developing. Defects were also deep within the pole, making heat from an external source less likely to reach the defective region. After a half an hour of exposing the pole to an external heat source, defects located more than three centimeters (one and three eighths of an inch) from the surface of the pole had no significant temperature change. Wyckhuyse [48] continued the study by examining lumber and looking for shallow defects. One side of the wood specimen was subjected to a heat source, and the heat was allowed to travel through the wood. After two centimeters, the heat differential decreased to the point of being immeasurable. The specimens were allowed to continue heating. The time required to create a one degree Celsius differential at a six centimeter depth was more than 2000 seconds (over 33 minutes). Thermographic techniques did not have the ability to discern defects at the depths necessary in the analysis presented in this report and were not used.

### 2.5. Electrical Resistance Approaches

Shortle [49] examined the use of electrical resistance as a means of identifying internal decay. The device used was called a Shigometer® Model 7950. It should be noted that one of the other authors is A.L. Shigo. A hole is drilled into a pole and a wire inserted into the hole. The wire picks up electrical impulses and the meter records the

electrical resistance up to 500 kΩ. The moisture content in decayed wood is typically higher than that of sound wood; therefore, a significant drop in resistance would likely be an indicator of internal decay. The resistance was recorded for wire positions between 25.4 mm (1 in) and 139.7 mm (5.5 in) in increments of 12.7 mm (0.5 in). A total of 174 poles were examined. Seven poles were removed from the sample as advanced decay was apparent from visual inspection and / or probing. The poles contained seven different species of wood and encompassed five different preservative treatments. A threshold resistance of 125 kΩ (a 75% drop from the maximum meter reading of 500 kΩ) was an indicator of internal decay. Nine poles were selected for extraction and wedges were cut from the poles to compare against the Shigometer® predictions. The method correctly predicted the internal condition of 161 of the poles. The poles that were not correctly identified were assumed to be decayed when they were actually sound.

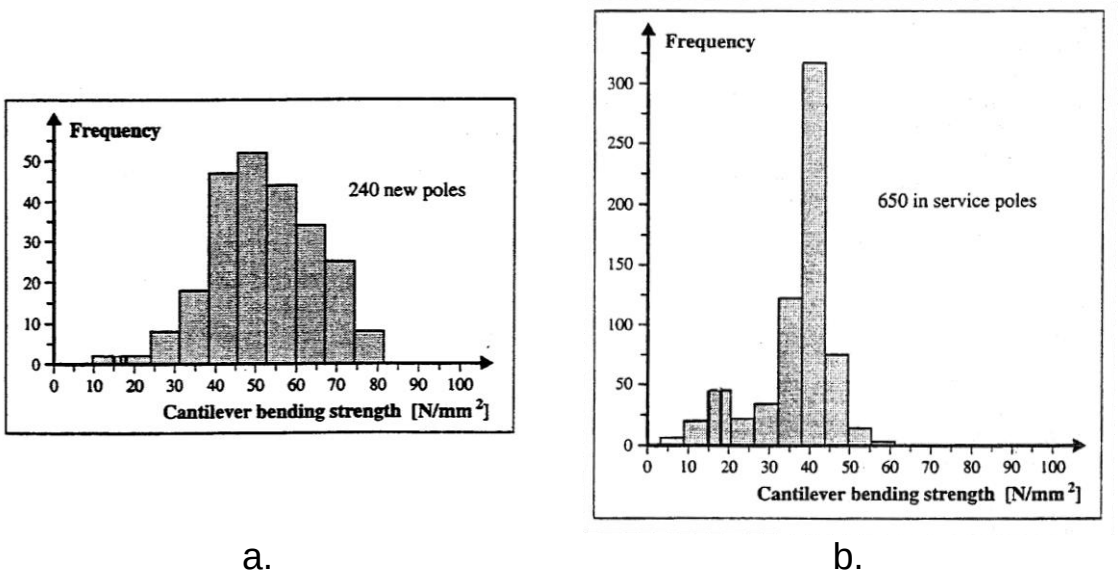


**Figure 20.** Pole cantilever bending strength, **a.** 240 new poles, **b**. 650 in service poles. Figures extracted from Sandoz [50].

Sandoz [50] used two penetrating electrodes to simultaneously obtain moisture content level and hardness data. The analysis included an examination of the bending strength of 240 new poles and 650 poles that had been in service. The strength histograms are shown in Figure 20. The analysis also examined the location of failures in

the in-service poles. Figure 21 shows the location of the failures with respect to ground level. A large portion of the failures occur at or about ground level.

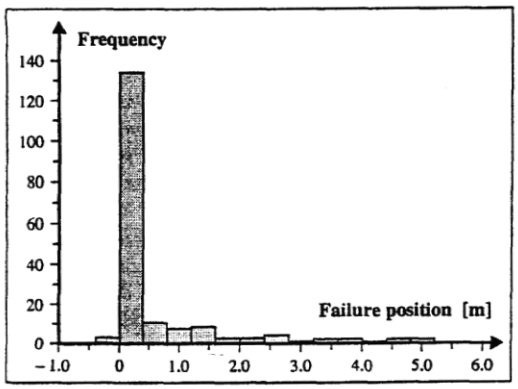


**Figure 21.** Pole failure location with respect to ground level. Sample size included 200 poles. Figure extracted from Sansoz [50].

There was weak correlation between moisture content and bending strength or hardness and bending strength with a goodness of fit parameter, $r^2$, values of 0.319 and 0.136, respectively. Sandoz developed an empirical relationship between moisture content and hardness to estimate pole residual strength. The correlation between the estimated residual strength and the actual residual strength was much higher than either of the individual metrics, $r^2$ of 0.701, but was still low overall. However, estimated strength showed clear differentiation between sound and rotten wood. It should be noted that the paper detailed the virtues of the Polux device which was apparently built by the authors.

Nicolotti [51] used electric tomography for detection of decay in trees. Wood resistivity is affected by the species, moisture content, and the presence of rot. The rotting process produces ions which lower wood resistivity. The tomography was performed by first driving sixteen electrodes into the surface of the tree spaced equidistant around the circumference. Each electrode was driven in a distance of one centimeter. Current was applied through two of the electrodes and resistance measurements were taken between them. Each tomography used 96 independent measurements. A strong relationship between wood resistivity and moisture content was noted. There was good agreement between test results and actual decay in the cross-section when the decayed geometry was regular and the decay region relatively

homogenous. Measurements became more difficult when the decay geometry was irregular and / or the decay region was inhomogeneous. Hardware and software issues contributed to error in the method. The measurement device used in the test was designed for low impedance materials. The inversion software used to calculate the tomography from the independent measurements assumed the body of the trunk was perfectly round.

### 2.6. Effects of Moisture Content on Nondestructive Evaluation of Wood

Moisture content (MC) affects almost every aspect of wood. Wood characteristics altered by changes in MC include, but are not limited to: density, attenuation, wave velocity, modulus of elasticity, and resistivity. DeGroot [52] concisely expressed the difficulties of developing a nondestructive testing method for wood when he stated, "Ideally, any NDE technique for monitoring residual strength or actual loss of material in biodegraded wood would be independent of mechanisms of degradation and should not be unduly influenced by variations in wood moisture content."

MC is the amount of water a piece of wood contains relative to its dry weight [53]. It is possible for wood to contain more water mass than wood mass, and therefore, have a MC above 100%. The equation for MC is shown in Equation 1.

$$MC = \frac{W - W_o}{W_o} \times 100\% \quad (1)$$

Where:
MC is moisture content
W is the weight of the wood specimen including water
$W_o$ is the weight of the oven dried specimen devoid of water

Wood has the capacity to hold water in two ways. Water molecules can bond to the cellulose and hemicelluloses in the cell walls. Water can also fill the interior of the wood cells. When water is first brought into the cell, it bonds with the cell walls. As it bonds to the wall, the cell swell and the walls soften, decreasing the elastic modulus. This continues until the bond locations in the cell walls are all filled. This is known as the fiber saturation point (FSP). The FSP is usually between 20% and 30% MC. At that

point, water begins to collect within the interior of the cell. The fibers in the cell wall do not take in additional water, so the elastic modulus of the cell wall does not change. However, as air within the interior of the cell is replaced with water, the elastic modulus of the cell increases [53].

In 1951, Fukada [54] examined the interaction between MC, frequency, and attenuation using mechanical excitations between 100 Hz and 5 kHz. The sample size was limited, but it was clear that both parameters affected attenuation in nonlinear manners. Eslyn [41] in 1959 indicated that intermediate and advanced decay saturated with water was difficult to detect using X-ray inspection. In developing an inspection tool for Detroit Edison in 1965, Miller [55] indicated that attempts were made to use resistivity, dielectric constant, and transmission of radio frequencies as a tool of inspection were tried, but the methods were too sensitive to MC. The decision to use a mechanical source (a hammer) and piezoelectric transducers was at least partially based upon the methods relative insensitivity to MC versus the other methods mentioned.

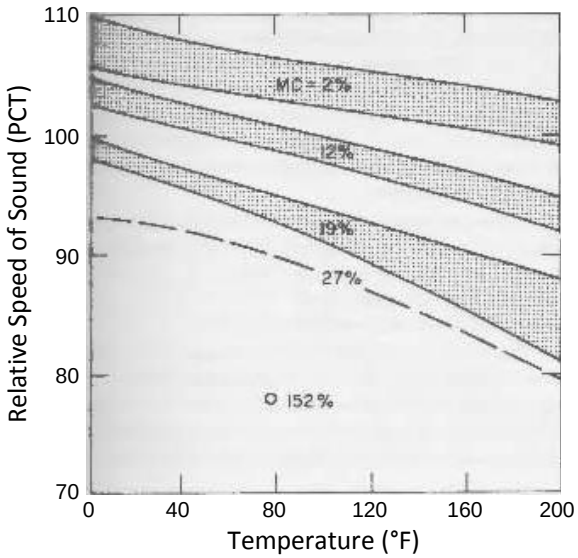


**Figure 22.** Temperature and moisture effects on wave speed through wood. Adapted from Gerhards [33].

In his review, Gerhard [33] compiled a variety of sources to show how stress wave speed parallel to the wood grain decreases as the MC and temperature increases. The plot is reproduced here as Figure 22.

James [56] examined the effect moisture gradients had upon longitudinal wave propagation in wood. No consistent relationship between usual drying moisture gradient

and the shape of the wavefront was identified. Wavefronts appeared to remain nearly planar in the presence of transverse moisture gradient. Wave speed measurements indicated the speed of sound through a specimen undergoing kiln drying increases immediately as the drying process begins. This was true even when the average MC level was well above the fiber saturation point. The observation led to the conclusion that wave energy travels through dry areas more than wet areas. This observation is supported by the phenomenon known as the Wielandt effect [57] which states that ray paths avoid areas where the wave velocity is low compared to an alternative path.

Quarles [58] examined how the ultrasonic wave propagation was effected by MC and grain angle. The test specimens were 20 mm cubes of Douglas-fir and California black oak. Six different moisture levels were used with approximate percentage values of: 0, 3, 9, 24, 70, and 120. Quarles conducted through-transmission experiments and measured signal attenuation using root mean square (RMS) voltage. The tests showed that attenuation was much greater at higher MC. This was especially true when the MC exceeded the fiber saturation point.

Sakai [53] examined the relationship between MC and ultrasonic velocity and attenuation in wood. The frequency range chosen was 1 MHz. Nine species of wood were examined: hinoki (Chamaecyparis obtusa), pine (species unspecified), cherry (Prunus verecunda), hoonoki (Magnolia obovata), metasequoia (Metasequoia glyptostrobides), Douglas-fir (Pseudotsuga menziesii), white lauan (Parasharea spp.), hiba arbor-vitae (Thujopsis doabrata), and Japanese cedar (Cryptomeria japonica). Of the woods tested, pine and Douglas-fir had the most distinct earlywood and latewood. Earlywood and latewood have different wave speeds; thus, the distinctness contributed to error in the velocity estimates for those two types of wood. The wave velocity decreases sharply (from 100% to about 80%) as the MC increases to the FSP (from 0% MC to between 20% and 30% MC). As the MC increases above the FSP, the velocity continues to decrease, but with a much shallower slope. Figure 23 shows the relationship between MC and longitudinal velocity in wood. The elastic modulus decreases up to the point of the FSP, but then increases as the air within the cell is replaced with water. Figure 24 shows the relationship between elastic modulus and MC. Attenuation remains relatively constant at low MC and then begins to decrease. Attenuation is greatly affected by free

water in the wood cell. The decrease in the attenuation does not exactly match the FSP as shown in the velocity versus MC graph. Some water begins to collect in the wood cells; prior to the FSP. The velocity is insensitive to the water within the cell, however, the attenuation is sensitive to it. Therefore the MC at which attenuation reduction becomes noticeable is lower than the FSP. Figure 25 shows the attenuation versus the MC. The attenuation is expressed in terms of decibel (dB) reduction between input and output.

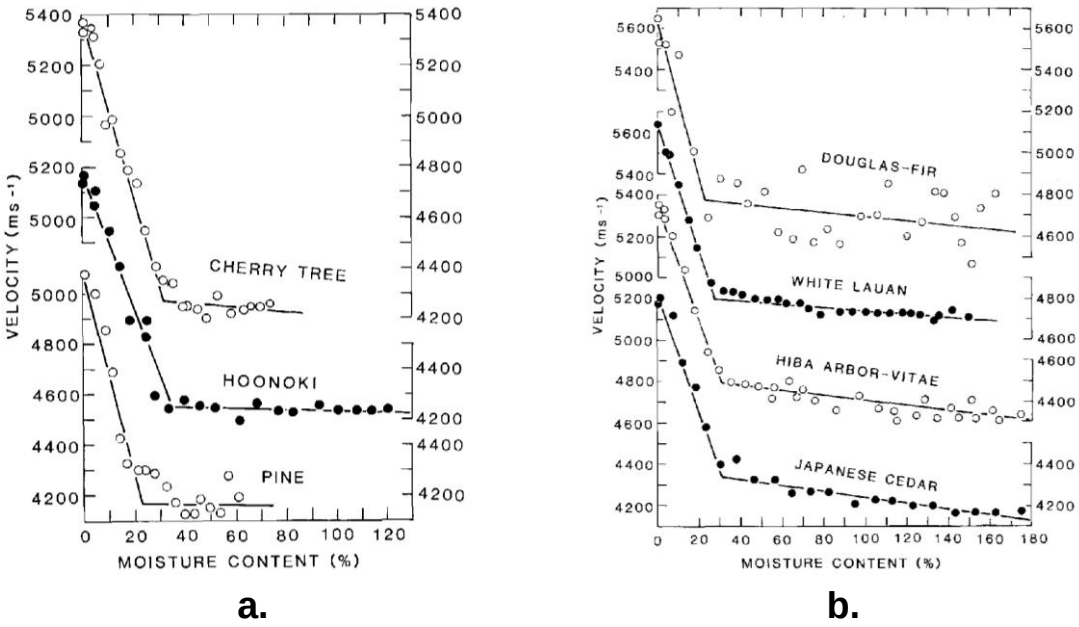


**Figure 23.** Longitudinal wave velocity in wood versus moisture content, **a.** Graph showing cherry tree, hoonoki, and pine, **b.** Graph showing Douglas-fir, white lauan, hiba arbor-vitae, and Japanese cedar. Figures extracted from Sakai [53].

Ross [59] indicated that MC greater than 30% is a condition suitable for fungal growth. In addition, if the MC of a pole exceeded 20% during a long dry period of the weather, then the pole likely contained interior rot. Mishiro [60] and Olivito [61] determined ultrasonic velocities in the longitudinal and radial directions for various wood species as a function of MC and concluded that it was possible to use the velocity to determine the MC as long as the MC was below the FSP. In a 2000 overview, Beall [36] discussed several MC sensing techniques. In 2002, Beall [37] also listed several sources that discuss the effects of MC on wood properties.

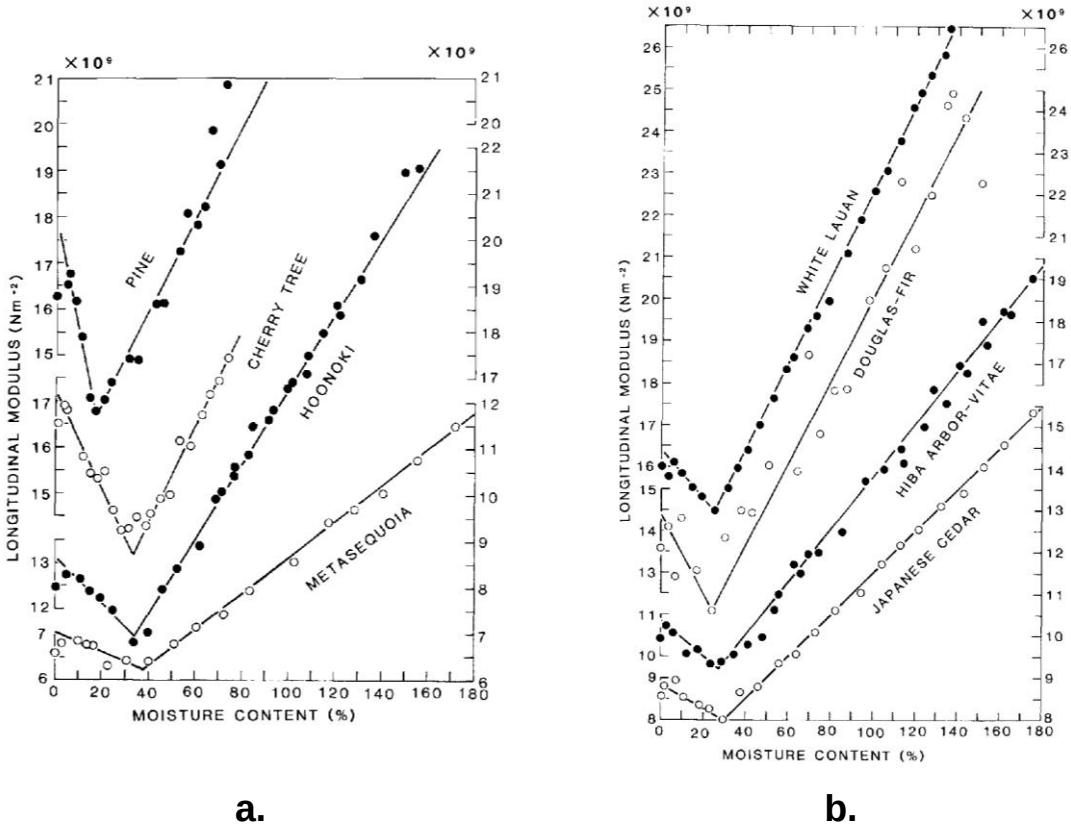


**Figure 24.** Longitudinal elastic modulus of wood versus moisture content, **a.** Graph of cherry tree, hoonoki, pine, and metasequoia, **b.** Graph showing Douglas-fir, white lauan, hiba arbor-vitae, and Japanese cedar. Figures extracted from Sakai [53].

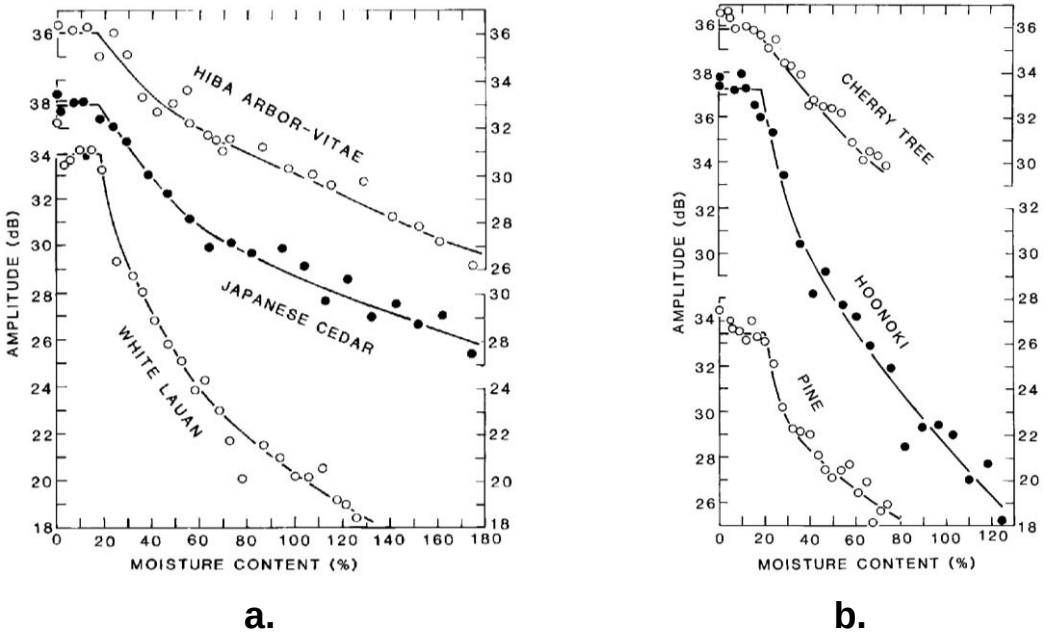


**Figure 25.** Decibel reduction of output versus moisture level, **a.** Graph of cherry tree, hoonoki, and pine, **b.** Graph showing white lauan, hiba arbor-vitae, and Japanese cedar. Extracted from Sakai [53].

When the glulam beams and utility pole specimens were received, they were placed in the climate controlled environment of the laboratory at approximately 35% relative humidity and a temperature of 70°F for several weeks prior to testing. The equilibrium moisture content of wood kept at those conditions is 6.9% [62]. No attempt was made to control MC beyond the environment of the lab. The assumption was made that MC changes within the stored specimens would be small and have little impact upon the testing results.

### 2.7. Acoustic and Ultrasonic Techniques

The analyses in this report are acoustic and ultrasonic in nature. For that reason, the emphasis in the literature review is placed upon describing similar techniques. The acoustic / ultrasonic section is divided into three subsections. The first is wood characterization. The papers presented therein describe techniques used to measure wood properties such as velocity, attenuation, modulus of elasticity (MOE), and modulus of rupture (MOR). The second section covers lumber and glulam beams; the third covers poles and trees. The main differences between the two groups are the dimension of the wood structure and the internal geometry. Wood is highly attenuating; thus, some techniques used to inspect lumber do not work on poles with larger dimensions due to signal loss. In addition, the cylindrically orthotropic nature affects wave propagation across the pole or tree cross-section, but in most lumber, that geometry is largely destroyed.

#### 2.7.1. Wood characterization

Acoustic and ultrasonic techniques have been used to measure a variety of wood characteristics including, but not limited to: wave velocity, elastic modulus, attenuation, and signal rate of decay. In 1950, Fukada [63] calculated the elastic modulus and the signal rate of decay of a signal in wood blocks. An electromotive force was applied to a wood block until a resonant frequency was excited. The frequency range examined was between 100 Hz and 5 kHz. At that point, the power was removed from the source and the drop in signal with respect to time was measured. The elastic modulus was calculated

from the excitation frequency and the mode of excitation. The results clearly showed that the signal rate of decay was frequency dependent, but elastic modulus appeared to be independent of frequency.

Dunlop [64] examined the effects that temperature had on damping and determination of elastic modulus. Moisture content and excitation frequency were strong influences on both damping and modulus of elasticity. The degree to which the temperature affects damping and modulus of elasticity appears to be greatly influenced by the moisture content.

Bucur [65] used an ultrasonic method to estimate wood stiffness and then compared the estimate to material testing results. Increment cores were extracted from living beech trees. The speed of the ultrasonic waves through the cores was recorded in the three primary directions: longitudinal, radial, and tangential. The frequencies examined were 80 kHz and 2 MHz. Primary and shear waves were both examined. The wave speeds were used to estimate the wood stiffness using relationship shown in Equation 2.

$$E = \rho c^2 \tag{2}$$

Where:
E is elastic modulus
ρ is density
c is wave velocity

The tests were accompanied by a regression analysis that attempted to correlate the variation in the measured elastic modulus to variations in one or more of the following: density, velocity, and velocity squared. Bucur found that over 99% of variations in wood stiffness were explainable by variations in some combination of the three variables. In addition, Bucur's results indicated that longitudinal velocity increased with frequency while radial and tangential velocities decreased with frequency. Bucur authored a second paper using largely the same methodology [66]. The test specimens were 16 mm cubes rather than increment cores. At that size, the ring curvature could be neglected. The tests were performed using two difference source frequencies, 500 kHz, and 1 MHz. In the follow up paper, Bucur examined the properties of Douglas-fir, spruce, pine, beech, oak, and yellow poplar.

Suzuki [67] looked at the effects of grain angle on ultrasonic velocity for two types of wood, sugi and lauan. The study was confined to the longitudinal - radial plane. No measurements of tangential velocity were made. Suzuki observed that the ultrasonic velocity decreased rapidly as the grain angle to the source increased from 0° to 45°. As the grain angle increased from 45° to 90°, the velocity continued to decrease but the change was not as pronounced.

In 1992, Bucur examined the attenuation of ultrasound in wood [68]. Bucur measured the attenuation in terms of decibels per centimeter. Five frequencies were used: 0.10, 0.25, 0.50, 1, and 1.5 MHz. The effects frequency, wave direction, and grain angle have upon attenuation were explored. Attenuation increased with frequency. The direction of the wave also affected attenuation. Tangential attenuation was highest and longitudinal attenuation was lowest. The frequency range studied was above the frequencies examined in this report. The attenuation values reported were large. Bucur authored another paper looking at factors that could potentially affect the attenuation values [69]. The geometry of the radiation field from the source, the wave scatter, and absorption characteristics of the wood were examined. McGovern obtained attenuation values close to those reported by Bucur when the transmission ratio between the transducer and the wood was neglected [21]. McGovern developed polynomials based upon empirical data relating attenuation and wave velocity to frequency. The attenuation values were corrected for losses at interface between the wood and transducer. A set of polynomials was developed for waves traveling in any of the three orthogonal directions of wood (longitudinal, radial, and tangential), and were developed for both dilatational and shear waves. McGovern developed her polynomials while examining loblolly pine. The polynomials are described in greater detail in the simulation section of this report. There was good agreement between Bucur's and McGovern's velocity values.

Mishiro examined the influence that density [70] and grain angle [71] had upon ultrasonic velocities. Mishiro found that, when outliers were removed, ultrasonic velocity was independent of density. Tangential velocities tended to increase as radial velocities increased. There appeared to be no relationship between longitudinal velocity and either radial or tangential velocity. Some of the conclusions were formed by comparing results between species of trees, which may not be valid. During the grain

angle tests, the minimum velocity was found to be at an orientation of 50° with respect to the wave propagation direction. It was thought that the velocity would begin at a value equal to the radial velocity at a grain angle of 0° (transducer is parallel to the rings and transmitting perpendicular to them) and would transition to a low value equal to the tangential velocity at 90° (transducer is perpendicular to the rings transmitting parallel to them). However, the transition from radial to tangential velocity for the three softwoods tested produced a "saxophone" shaped curve which had a minimum below both the tangential and radial velocities (The author does not refer to the shape of the curve as a saxophone; however, it conveys a descriptive image of the shape). Mishiro described the wave speed as a function of grain angle in Equation 3.

$$V_\theta = V_0 \cos^n \theta + V_{90} \sin^n \theta \tag{3}$$

Where:
$V_\theta$ is the velocity at grain angle $\theta$
$\theta$ is the grain angle
$V_0$ is the velocity at 0° grain angle (the radial velocity)
$V_{90}$ is the velocity at 90° grain angle (the tangential velocity)
n is an empirically determined exponent.

Berndt [72] created high resolution images of wood using ultrasound. The wood examined was waterlogged southern pine. The wood was submerged in water. Two sets of transducers were used with center frequencies of 1 and 5 MHz. The lateral dimensions of the test specimens were 70 mm by 100 mm. The dimension of the specimens in the direction of wave propagation was between 3 and 70 mm. The through-transmission data was sensitive enough to pick up differences in earlywood and latewood.

### 2.7.2. Inspection of glulam beams and lumber

Acoustic and ultrasonic techniques have been part of wood inspection for decades. In 1981, Szymani [3] compiled a report on defect detection in lumber. The report examined the feasibility of nondestructive evaluation in lumber production lines. Szymani examined inspection techniques based upon optical, ultrasound, microwaves, x-rays, and neutron methods. It was concluded that ultrasonic methods were the most promising for production line internal defect detection if the difficulty of achieving good

coupling between sensor and lumber could be overcome. Szymani summarized the benefits and disadvantages of each inspection technique. Those findings are reproduced in Table 3.

**Table 3.** Comparison of selected defect detection methods. Table adapted from Szymani [3]

| GENERAL CLASSIFICATION OF DEFECT DETECTION METHODS(major variation in methods) | PROPERTIES SENSED OR MEASURED | Lumber defects detected[a] | | | | | | | | | | | | ADVANTAGES | LIMITATIONS |
|---|---|---|---|---|---|---|---|---|---|---|---|---|---|---|---|
| | | Biological | | | | | | | Manufacturing | | | | | | |
| | | Knots | Cross grain | Rot | Stain | Holes | Pitch pocket | Bark inclusion | Pith | Wane | Torn grain | Split | Checks | Size dev. | |
| Optical (reflections or through transmission[b] of light) | Anomalies in light reflection or transmission | X | | X | X | X | X | X | X | X[c] | X | X | X | X[d] | Detect defects visible on the surface, readily automated | Cost (laser scanner), poor differentiation of defects |
| Ultrasonic (through transmission or pulsed echo inspection) | Anomalies in accoust. impedance (energy transmitted or reflected) and ultrasonic transit time | X | X[e] | X[f] | | X[g] | X | X | X | X | X | | | | Excellent penetration, readily automated, good sensitivity and resolution | Requires mechanical coupling to surface (water immersion) |
| Microwave (through transmission or reflection) | Anomalies in dielectric properties and reflection or scattering of electro mag. waves | X | X[e] | X | | X | | | | | | | | | Noncontacting, readily automated, rapid inspection | Comparatively poor differentiation of defects |
| X-Ray (film radiography, fluoroscopy or scintillography) | Inhomogeneities in density, composition, or thickness | X | | X[f] | | X | X | X | | | | | | X[h] | Detect internal flaws, instantneous inspection, easily adapted to production line | Relatively insensitive to thin laminar flaws, poor, diff. of defects, health hazard |
| Neutron (film radiography or scintillography) | Compositional inhomogeneities selectively sensitive to particular atomic nuclei | X | | X[f] | | X | X | X | | | | | | X[h] | Quantitative real time output, flexibility of sample size, high sensitivity, accuracy, & speed | Relatively insensitive to thin laminar flaws, poor diff. of defects, health hazard |

[a] An X indicates that the defect has been detected by a given test method
[b] Through-transmission of light is only suitable for thin sections (less than or equal to ¼ in.) and can detect knots, holes, and pitch pockets above ¼ in. in size
[c] Using light shadow technique
[d] Measured with the laser scanner
[e] Localized steep grain
[f] Advanced decay
[g] Above ¾ inch in diameter
[h] Significant variation in thickness

Gerhards [33] proposed using stress wave speed to grade lumber. It was noted that knots and grain angle both decrease the speed of stress waves. Gerhard showed how

stress wave travel around knots and the effect it has on wavefront shape. The wavefront shape is shown in Figure 26.

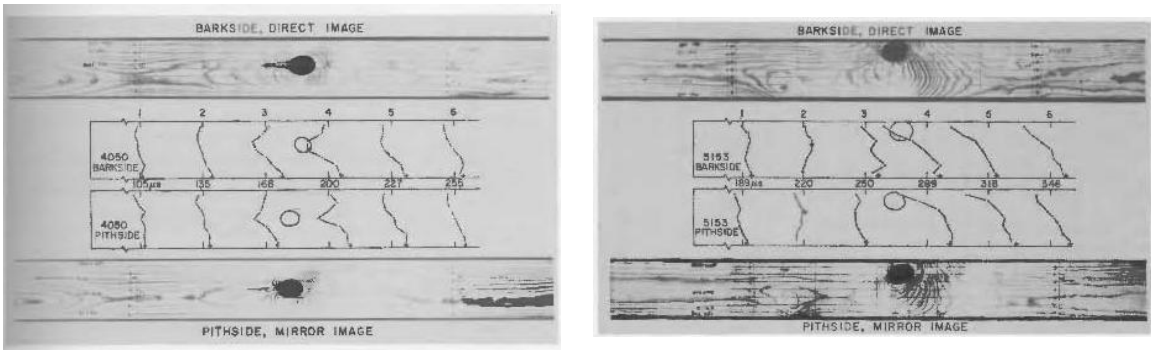


**a.** **b.**

**Figure 26.** Stress wave counters at fixed times across a 2 by 6 containing a knot, **a.** board containing a center knot, **b.** board containing an offset knot. Figures extracted from Gerhards [33].

Beall [5] investigated acoustic emissions of wood during radial compression. The tests were performed upon 10 x 10 x 20 mm white fir blocks. Some of the blocks were inoculated with a brown rot fungus (Poria placenta). The blocks were subjected to a radial compressive load as a sensor listened for acoustic emissions cause by microfractures within the specimens. The control blocks of sound wood were tested to provide information regarding a baseline number of events, the gain levels necessary to observe the emissions, and the voltage threshold necessary to discern an signal from background noise (a signal above the background noise was called an event). At two to three percent compression with a gain set to 100 dB and a voltage threshold set to 0.7 volts, approximately 50 events were recorded. When a block with three percent mass loss from decay was tested, the number of events was several orders of magnitude greater. A strong correlation was found between mass loss and the ratios of compressive stress to number of acoustic events. A summary of the relationships is shown in Figure 27. The first is the logarithm of the compressive stress when the event count was at 100 plotted versus the square root of mass loss. The second is the logarithm of the number of events at 0.75 percent of the elastic compression versus the square root of mass loss.

Lemaster [73] investigated the feasibility of using acousto-ultrasonics to measure defects in lumber. A pair of roller transducers was used to examine equipment likely to

be used on a production line. Transducers were dry coupled to the wood using neoprene rubber sheets. The study examined the effect decay, grain angle, and internal defects had upon stress waves traveling through wood and the difficulties of sensing those waves. Like Szymani [3], Lemaster found coupling to be an issue that was not easily overcome. As a result of the analysis, it was recommended that a study of coupling methods be performed. Sensor pressure noticeably affected signal strength and much of the variability in the tests came from difficulties in maintaining a constant pressure. The RMS of the voltage signal decreased linearly as the grain angle increased from 0° to 45°, but had little or no change between 45° and 90°. The presence of decay decreased the RMS voltage for both of the woods examined, Douglas-fir and white fir, with Douglas-fir showing greater correlation between mass loss and RMS decrease.

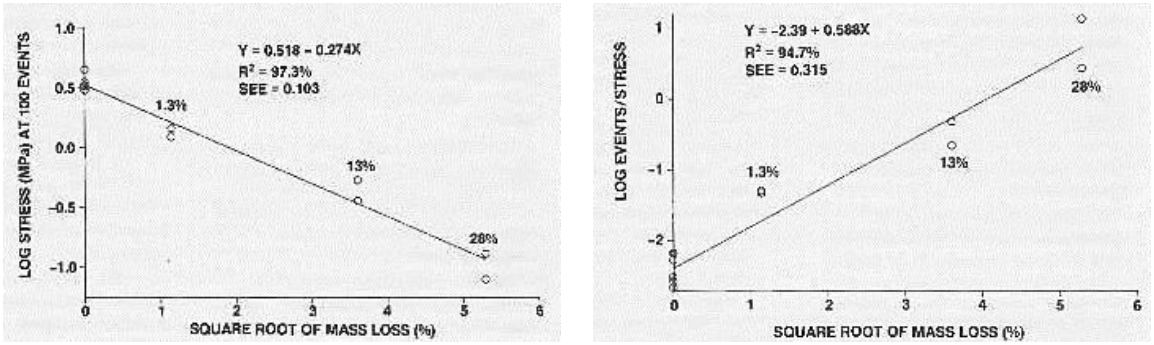


**a.** **b.**

**Figure 27.** Mass loss versus compressive stress and total acoustic events, **a.** logarithm of the compressive stress at an event count of 100 versus the square root of mass loss, **b.** logarithm of the events at 0.75 percent of the elastic compression versus the square root of mass loss. Figures extracted from Beall [5]

Wilcox [6] examined Douglas-fir beams that had been removed from service due to decay. The beams were 15 by 36 cm and between 3 and 4 m long. Four frequencies were examined: 37, 54, 150, and 500 kHz. The sensors were coupled with white petroleum jelly and held in place by hand pressure. The use of the 500 kHz frequency was discontinued due to difficulties with coupling. As the wood transitioned from sound to decayed wood, the through-transmission velocity decreased. Ultrasound velocity measurements were unable to detect early decay (less than 10% mass loss). Advanced decay was associated with sudden signal loss. After testing, a microscopic analysis was

performed on the beam cross-sections. It was found that the decay boundaries were abrupt with transition regions between decayed and sound wood measuring between one and five centimeters.

Sandoz [74] examined grading construction lumber using ultrasound. Ultrasonic sensors were dry coupled to beams and the longitudinal velocity was recorded. The beams were then subjected to a four point bending test to obtain values for MOE and MOR. MOE was plotted against the square of the wave velocity and MOR was plotted against wave velocity. The correlation coefficient values, r, for the two plots were 0.82 and 0.68, respectively. The plots are shown in Figure 28.

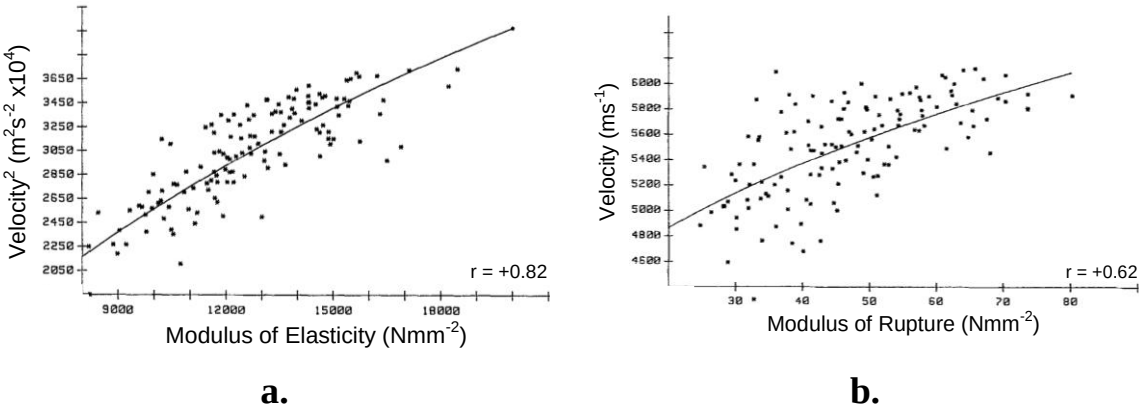


**Figure 28.** Experimental moduli as functions of longitudinal velocity, **a.** Modulus of elasticity versus velocity squared, **b.** Modulus of rupture versus velocity. Figures adapted from Sandoz [74].

Sandoz examined the influence of several variables upon MOE and MOR. The variables examined included, but were not limited to: velocity, density, diameter, age, and number of knots. Wave velocity was the most influential of all of the variables when determining MOE and MOR. Sandoz concluded that wave velocity could be the primary variable for grading lumber.

Sandoz [75] expanded the previous paper and examined several acousto-ultrasonic parameters in an attempt to correlate them with mechanical strength in glue laminated (glulam) beams. Parameters examined included wave velocity, maximum signal peak, signal energy, and attenuation. As in the previous paper, good correlation was found between modulus of elasticity and wave velocity. Maximum peak, signal energy, and attenuation brought no additional information regarding the elasticity and had

weaker correlations than velocity. However, signal energy and maximum peak appeared to be good indicators of crack depth.

Lord [76, 77] attempted to model an ultrasonic wave traveling through anisotropic medium using finite elements. The model was not specifically designed to model wood, but was applicable to it, nonetheless. The model was two dimensional and was capable of having directionally dependent stiffness values. Simulations were made of waves traveling at 0°, 45°, and 90°. Attenuation was attributed mainly to beam spreading of the pulse and energy absorption of the medium through viscous damping. The study clearly showed the effect anisotropy had upon the wavefront shape. The model was severely limited by the computational power available in 1990.

Ross [59] described the inspection process of timber bridges using stress waves. The members examined were glulam beams. It was noted that typical sounding techniques were not effective on members that were larger than 100 mm (four inches) in width. Through a series of tests, it was determined that the longest transmission times were observed for signals traveling 45° to the annual rings. Wood preservatives increased travel times by about 40%. Ross recommended that inspection using stress waves be performed along paths transverse to the rings as parallel paths could bypass regions of decay. Little variation was observed among transmission times of sound members. Any members with significant variation in transmission times were regarded as suspect.

Biernacki [78] developed a scanning system for evaluating wood and wood laminates using an acousto-ultrasonic method. Material variability, coupling conditions, and transducer misalignment were factors contributing to the lack of repeatability when using this technique. One focus of the experiment was to maximize the repeatability of the method. A wet couplant would be absorbed into the wood; therefore, a dry couplant (an elastomeric material) was used to prevent contamination. As the pressure holding the transducer to the surface was increased, the signal strength increased. At some pressure, there was no longer an increase in signal strength. This pressure was known as the saturation pressure. The pressure used to hold the sensor in place was set at or just above the saturation point. Misalignment of the probe and the test surface was minimized through the use of a flexible probe. Tests were run on Douglas-fir specimens with grain

angles of 0°, 30°, 45°, 60°, and 90°. The tests were given sufficient time to allow the signal strength to stabilize. The MOE and RMS voltage reached minimum values in the radial / tangential plane when the grain angle was between 45° and 60°. Another portion of the analysis used a through-transmission setup on a glulam beam with the pulser and the receiver offset by a single lamina. Since the grain angle is random in glulam laminates, each interface of each glulam beam would have a unique signal. The uniqueness of the signals was confirmed with testing.

Ross examined nondestructive evaluation of decayed wood. Several different types of structures were inspected using NDE methods [35]. Tested structures included: an eighteenth century mansion, a football stadium, a gymnasium, piers, bridges, a barn, a water cooling tower, wood utility poles, and the USS Constitution. Ross describes the various techniques used on each structure, but notes that no research had been published on the changes in wood behavior due to the manner of excitation.

Dickens [79] noted that ultrasonic frequencies normally used to examine engineering materials were between 2 and 20 MHz. However, in wood, those frequencies could have attenuation values in the range of several hundred decibels per meter. Therefore, frequencies used for wood inspection were typically below 1 MHz. Through the use of critically refracted longitudinal waves, $L_{cr}$, it was possible to use frequencies as high as 1.5 MHz and increase inspection resolution. This method allowed the excitation of longitudinal waves without access to the ends of the board. The tests were conducted on 2 by 6's. The calculation for the refracted velocity is shown in Equation 4.

$$V_R = \sqrt{\frac{V_0^2 V_{90}^2}{V_0^2 \cos^2\theta + V_{90}^2 \sin^2\theta}} \tag{4}$$

Where:
$V_R$ is the refracted velocity and all other variables are the same as defined in Equation 3.

The velocity value in Equation 4 is similar to the value obtained from Equation 3 when the empirical exponent, n, is given a value of 1.65. Dickens referred to Equation 3 as the Hankinson formula and noted it had been applied to wood properties for 75 years. The agreement between the two equations implied that use of the Hankinson formula is

equivalent to assuming a transversely isotropic medium. One issue with this technique was the depth of penetration. A notch was cut into the wood on the opposite side as the sensor and receiver. The sensor and the receiver were positioned on the opposite sides of the notch. The notch was cut to a depth such that only 5 mm of wood remained (a standard 2 by 6 is 38 mm deep, the notch depth was 33 mm). The notch had no effect on the amplitude or frequency of the transmitted signal bringing into question the ability of the technique to discern subsurface defects.

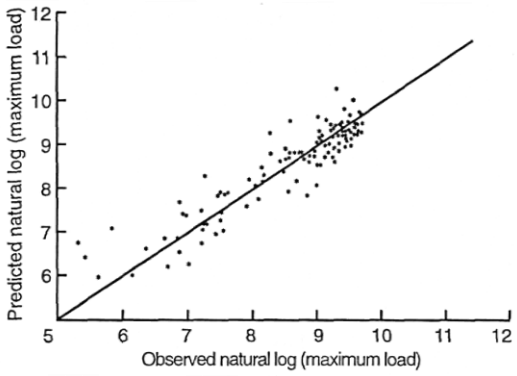


**Figure 29.** Predicted versus observed compressive strength of wood stakes. Extracted from Ross [81]

Ross [80, 81] and DeGroot [52] authored a series of papers in which stakes were driven into soil and allowed to decay. The stakes were 20 inches in length. Half the length of the stake was driven into the ground. Stakes were evaluated at two, four, six, nine, and fifteen months. A spring loaded impactor was used to generate a longitudinal wave. The stress waves were observed using an impact-echo method. Three sets of tests were performed: the stake was in place, the stake was in place and elevated one inch, and the stake was removed from the ground. Testing confirmed relationships between wave behavior and rot that had now been well established; with increasing levels of rot, mass decreased, wave velocity decreased and attenuation increased. A formula was developed relating compressive strength of the stakes to three variables: specimen weight, attenuation rate, and stress wave speed. The predicted compressive strength versus the observed compressive strength of the stakes is plotted in Figure 29. From the analysis, it became apparent that attenuation rate was not a factor when predicting compressive strength. Also, the number of reflections from the impact test appeared to be a useful

variable in identifying decayed wood. Ross [80] discussed the development of a database to show the relationship between wave parameters and the compressive strength of decayed wood.

Ross [82] documented the use of a rolling transducer to locate degraded regions in southern pine 2 by 4 boards. A through-transmission setup across the four inch dimension was used. The time of flight of the transmitted signal was measured at several locations as the board passed between the transducers. Sound wood had consistently low travel times of less than 250 µs. One specimen was tested and then placed outdoors for 45 months. Visual inspection of the board revealed signs of decay. The board was retested. The time of flight for the signals had elevated above 250 µs. The highest travel times were near the exposed ends of the board where decay is likely to intrude. Figure 30 shows the time of flight of the board before and after environmental exposure.

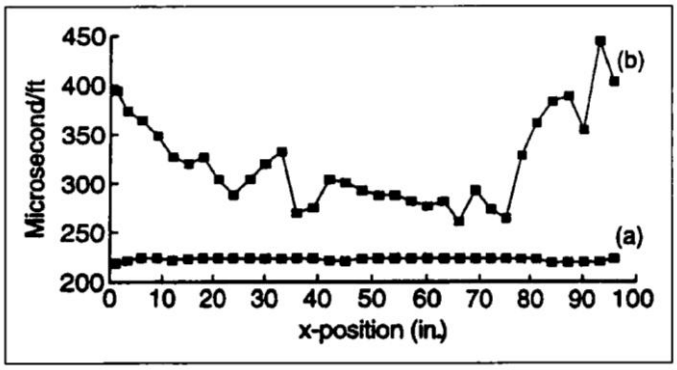


**Figure 30.** Time of flight measurements across a southern pine 2 x 4, a. Prior to board being exposed to the environment, b. after 45 months of environmental exposure. Figure extracted from Ross [82].

Tiitta [83, 84] and Beall [37] examined decayed glulam beams using the acousto-ultrasonic approach. The beams were decayed from brown rot. Tiitta used a through-transmission setup with a pair of 175 kHz resonant transducers. A variety of metrics was explored including: time of flight, time centroid, frequency centroid, the RMS of the signal, and the attenuation (1/RMS). The frequency centroid is "the center frequency of the signal relative to the amount of energy". The time centroid is the time at which "the bulk of the signal energy is received". The calculations for the frequency centroid and time centroid are similar and both are shown in Equations 5a and 5b, respectively.

$$f_c = \frac{\sum_{i=1}^{N_f} S_i f_i}{\sum_{i=1}^{N_f} S_i} \quad (5a)$$

$$t_c = \frac{\sum_{i=1}^{N} |A_i| t_i}{\sum_{i=1}^{N} |A_i|} \quad (5b)$$

Where:
$f_c$ is the frequency centroid
$N_f$ is the number of frequencies in the spectrum
$S_i$ is the magnitude of the *i*th frequency in the spectrum
$f_i$ is the *i*th frequency of the spectrum
$t_c$ is the time centroid
N is the number of time steps
$A_i$ is the amplitude of the *i*th time step
$t_i$ is the time at the *i*th time step

In the presence of decay, parameters generally exhibited a predictable pattern: attenuation and time centroid increased, velocity and frequency centroid decreased. The RMS, transit time, and the time centroid had good correlation to decay, but frequency centroid did not. However, frequency centroid was the most useful metric in detecting small levels of decay. The RMS was sensitive to decay detection, but other defects had similar effects on the signal.

The frequency spectrum of a signal passing through sound wood was compared against the spectrum of a signal passing through decayed wood. While all frequency magnitudes were noticeably diminished in the decayed wood, the higher frequencies suffered greater attenuation than the lower frequencies. The paper examines several features such as knots, grain angle, moisture gradient, and decay. The behavior of each of the four parameters is observed in conjunction with the respective defect. One of the more substantial conclusions of the papers is that, given the inherent variability of wood, the use of a single parameter will not reliably detect decay in all situations. The use of multiple parameters is recommended.

Im [85] examined the effect of impregnating wood with insect repelling preservatives. Exposure time of the specimens for impregnation was zero minutes (the control), ten minutes, and two hours. No information is given regarding the impregnation process. The tests were conducted on specimens of Douglas-fir. All specimens had heights and widths of 100 mm. There were four different specimen thicknesses: 3, 8, 12, and 16 mm. A through-transmission setup with 1 MHz transducer was used. Amplitude and time of flight of the received signals were the examined parameters. The transducers were dry coupled with an elastomer and the application force was measured with a force gauge. Amplitude and time of flight increased as impregnation time increased. Yang [86] expanded upon the work of Im by sealing the specimens in a polyester film and using an immersion setup to obtain C-scans. The C-scans used a combination of time of flight and amplitude measurements to map non-uniformity of the material. The non-uniformity in the wood caused by the preservative was less than that caused by the annual rings and wood density.

Lee [87] compared time of flight measurements with drill resistance. Drill resistance is the measured power required to penetrate a material. By plotting drill resistance versus the tip depth, a profile of the internal condition of the wood structure could be constructed. The profile provided a qualitative plot of the relative density of the wood structure. Nondestructive tests were conducted using accelerometers and ultrasonic transducers to compare against the drill resistance test. Good agreement in time of flight measurements was observed between the accelerometers and ultrasonic transducers.

Schubert [88] used ultrasound to excite resonant frequencies in small cubes of wood. The resonant frequencies were used to perform a modal analysis which allowed for the estimation of the shear modulus. Additional wood cubes were exposed to rot for periods of four, eight, and twelve weeks. The decayed cubes were subjected to a similar analysis as the original control cubes. The shear modulus decreased with increasing levels of decay.

### 2.7.3. Inspection of trees and utility poles

Miller [55] described the development of a sonic device to detect decay in wood poles. The development of the device was in response to a desire by officials at Detroit

Edison to reduce the cost of pole inspection. From the late 1930's to the time of his publication in 1965, Detroit Edison had used X-ray inspection. Experience had shown them that between 70% and 80% of the poles inspected were sound. The decision to X-ray a pole was made based upon sounding tests. There was a desire to come up with a better method of determining whether a pole should be subjected to X-ray inspection. Several parameters were examined including: electrical resistivity, dielectric constant, and transmission of radio frequencies, but those methods were deemed too sensitive to the presence of moisture content. The most reliable method that was relatively insensitive to the presence of moisture was time of flight of a wave across the pole. The device was tested on a set of 600 poles. In two percent of the poles, the sonic device located rot that the sounding test failed to identify. The author claimed the device could identify poles with 10% decay, though the author does not clearly indicate how the decay was measured.

Shaw [89] used a resonant sonic vibration technique for rot detection. Nails were driving into opposite sides of the pole. An electromagnetic hammer was affixed to one nail and used as the source. A piezoelectric transducer was affixed to the other and used as the receiver. A frequency range of 20 Hz to 1 kHz was used. The input frequency was varied until the maximum velocity from the source to the transducer was observed. Baseline velocity measurements were performed at the ground line of the pole. Measurements were taken along the vertical length of the pole. If the velocity above the ground achieved a value of 150% of the velocity at the ground line, then rot was assumed to be present in the pole. The method was good at evaluating untreated poles, but had little success evaluating preservative treated poles. Surface cracks cause false positive results (a sound pole identified as having internal decay). Application of a tourniquet above and below the test location reduced the number of false positives.

Dunlop [90] evaluated wooden poles using an acoustic pulse method. The method focused on using velocity and damping as parameters. The acoustic damping of the longitudinal compression wave was useful in detecting the presence of rot within a pole. Damping was affected by the frequency, temperature, and direction of propagation. Prior research [64] had shown that damping could change as much as 50% for moisture contents between 12% and 27% at a temperature of 30°C, but the change in damping was

much less at around 20°C. Therefore, the damping in the poles would only be marginally affected by variations in the temperature and MC encountered between poles. The biggest problem in running the test was the inability to produce controlled amounts of decay. Also, there were difficulties in measuring the longitudinal velocity and attenuation due to dispersion of the pulse. The attenuation values obtained were over ten times those obtained by McGovern [21], but matched the attenuation results obtained when no correction was made for the acoustic impedance mismatch between the wood and transducer.

McCracken [91] examined standing trees using acoustic and ultrasonic waves. The trees examined were willow oak, green ash, and cottonwood trees. A continuous mechanical vibrator was used to generate signals between 10 Hz and 100 kHz in decade (log scale) increments. For frequencies of 100 Hz and 1 kHz, the recorded signal amplitude for trees containing rot was greater than that of sound trees. The increase is likely caused by the fact that the wavelengths were much larger than the defect region and followed paths around the defect. The ray paths along which the energy traveled avoided the defect region effectively reducing the cross-sectional area over which the signal energy spreads. This theory was supported by the fact that increases in amplitude were also seen in the presence of internal defects measuring 5 cm or greater. As the frequency increases, the ray paths included into the decayed region and were likely attenuated to the point of being unobservable. Decay was not observed when using frequencies of 10 Hz, 10 kHz, and 100 kHz. The technique required the removal of bark to install the source and the receiver. The transit time was a good indicator of the presence of rot, but did not allow for an estimation of the size of the defect region.

Bulleit [92] attempted to develop a two dimensional model of a cross-section of wood. The model was meant to assist in studying stress wave motion in wood utility poles. A plane strain, finite element model was created that assumed a homogeneous, isotropic medium. No damping was included. The time of flight of the wave as it traveled from a single source at the edge of the cross-section is shown in Figure 31. Experimental data measured from a sound utility pole is included in the plot. The plot is normalized by the longest arrival time.

Bulleit noted good agreement between the model and the experimental data for angles from the source greater than 90°. The values of the experimental data are explainable assuming an isotropic medium. In an isotropic medium, the greatest distance would require the greatest time to travel. In this case, greatest distance would be the diameter (D) of the cross-section. The distance to the 90° (and 270°) location would be a quarter of the circumference ($\pi D/4$). The ratio of the two values is $\pi/4$, which have a value of 0.785. That value matches the values observed by Bulleit. In Table 16 of Section 4.3.1, the ratio of the arrival times at the 90° location and the diameter for Douglas-fir is calculated to be 0.916. This number assumes an orthotropic medium rather than an isotropic. The wood of the utility pole is not specified; however, the measured value of 0.90 is close to the calculated value of 0.916.

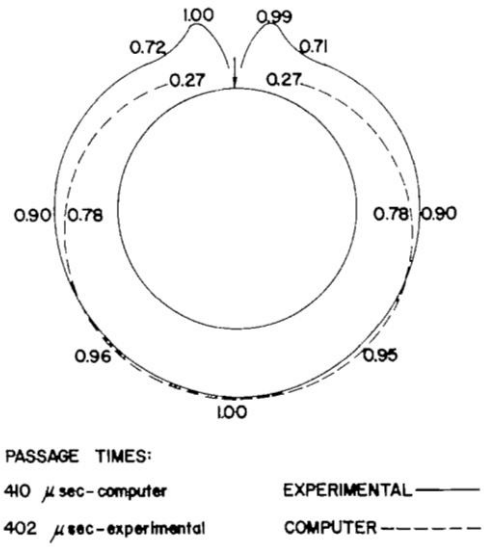


**Figure 31.** Normalized time of flight pattern for a sound pole. The center circle represents the geometry of the utility pole. The dashed line represents the results from the computer simulation. The outer solid line is the experimental results. All values are normalized against the maximum value for the data set. Figure extracted from Bulleit [92].

Another feature of note are the two lobes next to the impact source. During the execution of the finite difference model developed in the second half of this thesis, a change of phase was observed close to the point of impact. The model nodes near that phase change saw little displacement as the wavefront passed. The wavefront travels in two directions, radially and tangentially. When the wavefront arrives at the center point, it excites a wave in all radial directions. The two lobes are near the location of the phase

change, and the first observable arriving wave is a reflection of the wave from the center of the pole. The excited radial wave also explains why the wave arrives simultaneously along a portion of the pole opposite the source. Wave motion through a cylindrically orthotropic medium is described in greater detail later in this thesis. The isotropic finite element model was unable to accurately simulate the wave behavior as it traveled through the pole, but the experimental data collected by Bulleit matches the predicted wave behavior described by the finite element model in this thesis. Bulleit suggested the model would be improved by the implementation of a cylindrically orthotropic medium and growth rings.

Aggour [93] examined timber bridge piles using nondestructive testing techniques (a pile is a post driven into a riverbed or soft ground to support a superstructure). The goal of the research was to relate the in-place strength of timber piles to wave velocity and unit weight of the pile. The piles were constructed of yellow pine. Tests were performed on site and then the piles were brought back to the laboratory for cutting and strength testing. Deterioration effects such as density loss, increased permeability, strength loss, and loss of cross-sectional area were noted. The limited access to the piles in the field made decay assessment difficult with visual inspection. The unit weight was found to be much greater determinant of compressive strength than wave velocity for "old" piles. "Old" is not clearly defined; it describes wood that had previously been in service. "New" wood were piles not yet put into service.

Falk [94] discussed the lack of systematic inspection guidelines for utility poles. The paper outlines work performed by Forest Products Laboratory to develop such guidelines. The summaries indicate that acoustic / ultrasonic techniques were effective in detecting decay, and specifically brown rot, as well as having some success in estimating member strength.

Han [95] examined production line scanning of logs for lumber production. It was believed that a better inspection method to locate internal defects would allow cutting to be optimized and increase lumber output by ten percent. Han performed several ultrasonic inspection of logs using frequency ranges of 50 to 200 kHz. The same logs were X-rayed to obtain cross-sectional information. The ultrasound signals were then examined to correlate signal features to defects. Amplitude was found to be highly

sensitive to the surface quality and the internal geometry of the log. As a result amplitude was concluded to be an unreliable defect detection parameter. Due to computational and production line time constraints, most parameters were minimum / maximum values and simple comparison values. Han examined a series of other signal characteristics and developed a computerized algorithm to decide whether an internal defect was likely present. When the defect detection algorithm was compared against the X-ray data, the algorithm was found to have an error rate between 8% and 25%.

Beall [96] examined utility poles using acousto-ultrasonics to detect decay. The paper contained two different analyses. The first was an examination of the effect that different sized holes had upon signals passing through pole. The second was an acousto-ultrasonic examination of ten utility poles removed from service. Holes of 50 mm diameter or greater could be detected using acousto-ultrasonics. Several parameters were examined and relationships were noted. Decay was likely to develop near deep and / or large surface cracks. The wave velocity was insensitive to the number of surface cracks. Wave velocity was sensitive to moisture content and increasing levels of decay. Velocity had a fairly linear relationship to both bore size and area of deterioration. The time centroid was more sensitive to surface cracks than moisture content. The time centroid was more sensitive to bore size than deterioration. The RMS voltage was very sensitive to incipient decay. One particularly noteworthy conclusion was variability in the results which made single a parameter identification of interior decay unreliable.

Holt [97] proposed a method of determining installed timber piles. Two sensors were affixed to the side of timber piles. The piles were struck to initiate a bending wave. The sensors recorded the waves as they passed from the source upward to the top of the pile and downward to the bottom. Using estimates of the wave speed, the timber pile lengths were estimated. The estimates were within 10% of the true pile lengths. However, of the 40 piles tested, 14 did not yield results. It was unknown whether or not the technique was capable of analyzing piles with concrete footings.

Nicolotti [51] examined three different tomographic methods for detecting decay in trees. Electric tomography, ultrasonic tomography, and georadar tomography were used in the analysis. Nicolotti collected 120 independent measurements from sixteen different locations equidistantly spaced around the circumference of the tree. The center

frequency of the probes was 33 kHz. Ultrasonic tomography showed the location, size, shape, and mechanical properties of defects. Mass losses of 15% or greater were detectable. The major disadvantages using ultrasound were coupling, wood anisotropy, and signal attenuation. The ultrasonic velocity was sensitive to early wood degradation. Ultrasonic tomography suffered from an underestimation of the velocity as ray paths tended to avoid regions of low velocity and did not contain information about the decayed regions.

Schwarze [98] used acoustic waves to generate cross-sectional tomograms of trees. Twelve receiving sensors were place equidistant around the circumference of the trunk. Sound pulses were produced manually and the time of flight to each receiver is recorded. Long transit times were attributed to waves traveling through zones of decay or finding paths around those zones. The exact number of independent measurements is not stated, but it is implied that 132 measurements were taken. An impulse was inputted at each receiver location and the system output was recorded at the other eleven locations (12 * 11 = 132). Three trees of different species were examined: beech, horse chestnut, and Norway maple. Several conclusions were drawn using this technique. With respect to defects, the tomograms accurately measured size, and measured location with moderate accuracy. As the actual cross-section deviated from a circle, errors in the tomograms increased. Accuracy could be improved by increasing the number of sensors. The acoustic measurements appeared to be only slightly sensitive to high moisture contents.

Schwarze [98] encountered reaction wood during his experiments, but did not represent then in his simulations. Reaction wood is formed in most tree branches and in the trunks of leaning trees in order to maintain branches at their specific angles. It is also formed in the trunks of leaning trees in an attempt to straighten the growing angle of the tree back to vertical. There are two types of reaction wood, compression wood and tension wood. Their names imply the location within the trunk / branch cross-section, not stresses necessary for its formation. Imagine a simple tree branch model consisting of a fixed end cantilever beam subjected to a negative moment at the free end. The top of the beam would be in tension while the bottom of the beam would be in compression. In hardwoods, the reaction wood forms on the top of the branch and is referred to as tension

wood. In softwoods, the reaction wood forms on the bottom of the branch and is referred to as compression wood [11]. Reaction wood affects both wood density and wave velocity, and was likely a source of error between Schwarze's [98] simulation and experimental results.

Socco [99] also examined the creation of tomograms of living trees. Sixteen sensors were placed around the trunk. The operating frequency was 34 kHz. The frequency was chosen as a tradeoff between the higher attenuation associated with higher frequencies and the low resolution associated with low frequencies. A total of 120 independent readings were collected per tomogram. After the data was collected, the trees were cut and cubes of wood along the cross-section were analyzed. Some cubes showed signs of rot while others were sound. From the analysis of the cubes, it was shown that wood anisotropy decreased as decay increased. Also, changes to velocity through the cubes were mostly likely dominated by changes in elastic modulus rather than changes in density. The decay indicated by the tomogram data underestimated the decay in the cubic samples. The authors had several critiques of the technique. The technique was time consuming for a single channel instrument. Adapting the system to three dimensional analysis would be expensive. Signal to noise ratio and sensor coupling were issues. The statistical post processing required an expert operator. Differences in wave speeds could cause "ghosts" in the tomograms. The tomograms were created assuming isotropic wood, which may be useful for decay detection, but was not useful when studying mechanical properties of healthy wood. Lastly, the velocity values of low velocity anomalies were overestimated. The overestimation was likely caused by the Wielandt effect [57], which states that ray paths avoid low velocity regions. As a result, arrival times did not contain information about the decayed areas.

Kim [100 - 104], Lee [105], and Yanagida [106] published a series of papers describing the creation of computerized tomographic images using ultrasonic signal data. It should be noted that the goal of these papers was to describe nondestructive tests performed upon wood poles that were part of ancient buildings of cultural significance. There was a desire to avoid any technique that could change the condition of the building such as drilling and wet coupling of sensors. The transducers used had a center frequency of 68 kHz and were coupled with 10 mm diameter rubber plates. The first part

of the study was to use the image recreation software to attempt to recreate known cross-sections with defects of specific geometry. The software used time of flight data to construct the tomograms. Measurements were taken around the circumference of the test poles every 10° for a total of 36 test locations. Each tomogram was constructed using 270 time of flight measurements. Laboratory test specimens were created by cutting voids of specific geometries into pole cross-sections that were free of any other defects. One specimen had a circular hole and the other had a narrow rectangular hole. The defects that appeared in the tomograms were enlarged and shifted closer to the surface than the actual specimens. Anisotropy of the wood was not taken into account in the tomogram creation process and likely contributed to the error [102, 104]. The method was expanded beyond simple voids when a test pole was infected with fungal rot. A small hole was drilled into a test pole. A piece of infected wood was placed in the hole and the hole was plugged. The pole was examined eight months later. At that time, the tomogram was capable of detecting mass loss of 10% or greater [103].

The techniques were then applied to tests in the field. In a step that seemed incongruent with the stated desire to have a completely nondestructive method, resistance drill tests were used to find the specific gravity of the tested poles. The same test procedure was used (270 time of flight measurements) to construct tomograms. Also, portable X-ray units were used to scan the poles to provide verification of the ultrasonic based tomograms. In the instances where the tomograms yielded accurate images of the cross-section, only 30% of the 270 measurements were needed. In some cases, accurate results were not obtainable with the full 270 measurements. Anisotropy of the wood was again a source of error [105].

An attempt was made to computationally correct for the anisotropy of wood. The correction increased the accuracy of the model and allowed defects of 33 mm to be detected [101]. It should be noted that the velocity estimate used predicts the wave velocity will continually increase with angles ranging from 40° to 180° around the circumference of the pole. When actual velocity measurements were made around the circumference, it was clear that the velocity increased from 40° to approximately 120° and then remained relatively constant from 120° to 180°. The estimated and measured velocities are shown in Figure 32. Payton's model [107] of wave motion through a

cylindrically orthotropic material and the finite difference method used in this report predicts that at some angle from the source, the first arrival wave will be a radial wave that passed through the center point. Therefore, for a portion of the circumference, the measured velocity should be constant and matches the experimental data collected by Kim [101].

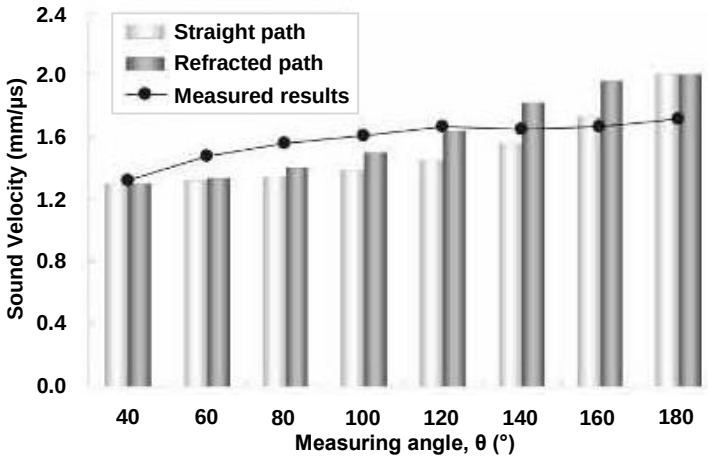


**Figure 32**. Estimated and measured velocity through a wood pole. Figure adapted from Kim [100].

Model adjustments continued with improvements in resolution and artifact correction. The model could accurately find a defect 18 mm in diameter and a slit with dimensions of 3 by 33 mm. Ring shaped artifacts had appeared in earlier versions of the tomograms. A correction procedure was implemented to remove the artifact. As a result, however, ring shaped defects, such as ring shake (a separation between two rings), were no longer visible. Holes and knots were identifiable, but were indistinguishable [106].

Kim [100] attempted to further correct skewing effects by the growth rings in the model. Distortion from the growth rings shifted the defect location towards the pole surface. A process of path adjustment was implemented to correct for times of flight. The correction process method makes assumptions regarding travel path and travel times to estimate the velocity. Figure 33 shows the assumed ray paths of waves traveling through wood poles. Payton showed that waves in cylindrically orthotropic media do not follow straight line paths [107].

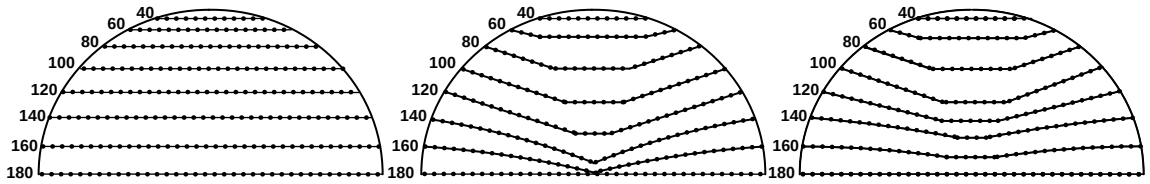


(a) Straight paths (b) Refracted paths (c) Adjusted paths

**Figure 33.** Assumed wave transmission paths through a wood pole. Figure adapted from Kim [100].

Wang [108] performed additional work on ultrasonic tomograms in wood. Twelve sensors were installed around the circumference of a red oak tree in a setup similar to that used by Schwarze [98]. One of the tested cross-sections had a large internal crack running through most of the midsection of the tree. The tomogram interpreted the long crack as a large region of decay. As a result, it was recommended that development of tomograms be used in conjunction with resistance drilling and visual inspection.

Schubert [109] explored what size of defect was detectable using acoustic tomography. The sensitivity of waveforms to the heterogeneity of wood made the use of time of flight suspect as a parameter for detecting decay. Amplitude variations in clear wood showed that it was a parameter very sensitive to wood heterogeneity. Times of flight were less sensitive to wood heterogeneity than amplitude. As a result of the analysis, it was concluded that in a tree described as "sufficiently homogeneous", acoustic wave tomography could detect decay regions large enough to be "dangerous". Neither "sufficiently homogeneous" nor "dangerous" are fully defined by the author.

## CHAPTER 3. GLULAM BEAMS

In this section, the detection and assessment of wood decay in glulam beams is studied. Density information, internal geometry, and defect locations are obtained from CT X-ray scans of the beams. The glulam beams are subjected to ultrasonic through-transmission and modified impact-echo inspection techniques. Signal characteristics from each type of analysis are correlated to the decay identified in the CT X-ray scans.

### 3.1. X-Ray Computer Tomography and Mass Loss due to Wood Decay

One Douglas-fir glulam beam with a nominal cross-section dimensions of 19.1 cm by 12.7 cm (7.5 in by 5 in) was salvaged from a construction site. The glulam beam was made from five 12.7 cm by 3.8 cm (5 in by 1.5 in) laminas, i.e., boards, which were laminated to yield the final glulam beam as shown in Figure 34.

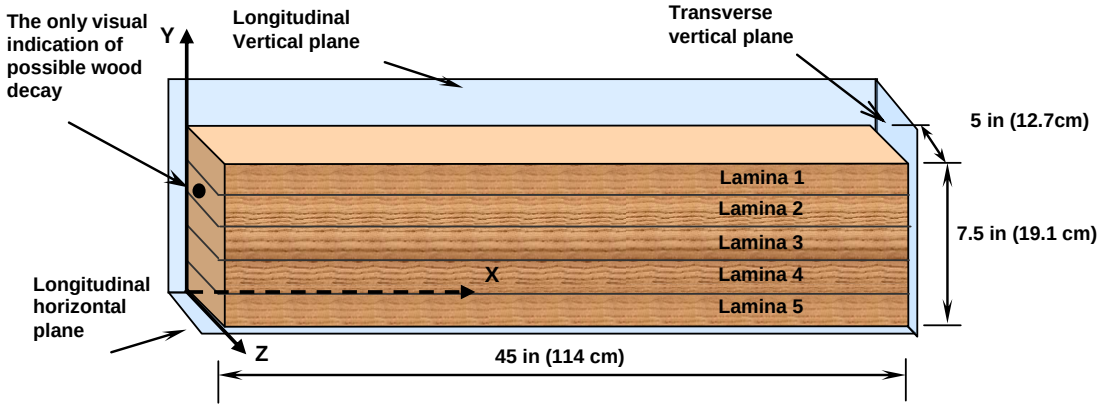


**Figure 34.** Schematic diagram of the glulam beam sample. Beam is made by the lamination of five thinner beams. This 45 in (114 cm) long segment was cut from a beam without visual indication of wood decay. The only indication of wood decay in the 45 in (114 cm) long segment is schematically shown.

Visual inspection of the original beam did not show any indications of decay on the entire beam. A 114 cm (45 in) long segment of this beam was then cut for this study. In this 114 cm (45 in) long segment, the only observed indication of decay was some decay at the end of the beam in Lamina 2 on the left side of the beam (as shown in Figure 34) where an interior small hole (~ 30 mm) caused by wood decay was observed on the face where the cut was made. However, the level of decay could not be assessed using

visual inspection. In addition to this sign of decay, a small (millimeter-wide) longitudinal crack, i.e., split, on the top surface was also observed. Before testing, the beam was marked every 2.54 cm (one inch) along the centerline of each of the five laminae for subsequent X-ray tomographic inspection and impulse-echo measurements. Using an energy level and intensity of 120 kV and 120 mA, respectively, and a focal spot of 0.9 mm by 0.62 mm, X-ray tomographic views were then made every centimeter along the glulam beam length for a total of 114 cross-sectional views.

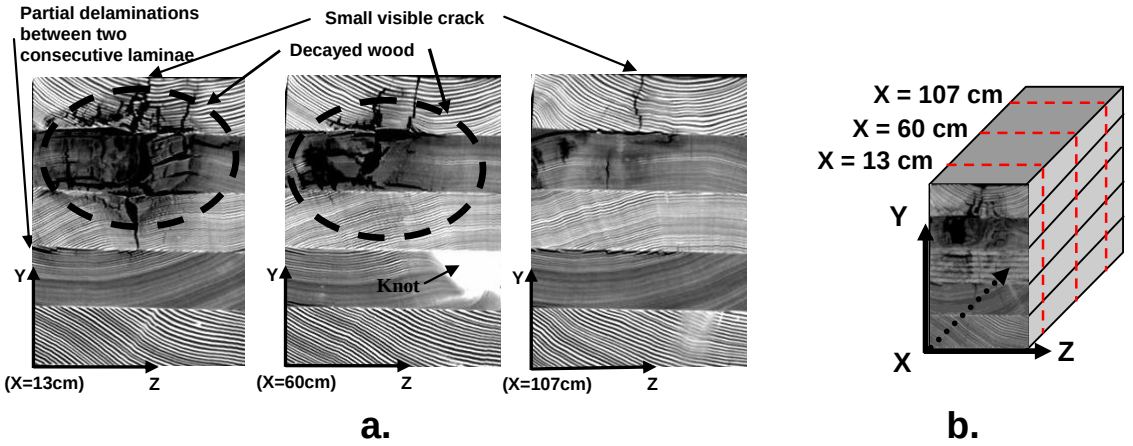


**Figure 35.** Three tomographic views of the glulam beam cross-sections, **a.** Cross-sections are located 13, 60 and 107 cm from the left end (where a visual indication of wood decay existed, see Figure 34). Note the different growth ring density for each of the five laminae the presence of a knot and the severe decay in Lamina 2 (second from the top), **b.** Schematic diagram showing locations of cross-sections within the beam

Figure 35 shows three (out of 114 cross-sectional views) representative cross-section tomographic views of the beam at 13 cm, 60 cm, and 107 cm from the left end of the beam (see Figure 34). The cross-sections show the areas of lower wood density, which correspond to decayed areas. Lamina 2 is in a severe state-of-decay. Decay has spread into the two adjacent laminae, i.e., Laminae 1 and 3. The growth ring orientation is clearly visible in each of the five laminae.

Figure 36a shows five partial longitudinal tomographic views that were assembled from the 114 cross-sectional views taken every centimeter along the length of the beam. Each of the five views shown in Figure 36a represents the tomographic view at the center of each of the five laminae, i.e., at the heights of Y = 2, 5.7, 9.5, 13, and 17 cm (0.75, 2.25, 3.75, 5.25, and 6.75 in) for the first 70 cm of the beam (i.e., $0 \leq X \leq 70$ cm). Please note the severe amount of decay in Lamina 2, which visual inspection alone failed to

assess. Figure 36a also shows that decay has already progressed into the adjacent laminae, i.e. Laminae 1 and 3.

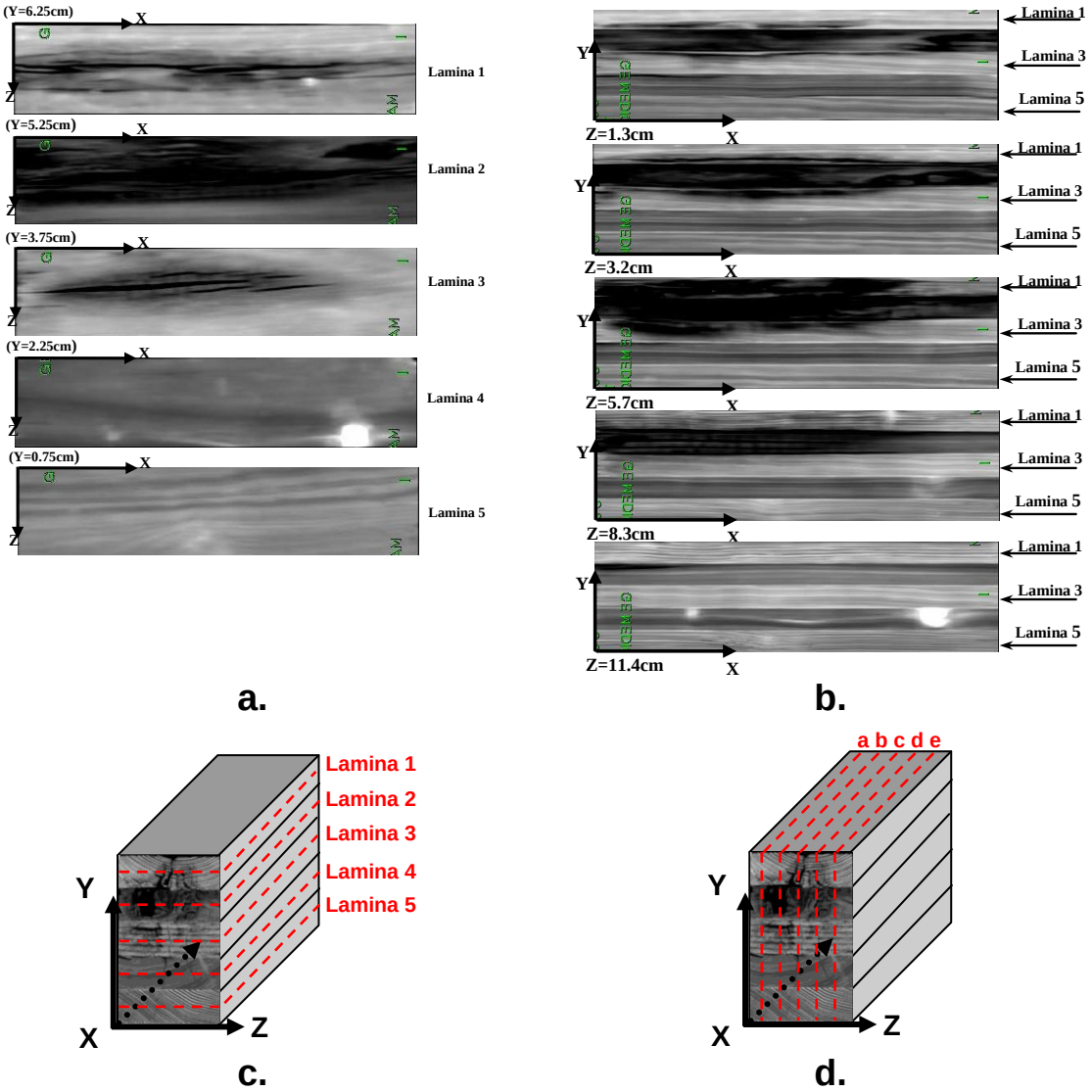


**Figure 36.** Partial longitudinal tomographic views. **a.** Partial longitudinal horizontal tomographic views of the center plane of each of the five laminae from the top to the bottom lamina (for X < 70 cm). Note the severe decay of the second lamina, which has propagated to the adjacent laminae. **b.** Partial longitudinal vertical tomographic views for (X < 70 cm) of cross-sections at 1.3, 3.2, 5.7, 8.3, and 11.4 cm. Note the severe decay in the second lamina from the top, which was not observed from visual inspection. The five laminae are clearly visible because of the different wood density and orientation of growth rings **c.** and **d.** Schematic diagram showing locations of cross-sections shown in (a) and (b) respectively

Figure 36b shows five longitudinal vertical topographical views at Z = 1.3, 3.2, 5.7, 8.3, and 11.4 cm (0.5, 1.5, 2.5, 3.5, and 4.5 in) from the left vertical side, respectively, for the first 70cm of the beam (i.e., $0 \leq X \leq 70$ cm). Again, the severe

decay in the second lamina from the top is clearly visible, but was not observable from visual inspection alone. The five laminae are clearly visible because of the different wood density and orientation in the growth rings.

The density of each glulam beam is obtained through a computerized axial tomography scan (a CAT scan or CT scan). The CT scan yields a cross-sectional image of the glulam beam. The pixels composing the image have varying brightness. The brightness of a pixel represents the relative density of the material at that location within the cross-section. Lower density areas have greater exposure during the CT scan and are darker. Conversely, higher density areas have less exposure during the CT scan and are lighter. Each pixel contains an integer value between zero and 255; black is zero, white is 255, and the values one to 254 are shades of gray from black to white.

The image is "fuzzy" at the wood / air boundary. The fuzziness is caused by the high change in density at the boundary. The fuzziness is eliminated by setting a threshold brightness value for air. If a pixel contained a brightness value of 20 or less, then it was assumed to be air and the pixel brightness was assigned a value of zero.

The pixels represent a particular area of a cross-section and volume within a beam. The images produced by this CT scanner were composed of square pixels. Based upon the scale provided on the images, the edge length of a pixel is 0.97 mm. Each pixel represents an area of 0.94 $mm^2$. The glulam beams were scanned every centimeter; therefore, each pixel represents a volume of 9.4 $mm^3$. The total volume of each beam is calculated by counting the number of pixels with non-zero brightness values and multiplying that number by the volume per pixel. This volume estimate method eliminates error from internal voids and cracks. The mass of each beam is determined using a scale. The beam density is calculated by dividing the beam mass by its volume.

The beam density is then used to estimate the conversion factor between pixel brightness and wood density. The average brightness value of a beam is calculated by averaging all of the non-zero brightness values across all of the cross-sectional images of a beam. The beam density is divided by the average brightness value. The resulting conversion factor, hereafter referred to as the density factor, relates the brightness value of individual pixels to a density value. Using the density factor and the CT scans, the density of the glulam beams can be estimated at any location along the beam.

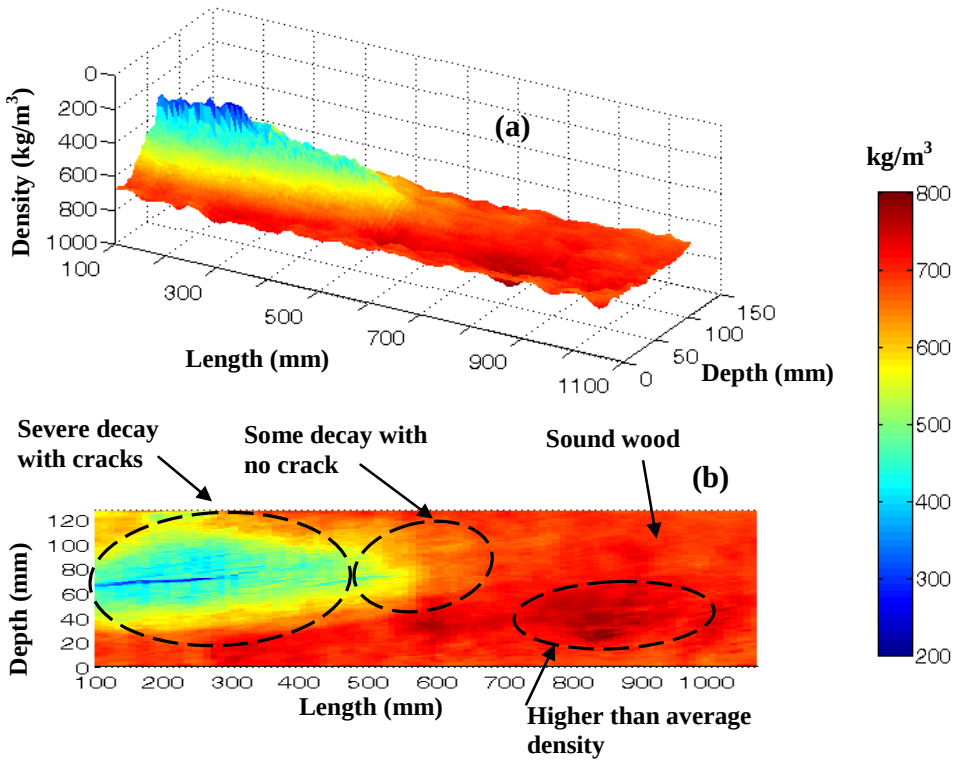


**Figure 37.** Average density across Lamina 3. (a) Average density across the thickness (i.e. across y, see Figure 34) for Lamina 3. Note the region of severe mass loss (~100-500 mm), region with a gradient of mass loss (~300-650 mm) and a region with no mass loss (~>700 mm). Note also a region with above average density; (b) Two-dimensional representation of the average density across the thickness of Lamina 3. Figure 37(b) is a horizontal projection of Figure 37(a). Note that in these Figures, regions of lower wood density, i.e. increased mass loss, correspond to regions of increased decay.

Figure 37a shows a three-dimensional density plot of the averaged wood density (across the thickness) for Lamina 3, while Figure 37b shows the two-dimensional representation of the average density (across the thickness) for Lamina 3. Please note the regions of severe mass loss with the presence of cracks, a region with a gradient of mass loss, a region of sound wood, and a region where the wood density is above the average. The regions with severe mass loss, with gradient mass loss, and with sound wood correspond to regions of severe decay, regions of transient/moderate decay and regions of no wood decay, respectively. The density values were calibrated with the total weight of the beam.

Based upon the X-ray computer tomography, an assessment of regions of decayed versus sound wood was made, and the results are shown in Figure 38, where the average cross-section density versus location is shown for each lamina. In Figure 38 solid and

dotted lines represent sound and decayed wood, respectively. Using these tomographic views, it was determined that some of the laminae were in various states-of-decay. It was observed that laminae four and five had relative uniform growth rings (see Figure 35) and were devoid of wood decay. It was also observed that Laminae 1 and 2 had severe decay, while Lamina 3 had a region of severe decay, a region of sound wood, and a region of transition from sound wood to severe decay.

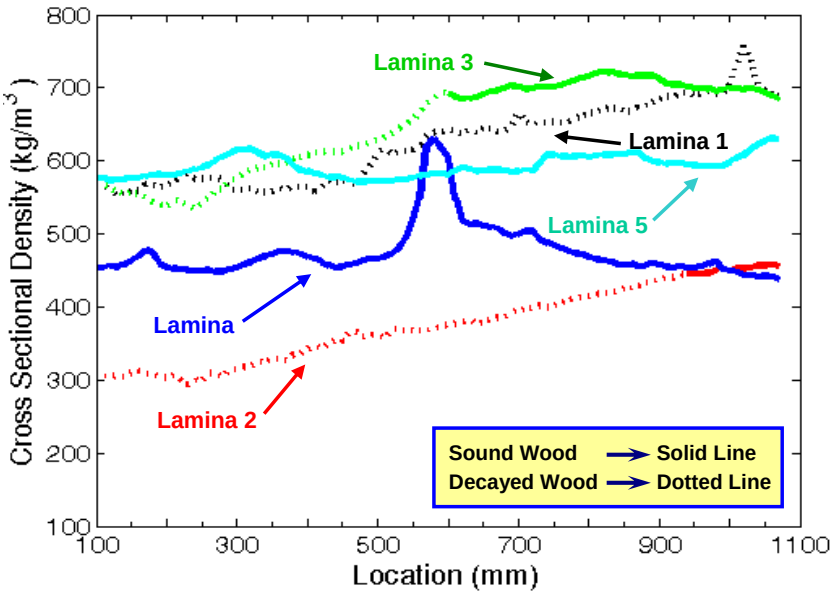


**Figure 38.** Cross-sectional density for all five lamina versus longitudinal location. Please note that the solid and dashed portions of each line represent sound and decayed wood, respectively.

Using samples exposed to decay under laboratory controlled conditions [110, 111], the authors have shown that the presence of wood decay leads to a continuous variation, i.e., gradation, of material properties from sound to decayed wood and not to the creation of an acoustic reflective surface separating sound wood from decayed wood. This lack of a reflective surface caused by wood decay damage explains some of the difficulties encountered in detecting and assessing decay using traditional ultrasonics. The sudden transition from solid to dashed lines in Figure 38 represent a necessary approximation of the gradation from sound to decayed wood made by the inspector based upon changes in wood density. Please note that the natural variability of wood (i.e., splits, humidity, different growth ring thickness and orientation, presence of knots, etc.) can mask the presence of decay.

### 3.2. Ultrasonic Through-Transmission Experimental Description

Figure 39 shows a schematic diagram of the data acquisition system used in the ultrasonic through-transmission study. Both the sending and receiving transducers were the acoustic emission compressional transducers (Digital Wave, Model 1025), which have a flat response in the frequency of interest. A function generator (Krohn-Hite, Model 5920) was used to create the signal. It was then amplified by the gated power amplifier (RITEC, Model GA-2500) with an operating range of 10 kHz to 400 kHz and sent to the sending transducer. The signal from the receiving transducer was amplified in the eight-pole filter/amplifier (Krohn-Hite, Model 3988) before being digitized at a rate of 6.25 MHz and stored for further processing. A tone burst of six pulses (400 Volts each) of 100 kHz each was used and a signal average of 128 waveforms to increase the signal to noise ratio. A thin (2 mm thick) silicone rubber layer was used as a dry couplant between the transducers and the wooden beam. An x-y table was used as a stable attachment and positioning base for the clamping system and transducer placement. Each lamina was scanned every 25.4 mm (1 in) along its center for the length of the entire beam as illustrated in Figure 39. At each location five independent measurements were made.

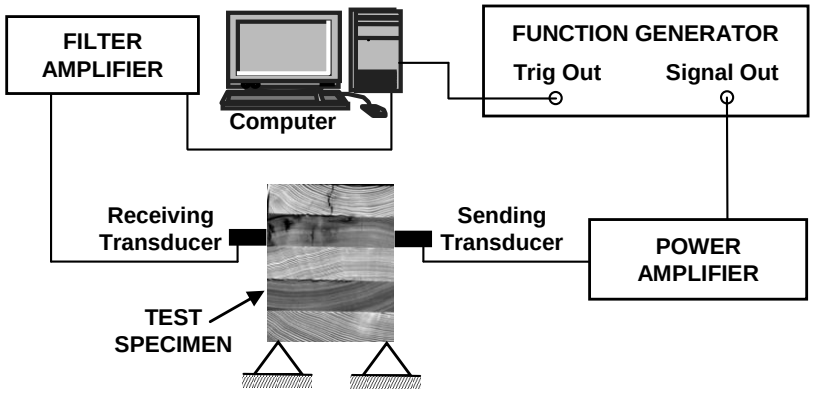


**Figure 39.** Ultrasonic through-transmission testing system schematic diagram

Figure 40 shows the four waveforms and the corresponding power spectral density (PSD) curves collected along Lamina 3 that correspond to four locations with different levels of decay, i.e., from sound wood to severe decay, at 45.7, 61.0, 73.7, and 104.2 cm (18, 24, 29, and 41 in). Figure 40 shows the reduction in signal amplitude and

area under the PSD curve with increase in wood decay.

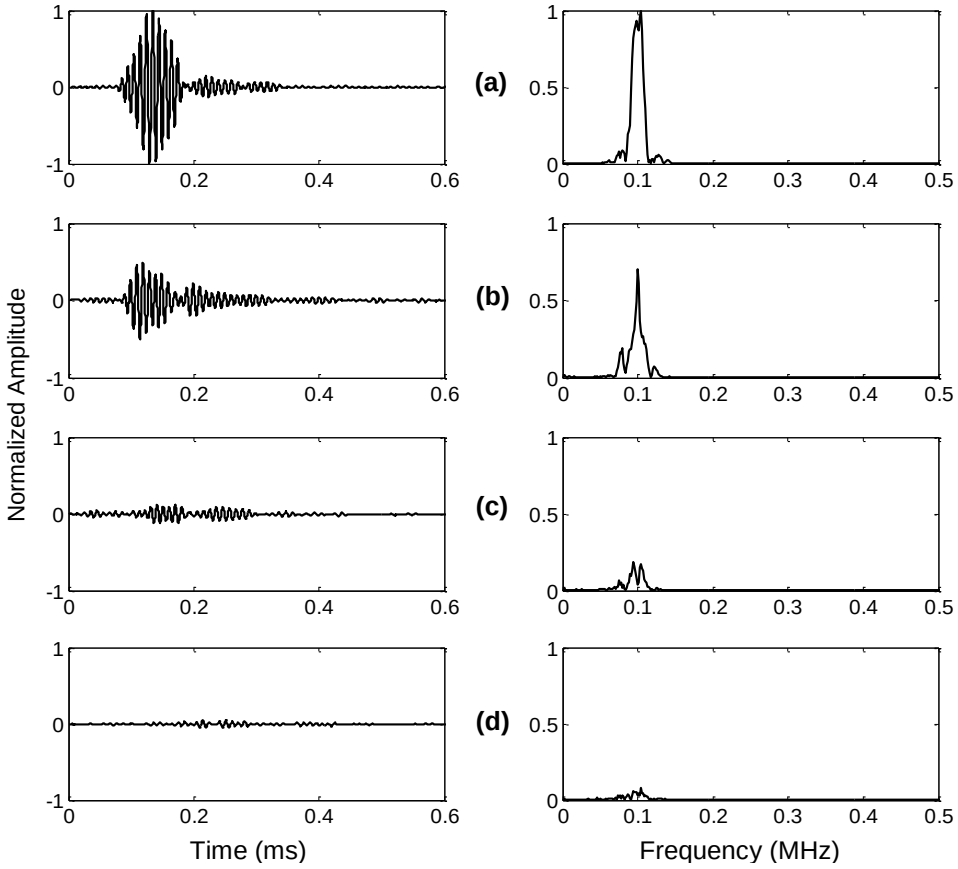


**Figure 40.** Ultrasonic signals collected along Lamina 3. Time domain waveforms and corresponding power spectral density curves collected at four points along the length of the beam for Lamina 3. Waveforms (a), (b), (c), and (d) correspond to the locations of 1041 mm (41 in), 737 mm (29 in), 610mm (24 in), and 508 mm (20in), respectively as shown in Figures 41. Please note that the wave form amplitudes have been normalized with respect to the maximum amplitude of the waveform shown in (a).

Figure 41 shows the area under the PSD curve versus location for all the five laminae. The four locations in Lamina 3 corresponding to the four waveforms shown in Figure 40 are also marked in Figure 41. Figure 41 shows that the area under the PSD curve is negligible for both Laminae 1 and 2 (please keep in mind that Lamina 1 had a visible longitudinal split). The area under the PSD is negligible for locations $X \leq 50$ cm. Figure 37b shows that region is severely decayed and has splits within the cross-section. The area under the PSD increases for Lamina 3 between 50 cm $< X \leq 100$ cm. Figure 37b shows an area of decayed wood between 50 cm and 70 cm. Between 70 cm and 90 cm there is a combination of wood that may have both higher than normal density on one side of the lamina while the opposite side may have some decay. Above 85 cm, the wood

in Lamina 3 is likely sound with some areas having a higher than normal density. Laminae 4 and 5 showed sound wood in every location along the beam.

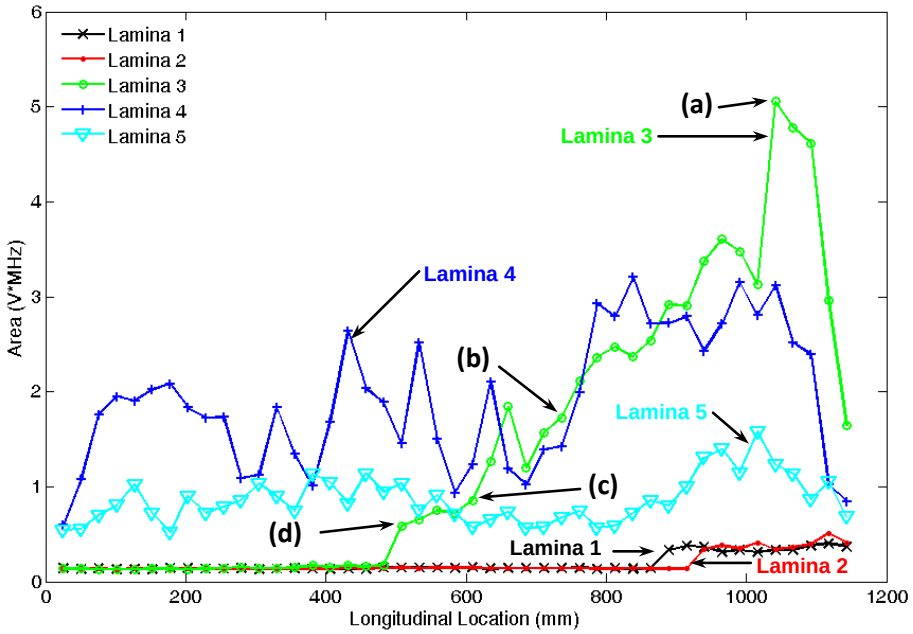


**Figure 41.** Area under the power spectral density curve versus location along the glulam beam for each of the five lamina. Please notice the location corresponding to the waveforms shown in Figure 40 for Lamina 3.

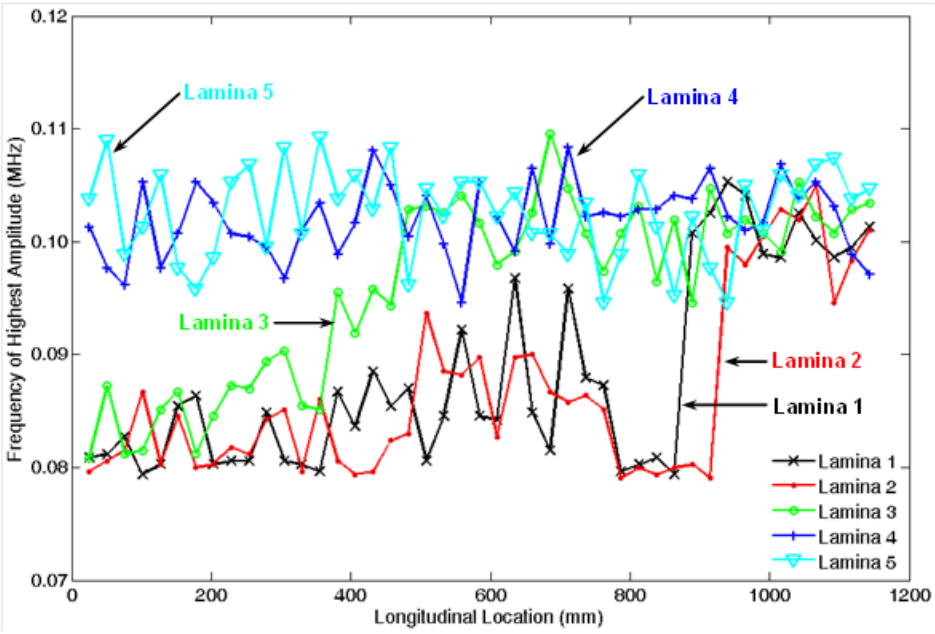


**Figure 42.** Frequency of highest amplitude for each of the five laminae along the glulam beam length

Figure 42 shows the frequency of maximum amplitude for each of the five

laminae along the length of the glulam beam. Figure 42 indicates that wood decay has an increased attenuating effect (mechanical filter) upon the higher frequency components of the waveform. This mechanical filtering effect is caused by the loss in mass density and material properties (i.e., stiffness) with increasing levels of decay. Figure 42 shows that Laminae 1 and 2 are severely decayed with the exception of locations with X > 90 cm. Figure 42 also shows that Laminae 4 and 5 are sound and that Lamina 3 has a gradient of decay; in Lamina 3, locations in the first 40 cm (i.e., X < 40 cm) are severely decayed and locations for X > 70 cm are of sound wood.

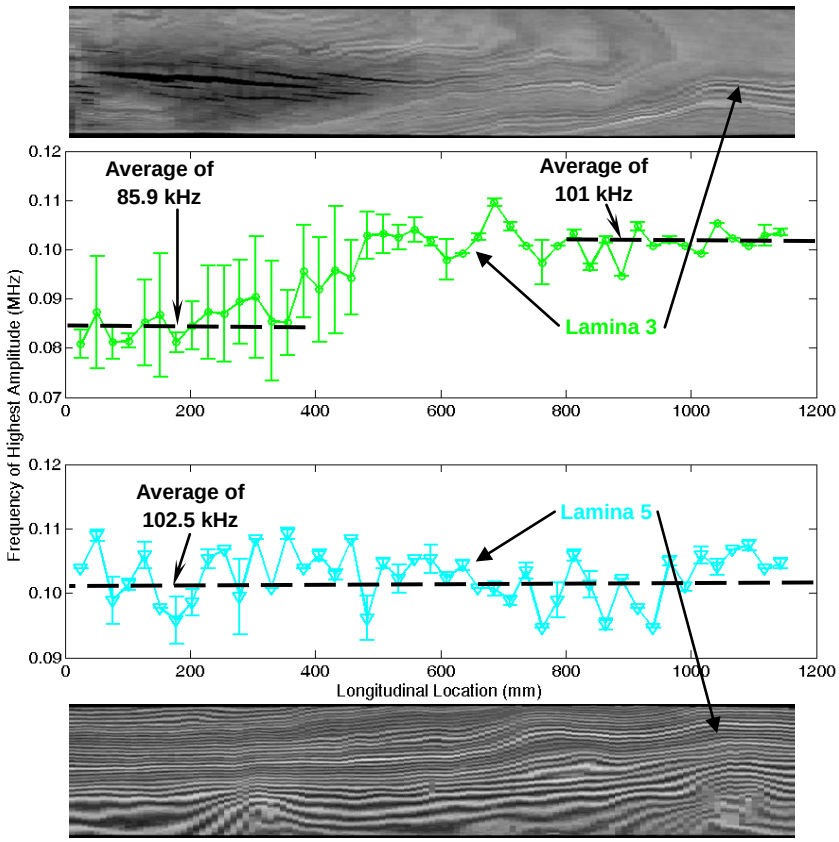


**Figure 43.** Frequency of highest amplitude along Laminae 3 and 5 showing error bars of three standard deviations. For comparison, the tomographic views are also shown. Dashed lines show the average frequency over the length of the line.

Figure 43 shows the frequency of maximum amplitude for Laminae 3 and 5 along the length of the glulam beam. For comparison Figure 43 also shows the longitudinal horizontal tomographic views of Laminae 3 and 5. Lamina 3 has a gradient of wood decay and Lamina 5 shows no decay and is used as reference lamina. In Figures 41, 42, and 43, each data point represents an average of five independent data points. In Figure

43, the average frequency of maximum amplitude for Lamina 5 with sound wood is 102.5 kHz as shown by the dashed line. For the Lamina 3 where a range of decay can be found, for the relative sound wood (X > 70 cm) the average frequency of maximum amplitude is 101 kHz, while regions with severe decay (X < 40 cm) show an average frequency of maximum amplitude of 85.9 kHz. Figure 43 also shows the error bars corresponding to three standard deviations, and it indicates that regions with decayed wood have larger variability than regions with sound wood.

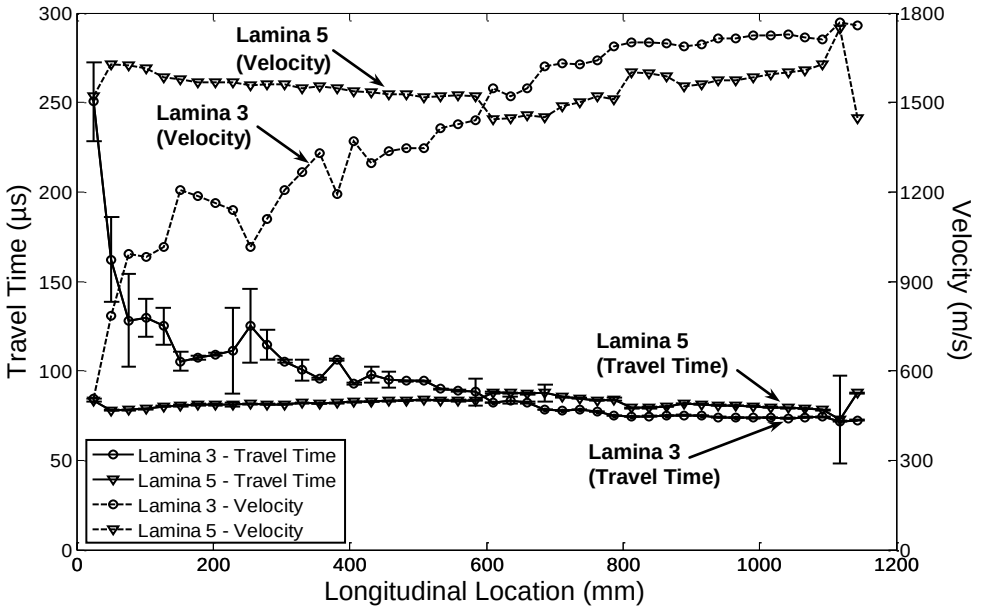


**Figure 44.** Arrival time and ultrasonic velocity along Laminae 3 and 5 showing error bars with three standard deviations. For clarity, the error bars are not shown on the corresponding velocity curves.

Figure 44 shows the time of arrival of the ultrasonic waveform versus location for Laminae 3 and 5 along the center horizontal plane. Based upon the time of arrival, Figure 44 also shows the corresponding computed ultrasonic velocity, where the travel distance is assumed to be 5 in (12.7 cm), i.e., the glulam beam thickness. This may not necessarily be true because of different growth ring orientation in each lamina as shown in Figure 35, where the material principal axes continuously vary along the growth rings. Furthermore, because of severe decay, which can lead to potential air pockets inside the lamina, the ultrasonic energy may follow a different path around the air pocket for a small perturbation in transducer position. Therefore, the time of arrival and ultrasonic velocity results for different laminae cannot be compared among them, and are only valid

for each individual lamina. For example, Lamina 5 (which has no decay) has higher ultrasonic time of arrivals (i.e., lower velocities) than Laminae 3 (which has a gradient of wood decay ranging from mild to severe decay). However, within Lamina 3 (which has a range of severe decay to sound wood) locations where X > 70 cm (sound wood) have lower time of arrival, i.e., higher velocities, than locations where X < 40 cm (decayed wood).

### 3.3. Modified Impact-Echo Experimental Description

Figure 45 shows a schematic diagram of the modified impact-echo data acquisition system. The voltage signal from the accelerometer (Model PCB309M12 with a resonance frequency of 120 kHz) was filtered using a Butterworth filter (Krohn-Hite, model 3988) with a band pass of 500 Hz to 500 kHz, and the waveforms were collected at a sampling rate of 1 MHz. The filtering of frequencies below 500 Hz removed any potential longitudinal resonances induced by the finite length of the glulam beam. Data was recorded after the voltage exceeded the trigger voltage of 19 mV.

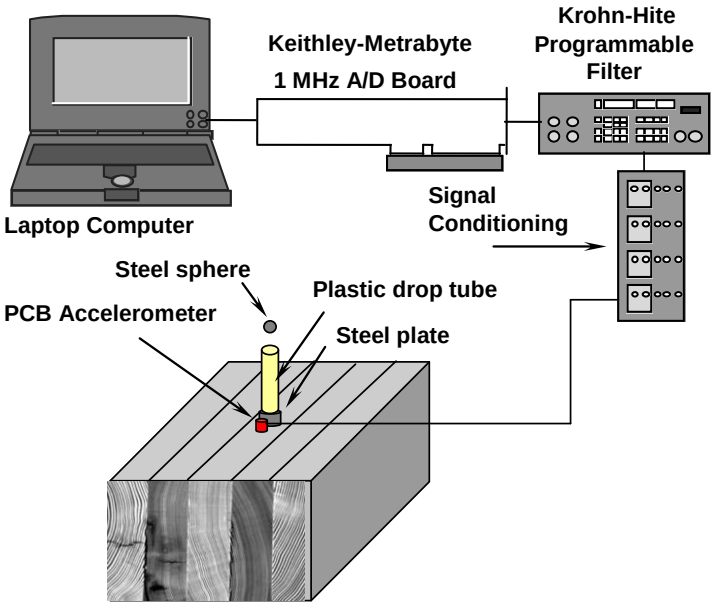


**Figure 45.** Modified impulse-echo data acquisition system schematic diagram showing the relative position of the impact plate and accelerometer. Both the steel plate and the accelerometer are coupled to the test surface using high vacuum grease; they are close but do not touch each other. The steel plate is ¼ inch thick with a diameter of ½ inch to avoid interference with beam resonance frequencies.

A steel ball bearing of diameter 12.7 mm and mass of 8.33 grams was used as the impactor. The steel ball bearing was dropped from a height of 200 mm onto the center of a circular steel plate with a mass of 6.27 grams, a thickness of 6.35 mm, and a diameter of 12.71 mm. The dimensions of the impact plate were chosen to place its resonance frequencies above the testing frequency band of interest. An impulse echo was performed every 2.54 cm (one inch) along each lamina as illustrated in Figure 45. At each of the forty-five locations along the length, five sphere drop tests were performed and five corresponding waveforms were collected. These five waveforms were averaged to obtain a single "waveform" for each of the 45 locations along the centerline of each lamina. For each averaged waveform, the corresponding frequency domain was also calculated using MATLAB tools.

The accelerometer was placed adjacent to the impact plate with their centers parallel from the edge of the lamina as shown in Figure 45. Care was taken to prevent contact between the impact plate and the accelerometer. Both the impact plate and the accelerometer were coupled to the lamina surface using Celvacene heavy, high vacuum grease. The presence of the plate prevented marring of the lamina top surface by the steel sphere and eliminated variability of the impact spectral power distribution caused by the presence of the growth rings on the top surface. The impact plate also increased the area across which the wave energy was distributed. The beam was fixed into a position such that a portion of the beam was cantilever to the test rig support. The location of testing was always within a cantilever portion of the beam in order to minimize potential signal loss due to leakage into surfaces abutting the beam.

### 3.4. Influence of the Growth Rings

To investigate the influence of the growth rings upon the wave propagation, lamina five was selected because of its distinct growth rings as illustrated in Figure 46, and because it was free of wood decay. At each of the forty five locations along lamina five waveforms were collected.

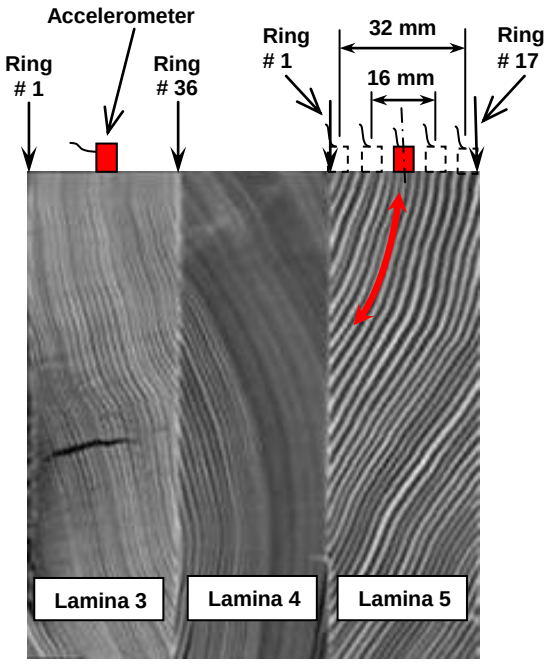


**Figure 46.** X-Ray CT computer tomography of Laminae 3, 4, and 5 showing different density of growth rings. Please notice the marked distinct rings (numbered 1 through 17) in Lamina 5. Please notice also the number of rings in contact with the accelerometer in Lamina 3 and Lamina 5. The accelerometer is a cylinder 6 mm high with a base 6 mm in diameter, and each lamina has a cross-section of 127 mm by 38.1 mm (5 in by 1.5 in).

As Figure 46 illustrates, at each test location, approximately three growth rings were beneath the accelerometer, indicating that three resonant peaks should be visible in the power spectral density curves (PSD). The PSD curves obtained at most locations along the length of the lamina had more than three resonant peaks; however, a few locations had three distinct resonant peaks in the range of 9 to 12 kHz. After identifying a respective frequency range of these peaks, the frequency domain data for all locations were examined for a grouping of three peaks within or near the range. The frequencies of each of the three peaks were recorded for each location. An average frequency was obtained for each of the three peaks, see Table 4. Based upon the size of the accelerometer and the X-ray tomographical images showing the tree rings, it was concluded that the accelerometer would most likely be positioned over the growth rings numbered 9, 10, and 11, with the lengths of 50.0, 55.7, and 62.5 mm, respectively. Using the average frequency and the measured growth ring lengths, three estimates of the wave speed tangential to the tree growth rings was obtained using the following Equation 6.

$$f_{res} = \frac{c_\theta}{2L_{ring}} \quad (6)$$

Where:
$f_{res}$ is the resonant frequency
$c_\theta$ is the tangential wave speed
$L_{ring}$ is the ring length

Equation 6 describes the relationship between frequency, growth ring length, and tangential wave speed (i.e., speed along the growth ring). The data used to obtain the three estimates is given in Table 4.

**Table 4.** Estimated wave velocity tangential to growth ring of Lamina 5

| Tree Ring Number | Resonant Frequency (kHz) | Wave Velocity (m/s) |
|---|---|---|
| 9 | 11.3 | 1130 |
| 10 | 10.7 | 1186 |
| 11 | 10.0 | 1255 |
| | Average | 1190 |

The three estimates were averaged to obtain a single working estimate of the tangential wave speed. Using this estimate of the wave speed tangential to the growth rings in conjunction with the measured distances for all of the tree rings obtained from the X-ray computer tomography images, predicted values for resonant peaks were calculated as shown in Table 5. Then, the characteristics of the reflected waves were examined across the width of the lamina at the same longitudinal location, i.e., location 20 (X = 20 cm). Here, five equally spaced test positions across the width of the Lamina 5 were identified, as illustrated in Figure 46. Please note that the accelerometer has the following cylindrical geometry: 7 mm high with a circular base 6 mm in diameter. At each transverse position five pulse echo tests were again performed and both the time domain and spectral power density curves were obtained.

Figure 47 shows the averaged time domain waveform and its corresponding power spectral density curve for the central position as indicated in Figure 46. The power spectral density curves were then examined for frequency peaks corresponding to the growth rings located beneath the accelerometer for each location. Please note that even though some growth rings did not fall directly beneath the accelerometer, the resonant peaks were still visible because of the energy leakage from one ring to the neighboring

rings. Table 5 also shows the measured frequency peaks. The predicted and the corresponding measured peak values of the frequency peaks are also shown in Figure 48.

**Table 5.** Estimated and measured resonant frequencies due to growth rings at location 508 mm (20 in) based upon estimated tangential wave velocity

| Ring Number | Ring Length (mm) | Resonant Frequencies (kHz) | |
|---|---|---|---|
| | | Estimated | Measured |
| 1 | 3.4 | 174.6 | 168.11 |
| 2 | 6.8 | 87.3 | 87.79 |
| 3 | 11.4 | 52.4 | 51.04 |
| 4 | 21.6 | 27.6 | 28.33 |
| 5 | 30.7 | 19.4 | 16.54 |
| 6 | 35.2 | 16.9 | 16.73 |
| 7 | 42.0 | 14.2 | 13.92 |
| 8 | 46.6 | 12.8 | 12.21 |
| 9 | 50.0 | 11.9 | 11.23 |
| 10 | 55.7 | 10.7 | 10.26 |
| 11 | 62.5 | 9.5 | 9.65 |
| 12 | 68.2 | 8.7 | 8.67 |
| 13 | 76.1 | 7.8 | 7.81 |
| 14 | 81.8 | 7.3 | 7.33 |
| 15 | 89.8 | 6.6 | 6.96 |
| 16 | 94.3 | 6.3 | 6.61 |
| 17 | 100.0 | 6.0 | 6.23 |

This experiment leads to the conclusion that the presence of the growth rings within the lamina results in several resonance peaks in the power spectral density curves. It also shows that the majority of the wave energy was reflected from the end of the growth rings and not from the bottom of the lamina, i.e., the energy is reflected prior to traveling completely through the depth of the lamina. It also shows that the wave velocity tangential to the growth rings of Lamina 5 is approximately 1190 meter per second. Another important observation is the leakage of energy from a growth ring to its neighboring rings. As a result of this energy leakage, regardless of the position of the impact plate and accelerometer across the lamina, the frequencies of 9.65, 10.26, and 11.23 kHz, which correspond to the growth rings 9, 10, and 11, respectively, were always present. This can be observed in Figure 47. Please notice that the resonance frequencies corresponding to the shorter rings (i.e., rings 1, 2, and 3) were also observed.

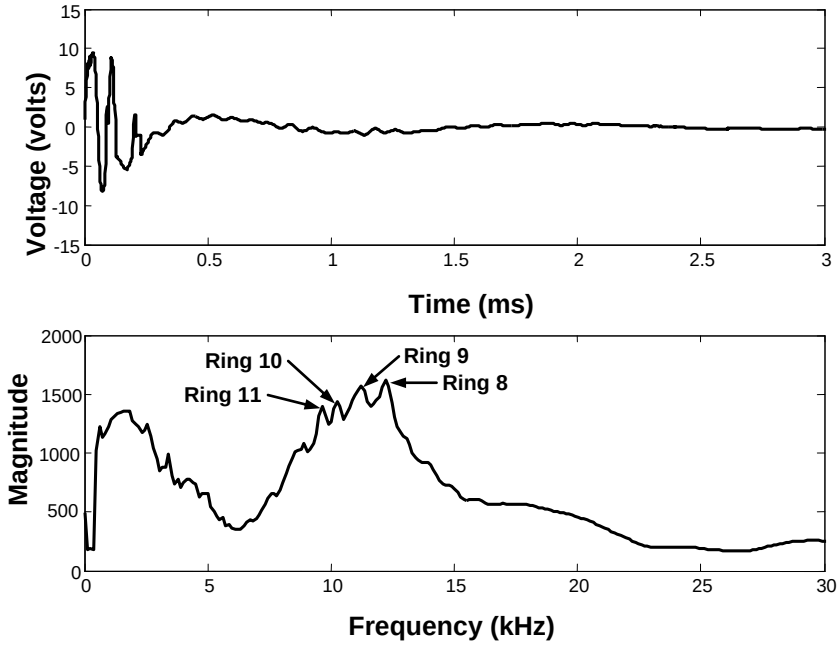


**Figure 47.** Time domain waveform and power spectral density curve for location X = 50.8cm (20 in) for Lamina 5. The accelerometer was in the central position of the lamina cross-section as indicated in Figure 45. Please notice the dominance of the frequencies corresponding to growth rings 8 to 11.

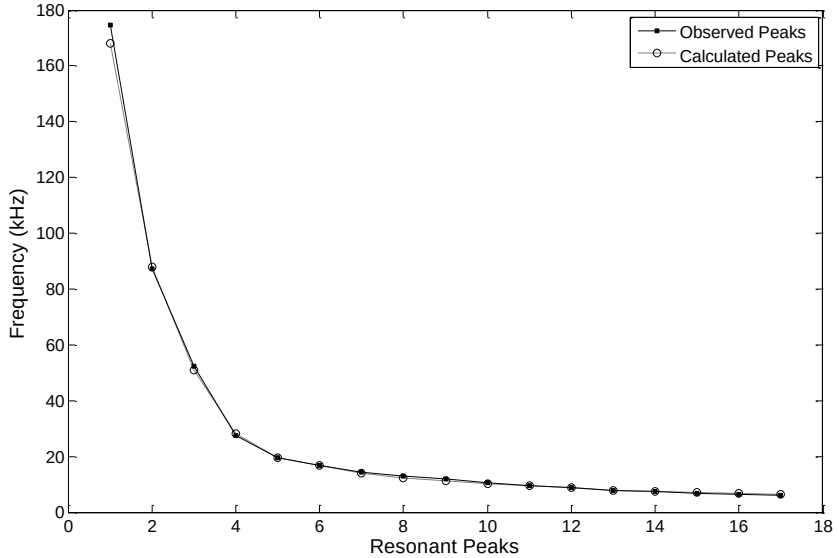


**Figure 48.** Predicted and measured values of frequency peaks in the power spectral density curves at location 50.8cm (20 in) of Lamina 5 from Table 5.

### 3.5. Modified Impulse-Echo Approach Analysis

Using MATLAB filtering tools, the recorded waveforms were further filtered using a low-pass Butterworth filter with edge frequency of 500 kHz. After filtering, the time domain data was then averaged to obtain a single "working set" for each gridline location along each lamina. The resulting frequency domain was then also calculated using MATLAB tools for each gridline location along each lamina.

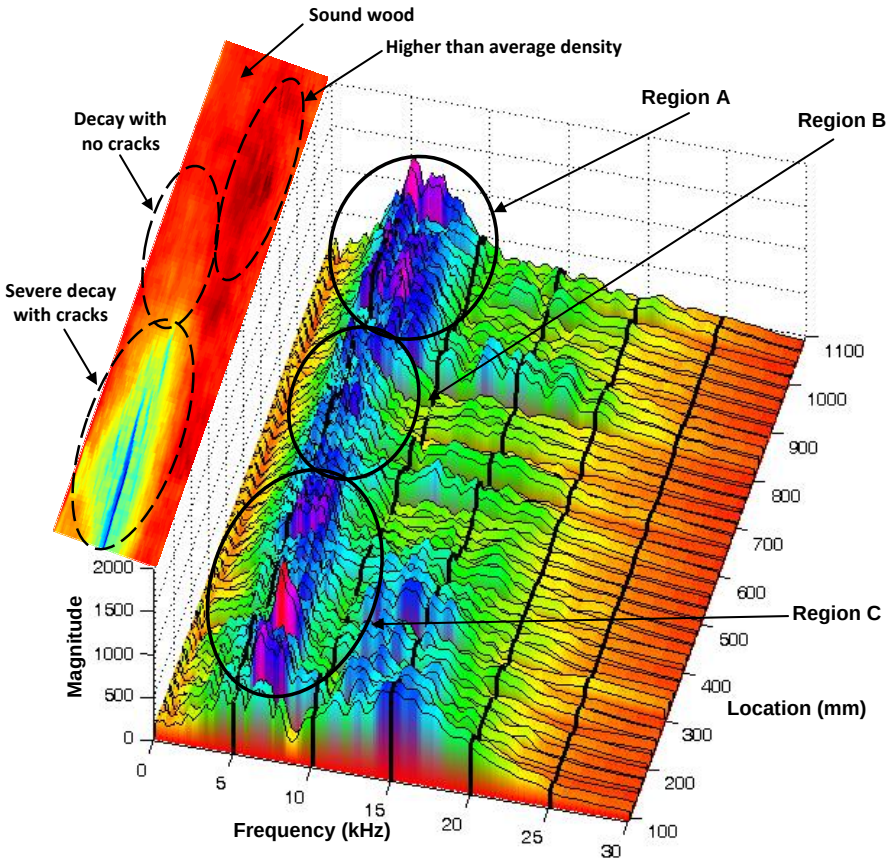


**Figure 49.** Cascade of power spectral density curve versus longitudinal location for Lamina 3. Figure also shows the average density across Lamina 3. Please note the influence of wood structure and condition (i.e., the presence of decay, presence of cracks, and regions of above average density) upon power spectra.

Figure 49 shows a cascade of power spectral density curves for locations 4 to 42 for Lamina 3 up to 30 kHz. In Figure 49 locations 1 to 3 and 43 to 45 were not shown to remove end effects. For each of the 45 locations, the accelerometer was located at the center of transverse dimension of Lamina 3. Following a similar study as in Lamina 5, the wave velocity tangential to the growth rings for Lamina 3 was measured to be 1130

m/s with a standard deviation of 65 m/s. For clarity, Figure 37b is also shown along the cascade of the power spectral density curves. All regions of Lamina 3 have a band of frequencies between six and eight kHz containing high magnitude frequencies. In the region of sound wood and higher than average density wood, locations 800 mm to 1100 mm, the frequency band broadens to a band of five to nine kHz and the magnitude of the frequencies within the band are some of the highest in the lamina. In regions with severe decay and with the presence of cracks, locations 100 mm to 400 mm, there is a shift of energy to higher frequencies. This is due to the presence of the crack, which reduces the distance traveled, i.e., the "back-echo" reflections. In the region containing decay with no cracks, locations 400 mm to 800 mm, the magnitude of the frequencies within the 6 to 8 kHz diminish, and the high frequencies disappear as the cracks no longer provide a "back-echo" reflection.

### 3.6. Waveform Decay Rate Analysis

Please note that (a) with the exception of the presence of knots, the structure of the growth rings and their orientation at the interface is relatively constant along the length of each lamina, (b) each lamina has a relatively high surface roughness, and (c) to secure a relatively strong bond there is an adhesive layer between each lamina and its adjacent laminae, the acoustic impedance mismatch between the material of each lamina and its adjacent material (i.e., adhesive) at the interface is assumed to be relatively constant along the length of the glulam beam. This means that the leakage of acoustic energy at the interfaces between the lamina being tested and its adjacent laminae can also be considered relatively constant at each testing station along the length of the lamina. Considering that the acoustic energy associated with longitudinal modes has been filtered out, and that decayed wood has higher attenuation values than sound wood [6], it is expected that the amplitudes of the frequency components of the spectra shown in Figure 49 will attenuate at a faster rate in cross-sections where decayed wood is present. As a result, an attenuation rate analysis of the averaged waveforms, corresponding to each of the 45 locations along the center-line for each lamina, was performed.

Figure 49 illustrates that most of the waveform energy exists in a frequency band from 500 Hz to 20 kHz. As a result, a window of 1024 points was moved across the

waveform point-by-point and at each location the corresponding fast Fourier transforms (FFT) were calculated. At each window, the frequency amplitudes corresponding to the FFT frequencies ranging from 976 Hz to 19.53 kHz with increments of 976 Hz were calculated. For each frequency, an exponential decay curve was fitted to the FFT amplitude values versus time, where the exponent is considered to be the attenuation, i.e., decay rate, of the magnitude with respect to time for that frequency. An average of the decay rates for the FFT frequencies in a frequency band of 500 Hz to 20 kHz (ranging from 976 Hz to 19.53 kHz with increments of 976 Hz) was then calculated. The solid line in Figure 50a shows the voltage amplitude, corresponding to 12.72 kHz, versus time for data collected from Lamina 3 at location 686 mm (27 in). The dashed line in Figure 50a represents the corresponding exponential fit ($r^2$ = 0.87), which led to a decay rate value of 1.26 Nepers/ms. Figure 50b shows the voltage amplitude versus time for all the FFT frequencies at the same location.

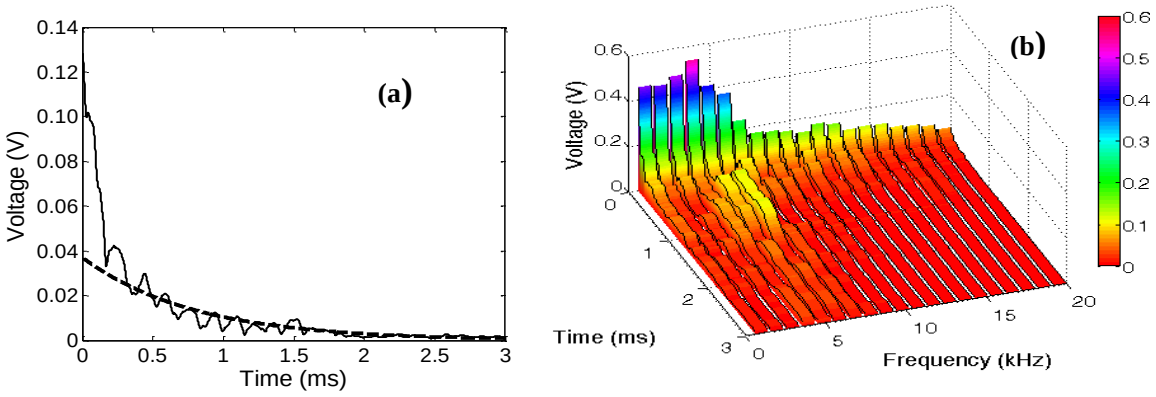


**Figure 50.** Frequency voltage decay versus time at location 27 (686 mm) of Lamina 3. (a) The solid line represents the decay of one of the amplitudes (corresponding to 12.72 kHz) and the dashed line represents the corresponding exponential fit ($r^2$ = 0.87). The data was collected from Lamina 3 at location 686 mm (27 in). This frequency component has a decay rate value of 1.26 Nepers/ms; (b) Voltage amplitude versus time for frequencies 500 Hz to 20 kHz (FFT amplitudes) at the same location.

Figure 51 shows the average exponential decay rate versus longitudinal location for all five laminae. Please note that for each curve, i.e., lamina, the solid lines represents cross-sections with sound wood and the dotted lines represent cross-sections with decayed wood. In Figure 51, Laminae 4 and 5 have no wood decay and have the lowest decay rate, while Laminae 1 and 2, which have the most decayed wood, have the highest decay rate. Lamina 3, as Figure 38 also indicates, has regions of sound wood, regions of

decayed wood and regions varying from sound to decayed wood. Figure 52 shows a histogram of the average exponential decay rate for sound and decayed wood showing the corresponding probability density functions, which are assumed to follow a normal distribution.

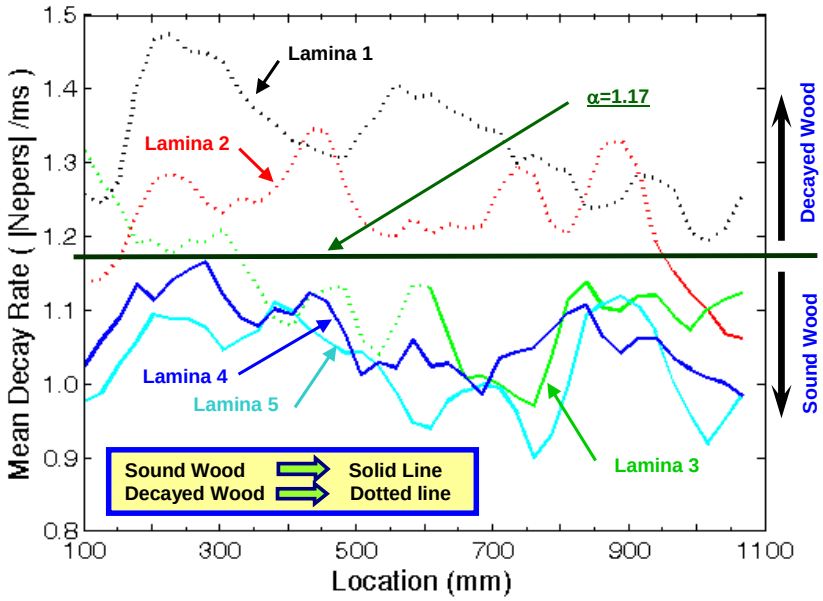


**Figure 51.** Mean exponential decay rate for all laminae. Please note that the solid and dashed lines represent sound and decayed wood, respectively.

Figure 52 shows that the two distributions intercept each other at the value of $\alpha$ = 1.17 Nepers/ms. Assuming that this average decay rate would be considered to serve as a decision criterion to differentiate between sound wood from decayed wood, the criteria would lead to 5.7% of false negative calls (decayed wood considered to be sound wood) and to 3.5% false positive calls (sound wood considered to be decayed). This leads to an overall false call rate of 7.2%.

Figure 53 shows the average decay rate versus the average cross-section density for each lamina. Figure 53 shows that, within each lamina, cross-sections with the presence of decayed wood have a higher rate of decay. It also indicates that laminae cannot be compared with each other because each lamina starts with a different wood density. As a result, in Figure 53 each data point within a lamina can only be compared with points within the same lamina. To avoid this difficulty, a cross-section density index is introduced.

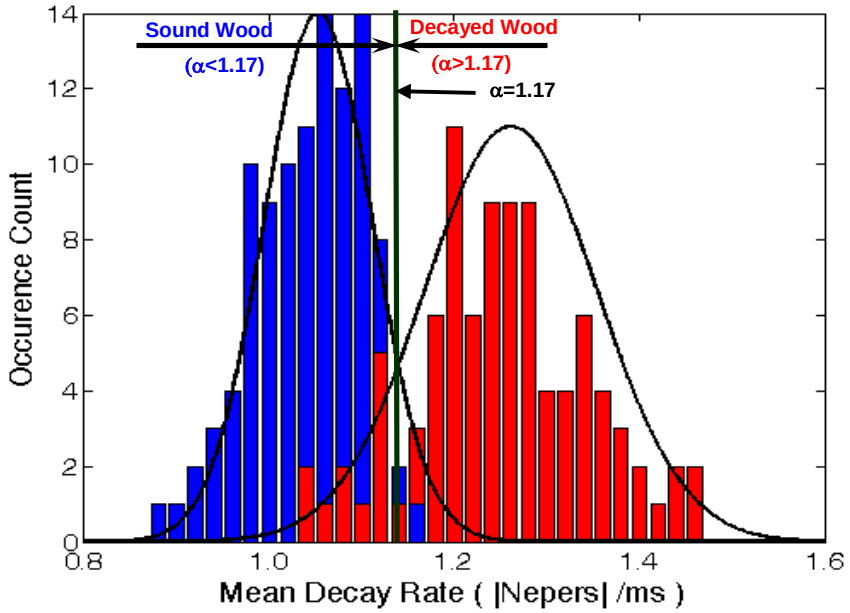


**Figure 52.** Histogram of the mean exponential decay rate for sound and decayed wood showing corresponding probability density functions.

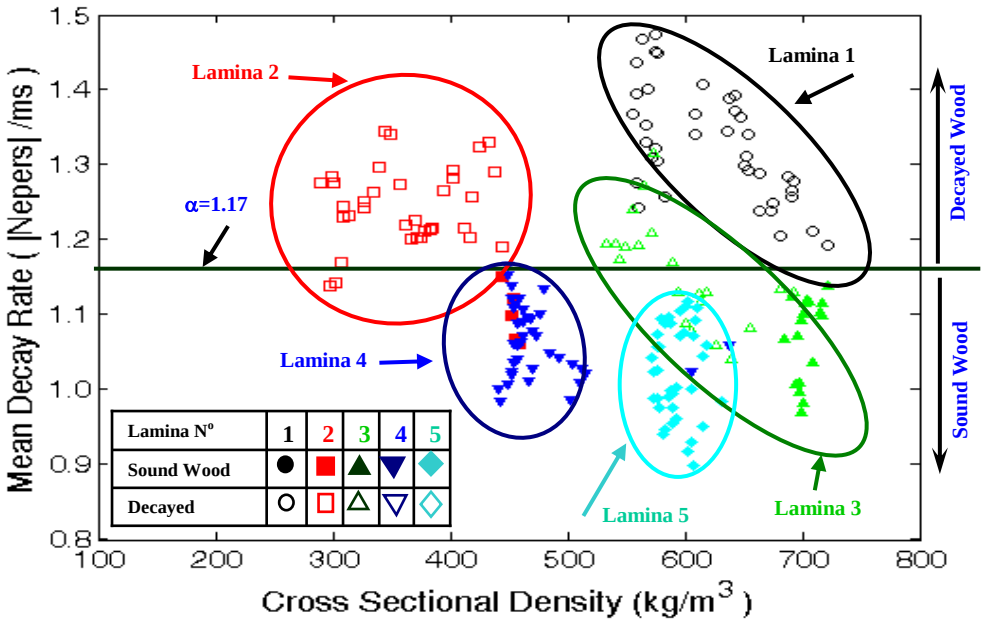


**Figure 53.** Mean decay rates versus laminae cross-sectional density.

Within each lamina it was observed that sound wood has a more consistent, i.e., less variable, density than decayed wood. It was also observed that wood with knots has higher density that sound wood without knots. Therefore, the cross-section with the smallest standard deviation in wood density was found for each lamina, and the mean density of this cross-section was assumed to be the density of sound wood for that

lamina. Then, the lamina was searched for locations where the average wood density values were higher than the corresponding calculated mean density for that lamina, and these higher values were replaced with the calculated mean density for that lamina. This had the effect of filtering out the effect of the knots' higher density on the mass loss due to decay. At each location of the "new lamina density," i.e., lamina with the knots filtered out, the mean and the standard deviation for each cross-section were calculated. Then, at each location along each lamina the cross-sectional density index was defined as

$$I = \frac{\mu - \sigma}{\mu} \tag{7}$$

Where:
$\mu$ is the mean cross-section density
$\sigma$ is the corresponding standard deviation for a particular cross-section.

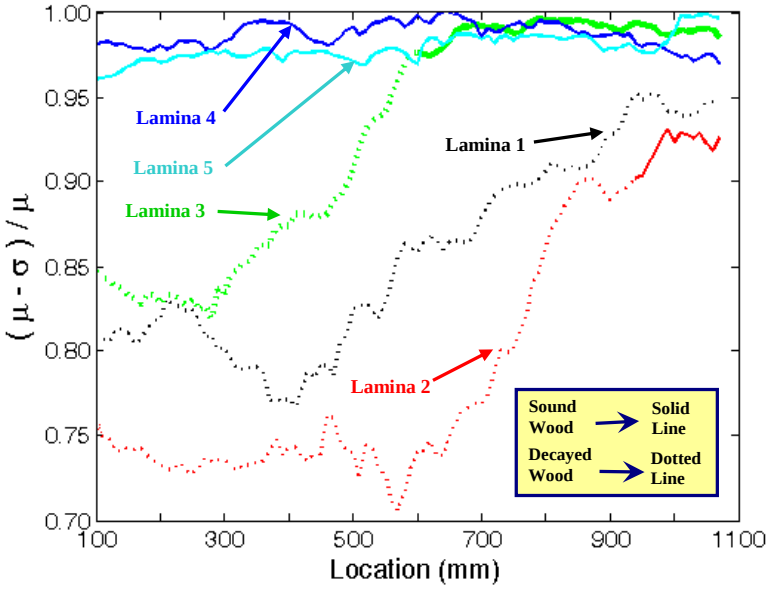


**Figure 54.** Cross-sectional density index, $I = (\mu - \sigma)/\mu$ versus location for all five laminae. Please note that the solid and dashed portions of each line represents sound and decayed wood, respectively.

Figure 54 shows the cross-sectional density index versus location for all five laminae, where solid and dashed lines denote sound and decayed wood, respectively. Figure 55 shows the average exponential decay rate versus cross-sectional density index. In Figure 55, solid symbols denote sound wood and non-solid symbols denote decayed wood. Figure 55 also indicates that sound wood has a higher cross-sectional density index and lower average exponential decay rate.

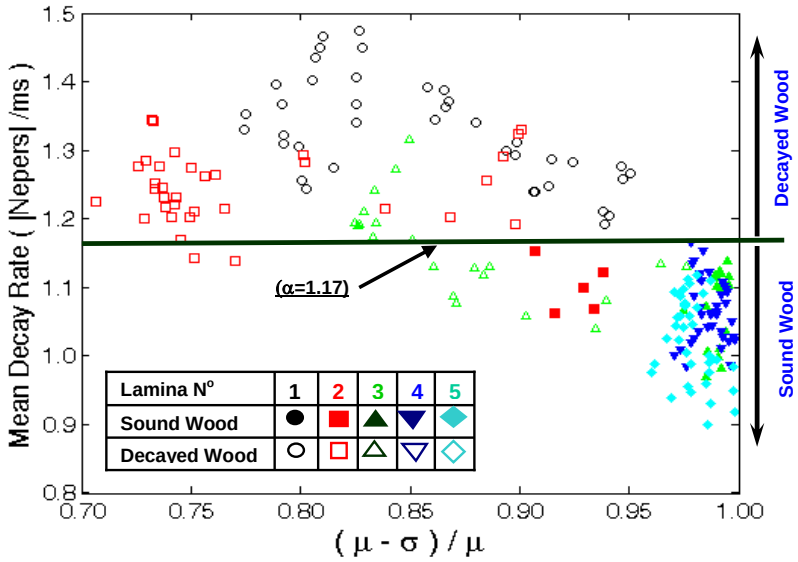


**Figure 55.** Mean decay rate versus cross-sectional density index, I = (μ - σ)/μ

### 3.7. Conclusions of Glulam Beam Testing

One Douglas-fir glulam beam with a cross-section of 19.1 cm by 12.7 cm (7.5 in by 5 in) was salvaged from a construction site. The glulam beam was made from five 12.7 cm by 3.8 cm (5 in by 1.5 in) boards. Visual inspection of the original beam did not show any indications of decay on the entire beam. A segment 114 cm (45 in) long of this beam was then cut for this study. In this beam segment, the only observed indication of decay was at the end of the beam in Lamina 2 where a small interior hole was observed. However, the level of decay for the beam segment could not be assessed using visual inspection. A small (millimeter-wide) longitudinal split on the top surface of Lamina 1 was also observed. Using X-ray computer tomography, severe decay, i.e., mass loss, was detected in the Lamina 2. It was observed that significant decay had also progressed to the adjacent laminae, i.e., Laminae 1 and 3. In addition, it was observed that Laminae 4 and 5 were made of sound wood, and that Lamina 3 had a region of severe decay, a region of sound wood, and a region with varying degrees of decay.

In the glulam beams, the loss of density was identified as a characteristic of rot. However, low density itself could not be used as a metric. The density variations between wood beam laminae composing the glulam beam were on the same order of magnitude as the rot within a beam. Laminae 1 and 3 contained areas of rot; however,

the density of those laminae were greater than Lamina 4, which was sound along its entire length.

The glulam beam was first inspected using ultrasonic transducers in a through-transmission setup to excite a frequency of 100 kHz and monitor a frequency range of 85 kHz to 120 kHz. Within that frequency range, good correlation was found between the frequency of highest magnitude and the presence of rot within the glulam beam. As the presence of rot increased, the frequency of highest magnitude shifted lower towards 80 kHz. Good correlation was found between the area under the power spectral density (PSD) curve and the presence of rot. As rot increased in severity, the area under the PSD decreased. Time of flight of propagating waves was also strongly correlated to the presence of rot. As rot increased, the time of flight increased. Access to both sides of the beam was necessary for this technique. In some locations, gains as high as 140 dB were necessary to obtain results. It is likely higher gains would be necessary in order to use a pulse echo technique, limiting its field potential.

Further analysis was performed using a modified impact-echo setup. A steel sphere was dropped onto the surface of the glulam beam and the dynamic response was monitored using an accelerometer. The frequency range examined using this technique was 500 Hz to 20 kHz. Within the same frequency range, good correlation was found between the presence of decayed wood and the mean attenuation rate. A mean attenuation rate of 1.17 Nepers per millisecond or higher was an indication of the likely presence of rot. The impulse-echo decay rate approach leads to a 5.7% probability of false negative calls (i.e., decayed wood assumed to be sound wood) and to a 3.5% probability of false positive calls (i.e., sound wood assumed to be decayed), with an overall rate of false calls of 7.2%. This approach has the advantage of only requiring access to one lateral side of the beam. Considering the variability that exists in wood including the presence of splits, different orientation and thickness of growth rings, etc., this relatively low rate of false calls makes this approach very attractive.

### 3.8. Recommendations for Future Work in Glulam Beam Analysis

In many in situ situations, access can only be gained to one side of a glulam beam. In that case, an input source other than a dropped metal sphere must be used. Designing

a test setup such that allows the examined beam to be at any orientation would greatly expand the applicability of the modified pulse echo technique. Such a test set up would necessarily include a means of coupling the sensor to the surface of the glulam beam in a manner that does not alter the condition of the beam.

Also, modifying the input source to excite frequencies higher than 20 kHz would be advantageous. Wave attenuation through decayed wood increases, and wave velocity through decayed wood decreases with increasing frequency; therefore, higher frequency input signals will have increased likelihood of detecting decay. There may exist a frequency range in which all three parameters: mean decay rate, the area under the power spectrum, and the frequency of highest magnitude are reliable indicators of the presence of rot. Identifying such a range would greatly increase the likelihood that internal rot would be identified.

# CHAPTER 4. WOODEN UTILITY POLES

In this chapter, wooden utility poles are examined. A two-dimensional, finite difference time domain (FDTD) model capable of simulating wave motion through a utility pole cross-section is constructed. The wave motion described by the FDTD model is first validated against an analytical model of waves passing through a cylindrically orthotropic medium. There is strong agreement between the two models. The FDTD model is validated against results obtained from testing of utility pole specimens in the laboratory. Discrepancies between the modeled output and the test results are described and explained. The theoretical and experimental validation demonstrates that the FDTD model is capable of accurately modeling wave behavior through a utility pole.

Using the validated model, several defects are introduced into the simulation space to examine their effects upon the system output. The output is examined to find characteristics, trends, and / or parameters that correlate to internal decay within the poles. Three metrics are presented as useful indicators. The metrics are then applied to the output from three different utility pole specimens. The predicted sizes of the defects are accurate to within 2.0% of the cross-sectional area of the utility pole, and the predicted center location of defects are accurate to within 17% of the cross-sectional radius.

## 4.1. Finite Difference Time Domain Model of Utility Pole

The structure of wood has many aspects making analytical modeling difficult. Sound wood is anisotropic, heterogeneous, attenuative, fibrous, porous, and hygroscopic. These characteristics complicate attempts to model wave motion through wood. As a result, most computational analyses of wood prior to 2004 (with the notable exceptions examined in this report) assumed wood to be homogeneous and isotropic. The work of Ting [112, 113] provided rigorous analysis of the behavior of anisotropic solids. Martin [114] provided additional analysis regarding anisotropic solids in cylindrical coordinates. Building upon the works of Ting and Martin, Payton [107] wrote a computationally impressive series of publications in which he derived the equation of motion for a unit impulse in a semi-infinite, two-dimensional, anisotropic solid in cylindrical coordinates.

While Payton's analytic solution provides great insight into wave motion, it is limited in its applicability in wood analysis as it does not allow for: signal attenuation, inclusion of local defects such as cracks and voids, and changes to material characteristics based upon the location within the solid. The limited scope of Payton's work, however, does provide a means of validation for any potential wood model.

The wood model used in this simulation is constructed using a finite difference time domain (FDTD) analysis technique. FDTD is commonly used to describe wave motion through a medium. The FDTD model used in this analysis employs a staggered grid formulation first proposed by Yee [115]. The grid allows for material characteristics to be changed by location allowing for the inclusion of decayed wood behavior, voids, and cracks. Gsell [116] described elastic wave propagation in three dimensional, anisotropic, cylindrical shells using FDTD. Schubert [117] developed a two dimensional, plane strain model based upon Gsell's model. Schubert's model provides the starting basis upon which the current model is built.

The present analysis expands upon Schubert's work by allowing wave continuity across the center point of the cross-section, implementing a grid enhancement scheme, implementing material attenuation, modeling wood as a dispersive medium for both velocity and attenuation, and implementing changes to velocity and attenuation as functions of mass loss due to rot.

One confounding aspect of decayed wood is the lack of reflections at the sound wood / decayed wood boundary. As wood decays there is an observable decrease in both wave speed and density. Changes in density and / or wave speed are typically associated with changes in acoustic impedance. Changes in acoustic impedance along wave travel paths are usually associated with wave reflections at the location of the change. However, as seen in Senalik [118] decayed wood shows no discernible wave reflections.

The reflectionless quality of rot is modeled using a combination of a sawtooth boundary and a perfectly matched layer. The boundary of the decayed region is given a sawtooth shape. A sawtooth boundary disrupts incident waves through a combination of scattering and multidirectional reflection [119]. Also, rot attenuation is applied through the use of a perfectly matched layer [120]. A perfectly matched layer enables waves entering the region to experience a large attenuation without causing reflections at the

region boundary. This is accomplished through the use of acoustic impedance matching and the use of complex dimensions [121]. Both of these techniques are described within this section.

The simulation is a dispersive model in both velocity and attenuation. The model is based upon empirical relationships between velocity, attenuation, frequency and mass loss developed by McGovern [21, 110]. McGovern fit the relationships to polynomials [21]. In order to implement the polynomials, the input signal must be decomposed into constituent frequencies and each must individually be used as a system input. The system response to the original input signal is the superposition of all of the individual frequency responses.

In this portion of the report, the derivation of the FDTD equations necessary to simulate the response of a two dimensional, circular, wooden cross-section to a user defined displacement disturbance function is given. The goal of the analysis is to simulate the changes of waves traveling through sound and decayed wood over time and after multiple reflections.

### 4.1.1. Theoretical foundation – simulation of wave motion

In this analysis, it is assumed that wood is an orthotropic material. The stiffness matrix for an orthotropic material expressed in cylindrical coordinates is shown in Equation 8.

$$\begin{bmatrix} \sigma_z \\ \sigma_r \\ \sigma_\theta \\ \tau_{r\theta} \\ \tau_{z\theta} \\ \tau_{zr} \end{bmatrix} = \begin{bmatrix} C_{zz} & C_{zr} & C_{z\theta} & 0 & 0 & 0 \\ & C_{rr} & C_{r\theta} & 0 & 0 & 0 \\ & & C_{\theta\theta} & 0 & 0 & 0 \\ & & & 2G_{r\theta} & 0 & 0 \\ & \text{Sym} & & & 2G_{z\theta} & 0 \\ & & & & & 2G_{zr} \end{bmatrix} \begin{bmatrix} \varepsilon_z \\ \varepsilon_r \\ \varepsilon_\theta \\ \varepsilon_{r\theta} \\ \varepsilon_{z\theta} \\ \varepsilon_{zr} \end{bmatrix} \tag{8}$$

Where:
σ represents a normal stress in Pascals
τ represents a shear stress in Pascals
ε represents a strain in meters per meter
z represents the longitudinal direction of the cylinder
r represents the radial direction of the cylinder

θ represents the tangential direction of the cylinder
$C_{jl}$ is the stiffness matrix value (j, l = z, r, θ) in Pascals
$G_{r\theta}$ is the shear modulus in Pascals as reported by the Forest Products Laboratory [10] and requires no modification for use in the stiffness matrix.

Plane strain conditions ($\varepsilon_z = \varepsilon_{z\theta} = \varepsilon_{zr} = 0$) are assumed throughout this analysis; therefore, the stiffness matrix is condensed to the form shown in Equation 9.

$$\begin{bmatrix} \sigma_r \\ \sigma_\theta \\ \tau_{r\theta} \end{bmatrix} = \begin{bmatrix} C_{rr} & C_{r\theta} & 0 \\ & C_{\theta\theta} & 0 \\ \text{Sym} & & 2G_{r\theta} \end{bmatrix} \begin{bmatrix} \varepsilon_r \\ \varepsilon_\theta \\ \varepsilon_{r\theta} \end{bmatrix} \tag{9}$$

The terms within the stiffness matrix are constructed using velocity values from McGovern [21] (described in Section 4.1.10), Poisson's ratio values from Forest Product Laboratory [10], and density values from the CT scans of the pole cross-sections (described in Section 3.1). Graff [122] supplies the equations for expressing radial, tangential, and in plane shear strains in terms of the radial displacement, $u_r$, and the tangential displacement, $u_\theta$. Displacements are in units of meters.

$$\varepsilon_r = \frac{\partial u_r}{\partial r} \tag{10}$$

$$\varepsilon_\theta = \frac{1}{r}\frac{\partial u_\theta}{\partial \theta} + \frac{u_r}{r} \tag{11}$$

$$\varepsilon_{r\theta} = \frac{1}{2}\left(\frac{1}{r}\frac{\partial u_r}{\partial \theta} + \frac{\partial u_\theta}{\partial r} - \frac{u_\theta}{r}\right) \tag{12}$$

Elasticity equations relating stresses and radial and tangential accelerations are found in the same reference [122].

$$\rho\frac{\partial^2 u_r}{\partial t^2} = \frac{\partial \sigma_r}{\partial r} + \frac{1}{r}\frac{\partial \tau_{r\theta}}{\partial \theta} + \frac{\sigma_r - \sigma_\theta}{r} \tag{13}$$

$$\rho\frac{\partial^2 u_\theta}{\partial t^2} = \frac{\partial \tau_{r\theta}}{\partial r} + \frac{1}{r}\frac{\partial \sigma_\theta}{\partial \theta} + \frac{2\tau_{r\theta}}{r} \tag{14}$$

Where ρ is the material density in units of kilograms per cubic meter.

Substituting Equations 9 through 12 into Equations 13 and 14 leads to Equations 15 and 16, which give the radial and tangential acceleration as functions of the stiffness matrix values and the zero and first order derivatives of the radial and tangential displacements.

$$\rho\frac{\partial^2 u_r}{\partial t^2} = C_{rr}\frac{\partial^2 u_r}{\partial r^2} + \frac{C_{rr}}{r}\frac{\partial u_r}{\partial r} - \frac{C_{\theta\theta}}{r^2}u_r - \left(\frac{G_{r\theta}+C_{\theta\theta}}{r^2}\right)\frac{\partial u_\theta}{\partial \theta} + \ldots + \left(\frac{G_{r\theta}+C_{r\theta}}{r}\right)\frac{\partial^2 u_\theta}{\partial r\partial\theta} + \left(\frac{G_{r\theta}}{r^2}\right)\frac{\partial^2 u_r}{\partial\theta^2} \tag{15}$$

$$\rho\frac{\partial^2 u_\theta}{\partial t^2} = \frac{C_{\theta\theta}}{r^2}\frac{\partial^2 u_\theta}{\partial\theta^2} + G_{r\theta}\frac{\partial^2 u_\theta}{\partial r^2} + \left(\frac{G_{r\theta}+C_{r\theta}}{r}\right)\frac{\partial^2 u_r}{\partial r\partial\theta} + \ldots + \frac{G_{r\theta}}{r}\frac{\partial u_\theta}{\partial r} + \left(\frac{G_{r\theta}+C_{\theta\theta}}{r^2}\right)\frac{\partial u_r}{\partial\theta} - \frac{G_{r\theta}}{r^2}u_\theta \tag{16}$$

### 4.1.2. Finite difference scheme

The model has the form shown in Figure 56. There are three regions and two distinct locations that are addressed. Please note the following two locations: the center point and the source.

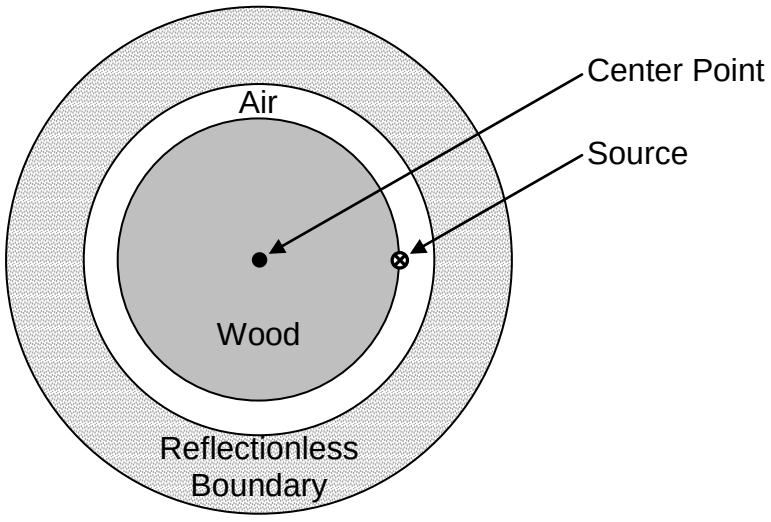


**Figure 56.** Utility pole wave propagation model schematic diagram.

The calculation of the center point displacement involves finding the mean displacement of the surrounding medium. The source is a Gaussian impulse. The wood model is similar to a model implemented by Gsell [116] and Schubert [117] and is assumed to be an elastic solid which is both anisotropic and inhomogeneous. Adjacent to the wood is a region of air. Between the region of air and the outer extents of the model is a reflectionless boundary. The reflectionless boundary is implemented through the use of perfectly matched layer (PML) as described by Berenger [120] with refinements relevant to this report by Liu [123, 124] and Chew [121].

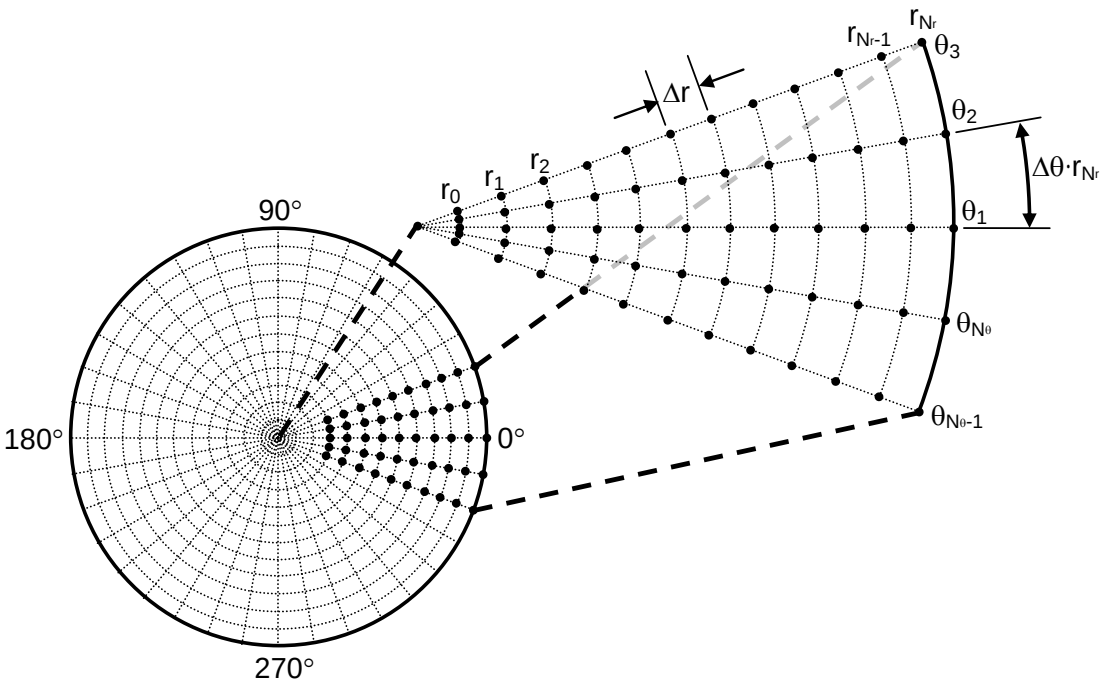


**Figure 57.** Model coordinate nomenclature

Where the symbols used in Figure 57 are as follows:
$N_r$ is the total integer number of radial divisions.
$N_\theta$ is the total integer number of circumferential divisions.
k is the integer radial index. $0 \le k \le N_r$
i is the integer circumferential index. $1 \le i \le N_\theta$
$r_k$ is the radial coordinate. Note that $r_0$ is the center point and requires special considerations which are discussed later.
$\theta_i$ is the circumferential coordinate.
$\Delta r$ is the radial spacing in meters between adjacent grid points.
$\Delta\theta$ is the circumferential angle between adjacent grid points in units of radians.

Figure 57 shows the coordinate system, grid layout, and nomenclature used in the model. Plane strain conditions are assumed and the longitudinal direction of the cylindrical coordinate system is positive outward from the page. The points at the intersections of the gridlines shown in Figure 57 represent locations where displacements are calculated. The grid points are situated collinearly along radial lines and are uniformly spaced by a distance of $\Delta r$. The radial lines are offset from each other by a radian angle of $\Delta\theta$. The number of grid points is constant for any distance $k\Delta r$. As a result, the circumferential distance between adjacent grid points increases as radius increased. A grid enhancement method is used to increase the number of circumferential points at user defined intervals to prevent the circumferential distance from becoming larger than desired. The grid enhancement scheme is described in Section 4.1.4.

The FDTD model used in this analysis employs a staggered grid formulation first proposed by Yee [115]. This analysis method requires two separate grids. One grid contains the displacements, $u_r$ and $u_\theta$, and the other grid contains the stress components, $\sigma_r$, $\sigma_\theta$, $\tau_{r\theta}$. The stress components' grid points are situated mid-distance between adjacent displacement grid points. Figure 58 shows the staggered grid composed of displacement and stress components.

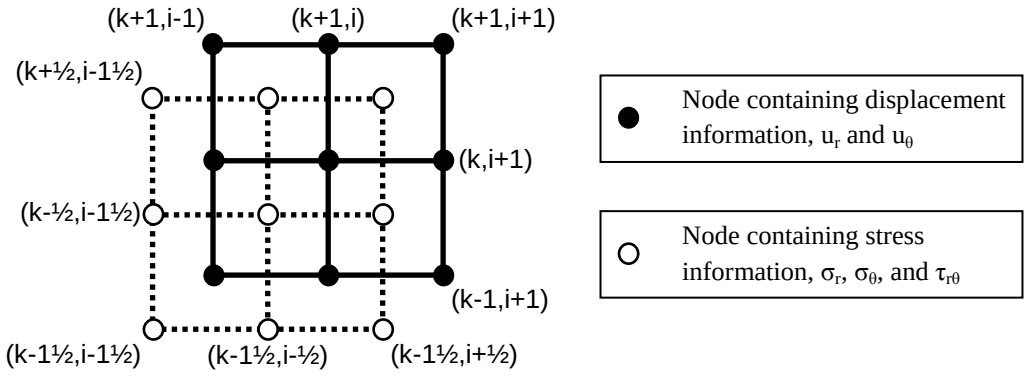


**Figure 58.** Staggered grids of displacements and stress used in FDTD as proposed by Yee [115]. Stress component nodes are offset from displacement nodes by one half of the nodes spacing.

In order to formulate the FDTD, the derivative terms in Equations 15 and 16 must be discretized. Three point central difference approximations for first derivative, second derivative, and second mixed derivative terms are shown in Equations 17, 18, and 19, respectively.

$$\frac{\partial f(x)}{\partial x} \approx \frac{f(x+h) - f(x-h)}{2h} \tag{17}$$

$$\frac{\partial^2 f(x)}{\partial x^2} \approx \frac{f(x+h) - 2f(x) + f(x-h)}{h^2} \tag{18}$$

$$\frac{\partial^2 f(x,y)}{\partial x \partial y} \approx \frac{\begin{pmatrix} f(x+h,y+g) + f(x-h,y-g) + \ldots \\ \quad - f(x+h,y-g) - f(x-h,y+g) \end{pmatrix}}{4gh} \tag{19}$$

As a result of using three point central difference derivative approximations, it is necessary to have additional "fictitious" data points beyond the outer extent of analyzed region. Also, special considerations are necessary for the center of the circular cross-section. These issues are addressed in Section 4.1.13 and Section 4.1.3, respectively.

The central difference approximations are applied to the displacement derivative terms in Equations 15 and 16. The displacements $u_r$ and $u_\theta$ use the grid designations shown in Figure 58. The current time is designated as $t_n$. Unless a displacement term has a superscript designating otherwise, the term is assumed to be at radial location $r_k$, circumferential location $\theta_i$, and time $t_n$. The first and second order approximations are then substituted into Equations 20 and 21. The resulting expressions are rewritten to give an explicit equation for the displacement at the current location but one time step in the future.

$$u_r^{n+1} = -u_r^{n-1} + 2u_r^n + \left( \frac{(\Delta t)^2}{\rho} \right) D_R(u_r, u_\theta) \tag{20}$$

$$u_\theta^{n+1} = -u_\theta^{n-1} + 2u_\theta^n + \left( \frac{(\Delta t)^2}{\rho} \right) D_\Theta(u_r, u_\theta) \tag{21}$$

Where:

$\Delta t$ is the simulation time step in units of seconds

$D_R$ and $D_\Theta$ represent the right hand sides of Equations 15 and 16, respectively, written as discrete functions of the radial and tangential displacements and are given as Equations 22 and 23, respectively.

$$D_R\left(u_r,u_\theta\right)=-u_r^n\left(\frac{2C_{rr}}{\left(\Delta r\right)^2}+\frac{C_{\theta\theta}}{r^2}+\frac{2G_{r\theta}}{\left(\Delta\theta\right)^2r^2}\right)+u_r^{k+1}\left(\frac{2r+\Delta r}{2r\Delta r}\right)\left(\frac{C_{rr}}{\Delta r}\right)+\ldots$$
$$+u_r^{k-1}\left(\frac{2r-\Delta r}{2r\Delta r}\right)\left(\frac{C_{rr}}{\Delta r}\right)+\left(u_r^{i+1}+u_r^{i-1}\right)\left(\frac{G_{r\theta}}{\left(\Delta\theta\right)^2r^2}\right)+\ldots \quad (22)$$
$$-\left(u_\theta^{i+1}-u_\theta^{i-1}\right)\left(\frac{G_{r\theta}+C_{\theta\theta}}{2\Delta\theta r^2}\right)+\left(\begin{matrix}u_\theta^{k+1,i+1}+u_\theta^{k-1,i-1}+\ldots\\-u_\theta^{k+1,i-1}-u_\theta^{k-1,i+1}\end{matrix}\right)\left(\frac{G_{r\theta}+C_{r\theta}}{4r\Delta\theta\Delta r}\right)$$

$$D_\Theta\left(u_r,u_\theta\right)=-u_\theta^n\left(\frac{G_{r\theta}}{r^2}+\frac{2G_{r\theta}}{\left(\Delta r\right)^2}+\frac{2C_{\theta\theta}}{\left(\Delta\theta\right)^2r^2}\right)+u_\theta^{k+1}\left(\frac{2r+\Delta r}{2r\Delta r}\right)\left(\frac{G_{r\theta}}{\Delta r}\right)+\ldots$$
$$+u_\theta^{k-1}\left(\frac{2r-\Delta r}{2r\Delta r}\right)\left(\frac{G_{r\theta}}{\Delta r}\right)+\left(u_\theta^{i+1}+u_\theta^{i-1}\right)\left(\frac{C_{\theta\theta}}{\left(\Delta\theta\right)^2r^2}\right)+\ldots \quad (23)$$
$$+\left(u_r^{i+1}-u_r^{i-1}\right)\left(\frac{C_{\theta\theta}+G_{r\theta}}{2\Delta\theta r^2}\right)+\left(\begin{matrix}u_r^{k+1,i+1}+u_r^{k-1,i-1}+\ldots\\-u_r^{k+1,i-1}-u_r^{k-1,i+1}\end{matrix}\right)\left(\frac{C_{r\theta}+G_{r\theta}}{4r\Delta\theta\Delta r}\right)$$

### 4.1.3. Center point

The FDTD calculation scheme assumes a locally rectangular grid in which every row of the grid has the same number of nodes as every other row and every column of the grid has the same number of nodes as every other column. A locally rectangular grid does not necessarily indicate uniform spacing between nodes. In the circular grid arrangement, the radial spacing between nodes, Δr, is uniform for all points; however, the circumferential distance, rΔθ, increases with increasing radius. Intuitively, the center point of the pole is a single node and should have a single radial displacement. If this were the case, each of the nodes at radial distance Δr would be connected to the center point. Therefore, while there are multiple nodes at the second row of points, there is only one node in the first row of the grid. A single node at the center of the circular grid arrangement would violate the locally rectangular grid necessity of the FDTD calculation.

From Figure 59, it is apparent that the inner boundary of the rectangular grid representation has several nodes while the circular grid representation has only one. It is intuitive that any displacement of the central point of the circular grid representation should affect the displacement of all of the surrounding nodes. In order to realize this relationship in the rectangular grid representation, it is necessary that displacement of any

of the points along the inner boundary (at radius $r_0 = 0$) affect the displacement of all of the nodes in the first column of rectangular grid (at radius $r_1 = \Delta r$). Schubert's model does not appear to utilize this relationship.

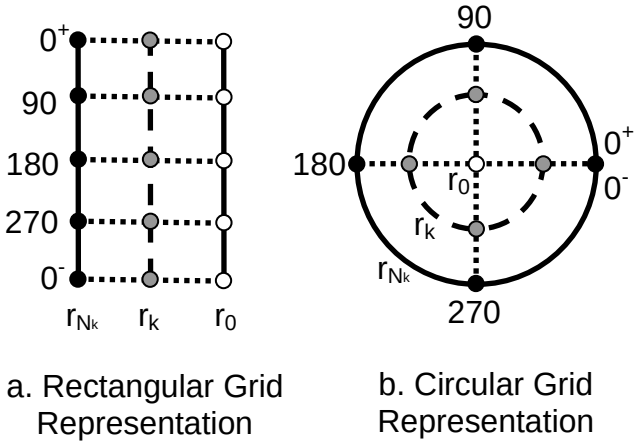


**Figure 59.** Inner and outer boundaries by coordinate system as defined in **a.** Rectangular Grid and **b.** Circular Grid coordinate systems.

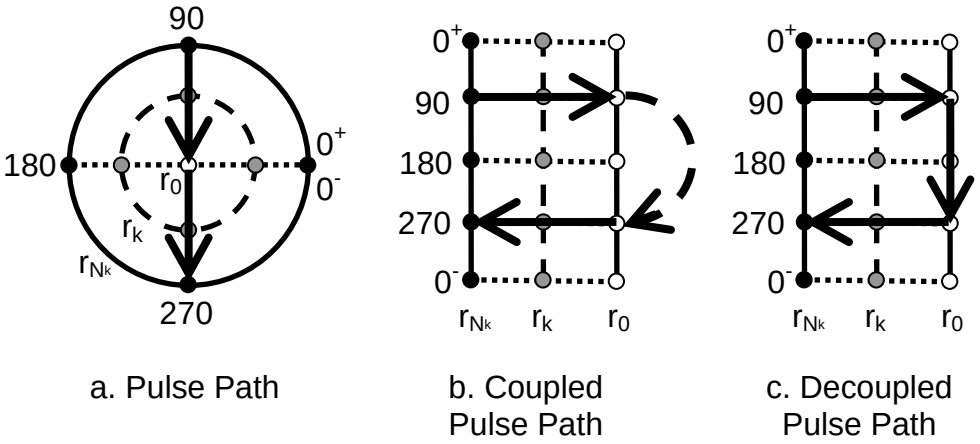


**Figure 60.** Pulse propagation path **a.** in circular representation, **b.** in grid representation with the displacement of all inner boundary points coupled, and **c.** in grid representation without the displacement of inner boundary points coupled

Assume a radial pulse is initiated at the 90° location of the circular representation of Figure 60. The pulse should travel inwards radially toward the center point. Upon reaching the center point, the pulse should cross the center and travel outwardly towards the 270° location. This type of pulse propagation is shown in Figure 60a.

When implementing the pulse propagation in the rectangular grid representation, the model should follow the coupled pulse path behavior shown in Figure 60b. The pulse

propagates directly from the 90° row to the 270° row. Schubert's model apparently exhibits the decoupled pulse path behavior shown in Figure 60c. The pulse propagates to the inner boundary, and then must propagate along the inner boundary until reaching the 270° row before propagating radially outwards. This type of propagation increases the wave travel time. Schubert notes that the simulated travel times were longer than predicted based upon estimated wave speeds. The observed delay may partially be caused by the additional travel distance around the inner boundary.

Implementing the center point coupling in a rectangular grid representation requires knowledge of the radial and circumferential displacements along the $r_1$ row of nodes. It is assumed that the material is isotropic and homogeneous from the center point of the pole to the radial distance, $r_1$. Given that the center of the pole is composed of pith, this assumption is not unreasonable. The displacements around the center point are translated into Cartesian coordinates. The mean of the Cartesian displacement components are calculated using Equations 24 and 25. The mean displacement values are the displacements of the center point. The mean Cartesian displacements are converted into polar coordinates composed of a magnitude, $u_0$, and angle, $\varphi$. The displacements along the $r_0$ row of nodes of the rectangular grid are then calculated for the radial and tangential directions using a cosine and sine term, respectively, with magnitude $u_0$ and phase shift of $-\varphi$.

$$u_{x0}\left(t_{n+1}\right)=\frac{1}{N_\theta}\sum_{i=0}^{N_\theta-1}\left(u_r\left(r_1,\theta_i,t_n\right)\cos\left(i\Delta\theta+\frac{\Delta\theta}{2}\right)+u_\theta\left(r_1,\theta_i,t_n\right)\sin\left(i\Delta\theta+\frac{\Delta\theta}{2}\right)\right) \quad (24)$$

$$u_{y0}\left(t_{n+1}\right)=\frac{1}{N_\theta}\sum_{i=0}^{N_\theta-1}\left(u_r\left(r_1,\theta_i,t_n\right)\sin\left(i\Delta\theta+\frac{\Delta\theta}{2}\right)+u_\theta\left(r_1,\theta_i,t_n\right)\cos\left(i\Delta\theta+\frac{\Delta\theta}{2}\right)\right) \quad (25)$$

Where:
$u_{x0}$ is the center point displacement parallel to the 0°, 180° axis of Figures 59 and 60
$u_{y0}$ is the center point displacement parallel to the 90°, 270° axis of Figures 59 and 60

Equations 26 and 27 are the angle and magnitude of the polar coordinates, respectively, calculated from the mean horizontal and vertical components.

$$\phi = \tan^{-1}\left(\frac{u_{y0}}{u_{x0}}\right), \quad u_{r0} > 0, \qquad \phi = \pi + \tan^{-1}\left(\frac{u_{y0}}{u_{x0}}\right), \quad u_{r0} < 0 \tag{26}$$

$$u_0 = \sqrt{u_{x0}^2 + u_{y0}^2} \tag{27}$$

The $N_\theta$ pairs of radial and tangential displacements along row $r_0$ are calculated using Equations 28 and 29.

$$u_{r0}\left(0, \theta_i, t_{n+1}\right) = u_0 \cos\left(i\Delta\theta - \phi\right), \quad 1 \le i \le N_\theta \tag{28}$$

$$u_{\theta 0}\left(0, \theta_i, t_{n+1}\right) = u_0 \sin\left(i\Delta\theta - \phi\right), \quad 1 \le i \le N_\theta \tag{29}$$

### 4.1.4. Grid enhancement

No factor more greatly affects the simulation calculation time than the time step. The time step is dictated by the speed of the wave and the minimum distance between nodes. Choosing node spacing is a compromise between accuracy of the simulation and minimizing calculation time. One of the goals of the simulation was to allow density information obtained from CT scan images to be used as an input. The CT scan images are pixilated. The images used in this simulation have square pixels. Each pixel represents a scaled area of 0.94 $mm^2$, with a scaled edge length of 0.97 mm. Since every pixel represents a real piece of datum, it is desirable to use as many pixels as possible. The maximum distance between nodes is chosen such that it does not exceed three pixel edge lengths. The radial distance, $\Delta r$, is set equal to three pixel edge lengths. Nodes are positioned along radial rays. The angle between the rays is $\Delta\theta$. The circumferential distance between nodes is the product of the radius, r, and $\Delta\theta$; therefore, the circumferential distance increases with the radius. When the circumferential distance exceeds three pixel edge lengths, the angle between the radial rays is halved, decreasing the node spacing to one and a half pixel edge lengths, and doubling the number of circumferential nodes.

As a result of the change in circumferential angle, $\Delta\theta$, an interface boundary exists between regions containing differing number of circumferential nodes as shown in Figure 61. Special consideration must be paid to this interface boundary in order to accurately transmit displacement information between the regions. The outermost row of nodes of the base grid and the innermost row of the enhanced grid are located at the same radial distance from the center point, $r_k$. Along the common row, the circumferential distance between the nodes of the base grid is $\pm\ r_k\Delta\theta$, the circumferential distance between the nodes of the enhanced grid is $\pm\ r_k\Delta\theta/2$, and the nodes of the enhanced grid are circumferentially offset from the nodes of the base grid by a distance of $\pm\ r_k\Delta\theta/4$ as shown in Figure 61b.

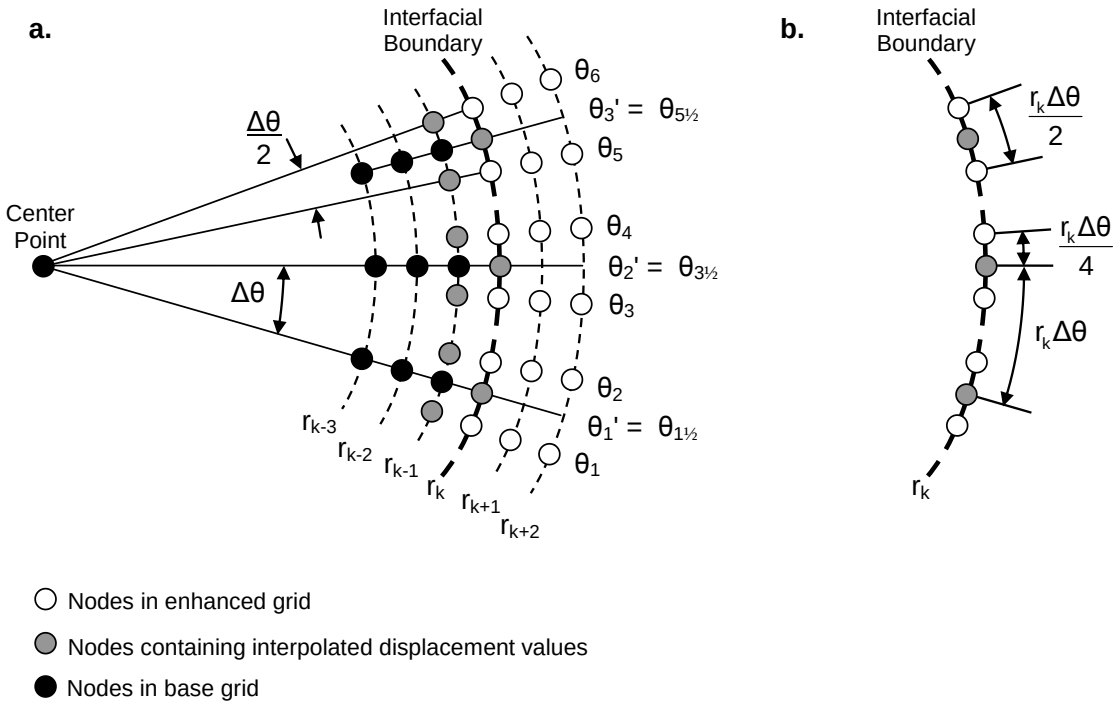


**Figure 61.** Grid enhancement interfacial boundary **a.** node layout on either side of boundary, **b.** nodal arrangement along the interface boundary

In order to maintain a locally rectangular grid for the enhanced grid, it is necessary to estimate values for the $r_{k-1}$ row. The displacement values are estimated using linear interpolation of the base grid points along row $r_{k-1}$ shown in Equations 30 and 31.

$$u_r\left(r_{k-1},\theta_{2i},t_n\right)=\frac{3}{4}u_r\left(r_{k-1},\theta'_i,t_n\right)+\frac{1}{4}u_r\left(r_{k-1},\theta'_{i+1},t_n\right)$$
$$u_r\left(r_{k-1},\theta_{2(i+1)-1},t_n\right)=\frac{1}{4}u_r\left(r_{k-1},\theta'_i,t_n\right)+\frac{3}{4}u_r\left(r_{k-1},\theta'_{i+1},t_n\right) \quad (30)$$

$$u_\theta\left(r_{k-1},\theta_{2i},t_n\right)=\frac{3}{4}u_\theta\left(r_{k-1},\theta'_i,t_n\right)+\frac{1}{4}u_\theta\left(r_{k-1},\theta'_{i+1},t_n\right)$$
$$u_\theta\left(r_{k-1},\theta_{2(i+1)-1},t_n\right)=\frac{1}{4}u_\theta\left(r_{k-1},\theta'_i,t_n\right)+\frac{3}{4}u_\theta\left(r_{k-1},\theta'_{i+1},t_n\right) \quad (31)$$

Where:
$\theta$ represents a circumferential angle on the enhanced grid
$\theta'$ represents a circumferential angle on the base grid

The interpolated displacements along row $r_{k-1}$ in addition to the known displacements along rows $r_k$ and $r_{k+1}$, allow the calculation of displacements along row $r_k$ for the next time step, $t_{n+1}$. The interpolated displacements introduce additional error into the calculation at the interface boundary. The magnitude of the error grows through constructive interference every time step and the displacement value will eventually become unbounded. The error is reduced and system stability at the interface boundary is ensured through the use of a weighted smoothing of the displacement values.

After the displacement values at the interface boundary for time step $t_{n+1}$ are calculated using the FDTD calculation scheme, a smoothing scheme is applied. The change in the displacements between time $t_n$ and $t_{n+1}$ is calculated at each node of the interface boundary as shown in Equations 32 and 33.

$$\Delta u'_r\left(r_k,\theta_i,t_{n+1}\right)=u'_r\left(r_k,\theta_i,t_{n+1}\right)\ -\ u_r\left(r_k,\theta_i,t_n\right) \quad (32)$$

$$\Delta u'_\theta\left(r_k,\theta_i,t_{n+1}\right)=u'_\theta\left(r_k,\theta_i,t_{n+1}\right)\ -\ u_\theta\left(r_k,\theta_i,t_n\right) \quad (33)$$

Where:
$u'_r$ is the interface boundary radial displacement
$u'_\theta$ is the interface boundary circumferential displacement
$\Delta u'_r$ is the change in radial displacement between time $t_n$ and $t_{n+1}$
$\Delta u'_\theta$ is the change in circumferential displacement between time $t_n$ and $t_{n+1}$

The three point weighted smoothing scheme applied to the change in displacement is described in Equations 34 and 35.

$$\Delta u_r\left(r_k,\theta_i,t_{n+1}\right)=\frac{\Delta u'_r\left(r_k,\theta_{i-1},t_{n+1}\right)+2\Delta u'_r\left(r_k,\theta_i,t_{n+1}\right)+\Delta u'_r\left(r_k,\theta_{i+1},t_{n+1}\right)}{4} \tag{34}$$

$$\Delta u_\theta\left(r_k,\theta_i,t_{n+1}\right)=\frac{\Delta u'_\theta\left(r_k,\theta_{i-1},t_{n+1}\right)+2\Delta u'_\theta\left(r_k,\theta_i,t_{n+1}\right)+\Delta u'_\theta\left(r_k,\theta_{i+1},t_{n+1}\right)}{4} \tag{35}$$

Where:
$\Delta u_r$ is the change in radial displacement between time $t_n$ and $t_{n+1}$ with smoothing
$\Delta u_\theta$ is the change in circumferential displacement between time $t_n$ and $t_{n+1}$ with smoothing

The displacements at the interface boundary for time $t_{n+1}$ are then calculated using the displacement at time $t_n$ and the smoothed change in displacement values as shown in Equations 36 and 37.

$$u_r\left(r_k,\theta_i,t_{n+1}\right)=\Delta u_r\left(r_k,\theta_i,t_{n+1}\right)\ +\ u_r\left(r_k,\theta_i,t_n\right) \tag{36}$$

$$u_\theta\left(r_k,\theta_i,t_{n+1}\right)=\Delta u_\theta\left(r_k,\theta_i,t_{n+1}\right)\ +\ u_\theta\left(r_k,\theta_i,t_n\right) \tag{37}$$

The displacement values for the base grid along the interface boundary are then calculated by taking two point means of the enhanced grid as shown in Equations 38 and 39.

$$u_r\left(r_k,\theta'_i,t_n\right)=\frac{1}{2}u_r\left(r_k,\theta_{2i},t_n\right)+\frac{1}{2}u_r\left(r_k,\theta_{2i-1},t_n\right) \tag{38}$$

$$u_\theta\left(r_k,\theta'_i,t_n\right)=\frac{1}{2}u_\theta\left(r_k,\theta_{2i},t_n\right)+\frac{1}{2}u_\theta\left(r_k,\theta_{2i-1},t_n\right) \tag{39}$$

The new model with grid enhancement is shown in Figure 62.

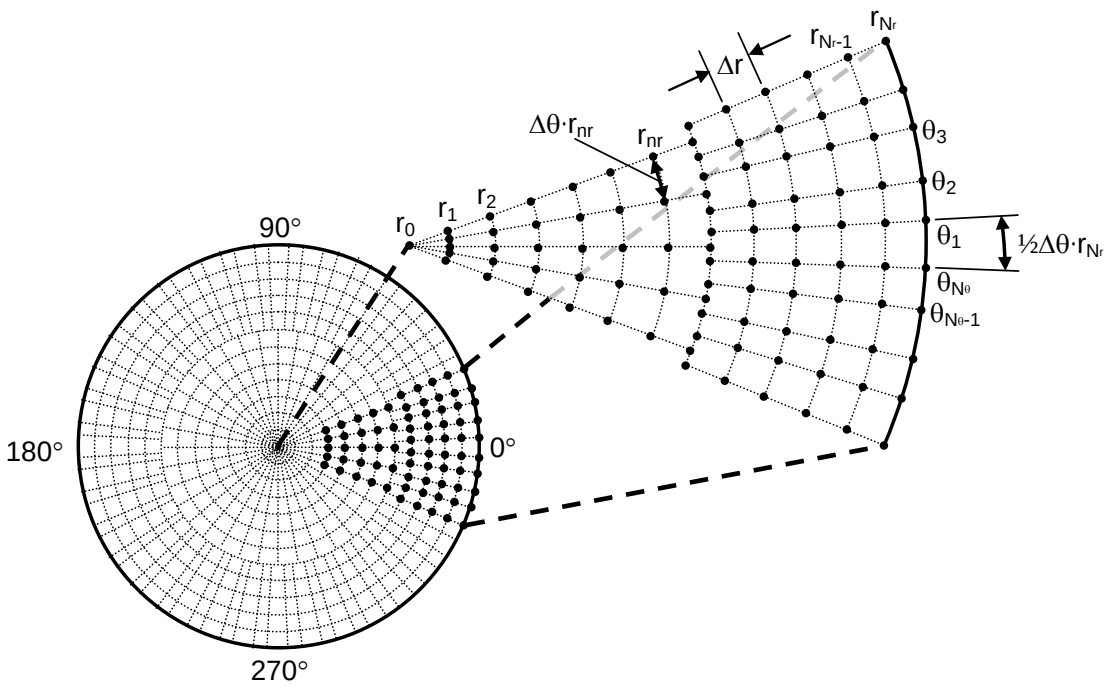


**Figure 62.** Model updated with grid enhancement scheme.

### 4.1.5. Sound wood / decayed wood boundary

Waves incident upon the sound wood / rotten wood boundary do not produce distinct reflections. The presence of rot wood causes reduction in both wood density and wave speed. Both of these factors should affect the acoustic impedance of rotten wood. If two materials of differing acoustic impedance share a boundary, then waves incident upon that boundary should have measureable reflections. Despite changes in the acoustic impedance, wood rot does not exhibit distinct reflections from incident waves. The lack of reflections from wood rot is at least partially explained by two factors: gradual changes in material characteristics, and an irregular boundary. Changes in material characteristics due to rot occur gradually across a distance as opposed to the sudden change such as at the wood / air boundary. The boundary between sound wood and rotten wood is irregular. Irregular boundaries increase scattering of incident waves.

Material characteristics that change in accordance with some function with respect to position are known as functionally graded materials. In this model, wood transitions from sound to severely rotten. Sound wood has lost none of its density to rot. In this report, severely rotten wood is defined as wood that has lost 30% of its density to

rot. The threshold of 30% was chosen due to observations made of rotten wood. At approximately 30% mass loss, voids begin to appear in the region of rotten wood. This observation was supported by CT scans of the glue laminated beams and the utility poles. It was further supported by McGovern [110] from the CT scans of the loblolly pine blocks used in her analysis. For consistency with the velocity and attenuation equations, decayed regions are referenced by their percentage of sound wood mass (i.e. a severely decayed region of wood has 70% mass). A half cosine function was used to define the transition from sound wood to severely rotten wood. The distance over which the transition occurs is assumed to be 25 mm [6]. The function defining the change in mass within the transition region is given in Equation 40.

$$k_\rho = 0.15\cos\left(\left(\frac{r_r - R_{ri}}{R_{ro} - R_{ri}}\right)\pi\right) + 0.85 \tag{40}$$

Where:
$k_\rho$ is the fraction of sound wood mass in the transition region
$R_{ri}$ is the inner radius of the transition region
$R_{ro}$ is the outer radius of the transition region
$r_r$ is the radius of an arbitrary location within the transition region such that $R_{ri} \leq r_r \leq R_{ro}$
$w_R$ is the width of the transition distance, $R_{ro} - R_{ri}$

The rotten region is assumed to be circular. The transition region encircles the rotten region. The rotten region is assumed to be either a region of severely decayed wood (30% mass loss due to decay) or a void (100% mass loss). A schematic of the transition from sound wood to rot is shown in Figure 63.

The reflection coefficient of a wave incident on the functionally graded regions is governed by the wavelength of the incident wave with respect to the width of the transition region. If the wavelength is very small with respect to the width of the transition region, then the reflection coefficient approaches zero. If the wavelength is approximately the same length as the transition region, the reflection coefficient is governed by the change in the acoustic impedance within the transition region. If the wavelength is large with respect to the width of the transition region, then the reflection coefficient is governed by the acoustic impedance of the sound wood region and the

decayed wood region. The relationship between reflection coefficient and wavelength is summarized in Table 6.

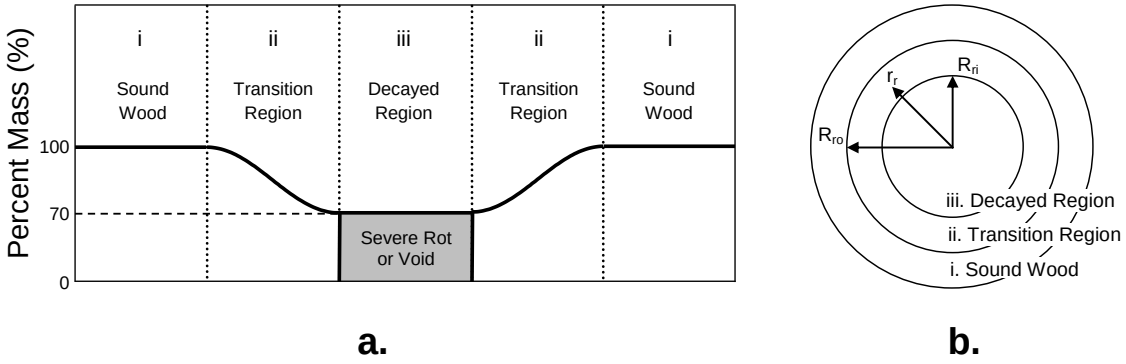


**Figure 63.** Model of rot depicting transition from sound to rotten wood. **a.** Cross-section of decayed region comprised of **i.** sound wood, **ii.** transition from sound wood at 100% mass to severely decayed wood at 70% mass, **iii.** decayed region comprised of severely decayed wood (70% mass) or a void. **b.** Plane view of the decayed region showing the outer radius of the transition region, $R_{ro}$, inner radius, $R_{ri}$, and a radius within the transition region, $r_r$. The change in mass is described by a half cosine function defined in Equation 40.

**Table 6.** Reflection coefficients as a function of incident wavelengths.

| Relative Wavelength Size | $\lambda << w_R$ | $\lambda \sim w_R$ | $\lambda >> w_R$ |
|---|---|---|---|
| Reflection Coefficient | $R_Z = 0$ | $R_Z = \frac{Z_i - Z_{ii}}{Z_i + Z_{ii}}$ | $R_Z = \frac{Z_i - Z_{iii}}{Z_i + Z_{iii}}$ |

Where:
$R_Z$ is the reflection coefficient
$w_R$ is the width of the transition region
$\lambda$ is the wavelength
$Z_i$ is the acoustic impedance of sound wood
$Z_{ii}$ is the acoustic impedance of some location within the transition region
$Z_{iii}$ is the acoustic impedance of the decayed region

Another phenomenon that reduces reflections is wave scattering at the rot boundary. Brown rot grows in seemingly random directions. Highly decayed wood cells may be adjacent to completely sound cells. On both a microscopic and macroscopic level, the boundary between regions of rot and regions of sound wood are irregular. Irregular boundaries cause scattering of incident waves. Within the simulation, irregularity of sound wood / rotten wood boundaries is limited by nodal density. The nodal density required to precisely depict such a boundary requires too great a cost in

computational time. A sawtooth profile along the boundary is a solution that is implementable with the current nodal density. Proud [119] analyzed wave reflections from a surface with a sawtooth profile for waves of differing incident angles. The sawtooth profile reflects incident waves away from the source direction. As a result, signals gathered using techniques where the source and receiver are collocated (impact-echo and pulse echo) do not show distinct reflections. In the simulation, the spatial period of the sawtooth profile is approximately 25 mm. The spatial period is adjusted based upon the circumferential distance around the decay region in order to achieve an even integer number of profile cycles to ensure symmetry, but the adjusted lengths are usually within ±8 mm of 25 mm. The decision to maintain symmetry was made to minimize unquantifiable sources of error in the simulation. Figure 64 shows the cross-section of the decayed region as implemented within the simulation space using both the functionally graded transition region and the sawtooth boundary.

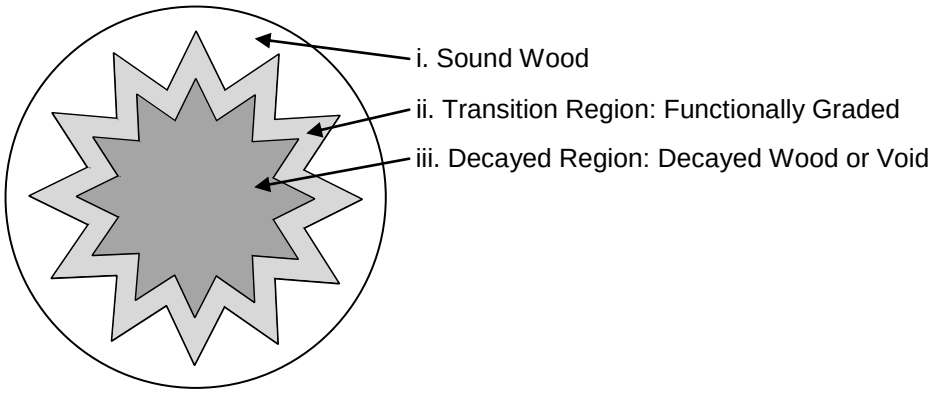


**Figure 64.** Plane view of decayed region showing transition from sound to rotten wood with sawtooth boundary, **i.** sound wood, **ii.** Transition region is functionally graded according to Equation 40 from sound wood at 100% mass to severely decayed wood at 70% mass, **iii.** decayed region comprised of severely decayed wood (70% mass) or a void.

### 4.1.6. Surface cracks

During early simulations of ideal pole cross-sections, surface waves were clearly present. Tests of actual pole cross-sections showed no surface waves. Shallow surface cracks are common on all of the poles received for analysis, and the presence of these cracks around the circumference of the pole specimens prevented surface waves from traveling from the source to the receivers. Surface cracks were implemented in the ideal cross-section to more closely model real world behavior of the poles.

Shallow surface cracks were ubiquitous in all CT scans of the pole specimens. The cracks vary greatly in length and position, but some generalities are drawn. It should be noted that the approximate diameter of the pole specimens is 381 mm (15 inches) and the generalities presented are made for poles of this size. Most surface cracks are 25 ± 12 mm in length. The circumferential spacing between the cracks is generally 75 ± 15 mm. Assuming a radius of 190.5 mm, the angular spacing between cracks is generally 21.5°. In the simulation, cracks are spaced 22.5° from each other resulting in a spacing of 73 mm and are assigned lengths of 25 mm. Assuming the input source is at the 0° location, the first surface crack is offset to an angle of 11.25°. The offset insures that the cracks are located the maximum distance possible from the receivers located at 0°, 90°, 180°, and 270°. After the surface cracks were implemented, the simulation results were examined for the presence of dimensional resonance caused by the presence of the surface cracks at regular intervals. Examination of the results showed the surface cracks remove the surface wave from the simulation output but do not affect simulation stability.

### 4.1.7. Estimating density and mass loss from CT scans

The density of the utility poles is estimated using the same technique employed to estimate the density of the glulam beams as described in Section 3.1 Since the utility poles were scanned every 2.5 mm as opposed every centimeter for the glulam beams, each utility pole pixel represented a volume of 2.3 $mm^3$. Four poles were received for testing. The poles were identified with numbers that were either attached to the pole on a metal identification plate or written on the pole with a grease pen. Table 7 contains identification number, mass, volume, density, and density factor for each pole.

**Table 7.** Utility pole specimens' mass, volume, density, and density factor

| Pole Identification Number | Mass (kg) | Volume ($m^3$) | Density ($kg/m^3$) | Density Factor ($kg/m^3$)/(Brightness Value) |
|---|---|---|---|---|
| 966 | 86.5 | 0.157 | 551 | 6.20 |
| 477 | 75.3 | 0.136 | 554 | 6.74 |
| 242 | 104 | 0.182 | 571 | 6.93 |
| 491 | 94.2 | 0.171 | 551 | 6.13 |

Figure 65a shows a selected tomographic view of pole 966. A region of decayed wood exists just above center of the tree. The decayed region extends through multiple rings. It is apparent that each ring is composed of two types of rings: a high density portion (latewood), and a low density portion (earlywood). In sound Douglas-fir it is not uncommon for the ratio between high density late wood and low density early wood to be as high as 3:1. The density disparity poses a problem when considering wood decay. The decayed portion of the high density latewood may have a greater density than a sound portion of the low density earlywood. McGovern's equations require an estimation of the percent mass loss due to decay. In order to estimate the percent mass loss, the original density must be approximated for the decayed region.

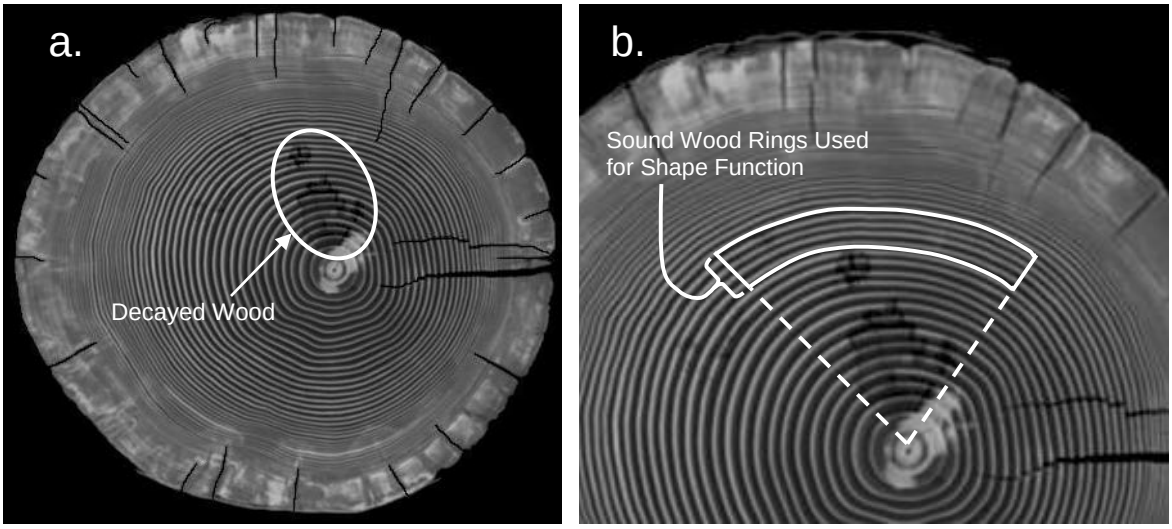


**Figure 65. a.** Tomographic view 41 of Douglas-fir pole 966. Note the dark areas of decay just above the center of the pole. The bright area at the tree center is the locations where a branch sprouted off the young tree. **b.** Regions used to construct a sound wood shape function. The white box contains rings of sound wood used to construct a representative shape function for sound wood. The dashed lines represent rays of sound wood that extend from the center of the tree to the shape function region. It is assumed that the shape functions describing the variation in density for the region within the white box are representative of sound wood variation for all tree rings bounded by the white dashed lines.

Sound wood has density variations within a single annual ring. It was necessary to approximate the expected changes in density within a sound ring. Figure 65b is a close-up view of the decayed region shown in Figure 65a. The rings enclosed within the white box were composed of sound wood and were used to obtain a pair of density shape functions: a latewood function and an earlywood function. The dashed lines represent rays of sound wood that extend from the center of the tree to the white box. The density

shape functions begin and end at a point of sound wood. In this analysis, it is assumed that the density shape function is constant for all like rings. Therefore, the density shape function obtained from the region within the white box for latewood (earlywood) is assumed to be representative of all of the sound latewood (earlywood) rings within the region bounded by the white dashed lines. The shape functions were then used to approximate the sound wood density across rings that contained decayed wood. The wood between the early and latewood rings was approximated by linearly interpolating between the two shape functions. Using the sound wood density estimation of the decayed region and the true density of the decayed region from the CT scan, the percent mass loss is estimated.

### 4.1.8. Converting CT image into cylindrical coordinates

In Section 4.1.4, the grid spacing of the simulation was set to three pixels in order to balance the desire to use as many pixels as possible and minimize simulation time. With that decision made, density information from a CT image was converted from square pixels arranged in Cartesian coordinates into cylindrical coordinates for use in the simulation. First, the brightness value of each pixel within the CT image was averaged with all of the contiguous pixels (all pixels within a three by three grid). If any of the nine pixels (the center pixel and the eight surrounding pixels) had a brightness value equal to that of air, then the average was discarded, and the center pixel was given the brightness value equal to air. This step was performed to ensure that cracks present in the original image appear in the converted image. The conversion process involved selected sampling from the averaged values. Since every pixel was not used, it would be possible for a crack to fall between two sampled locations and would therefore not appear in the converted image. Cracks and voids greatly affect simulation output and must be included in the analysis.

The center of the pole cross-section was defined as the center of the cylindrical coordinate system. From the grid enhancement scheme, the angle and distance of every node relative to the center was known. The polar coordinates of each node of the enhanced grid were converted to Cartesian coordinates which were used to locate the associated brightness value within the set of averaged values. Figure 66a shows the

original CT image of the pole cross-section; Figure 66b shows the image converted into cylindrical coordinates and ready to use in the simulation.

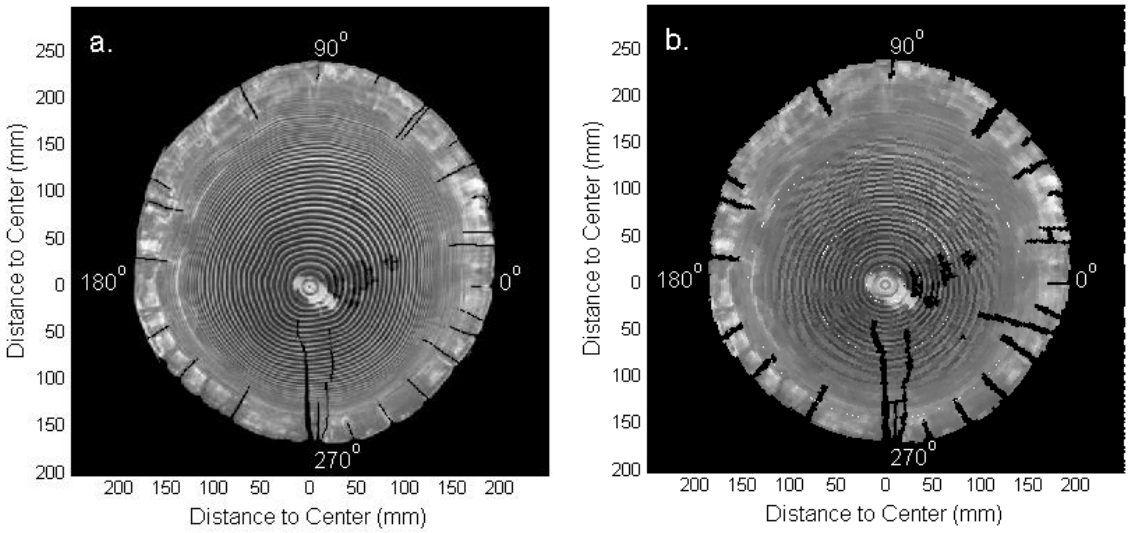


**Figure 66.** Douglas-fir image converted to cylindrical coordinates for use in the simulation. **a.** Tomographic image of Douglas-fir pole. Note the dark areas of decay just to the right of the center of the pole. The bright area at the tree center is the locations where a branch sprouted off the young tree. **b.** Image remapped into a cylindrical coordinate system. The angles shown on the figure are the same angles used in the simulations.

### 4.1.9. System input

Accurate modeling of a signal traveling through a dispersive medium requires the signal frequency to be known. If multiple signals of different frequencies are traveling through the medium simultaneously, then each of those signals behave differently. To properly model a dispersive medium, each frequency must be given individual consideration. Due to the large size of the utility poles and highly attenuative nature of wood, it is necessary that the input signal have high energy. The input source was a lead pellet shot from an air gun which impacted a steel plate coupled to the surface of the pole.

The pellet impact closely matches a Gaussian pulse. A Gaussian pulse is comprised of many frequencies. Figure 67a shows the Gaussian pulse used to model the pellet impact. In order to input the pulse into the numerical simulation, it was decomposed into constituent frequencies. Figure 67b shows the frequency spectrum of the Gaussian pulse. Each constituent frequency has a particular phase and displacement

magnitude. Figure 67c shows the sinusoid created from the 12 kHz signal with a magnitude of 0.037 μm and a phase of 291°.

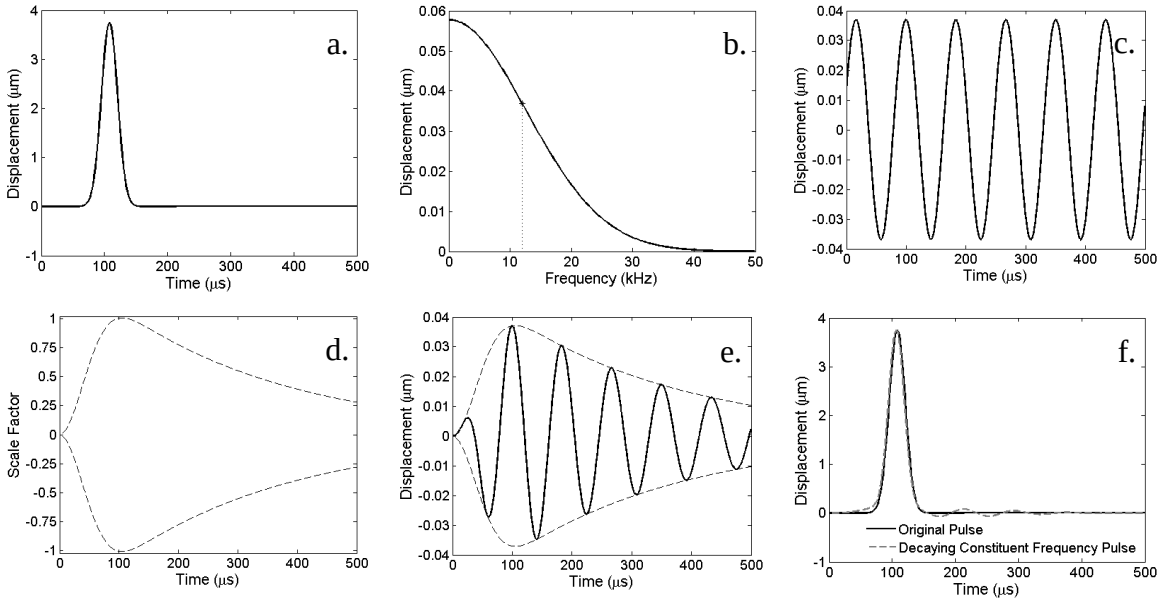


**Figure 67.** Constructing the simulation input signals from a Gaussian pulse: **a.** Gaussian pulse modeling a pellet impact, **b.** frequency spectrum of the Gaussian pulse, **c.** selected sinusoidal frequency (12 kHz), **d.** scale factor envelope to eliminate noise and model signal attenuation with time, **e.** scale factor envelope applied to the sinusoidal frequency, **f.** comparison of original pulse with pulse comprised of decaying constituent frequencies.

There are two potential issues with a sinusoidal input: the nonzero starting value, and the failure of the signal to diminish over time. If the phase of the sinusoidal input is not zero or 180°, then the first time input is a non-zero value. The simulated system is assumed to be at rest prior to the input. The system will react to the first nonzero input as a step function. A step function is composed of many high frequencies outside of the desired analysis range and increases the overall noise level of the outputs. It is desirable that the first nonzero point have a low magnitude in order to minimize high frequency noise. The second issue is the failure of the input signal to diminish over time. In the real system, the input pulse lasts a relatively short time. The sinusoidal inputs do not diminish and are equally strong throughout the signal life. If the input pulse has a duration less than 200 μs, then it is unrealistic to expect any component frequency of an input pulse to last much longer than that 200 μs. A more realistic input sinusoid would be of finite duration. In addition, the final point of the input sinusoid must satisfy the

same criteria as the first point: it must minimize high frequency noise. A sinusoid that diminished with time would satisfy both requirements. The duration would be limited by the magnitude of the original signal and the attenuation of the signal at that frequency. Rather than having a sudden change in the input value at the end of the signal, the final point would be of low magnitude and high frequency noise would be minimized. Both the starting point and the signal duration issues are addressed by creating a scale factor envelope for the sinusoidal input shown in Figure 67d.

The envelope begins with a Gaussian curve. The first point of the curve has a value of approximately $10^{-4}$ and increases to a maximum value of one. The time at which the curve reaches the maximum value is the same time as the peak of the input Gaussian pulse. After the maximum value, the curve then decreases at an attenuation rate dictated by McGovern's equations **[**21**,** 125**]** for the particular input frequency. Figure 67e shows the sinusoidal input modified by the scale factor envelope.

The process is repeated for each constituent frequency. In order to insure that applying the scale factor envelope does not change the original pulse, the modified constituent frequencies inputs are summed to produce a single time domain signal. The time domain signal constructed from the decaying constituent frequency is a pulse similar in shape to the original Gaussian pulse. Figure 67f shows both the original pulse and the pulse constructed from the decaying constituent frequencies. By observation, there is strong agreement between the pulse shapes. The root mean square of the residuals between the original pulse and the new pulse are 4.5 percent of the root means square of the original pulse.

### 4.1.10. Wave velocity

Wood is a dispersive medium. In a dispersive medium, waves of different frequencies travel at different velocities and / or attenuate at different rates. A Gaussian pulse, similar to the input used in the experiments presented here, is composed of several frequencies. As the pulse travels through the wood, the constituent frequencies travel at different velocities and attenuate at different rates. As a result, a receiver placed at an arbitrary distance from the pulse source would record a signal that was different in shape than the original pulse. Generally speaking, as frequency increases, velocity and

attenuation increases. The dispersive nature of wood is increased if portions of the wood are decayed.

As wood decay increases, wave velocity decreases and attenuation increases. McGovern [21] constructed a series of polynomial equations that relate wave frequency and percentage of mass loss due to decay to wave velocity. McGovern analyzed loblolly pine. The utility poles used in this analysis were Douglas-fir. Using the elastic moduli, specific gravity, and Poisson's ratios provided by Forest Products Laboratory [10], it is possible to calculate theoretical values of Douglas-fir for the primary radial velocity, the primary tangential velocity, and shear velocity in the radial / tangential plane. The analysis in this report assumes plane strain in the radial / tangential plane; therefore, no longitudinal velocities are provided. The theoretical wave velocities for Douglas-fir fall within the bounds of the velocities of sound loblolly pine as predicted by McGovern's empirical polynomials. As a result, McGovern's polynomials were used for velocity estimation in the numerical simulation. The values are provided in Table 8.

In the same study, McGovern related wave frequency and percentage mass loss due to decay to wave attenuation (in Nepers per centimeter). The manner in which the attenuation is incorporated into the model is discussed later in the paper.

**Table 8.** Theoretical velocity (m/s) of Douglas-fir from elastic moduli [10] and sound loblolly pine velocities as predicted by McGovern [21]

| Velocity | Douglas-fir | Loblolly Pine | |
|---|---|---|---|
| | | 4.5 kHz | 30 kHz |
| Radial | 1560 | 1472 | 1653 |
| Tangential | 1340 | 954 | 1422 |
| Shear | 464 | 419 | 599 |

McGovern's polynomials require a frequency and a percentage mass loss due to decay. The percentage mass loss is approximated from the CT scans. The frequency is dictated by the input signal.

**Table 9.** Polynomial fits for velocity as a function of frequency and percent mass loss for the nine different measured directions for a frequency range of 4.5 kHz to 20 kHz [125].

**Acoustic Range Velocity**
**4.5 kHz to 20 kHz**

$$V(x,y) = A_V + B_V x + C_V y + D_V x^2 + E_V x y + F_V y^2 *$$

| Coefficient | Principal Material Direction – Polarization Direction | | | | | | | | |
|---|---|---|---|---|---|---|---|---|---|
| | L-L | L-R | L-T | R-R | R-L | R-T | T-T | T-L | T-R |
| $A_V$ | 2920 | 291.8 | 369.2 | 1225 | 357.9 | 327.1 | 1009 | 359.5 | 341.2 |
| $B_V$ | -240.6 | -28.12 | -7.307 | -194.5 | -53.20 | -52.94 | -85.74 | -71.19 | -59.01 |
| $C_V$ | 118.7 | 75.71 | 97.72 | 25.48 | 29.44 | 26.99 | 74.91 | 24.51 | 20.09 |
| $D_V$ | -71.18 | 4.614 | 0 | -12.20 | 4.206 | 23.81 | -12.21 | -27.80 | -0.959 |
| $E_V$ | -12.67 | 10.26 | 0 | -6.759 | -2.996 | -5.360 | -12.40 | -2.307 | -3.843 |
| $F_V$ | 0.394 | -0.564 | 0 | -0.607 | -0.159 | -0.083 | -4.273 | -0.173 | -0.069 |

*Values are centered by the mean and scaled by the standard deviation.
x = (mass loss (%) – $\mu_m$)/ $\sigma_m$ where $\mu_m$ = 19% and $\sigma_m$ = 10.6%
y = (frequency (Hz) – $\mu_{freq}$)/ $\sigma_{freq}$ where $\mu_{freq}$ = 12,000 Hz and $\sigma_{freq}$ = 4,611 Hz

**Table 10.** Polynomial fits for velocity as a function of frequency and percent mass loss for the nine different measured directions for a frequency range of 20 kHz to 200 kHz [125].

**Ultrasonic Range Velocity**
**20 kHz to 200 kHz**

$$V(x,y) = G_V + H_V x + I_V y + J_V x^2 + K_V x y + L_V y^2 + M_V x^2 y + N_V x y^2 + O_V y^3 + P_V x^2 y^2 + Q_V x y^3 + R_V y^4 + S_V x^2 y^3 + T_V x y^4 + U_V y^5 *$$

| Coefficient | Principal Material Direction – Polarization Direction | | | | | | | | |
|---|---|---|---|---|---|---|---|---|---|
| | L-L | L-R | L-T | R-R | R-L | R-T | T-T | T-L | T-R |
| $G_V$ | 5048 | 1591 | 1632 | 1550 | 782.9 | 756.7 | 1498 | 720.0 | 695.1 |
| $H_V$ | -422.3 | 4.779 | -123.5 | -301.7 | -82.73 | -119.0 | -242.8 | -74.88 | -125.7 |
| $I_V$ | 750.8 | 809.8 | 790.9 | 65.74 | 101.2 | 116.7 | 386.5 | 125.2 | 180.9 |
| $J_V$ | -105.6 | 0 | 76.25 | -59.04 | 1.717 | 16.92 | 6.882 | -22.77 | 1.890 |
| $K_V$ | -32.40 | -54.68 | -132.1 | -26.58 | -29.78 | -8.011 | -109.1 | 18.02 | -19.21 |
| $L_V$ | -623.0 | 32.76 | 225.7 | -60.60 | -44.23 | -60.99 | 308.2 | -27.40 | -14.20 |
| $M_V$ | -52.11 | 0 | 125.5 | -19.23 | 19.92 | 7.940 | 34.25 | 9.874 | -24.11 |
| $N_V$ | 45.22 | -12.11 | -42.19 | 34.97 | -22.51 | 6.575 | -49.61 | 1.769 | 16.31 |
| $O_V$ | 90.74 | 23.51 | 8.666 | 33.33 | 102.6 | 95.13 | -27.63 | 60.89 | 52.43 |
| $P_V$ | 3.542 | 0 | 2.007 | 8.422 | 7.136 | 3.131 | 0.326 | 1.938 | -11.62 |
| $Q_V$ | -15.97 | 15.84 | 12.69 | -2.170 | -2.270 | -10.91 | -9.912 | -5.452 | -3.800 |
| $R_V$ | 106.6 | -5.083 | -72.47 | 0.790 | 8.496 | 14.49 | -85.20 | 3.676 | 8.766 |
| $S_V$ | 14.94 | 0 | -22.99 | -0.036 | -6.117 | -4.312 | -5.750 | -2.251 | 4.160 |
| $T_V$ | -4.758 | -6.053 | 11.13 | -4.502 | 5.179 | 0.568 | 12.92 | 1.661 | -2.544 |
| $U_V$ | -39.33 | -0.566 | 14.11 | -4.517 | -20.03 | -20.52 | 29.20 | -12.41 | -13.64 |

*Values are centered by the mean and scaled by the standard deviation.
x = (mass loss (%) – $\mu_m$)/ $\sigma_m$ where $\mu_m$ = 19% and $\sigma_m$ = 10.6%
y = (frequency (Hz) – $\mu_{freq}$)/ $\sigma_{freq}$ where $\mu_{freq}$ = 100,100 Hz and $\sigma_{freq}$ = 56,580 Hz

McGovern's equations relate frequency and percent mass loss due to decay to velocity and attenuation [21]. The previous sections have described the methods used to obtain the frequency and percent mass loss. Tables 9 and 10 contain the polynomial coefficients for wave velocity for the frequency ranges of 4.5 kHz to 20 kHz and 20 kHz to 200 kHz, respectively. Table 11 contains the polynomial coefficients for attenuation for the frequency range 4.5 kHz to 200 kHz and is printed in Section 4.1.12. The tables are reprinted from [125].

The FDTD equations have several material constants that must be defined. These constants include density and stiffness matrix entries. The method for obtaining the density by location has already been described. The FDTD model is a two dimensional symmetric stiffness matrix constructed assuming plane strain in the radial / tangential cross-section. The stiffness matrix is made up of four unique values: the radial stiffness, $C_{rr}$, the tangential stiffness, $C_{\theta\theta}$, the shear modulus $G_{r\theta}$, and the radial / tangential coupling stiffness, $C_{r\theta}$. Three of these terms, $C_{rr}$, $C_{\theta\theta}$, and $G_{r\theta}$, are determined directly from the density and values for the radial, tangential, and shear velocities as shown in Equation 41. The radial / tangential coupling term is calculated using the other stiffness terms and the Poisson's ratio for Douglas-fir relating radial and tangential displacements.

$$C_{rr}^{k,i} = \rho^{k,i} c_r^2 \quad , \quad C_{r\theta}^{k,i} = \mu_{r\theta} \rho^{k,i} c_r^2 \quad , \quad C_{\theta\theta}^{k,i} = \rho^{k,i} c_\theta^2 \quad , \quad G_{r\theta}^{k,i} = \rho^{k,i} c_{r\theta}^2 \tag{41}$$

Where:

$\rho^{k,i}$ is the density of sound wood at a particular location, k = r, i = θ, within the model cross-section.

$C_{jl}^{k,i}$ is the stiffness matrix value (j, l = r, θ) in Pascals at a particular location, k = r, i = θ, within the model cross-section.

$G_{jl}^{k,i}$ is the shear modulus in Pascals at a particular location, k = r, i = θ, within the model cross-section.

$c_r$ is the radial wave velocity

$c_\theta$ is the tangential wave velocity

$c_{r\theta}$ is the shear wave velocity

$\mu_{r\theta}$ is the Poisson's ratio for Douglas-fir relating radial displacement to tangential displacement. It has a value of 0.382 [10].

### 4.1.11. Time step

The time step chosen for the FDTD simulation must be sufficiently small to insure stability. Chen [126] gives an empirically strict time step criteria for cylindrical coordinates reproduced here as Equation 42.

$$\Delta t \le \frac{1}{c_{\max}\sqrt{\frac{1}{(\Delta r)^2}+\frac{1}{(r_{\min}\Delta\theta)^2}+\frac{1}{(\Delta z)^2}}} \tag{42}$$

Where:
$c_{max}$ is the maximum wave velocity in the medium.
$r_{min}$ is the minimum radial distance in the model. In this model $r_{min}$ is equal to $\Delta r$.
$\Delta z$ is the distance between adjacent points in longitudinal direction. The model in this analysis is assumed to be plane strain, so the $\Delta z$ term is ignored.

In this analysis, the radial velocity, $c_r$, is the maximum velocity. Equation 43 is rewritten to include the new velocity component.

$$\Delta t \le \frac{1}{c_r\sqrt{\frac{1}{(\Delta r)^2}+\frac{1}{(r_{\min}\Delta\theta)^2}}} = \frac{\Delta r\Delta\theta}{c_r\sqrt{1+(\Delta\theta)^2}} \tag{43}$$

### 4.1.12. Material attenuation

All attenuation in the system is applied through the use of a perfectly matched layer (PML). As previously stated, the PML allows the application of attenuation without causing spurious reflections. Berenger [120] first developed the PML for electromagnetic waves. At the time of creation, the PML was primarily used as an absorptive, non-reflective outer boundary to a simulation space. The PML simulates an infinite space surrounding the analysis region. Outward traveling waves would reach the edge of the simulation space and attenuation below observable levels; this effect is the same as a wave traveling away from the analysis region and never returning. Gedney refined the PML by making a more computationally efficient calculation method and proving the stability of the refined method. Gedney also implemented the PML in a FDTD model [127]. Chew adapted the technique for elastodynamic equations in a

inhomogeneous medium. Chew showed that the PML completely absorbs elastic waves despite coupling between compressional and shear waves [121]. Liu extended Chew's work for scalar acoustic waves in Cartesian, cylindrical, and spherical coordinates [123, 124]. Hu identified a potential instability that existed in the PML when the group velocity was positive, but the phase velocity was negative. Hu refined the PML to eliminate the instability in a manner easy to implement in a FDTD simulation [128].

**Table 11** Polynomial fits for attenuation coefficients as a function of frequency and percent mass loss for the nine different measured directions for a frequency range of 4.5 kHz to 200 kHz [125].

**Attenuation**
**4.5 kHz to 200 kHz**

$$\alpha(x,y) = A_\alpha + B_\alpha x + C_\alpha y + D_\alpha x^2 + E_\alpha x y + F_\alpha y^2 + G_\alpha x^2 y + H_\alpha x y^2 + I_\alpha y^3 *$$

| Coefficient | Principal Material Direction – Polarization Direction | | | | | | | | |
|---|---|---|---|---|---|---|---|---|---|
| | L-L | L-R | L-T | R-R | R-L | R-T | T-T | T-L | T-R |
| $A_\alpha$ | 0.45937 | 0.93749 | 0.93989 | 1.31110 | 1.64566 | 1.93714 | 1.27111 | 1.66975 | 1.76142 |
| $B_\alpha$ | 0.17677 | 0.22694 | 0.20719 | 0.60610 | 0.58013 | 0.85167 | 0.42770 | 0.40410 | 0.44761 |
| $C_\alpha$ | 0.05638 | 0.01021 | -0.01041 | 0.03540 | 0.22686 | 0.32096 | 0.11495 | 0.31784 | 0.32387 |
| $D_\alpha$ | -0.00363 | 0.05056 | 0.05968 | 0.07174 | 0.05055 | 0.17319 | 0.07736 | 0.02911 | 0.13941 |
| $E_\alpha$ | 0.01073 | 0.00355 | 0.01157 | 0.03467 | 0.17461 | 0.15555 | 0.02009 | 0.11523 | 0.06093 |
| $F_\alpha$ | -0.01161 | -0.02839 | -0.06810 | -0.06143 | -0.08166 | -0.11495 | -0.07227 | -0.09389 | -0.10422 |
| $G_\alpha$ | -0.00252 | 0.00756 | 0.01017 | 0.02375 | 0.07800 | 0.05875 | -0.00352 | 0.01604 | 0.00716 |
| $H_\alpha$ | -0.00253 | 0.00967 | 0.00803 | -0.02354 | -0.0498 | -0.05808 | -0.01576 | -0.04268 | -0.02528 |
| $I_\alpha$ | -0.00160 | 0.00681 | 0.03601 | 0.00622 | -0.01124 | -0.01124 | 0.00194 | -0.01086 | -0.01965 |

*Values are centered by the mean and scaled by the standard deviation.
$x = (\text{mass loss } (\%) - \mu_m)/\ \sigma_m$ where $\mu_m = 19\%$ and $\sigma_m = 10.6\%$
$y = (\text{frequency (Hz)} - \mu_{freq})/\ \sigma_{freq}$ where $\mu_{freq} = 102{,}000$ Hz and $\sigma_{freq} = 56{,}580$ Hz

Senalik showed that rot does not produce discernible reflections of an incident wave [118]. The lack of reflections can partially be attributed to wave scattering along the rot / sound wood boundary. The wave scattering boundary was addressed in Section 4.1.5 It is known that rapid changes in signal attenuation across a small distance relative to the size of the incident wavelength can cause spurious reflections. The PML appears to be a perfect tool for implementing high attenuation normally associated with rot while avoiding attenuation based reflections. During implementation of the PML, it became apparent that there exists no requirement that the user specified attenuation must be high. Most of the restrictions on the use of the PML at the time that the technique was originally developed appear to be hardware related. It was strongly desirable to minimize the use of the PML due to the speed of available computers [127, 121]. Current

microprocessor computers can execute the PML much more quickly and have the added benefit of parallel computation, further decreasing computation time. As a result, the PML is used to implement the attenuation from McGovern's polynomials throughout the cross-section. Table 11 contains the polynomial coefficients for attenuation for the frequency range 4.5 kHz to 200 kHz. The table is reprinted from [125].

Below is the description of the implementation of the PML within the cross-section. Proofs of the method conformance with analytical solutions and stability are found in [120, 121, 123, 124, 127, 128]. The derivation below is primarily from Chew [121]. Implementation of the PML starts with the basic wave equation in Equation 44.

$$\rho \frac{\partial \vec{v}}{\partial t} = \nabla \vec{\sigma} \tag{44}$$

Where:
v is the velocity
t is time
σ is the stress
ρ is the density

It is assumed that all of the variables are frequency dependent and the time derivative of the velocity term can be expressed as Equation 45.

$$\frac{\partial \vec{v}}{\partial t} = -i\omega\vec{v} \tag{45}$$

The attenuation is applied to the system by use of coordinate stretching into an imaginary dimension. In the absence of any attenuation, the real component of the dimesion, $a_\eta$, would take on a value equal to the frequency ω and the imaginary component, $b_\eta$, would have a value of zero. Equation 46 shows the stretched spatial variable.

$$e_\eta = \frac{a_\eta}{\omega} + i\frac{b_\eta}{\omega} \qquad \eta = r, \theta \tag{46}$$

Where:
e is the stretched spatial variable
η represents the direction of stretching: radial, r, or tangential, θ
ω is the frequency

The divergence operation for the complex coordinate stretching variable is shown in Equation 47.

$$\nabla_e = \sum_{\eta=r,\theta} \hat{\eta} \frac{1}{e_\eta} \frac{\partial}{\partial \eta} \tag{47}$$

Where $\hat{\eta}$ is the unit vector of the stretched coordinate system.

The wave equation is rewritten in the stretched coordinate system in Equation 48. Equation 49 shows the rewritten wave equation for a single coordinate dimension.

$$-i\omega\rho\vec{v} = \sum_{\eta=r,\theta} \hat{\eta} \frac{1}{e_\eta} \frac{\partial \sigma}{\partial \eta} \tag{48}$$

$$-i\omega\left(\frac{a_\eta}{\omega} + i\frac{b_\eta}{\omega}\right)\rho v_\eta = \frac{\partial \sigma}{\partial \eta} \tag{49}$$

Equation 49 is rewritten to eliminate the complex terms and shown as Equation 50.

$$\rho\left(\frac{a_\eta}{\omega}\right)\frac{\partial v_\eta}{\partial t} + b_\eta \rho v_\eta = \frac{\partial \sigma}{\partial \eta} \tag{50}$$

The velocity and stress terms of Equation 50 are rewritten in terms of displacements and shown in Equation 51.

$$\rho\left(\frac{a_\eta}{\omega}\right)\frac{\partial^2 u_\eta}{\partial t^2} + b_\eta \rho \frac{\partial u_\eta}{\partial t} = C_{\eta_1\eta_2} \frac{\partial^2 u}{\partial \eta^2} \tag{51}$$

Where:
u is the displacement
$C_\eta$ is the stiffness in the direction of the stretched coordinate

The time derivative terms in Equation 51 are converted into a finite difference expression in Equation 52. The spatial derivatives are not used in the PML creation process, and are not converted.

$$\left(\frac{a_\eta}{\omega}\right)\left(\frac{u_\eta^{n+1}-2u_\eta^{n}+u_\eta^{n-1}}{(\Delta t)^2}\right)+b_\eta\left(\frac{u_\eta^{n+1}-u_\eta^{n-1}}{2\Delta t}\right)=\left(\frac{C_{\eta_1\eta_2}}{\rho}\right)\frac{\partial^2 u}{\partial \eta^2} \tag{52}$$

Where the superscripts n represent the time step.

Equation 52 is rewritten to solve for the displacement one time step in the future, un+1, and is shown as Equation 53.

$$u_\eta^{n+1}=-u_\eta^{n-1}\left(\frac{1-\frac{b_\eta\omega\Delta t}{2a_\eta}}{1+\frac{b_\eta\omega\Delta t}{2a_\eta}}\right)+2u_\eta^{n}\left(\frac{1}{1+\frac{b_\eta\omega\Delta t}{2a_\eta}}\right)+\left(\frac{C_{\eta_1\eta_2}(\Delta t)^2}{\rho}\right)\left(\frac{\frac{\omega}{a_\eta}}{1+\frac{b_\eta\omega\Delta t}{2a_\eta}}\right)\frac{\partial^2 u}{\partial \eta^2} \tag{53}$$

The following definition is implemented to simplify Equation 53.

$$\alpha=\frac{b_\eta}{2a_\eta}=\frac{100\beta_\eta c_\eta\Delta t}{2} \tag{54}$$

Where:
β is the attenuation coefficient from McGovern's equations in Nepers per centimeter
c is the velocity from McGovern's equations in meters per second

If the value of $b_\eta$ is small compared to $a_\eta$, then the value of aη is approximately equal to the frequency, ω.

$$\frac{\omega}{a_\eta}\approx 1 \tag{55}$$

Equations 54 and 55 are substituted into equation 53.

$$u_\eta^{n+1}\approx -u_\eta^{n-1}\left(\frac{1-\alpha\omega\Delta t}{1+\alpha\omega\Delta t}\right)+\left(\frac{1}{1+\alpha\omega\Delta t}\right)\left(2u_\eta^{n}+\left(\frac{C_{\eta_1\eta_2}(\Delta t)^2}{\rho}\right)\frac{\partial^2 u}{\partial \eta^2}\right) \tag{56}$$

Equations 57 and 58 contain approximations for the coefficients of the $u^{n-1}$ and $u^n$ terms, respectively. Equation 59 shows the final expression for $u^{n+1}$.

$$\left(\frac{1-\alpha\omega\Delta t}{1+\alpha\omega\Delta t}\right) \approx e^{-2\alpha\omega\Delta t} \tag{57}$$

$$\left(\frac{1}{1+\alpha\omega\Delta t}\right) \approx e^{-\alpha\omega\Delta t} \tag{58}$$

$$u_\eta^{n+1} \approx -u_\eta^{n-1} e^{-2\alpha\omega\Delta t} + \left(2u_\eta^n + \left(\frac{C_{\eta_1\eta_2}(\Delta t)^2}{\rho}\right)\frac{\partial^2 u}{\partial \eta^2}\right) e^{-\alpha\omega\Delta t} \tag{59}$$

McGovern's equations assume the attenuation follows an exponential decay. It is desirable to implement the attenuation values in the manner they were originally posed. The coefficients for $u_n$ and $u_{n-1}$ from the creation of the PML can be approximated as exponential terms. The percent error associated with these approximations is given in Table 12. Most values of $\alpha\omega\Delta t$ used in the simulations are less than 0.001. The highest values approach 0.01. The approximation for a value of 0.1 is given for completeness.

**Table 12.** Percent error of exponential approximation for values of $\alpha\omega\Delta t$

| Value of $\alpha\omega\Delta t$ | $\frac{\left\lvert\left(\frac{1}{1+\alpha\omega\Delta t}\right) - e^{-\alpha\omega\Delta t}\right\rvert}{\left(\frac{1}{1+\alpha\omega\Delta t}\right)} \times 100\%$ | $\frac{\left\lvert\left(\frac{1-\alpha\omega\Delta t}{1+\alpha\omega\Delta t}\right) - e^{-2\alpha\omega\Delta t}\right\rvert}{\left(\frac{1-\alpha\omega\Delta t}{1+\alpha\omega\Delta t}\right)} \times 100\%$ |
|---|---|---|
| 0.001 | $5.00\times10^{-5}$ | $6.67\times10^{-8}$ |
| 0.01 | $4.97\times10^{-3}$ | $6.67\times10^{-5}$ |
| 0.1 | $4.68\times10^{-1}$ | $6.71\times10^{-2}$ |

### 4.1.13. Outer boundary

The outer surface of the wood is met by a layer of air. The material attenuation for air is assumed to be zero. The stiffness matrix for air is rewritten and is shown in Equation 60.

$$\begin{bmatrix} \sigma_r \\ \sigma_\theta \\ \tau_{r\theta} \end{bmatrix} = \begin{bmatrix} \rho c^2 & 0 & 0 \\ & \rho c^2 & 0 \\ \text{Sym} & & 0 \end{bmatrix} \begin{bmatrix} \varepsilon_r \\ \varepsilon_\theta \\ \varepsilon_{r\theta} \end{bmatrix} \quad (60)$$

Where:
c is the speed of sound through air, 343 meters per second
ρ is the density of air, 1.21 kilograms per cubic meter

Air is a homogeneous gaseous medium; therefore, the stiffness matrix value for $C_{rr}$ and $C_{\theta\theta}$ are equal and the coupling term $C_{r\theta}$, and the shear modulus value $G_{r\theta}$ are set to zero. The layer of air allows some signal energy in the wood to be lost to the surrounding environment. Waves transmitted into and through the surrounding air encounter a reflectionless boundary. The reflectionless boundary simulates an infinitely large medium in which energy leaving the wood never returns. The reflectionless boundary is a PML used as it was originally intended. The formulation of the PML is the same as in Section 4.1.12; however, the attenuation is set arbitrarily high such that incident waves are attenuated to the point of insignificance. The reflectionless boundary layer is several nodes wide; however, the outermost nodes are fixed to a value of zero. It should be noted that the high acoustic impedance mismatch between wood and air is such that there is no noticeable difference in the simulation outputs when air is given stiffness values in accordance with Equation 60 or when air is assumed to have a stiffness of zero. To minimize calculation time, it is recommended that air be given a stiffness of zero and the air layer within the simulation space be restricted to a single node layer extending beyond the wood.

## 4.2. Validation of Simulation Results

In this section, simulation results are validated against theoretical and experimental results. Simulation outputs from an ideal cross-section are compared to wave behavior as predicted by analytical models. The ideal cross-section is perfectly round and free of defects. Good agreement exists between the analytical model and the simulation results for both primary and shear waves.

A simulation is also run using the utility pole cross-section shown in Figure 66b (page 107). The image provides density information, internal geometry, and mass loss information for the simulation. The results obtained from the simulation are compared against experimental data collected from tests performed on the actual wood pole. Discrepancies are explained.

### 4.2.1. Comparison of analytic and simulated results

A comparison was made between the wavefront behavior as predicted by the FDTD simulation and an analytic model of a wavefront traveling through a cylindrically orthotropic medium. The analytic wavefront model was developed by Patyon [107]. A condition of plane strain is assumed within the analytic model. The system input for the analytic model is a unit impulse. The simulation model was subjected to a narrow Gaussian pulse of six microseconds for results comparison. The narrow Gaussian pulse was chosen as the input rather than a unit impulse as it produced distinct dilatational and shear waves without causing significant noise. The area of consideration is a circular cross-section of Douglas-fir with a diameter of 381 mm, and individual ring thickness of 6 mm (3 mm earlywood, 3 mm latewood). These dimensions were selected as they are approximately the same as the physical specimens obtained for the experimental testing comparison presented later in this report. However, Payton's model disregards air / wood boundary effects, essentially assuming the wave is traveling in a semi-infinite media. In order to produce a fair comparison, the diameter of the cross-section was extended to 762 mm while the comparison area remained the inner diameter of 381 mm. The transit time of waves traveling away from the center is of sufficient length that boundary reflections do not return within the time of analysis. The simulation results presented here use the model with the grid enhancement scheme.

The results of the simulation and analytic models are shown in Figure 68. The radial displacements caused by the dilatational wave as predicted by the simulation at 116 μs after the Gaussian impulse input are shown in Figure 68a. The figure is produced in grayscale, with black indicating negative radial displacement (towards the center of the cross-section) and white indicating positive radial displacement (away from the center of the cross-section). The gray color composing the entirety of the left half of Figure 68a

indicates an undisturbed region with no radial displacement. The radial displacements do not clearly convey the anisotropic nature of the simulated media. To aid the reader, tree rings are projected onto Figure 68a and Figure 68c. The tree rings shown are merely a demonstrative tool to convey the nature of the media to the reader and are not indicative of true size of the rings (6 mm) used during the simulation calculations.

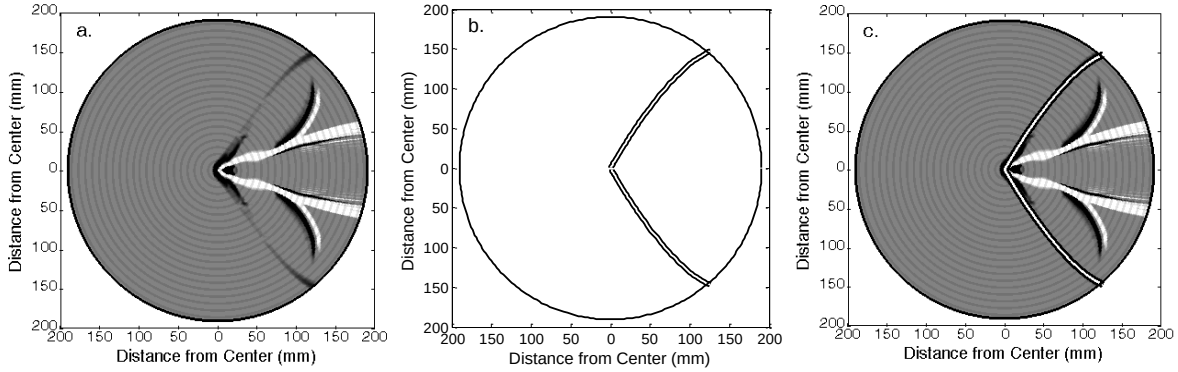


**Figure 68.** Predicted dilatational wave motion at 116 μs after the time of input. Results as predicted by **a.** simulation, **b.** analytic model, and **c.** the overlay of the simulation and analytic results.

The white and black line shown in Figure 68b is the dilatational wavefront as predicted by the analytic model. The analytic model assumes the absence of an outer boundary. The circle drawn in solid black indicates the extent of the area of comparison, but has no bearing on the analytic calculations and it placed merely as a demonstrative tool. Figure 68c contains an overlay of Figures 68a and 68b. The agreement between the leading edge of the disturbance region as predicted by the simulation and the wavefront location predicted by the analytic model is apparent in Figure 68c.

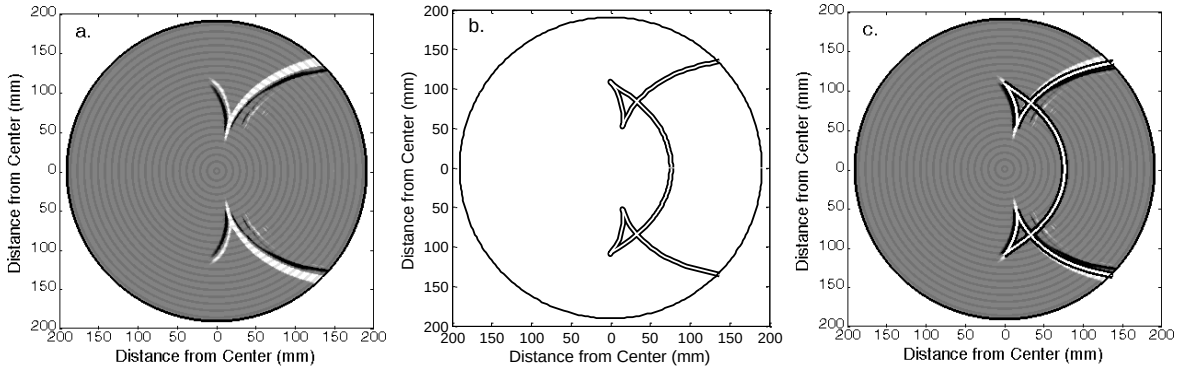


**Figure 69.** Predicted shear wave motion at 259 μs after the input. Results as predicted by **a.** simulation, **b.** analytic model, and **c.** the overlay of the simulation and analytic results.

The shear wave motion predicted by the simulation and analytic model are shown in Figure 69. The format of Figure 69 is similar Figure 68. The radial displacements caused by the shear wave predicted by the simulation at 259 μs after the Gaussian impulse are shown in Figure 69a. The presence of the cuspated corners indicates there should be a sudden change in phase of the wave. The simulation results clearly show negative radial displacements (a darker region) ahead of the cuspated corners that quickly change to positive radial displacements (the white bands) of the shear wave.

The dilatational wave motion predicted by the simulation and analytic model are shown in Figure 70 for 43, 116, 129, and 172 μs after the input. Figure 68 is an enlargement of Figure 70b. Figure 70 has a similar format as Figure 68: the simulation results are in Column 1, the analytic results are in Column 2, and the overlay of the two set of results are presented in Column 3.

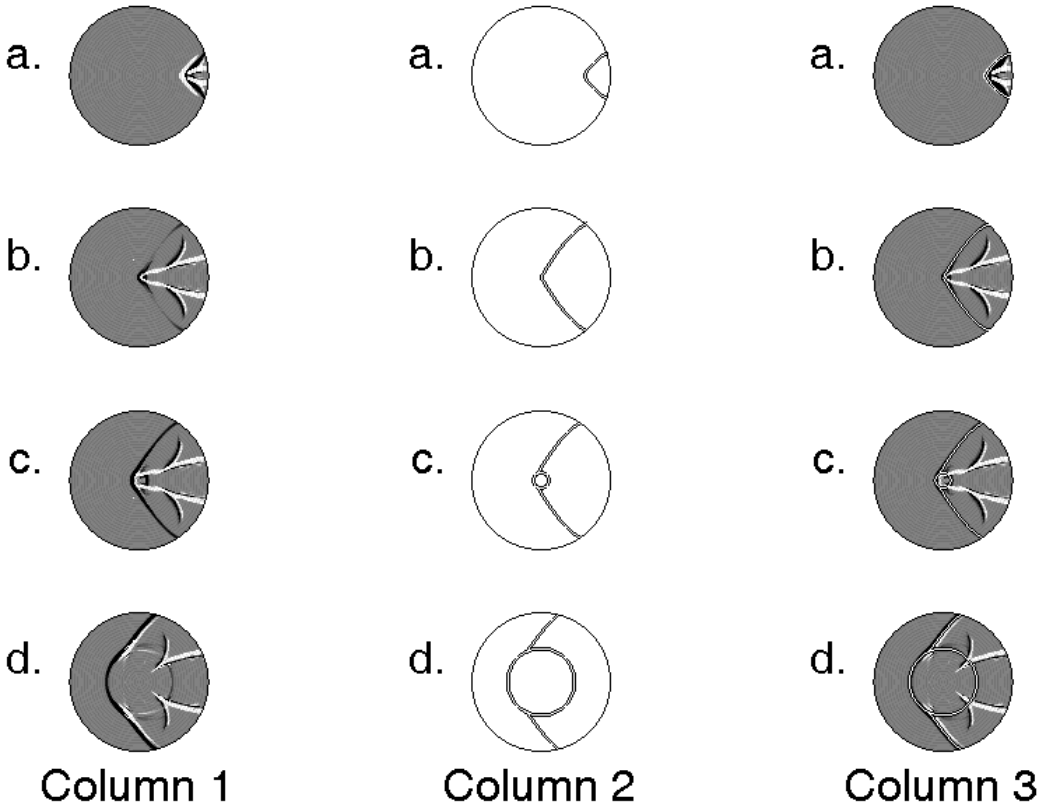


**Figure 70.** Dilatational wave motion in cylindrically orthotropic medium. Column 1. Wave motion predicted by the simulation. Column 2. Wave motion predicted by Payton's [107] analytical model. Column 3. The overlay of both sets of results. The results are shown for times **a.** 43 μs, **b.** 116 μs, **c.** 129 μs, and **d.** 172 μs after the input.

The shear wave motion predicted by the simulation and analytic model are shown in Figure 71 for 172, 215, 249, and 345 μs after the input. Figure 69 is an enlargement of Figure 71c. Figure 71 has a similar format as Figure 68.

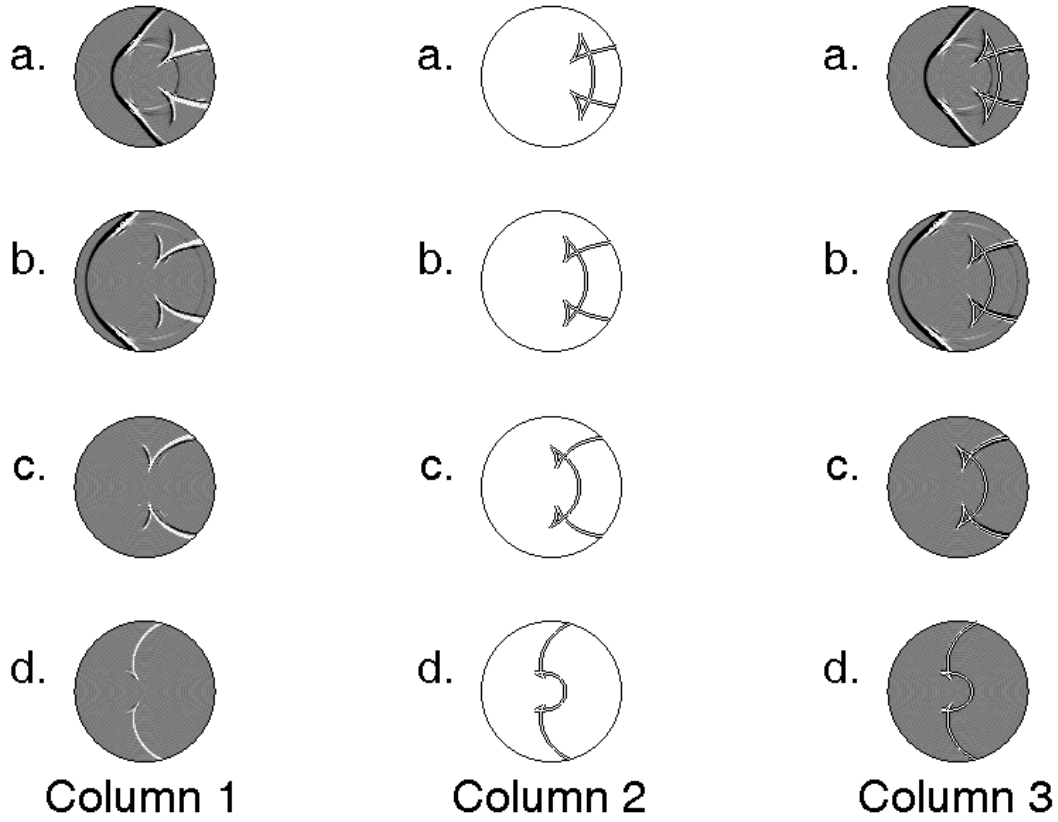


**Figure 71.** Shear waves motion in cylindrically orthotropic medium. Column 1. Wave motion as predicted by the simulation. Column 2. Wave motion as predicted by Payton's [107] analytical model. Column 3. The overlay of both sets of results. The results are shown for times **a.** 172 μs, **b.** 215 μs, **c.** 259 μs, and **d.** 345 μs after the input.

### 4.2.2. Experimental validation

Figure 72 shows a schematic diagram of the pole impact data acquisition system. An impact plate and accelerometers were affixed to a utility pole using heavy vacuum grease. The same test setup used to evaluate the glulam beams (Figure 45 on page 70) was used to evaluate the utility poles with three notable exceptions: first, two sensors were used for data collection; second, the utility pole was standing; and third, the input impact was a lead pellet propelled by an air gun against a steel plate coupled to the pole surface.

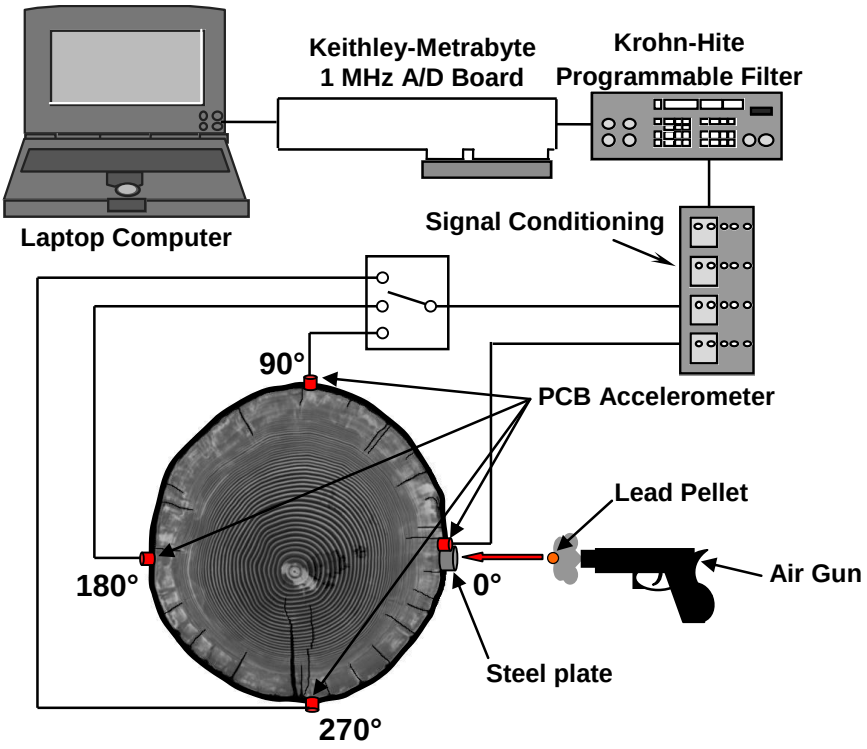


**Figure 72.** Schematic diagram of utility pole data acquisition system. The system excitation is an air gun shooting lead pellets. Data is recorded by accelerometers at 0°, 90°, 180°, and 270°.

The input impact location for all tests was at the 0° location as shown in Figure 72. A steel, cylindrical impact plate of dimensions 13 mm (0.5 in) diameter and 6 mm (¼ inch) thick was affixed at the 0° location. An accelerometer was affixed adjacent to the impact plate and will hereafter be referred to as the source accelerometer. The distance between the edge of the impact plate and the edge of the source accelerometer never exceeded 3 mm (⅛ inch). A second accelerometer, hereafter called the receiving accelerometer, was affixed at one of three locations: 90°, 180°, and 270°. Data was monitored continuously from both the source and receiving accelerometers; however, data collection began only after the voltage from source accelerometer surpassed a user defined threshold of 19 mV. During each test, both accelerometers collected 4096 data points at a sampling rate of 500 kHz. There was a 1 μs delay between the sampling of the source accelerometer and the receiving accelerometers. Five independent tests were conducted for each receiver location. The five signals were averaged to obtain a representative experimental signal.

The input was an impact from a lead pellet fired from an air gun. The air gun was a StingerP30 which fired 0.50 g, 6 mm lead pellet. The air gun was positioned 152 mm (6 inches) from the impact plate. The presence of the impact plate prevented scarring of the exterior of the wooden pole. The BB gun provided a consistent and repeatable input pulse. At each of the four monitored locations, the magnitude of the recorded signals was averaged to construct a single representative experimental signal for comparison against the simulation.

Figure 73 shows the representative experimental signals recorded at each of the four receiver locations, 0°, 90°, 180°, and 270° (received acceleration signal and the corresponding frequency domain signal). The experimental data is plotted in black. The simulated system responses at the respective locations are plotted on the same figures in red.

As shown in Figure 73a, the system input for the simulation was based upon the signal recorded at the 0° location. The high degree of correlation between the experimental data and the simulation data at the 0° is expected and provides evidence that the simulation input is representative of the experimental input.

Figure 73b shows the experimental data and simulated data for the 90° location. The bandwidth of the simulated data spans a frequency range of 4 kHz to 18 kHz. The bandwidth of the experimental data spans a frequency range of 5 kHz to 20 kHz. Assuming a full frequency range of 4 kHz (lowest frequency from the simulated data) to 20 (highest frequency of the experimental data), the true positives (the simulated data excited frequencies that were shown in the experimental data), constitute 82 percent of the range ($5^+$ kHz to 18 kHz). False negatives (the experimental data shows excitation but the simulation data shows none) constitute 12 percent of the range ($18^+$ kHz to 20 kHz). False positives (the simulation data shows excitation but the experimental data shows none) constitute 6% of the range (4 kHz to $5^-$ kHz). The maximum magnitude of the simulated data is 45 $ms^{-2}$. The maximum magnitude of the experimental data is 18 $ms^{-2}$. The error in the magnitude between the experimental and simulated data is 150 percent. This is the largest magnitude error between the simulated and experimental data. The probable source of the error is the presence of reaction wood, specifically compression wood, in the area of the receiver.

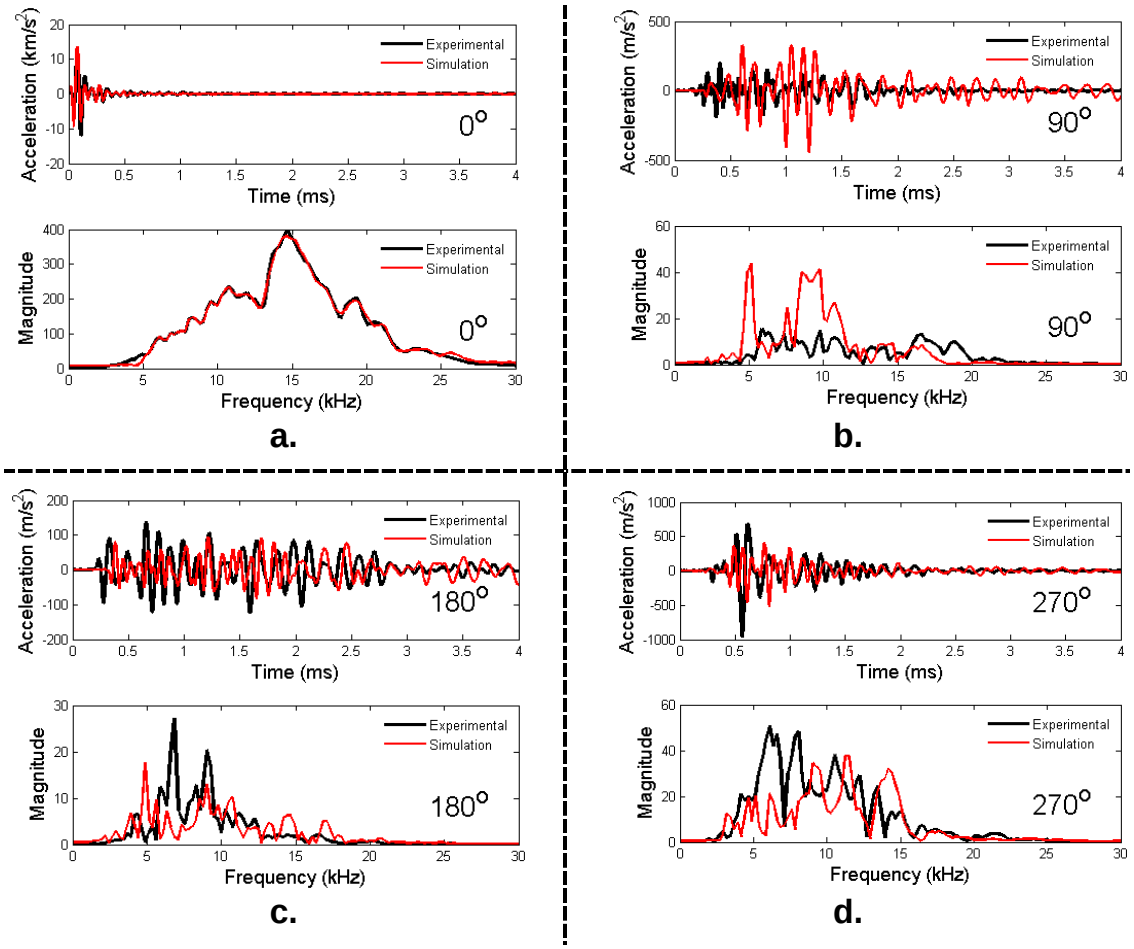


**Figure 73.** Experimental and simulated system responses. Experimentally recorded time domain and corresponding frequency domain records due to lead pellet impact compared to the corresponding simulation responses at **a.** 0°, **b.** 90°, **c.** 180°, and **d.** 270° locations, respectively.

Annual growth rings containing compression wood are usually exceptionally wide when compared to the rings on the opposite side of the branch or trunk. Consequently, the pith center is eccentrically located within the cross-section. The rings contain an abnormally high proportion of latewood and the density contrast between latewood and earlywood is often indistinct. The high proportion of latewood causes compression wood to have a higher density than normal wood [11]. Figure 74a shows the radial density of the utility pole cross-section shown in Figure 66a (page 107) with respect to angle from the source. Figure 74b shows the radius with respect to angle from the source. The same angle convention is used in Figure 66 and Figure 74. The accelerometer at the 90° location is located in a region that is both higher in density and highly eccentric, indicating that it is in a region of compression wood.

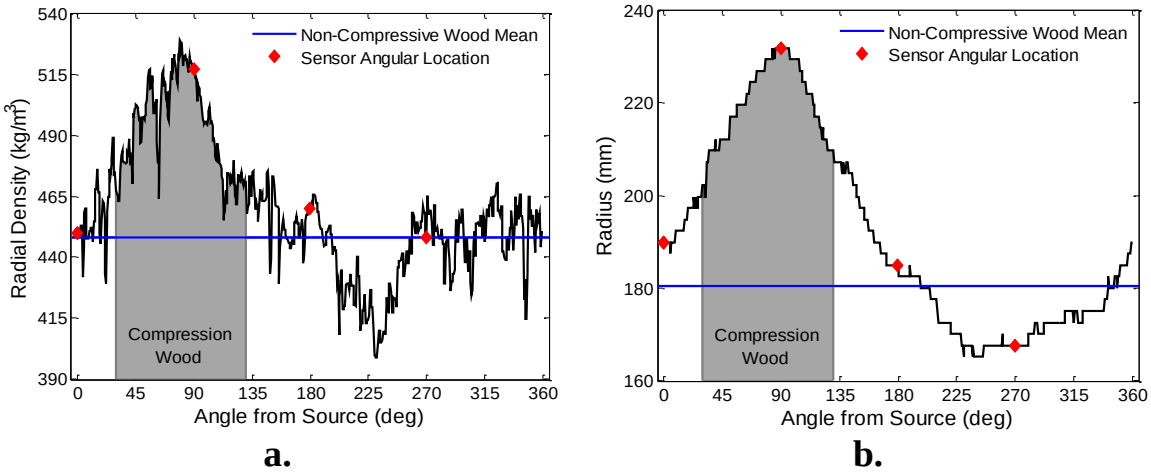


**Figure 74.** Radial density and radius as indications of compression wood. The gray shaded region is likely compression wood. The blue lines represent the mean value of the cross-section without the compression wood. The red diamonds indicate the location of the receiver accelerometers. **a.** Radial density with respect to angle from the input source. The angle convention used here is the same as Figure 66. **b.** Utility pole radius with respect to the angle from the input source.

From a utility standpoint, compression wood has several characteristics that make it less desirable than normal wood. Compression wood is more dense (between 10 percent and 40 percent higher than normal wood), but about equal in strength to normal wood. Compression wood should not simply be viewed as thick wood; its microstructure is considerably different than normal wood. With respect to normal wood, compression wood has less cellulose and more lignin. The microfibril angle of the S2 layer has a greater angle from vertical. The microfibrils in the S2 layer of normal wood have an angle from vertical of approximately 10°, but in compression wood, the angle can be as high as 45°. Haygreen [11] provides a concise overview of the properties of compression wood as they relate to wood products.

Bucur performed wave velocity measurements on both normal and compression wood of Douglas-fir and found tangential velocity decreased as the presence of compression wood increased [13]. In Bucur's original study, the decrease in speed was attributed solely to the increase in density. Gindl [129] compared the mechanical properties of compression wood and normal wood of Norway spruce within single annual rings of trees. During his study, he normalized values of Young's modulus with respect to density. In doing so, he found that compression wood had a lower Young's modulus

value than normal wood within the same annual ring. According to Equation 41, the wave velocity can be decreased by either decreasing the Young's modulus or maintaining the same Young's modulus and increasing the density. Compression wood has both effects; therefore, the wave velocity through compression wood is significantly reduced.

Erhard Wielandt, a seismologist, described a phenomenon in which ray paths of transverse waves through a cross-section avoid regions in which the wave velocities are lower [57]. This phenomenon became known as the "Wielandt effect." This phenomenon has been observed in wood by several authors [51, 98, 99, 130]. Socco [99] specifically mentions that Wielandt effects emerged often during ultrasonic tomography of decay in living trees. Nicolotti did not specifically mention the effect by name; however, the ability of the proposed technique to identity the presence of decay while unable to identify the degree of decay was attributed to the fact that "ray paths avoid low-velocity regions" [51]. Maurer developed an anisotropy correction procedure for acoustic wood tomography and attributed the inability to sense a hole as a void to the fact that "rays tend to avoid low-velocity zones" [130]. Maurer likened this to Fermat's principle, which states that that the path between two points taken by light is the path that can be traveled in the least time. In the context of seismological study, Mavko [131] described the diffraction of wave around slower inhomogeneities as Fermat's principle and further indicated that this phenomenon was sometimes referred to as the Wielandt effect.

The mechanical characteristics of compression wood lead to an explanation of the discrepancy between the experimental and simulated system response at the 90° location. The receiver accelerometer at the 90° location is within a region of compression wood. Wave energy is diverted away from the sensor located at the 90° location. As a result, less wave energy arrives at the accelerometer and the magnitude of the arriving wave decreases. Since, the simulation does not have a mechanism to simulate the effects of compression wood, the simulated signal arriving at the 90° location is the signal expected for a wave traveling through normal wood.

Figure 73c shows the experimental data and simulated data for the 180° location. The bandwidth of the simulated data spans a frequency range of 3 kHz to 18 kHz. The bandwidth of the experimental data spans a frequency range of 4 kHz to 17 kHz. Assume a full frequency range of 3 kHz (lowest frequency from the simulated data) to 18 (highest

frequency of the simulated data). True positives constitute 87 percent of the range (4 kHz to 17 kHz). False positives constitute 13 percent of the range (3 kHz to $4^-$ kHz and $17^+$ kHz to 18 kHz). The maximum magnitude of the simulated data is 18 $ms^{-2}$. The maximum magnitude of the experimental data is 28 $ms^{-2}$. The error in the magnitude between the experimental and simulated data is 36% percent. The error in magnitude is due to the assumption that the frequency dependent attenuation for loblolly pine is representative of Douglas-fir. If the true attenuation is smaller in magnitude, then the magnitude will increase. Also, the presence of compression wood at the 90° location diffracts wave energy from a large portion of the cross-section. The diffracted wave energy travels through the remainder of the cross-section, raising the energy density for the non-compression wood portion of the cross-section. It is worth noting that both the experimental data and the simulated data have a single prominent peak below 8 kHz. There is a clear peak in the experimental data at approximately 7 kHz. In the simulated data, there is a peak at approximately 5 kHz. The peaks correspond to resonances of the internal geometry of the cross-section. The geometries likely to excite a peak are the cross-sectional radius and the tangential distance between the surface cracks. If the wave velocity assumed in the model is less than the true velocity, then the peak excited by the geometry will be shifted to a lower frequency. There is general agreement between the magnitude and shape of the frequency spectra within the range of 8 kHz to 13 kHz. Both the experimental data and the simulated data share a prominent peak at approximately 9 kHz. Above 13 kHz, the simulated data contains more energy than the experimental data. This discrepancy can be explained by mode conversion within the cross-section that can cause energy from lower frequency inputs to shift to higher frequencies. Within the simulation, the attenuation rate of the mode converted frequencies remains that of the frequency of the input. If mode conversion does occur, then the energy in the higher frequencies will be larger than the experimental data. Since the energy contained in the high frequency spectra of the experimental data at the 90° and the 270° locations are higher than the simulated data, it is likely that the mode conversion at the 180° location is due to a localized geometric feature and the higher frequencies signals are attenuated before traveling to either of the 90° and the 270° locations.

Figure 73d shows the experimental and simulated data for the 270° location. The frequency range of the simulated data spans a frequency range of 3 kHz to 20 kHz. The frequency range of the experimental data spans a frequency range of 3 kHz to 22 kHz. Assume a full frequency range of 3 kHz (lowest frequency from the simulated data and experimental data) to 22 kHz (highest frequency of the experimental data). True positives constitute 89 percent of the range (3 kHz to 20 kHz). False negatives constitute 11 percent of the range ($20^{+}$ kHz to 22 kHz). The maximum magnitude of the simulated data is 38 $ms^{-2}$. The maximum magnitude of the experimental data is 50 $ms^{-2}$. The error in the magnitude between the experimental and simulated data is 24%. Similar to the 180° location, the error in magnitude is due to the assumption that loblolly pine attenuation is representative of Douglas-fir attenuation. If the true attenuation value is less, then the signal magnitude will increase. There is general agreement between the spectra of the two data sets between 9 kHz and 13 kHz, though the peaks of the simulated data at are shifted to lower frequencies. Like the 180°, the shift in the peaks is likely due to the actual wave velocity being higher than the model velocity. Between 13 kHz and 16 kHz, it appears that the two separate peaks of the experimental data are combined into a single peak in the simulated data. The largest discrepancy between the experimental and simulated data at the 270° experimental location is the presence of two high magnitude peaks in the experimental data at approximately 7 kHz and 8 kHz. These peaks are absent in the simulated data. This discrepancy is caused by destructive interference in the simulation. In the 270° time domain signal, note the high magnitude peak between 0.5ms and 0.6ms. The simulated data shows two full cycles within the same time period. In Figure 66a, it is apparent that the 270° location is next to a deep split in the utility pole. Shear waves that would normally travel tangentially around the interior impact the air / wood boundary at the crack and are reflected, redirected, and mode converted. Some redirected energy is directed towards the center of the pole while some is directed to the exterior. In the experimental data, the redirected energy arrives at the 270° as a shear wave at the same time that the shear wavefront from the 0° location is arriving. The two waves constructively interfere and a large peak is produced. In the simulated data, the shear wave velocity is slower than the experimental wave velocity and the redirected wave energy arrives at time when it destructively interferes with the shear

wavefront. Constructive interference within the observed time frame can be produced within the simulation by making small changes to the simulation parameters (e.g. increasing shear wave velocity or changing the 270° receiver location to be farther from the split). In the simulated frequency spectrum, such constructive interference causes an increase within the frequency range of 4 to 6 kHz. In the simulated spectrum, there is a double peak centered around 5 kHz and the single peak at 6 kHz. In the experimental data, there is a double peak centered around 7 kHz and a single peak at 8 kHz. Note that a two kHz shift was observed between the simulated and experimental peaks at the same frequency range at the 180° location. The shift is likely caused by the model wave velocity being lower than the actual wave velocity.

There are two main magnitude errors between the simulated and the experimental frequencies spectra. At 90°, compression wood causes the magnitude of the experimental data to be less than the simulated data, because the simulation contains no model for compression wood. At 270°, prominent peaks at 7 kHz and 8 kHz are present in the experimental data, but destructive interference causes them to be absent in the simulated spectrum. At both 180° and 270°, peaks within the simulation spectra are shifted lower than the peaks in the experimental spectra, because simulated wave velocity is less than the experimental wave velocity. Also, the magnitude of the simulated data spectra is between 24% and 36% lower than the experimental data spectra. This can be explained by simulated attenuation being greater than the experimental attenuation and the presence of the compression wood causing the energy density of the non-compression wood within the cross-section to increase. Figure 44 shows that two pieces of wood of the same species can have difference velocities. "Correcting" the model wave velocity to match the experimental data would give improved results for this utility pole, but would not necessarily be more correct than the current model velocity when analyzing any other utility pole. Currently, the simulation excites a frequency range that agrees with 82% of the experimental frequency range at worst, and 89% of the frequency range at best. Since the discrepancies between the experimental data and the simulated data are explainable and similar discrepancies could be present between any two pieces of wood, the model is considered to be sufficiently accurate to simulate a variety of cross-sections with the goal of developing metrics useful in determining the presence of internal decay.

### 4.3. Metrics of Internal Decay

Several researchers have constructed tomographic views of trees and / or wood poles from acoustic / ultrasonic measurements [99 - 103, 105, 106, 132, 133]. The results of those analyses have demonstrated the feasibility of acoustic / ultrasonic inspection as a means of locating and evaluating internal decay. Socco [99] required 120 independent measurements taken at 16 locations around the circumference of the cross-section. Lee [105], Kim [100 - 103], and Yanagida [106] required 270 measurements taken at 36 locations. Hagrey [132] and Liang [133] did not state the number of required measurements or number of locations. If a complete tomographic view of the cross-section can be constructed from 120 measurements, then positive identification of decay should be possible with significantly fewer measurements. In this analysis, four independent measurements are used to determine size, general location, and depth within the pole of a decay region.

Using the simulation developed in Section 4.1, the effect of varying defect size on output surface acceleration signals is explored. The responses are analyzed to identify signal characteristics that correlate to the defect size. The goal of the research is to develop metrics useful in determining the presence of internal decay from signal responses collected around the circumference of the utility pole. The simulated results, the developed metrics, and the validation of the metrics against real utility pole cross-sections are presented in this section.

A series of simulations were run for cross-sections of five different diameters: 305 mm (12 inch), 343 mm (13.5 in), 381 mm (15 in), 419 mm (16.5 in), and 457 mm (18 in). A cross-section of 381 mm (15 in) was included as part of the set as it was representative of the diameters of the utility pole specimens used in this study. The annual rings were assumed to be 3 mm (0.12 in) wide. The ratio of the density of earlywood to latewood was assumed to be 0.318:1, to be representative of the ratios seen in the CT scans of the glulam beams and utility poles. The simulation input was the signal shown in Figure 73a (page 126). A control cross-section free of internal defects was run for each pole diameter. After the control simulation was complete, cross-sections with center defects

were simulated. The diameters of the center defects were varied in proportion to the pole radii with fractional values of: 0.133, 0.267, 0.400, 0.533, 0.667, 0.800, and 0.933. For a 381 mm (15 in) pole, the fractional values correspond to a center defect diameters ranging from 25 mm (1 in) to 175 mm (7 in) in 25 mm (1 in) increments. A simulation was run for each pole diameter and each center defect for a total of 40 simulations (five pole sizes, seven center defect sizes, and a control). To more closely model the type of defects seen in the cross-sections, the simulated defect was assumed to be a void surrounded by 25 mm (1 inch) of rot as shown in Figure 64 (page 103). Acceleration signals were recorded from each simulation at each of the four fixed locations around the circumference of the poles. The first was next to the source and is referred to as the 0° location. The other three locations were +90°, 180°, and -90° (270°). The angles refer to the angle constructed by drawing lines from the source to the center of the pole and then from the center of pole to the location of the receiver. The positive angle direction of the CT Scan images is counterclockwise from the source.

After the signals were recorded, they were examined for noticeable changes in signal characteristics attributable to increasing defect size. The characteristics were then examined to determine if non-dimensionalized metrics could be developed and correlated to the size of the center defect.

### 4.3.1. Factors complicating signal analysis on wood specimens

There are several complicating issues with respect to using signal analysis techniques on wood specimens. First, wood is anisotropic and heterogeneous. The anisotropy causes waves to travel along non-linear ray paths. Wavefronts traveling across the center excite waves in all directions. The natural ring structure causes wave guide effects. Second, each piece of wood is unique. Internal voids can develop through natural growth or by external mechanisms. Cracks lengths range from just below the surface to the center of the tree and beyond. Knots present discontinuities. Eccentricity of the tree center causes variations in the ray paths. Trees of the same species may have different attenuation and velocity characteristics depending upon temperature and rainfall during growth. Third, the signal shape is sensitive to changes in the cross-section. Cracks near the receiver locations may cause high frequencies to appear in the output

signal due to mode conversion. In several simulations, changes in internal defect sizes caused delays in traveling waves resulting in constructive or destructive interference, which can exaggerate or mask defect severity. Fourth, the assumption that waves traveling across a cross-section contain information about decay within that cross-section is not always true. Small regions of incipient decay that are absent of voids are difficult to identify using acoustic and / or ultrasonic inspection as the wave ray paths tend to avoid regions of low velocity due to the Wielandt effect [51, 57, 98, 99, 130].

### 4.3.2. Metric uncertainties

The voltage signal is sensitive to phase and time shifts of the arriving waves and changes to the cross-sectional geometry. In addition, mode conversion is likely to occur at boundaries, converting shear waves into dilatational waves. Using the simulation described previously, the changes in the system responses were recorded for varying sized defects. The output signals consisted of several waves: radially traveling dilatational waves, tangentially traveling dilatational waves, radially travelling shear waves, and tangentially traveling shear waves. Slight changes in arrival times and / or phase may cause constructive or destructive interference that significantly alters the signal shape.

To better examine the change in wave behaviors as a function of the defect size, a log scale representation of signals is constructed. The log scale representation allows smaller peaks and troughs to become more visible when compared to the higher magnitude peaks in the signal. The numerical equation of the log scale representation is shown in Equation 61. An example of the log scale representation is shown in Figure 75.

$$a^* = \mathrm{sgn}(A) \times \ln(1+|A|) \tag{61}$$

Where:
A is the signal amplitude
a* is the log scale representation of the signal amplitude

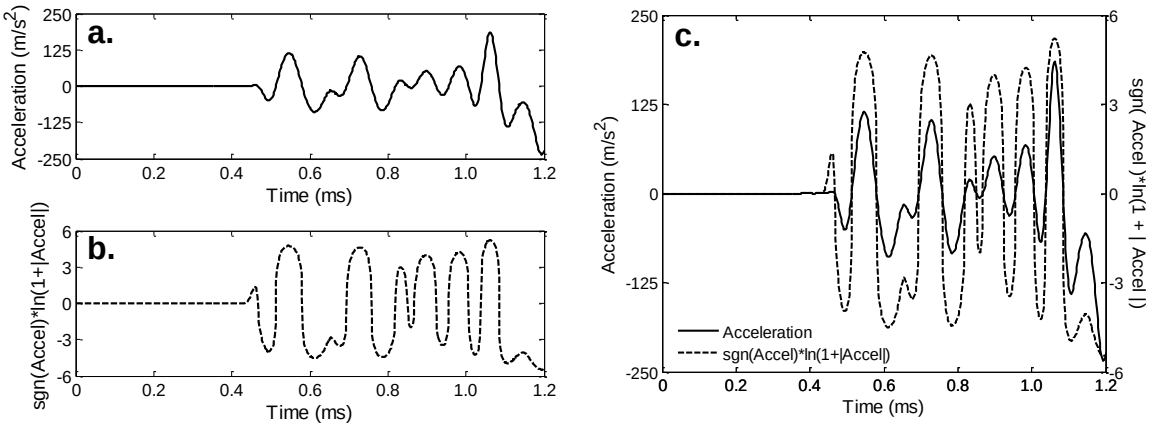


**Figure 75.** Log scale representation of a typical system response at the 180° location. **a.** Typical system response, **b.** log scale representation of system response, **c.** Overlay of typical system response and log scale representation of the system response

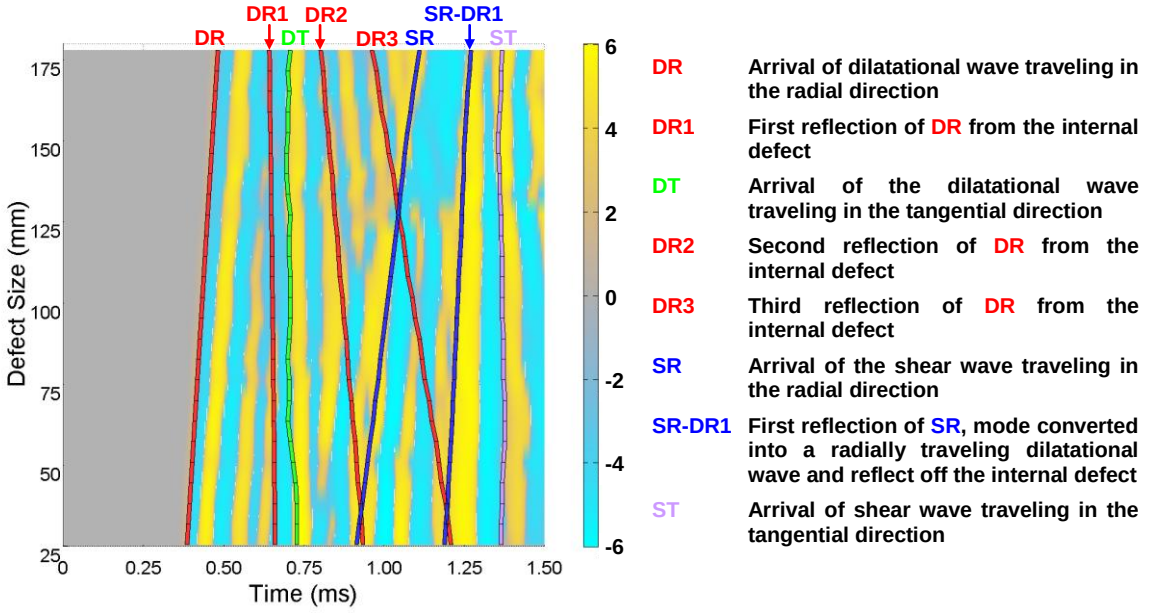


**Figure 76.** Plane view of the log scale representation surface of the signal response at the 180° location for varying defect sizes. The arrival of different waves are depicted as lines across the surface. The signals shown were collected from a cross-sectional with diameter of 381 mm (15 in).

Small magnitude peaks and troughs from the original acceleration signal become more prominent in the log scale representation shown in Figure 75c. The sign convention is also conserved. A series of simulations for a 381 mm (15 in) diameter pole with center defect diameters ranging between 25 mm and 175 mm in 6.4 mm increments (1 to 7 inches in ¼ inch increments) were run. For each simulation, the system response at the 180° location was collected and converted into the log scale representation. Figure 76

contains a plane view of a surface created from all of the log scale representations. The color scale is chosen such that yellow represents peaks, cyan represents troughs, and gray represents values near zero.

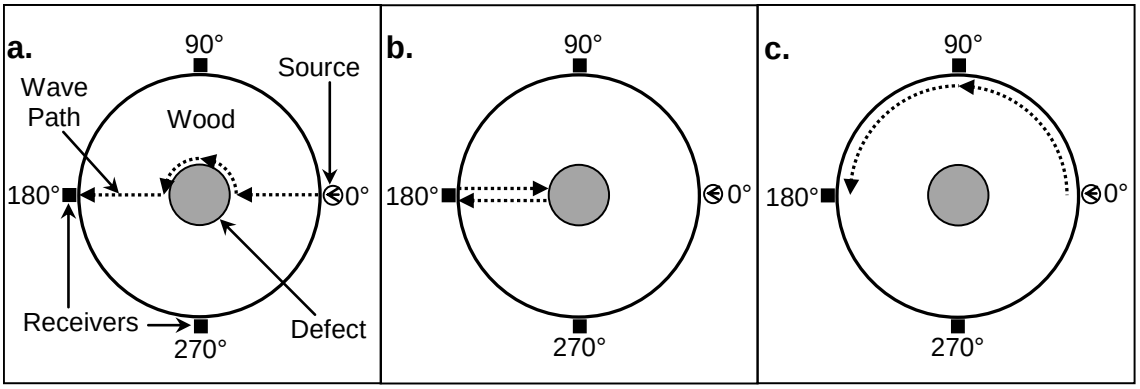


**Figure 77.** Paths of waves fronts in cross-sections with internal defects. **a.** radially traveling wavefront with an internal defect (waves DR and SR from Figure 76 follow this path), **b.** reflection of radially traveling wavefront from the center defect (waves DR1, DR2, DR3 and SR-DR1 follow this path) , and **c.** tangentially traveling wavefronts (wave LT and ST follow this path).

Within the first 1.5 ms, eight wavefronts are clearly visible in the log scale representation. Wavefront DR is the dilatational wave traveling in the radial direction. It travels from the source, around the defect, to the receiver as shown in Figure 77a. Wavefront DR1 is the first reflection for the radial wave from the center defect. After the wavefront arrives at the receiver, it reflects from the air / wood boundary and then travels back to the internal defect. There the wavefront strikes the air / wood boundary of the internal defect and travels back to the receiver as shown in Figure 77b. Wavefront LT is the dilatational wave that travels tangentially from the source across the 90° receiver location to the 180° receiver location as shown in Figure 77c. Wavefronts DR2 and DR3 are the second and third reflections of the dilatational wave traveling in the radial direction from the internal defect (Figure 77b). Wavefront SR is the shear wave traveling in the radial direction. Like wavefront DR, it travels from the source cross the center to the receiver (Figure 77a). Wavefront SR-DR1 is the first reflection of the shear wave from internal defect. As the shear wave arrives at the receiver, it reflects at the air / wood boundary. At the reflecting boundary, some of the wave energy mode converts from a shear wave into a dilatational wave. The dilatational wave travels from the 180° location back to edge of the defect, reflects and then back to the receiver (Figure 77b). Wavefront

ST is the shear wave that that travels tangentially from the source across the 90° receiver location to the 180° receiver location (Figure 77c).

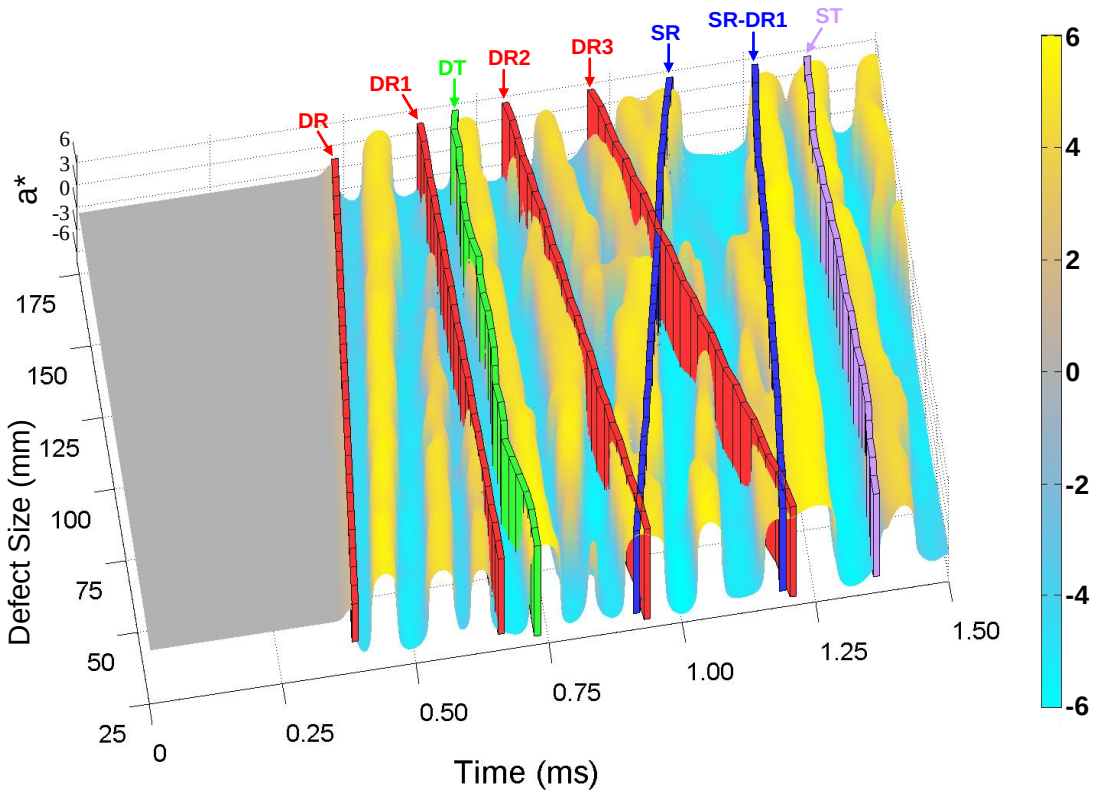


**Figure 78.** Oblique view of the log scale representation surface of the signal response at the 180° location for varying defect sizes. Wave nomenclature is given in Figure 76. The log scale representation, a*, is defined in Equation 61. The cross-sectional diameter is 381 mm (15 in).

Figure 78 is an oblique view of the surfaces created from the log scale representations (Figure 76 was the plane view). The abbreviations are defined in Figure 76 and a* is defined in Equation 61. The effects of the internal defect become more noticeable as the defect size increases. In Figures 76 and 78, the time of flight of the DR wave increases with increasing defect size. The reason for this delay is the redirection of the radially traveling dilatational wave around the center defect as shown in Figure 77a. After the wave arrives at the 180° location, the reflected wave travels back towards the center where it impacts the internal defect. The jagged edge implemented in Section 4.1.5 was designed to scatter incident wave energy, however a small portion of the wave energy does reflect from the defect and return to the 180° location. The reflected wave is small in magnitude and difficult to see in normal scale. The log scale representation,

shown in Figure 75, makes the reflected waves more prominent and easily observable. As the defect size increases, the distance from the edge of the pole and the edge of the defect decreases and the time between the reflections decreases. In Figure 78, the largest time of flight between the reflections (DR to DR1, DR1 to DR2, etc.) is 274 μs at a defect size of 25 mm. The smallest time 142 μs at a defect size of 175 mm. Since the time of flight of the waves change with respect to the size of the defect, constructive and destructive interference becomes a concern when developing metrics to identify internal decay.

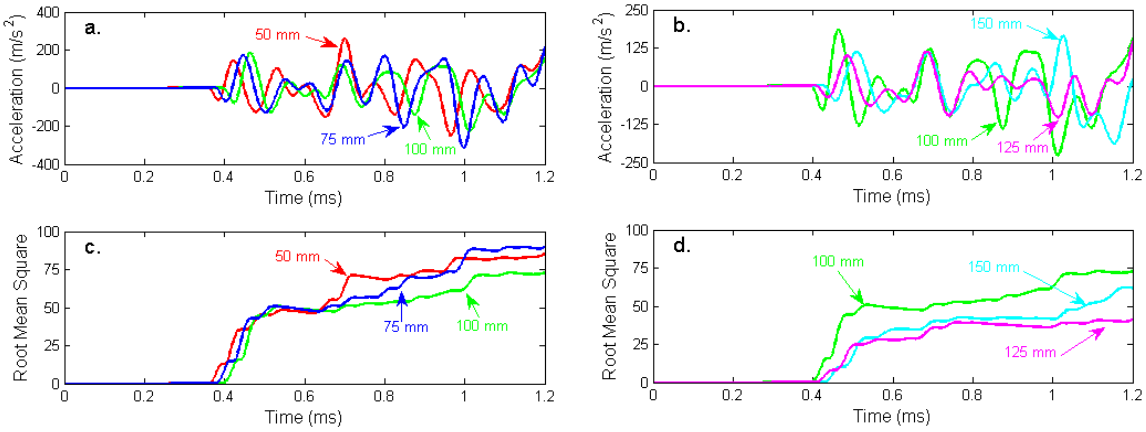


**Figure 79.** Acceleration and root mean square (RMS) plots. Acceleration versus time plots with associated RMS plots for simulated signals at 180° location for various sizes of center holes. The signal shapes are affected by constructive (**a.** and **c.**) and destructive (**b.** and **d.**) interference. The 75 mm hole RMS (blue) should lie below the 50 mm RMS (red) and above the 100 mm RMS (green), but constructive interference causes it to exceed the 50 mm RMS. The 125 mm RMS (magenta) should lie between the 100 mm RMS and the 150 mm RMS (cyan), but destructive interference causes it to diminish below the 150 mm RMS.

Two cross-sections in which the effects of interference are most prominent are the cross-sections containing the 75 mm defect and the 125 mm defect. For the 75 mm defect, the arrival time of the DR2 wave falls between the tail of the tangentially traveling dilatational wave, LT, and the arrival of radially traveling shear wave, SR. As a result of constructive interference between the three waves, the troughs at 0.884 ms and 1.036 ms for a 75 mm defect are lower than the corresponding troughs on either the 50 mm defect or the 100 mm defect, as shown in Figure 79a. The cross-section containing the 125 mm defect has two notable destructive interference occurrences within it. The first occurs at 0.630 ms. The tail of the arriving DR wave destructively interferes with the first

reflection of the radially traveling dilatational wave, DR1. Also, third reflection of the radially traveling dilatational wave, DR3, destructively interferes with the arriving radially traveling shear wave, SR. As a result, the magnitude of the troughs / peaks between 0.8 and 1.1 ms in the 125 mm defect signal are greatly diminished, as shown in Figure 79b. As a final note, the destructive interference is readily apparent within the 125 mm signal when compared against the 100 mm and 150 mm signals. Within the time frame shown, the 100 mm signal has four peaks above 125 $m/s^2$, the 150 mm signal has three, and the 125 mm signal has none.

Metrics that rely upon early simulated values of the signals such as the first arrival time should have smooth and predictable curves. Early in time, there is little opportunity for phase and time shifts to result in significant interference. The predictability of the metric values decreases as the number of points used to develop a particular metric increases. Take for example, root mean square (RMS). Given a signal of arbitrary length, the RMS depends upon all of the points within that signal. Interference phenomenon within a signal greatly affects the RMS value. It is expected that the RMS value of the signals will decrease with increasing size of internal defect. A larger internal defect has a larger area of rot and a greater loss of signal magnitude resulting in a diminishing RMS. The simulated signals show that while the overall downward trend of RMS is present for increasing defect size, individual values do not necessarily obey that trend. The two large troughs previously described within the 75 mm defect signal cause the RMS value of the signal to increase above the RMS value of the 50 mm defect signal as shown in Figure 79c. Conversely, the destructive interference within the 125 mm signal causes the RMS value to decrease below the RMS value for the 150 mm signal as shown in Figure 79d.

Interference effects introduce additional uncertainty to several types of metrics. Metrics based upon phase or frequency content are especially sensitive. Amplitude fluctuations caused by interference regularly exceeded the changes attributable to internal decay. As a result, those metrics are not considered reliable decay detectors. It has been observed that the ratio of high frequency signal energy to low frequency signal energy decreases as internal rot increases [7]; however, the positions of surface cracks relative to the receiving sensor can skew the frequency content through resonance and mode

conversion. Surface cracks on wood poles are common and may not be easily identified by surface examination. Several of the surface cracks on the wood pole specimens used in this analysis can only be identified from CT scans. As a result, the high to low frequency energy ratio may be skewed under conditions commonly encountered and difficult to identify. Energy metrics are also affected by the presence of surface cracks, but are less sensitive. Metrics based upon signal energy are largely effective in determining the presence of an internal defect, but interference effects impact the accuracy of the defect size estimation.

### 4.3.3. Metrics

In previous studies by Tiitta [83, 84] and Beall [37], it was noted that no single metric reliability showed the presence of rot in every cross-section. Thus, a process of looking at several metrics was adopted. A similar process is adopted here. Three metrics have been developed using the simulated data and are validated against real utility pole cross-sections. The three metrics described here were chosen due to their robustness in accurately estimating defect size across a variety of cross-sectional geometries. In all cases, the final metrics are ratios of the values obtained at the 180° location to the values obtained at the 90° location in order to normalize the metric values for a particular piece of wood. The three metrics are described in this section. Several other metrics were explored, but were found to be sensitive to changes in cross-sectional geometry which lead to inaccurate defect size estimates. Those metrics are described in the Appendix (page 218).

The first metric is the ratio of the area of the radially traveling dilatational wave to the tangentially traveling dilatational wave. Hereafter, this metric is referred to as the wave area metric. The wave motion through the cross-section is such that the radial wave and the tangential waves can be examined separately. The ratio of the rectified areas of each wave can be related to the defect size. This metric is based upon points taken early within the recorded signals and should be insensitive but not completely independent of interference phenomena.

The second metric is the percent difference between the area time centroid and the energy time centroid. This metric is based upon a large number of points taken from the

recorded signals and is sensitive to interference phenomena. As the size of the internal defect increases, the value of area time centroid and the energy time centroid increase and begin to converge. As a result, the percent difference between the centroid values decreases as the size of the defect increases. Hereafter, this metric is referred to as the time centroid metric. The time centroid metric is used to estimate the size of the defect.

The third metric is the time of flight (ToF) of the wavefront through the cross-section. The ToF is the time necessary for the first wavefront to travel from the source to the receiver. It is used to determine several factors relating to the internal defect: the general location of the defect within the cross-section, the size of the defect, and the approximate depth of the defect within the cross-section. This metric is based upon a single value early in the recorded signals and should not be affected by interference phenomenon. Hereafter, this metric is referred to as the time of flight metric.

#### 4.3.3.1. Wave area metric

The wave area metric is the ratio of the rectified areas of the radial and tangential waves. Based upon the motion of the wavefront the tangentially traveling dilatational wave and the radially traveling dilatational wave can be examined separately.

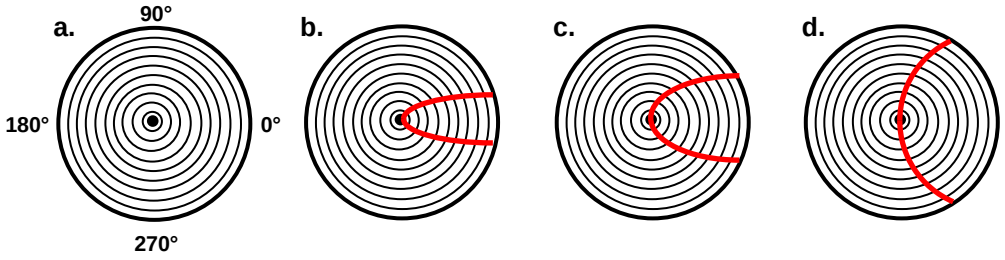


**Figure 80.** Wavefront shape by ratio of radial to tangential velocity with input source at 0° **a.** prior to input, **b.** ratio of 4, **c.** ratio of 2, **d.** ratio of 1.

Payton's [107] analytical model predicts the shape of the first wavefront as it travels across a cylindrically orthotropic solid cross-section (as wood is assumed to be in this analysis). Prior to reaching the center of the cross-section, the wavefront has a triangular shape with the vertex between the input source and the center of the cross-section. The aspect ratio of the triangle is dictated by the tangential wave speed and the

radial wave speed. Figure 80 shows the shape of the wavefront for differing ratios of radial to tangential velocities traveling from a source at 0°. If the tangential speed is similar in value to the radial speed, then the triangular wavefront will be wide (an obtuse triangle), as in Figure 80d, but if the tangential speed is low relative to the radial wave speed, then the triangular wavefront will be narrow (an acute triangle) as in Figure 80b.

Figure 81 shows a wavefront traveling from the source at 0°. The radial wave travels from the source towards the center of the cross-section (Figure 81b and 81c). At the center, a radial wave is excited in all directions (Figure 81d through 81f). The first arriving wave at the 180° location is the excited radial wave, as shown in Figure 81f. The excited radial wave arrives at all locations around the circumference simultaneously; the arrival time of the radial wave is designated as $\tau_{180}$. The tangential wave travels from the source circumferentially around the cross-section (Figure 81b through 81e) and, for both loblolly pine and Douglas-fir, is the first wave to arrive at the 90° and 270° locations; the arrival time of the tangential wave is designated $\tau_{90}$. Comparing characteristics of the first arriving wave at either the 90° or 270° location to the first arriving wave at the 180° location, is equivalent to comparing the tangentially traveling dilatational wave and the radially traveling dilatational wave.

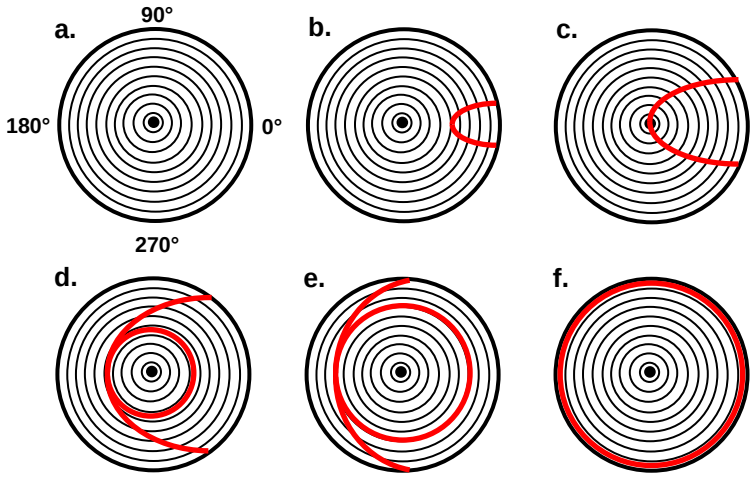


**Figure 81.** Wavefront traveling through a wooden pole at differing times with a source at 0°, **a.** prior to input, **b.** after input, **c.** wavefront arrives at the center of the pole, **d.** wavefront crossing the center of the pole excites a radial wave in all directions, **e.** the wavefront traveling in the tangential direction reaches the receiver locations at 90° and 270°, **f.** the radial wavefront reaches the 180° location and arrives prior to the tangentially traveling wavefront.

In Figure 82, two signals are shown. Figure 82a shows the signal recorded at the 90° location for a 381 mm (15 in) cross-section with no internal defects. Figure 82b is the rectified acceleration signal shown in Figure 82a. Figures 82c and 82d are the acceleration and rectified acceleration signals collected at the 180° location, respectively.

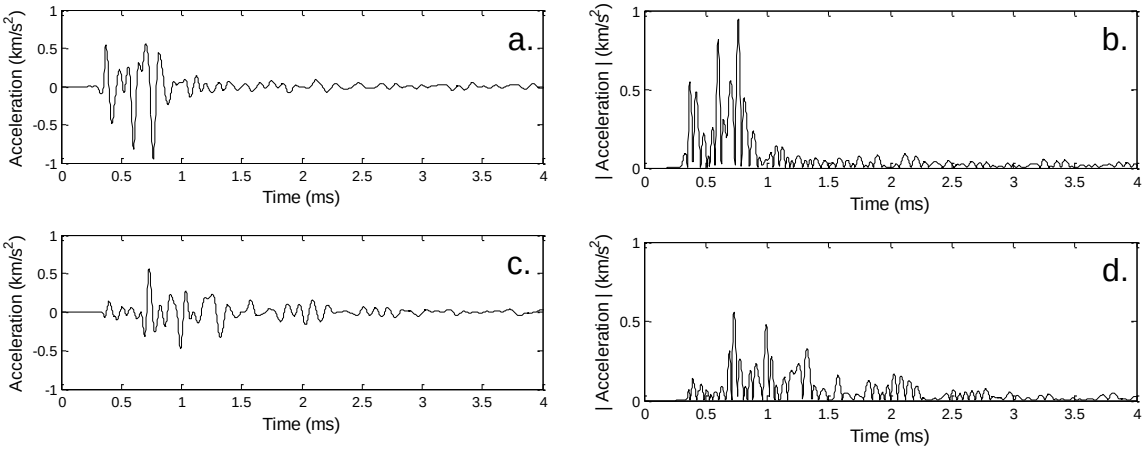


**Figure 82.** Acceleration and rectified acceleration time domain signals collected for a 381 mm (15 in) cross-section containing no defects. The collection signals are: **a.** acceleration at the 90° location, **b.** rectified acceleration at the 90° location, **c.** acceleration at the 180° location, and **d.** rectified acceleration at the 180° location.

The arriving wavefront of the tangential wave and radial wave are shown in Figures 83a and 83b, respectively. By examining a portion of the 90° location acceleration signal between the time of the source input at time t = 0 and the arrival of the radial wave at time t = $\tau_{180}$, the tangential wave, arriving at time t = $\tau_{90}$, can be examined without influence from the radial wave. Figure 83c shows the time partition used to isolate the tangential wave within the 90° location acceleration signal. The time partition used is t = 0 to t = 0.95*$\tau_{180}$. The tangential wave continues to travel circumferentially around the cross-section and arrives at the 180 location at time t = 2*$\tau_{90}$. By examining a portion of the of the 180° location acceleration signal between time t = 0 and the arrival of the tangential wave time t = 2*$\tau_{90}$, the radial wave can be examined without influence from tangential wave. Figure 83d shows the time partition used to isolate the radial wave within the 180° location acceleration signal. The time partition used is t = 0 to t = 1.9*$\tau_{90}$.

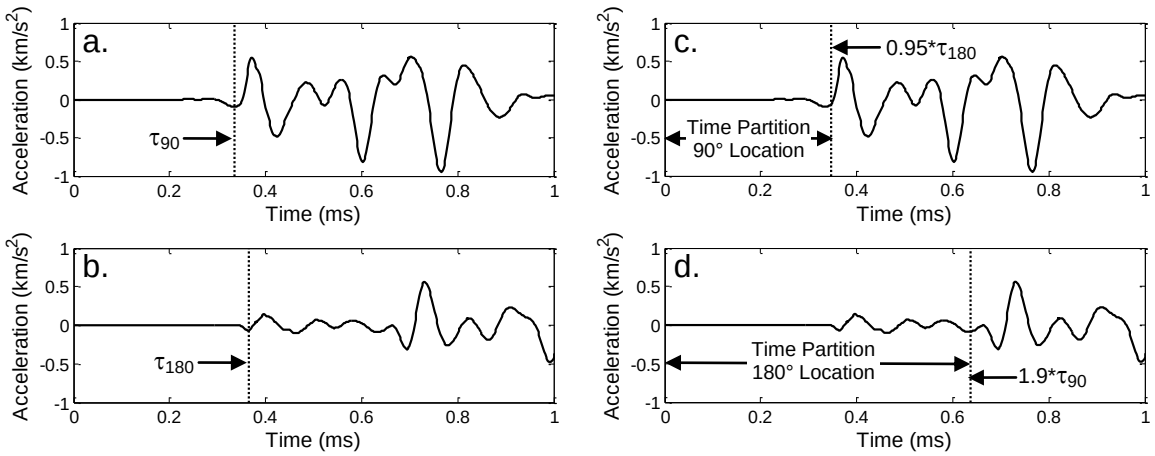


**Figure 83.** Radial and tangential wave time partitions. **a.** The tangential wave arrives at the 90° location at time t = $\tau_{90}$. **b.** The radial wave arrives at the 180º location at time t = $\tau_{180}$. **c.** The time partition used to examine the arriving tangential wave at the 90° location is t = 0 to t = 0.95*$\tau_{180}$. **d.** The time partition used to examine the arriving radial wave at the 180° location is t= 0 to t = 1.9*$\tau_{90}$.

After the time partitions are determined, the acceleration signals are rectified. The area under the rectified acceleration signals within the time partition is calculated and is normalized by the root mean square of the time partition. The area under the rectified acceleration curve is related to the rate of displacement at the receiver locations. The area of 180° location signal is normalized by the area of the 90° location signal. This ratio gives an indication of the relative rate of displacement between the 180° and the 90° locations. The shaded regions of Figure 84a and 84b show the areas examined from the rectified signals collected at the 90° and 180° locations, respectively. The equation of the ratio is expressed in Equation 62.

$$R_P = \frac{\frac{1}{RMS_{180}^{1.9*\tau_{90}}} \sum_{t=0}^{t=1.9*\tau_{90}} \left|A_{180}(t)\right|}{\frac{1}{RMS_{90}^{0.95*\tau_{180}}} \sum_{t=0}^{t=0.95*\tau_{180}} \left|A_{90}(t)\right|} \qquad (62)$$

Where:

$R_P$ is the wave area metric of the time partitioned rectified area normalized by the RMS

$RMS_{\angle}^{w}$ is the root mean square taken at a location corresponding to angle $\angle$ and has a time window beginning at time t = 0 ending at time w

$A_{\angle}(t)$ is acceleration amplitude recorded at location corresponding to angle $\angle$ at time, t

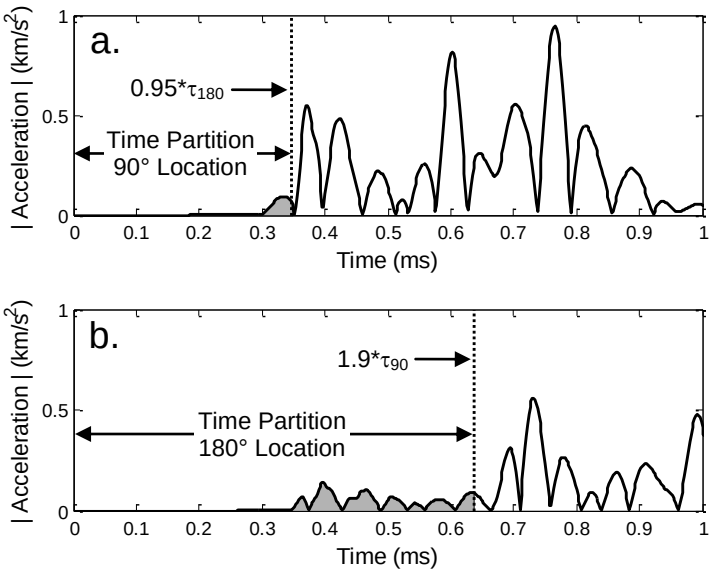


**Figure 84.** Time partitions used to compare radial and tangential waves. The shaded regions show the area used in the calculation of the wave area metric **a.** The time partition used to examine the arriving tangential wave at the 90° location is t = 0 to $0.95*\tau_{180}$. **b.** The time partition used to examine the arriving radial wave at the 180° location is t = 0 to $1.9*\tau_{90}$.

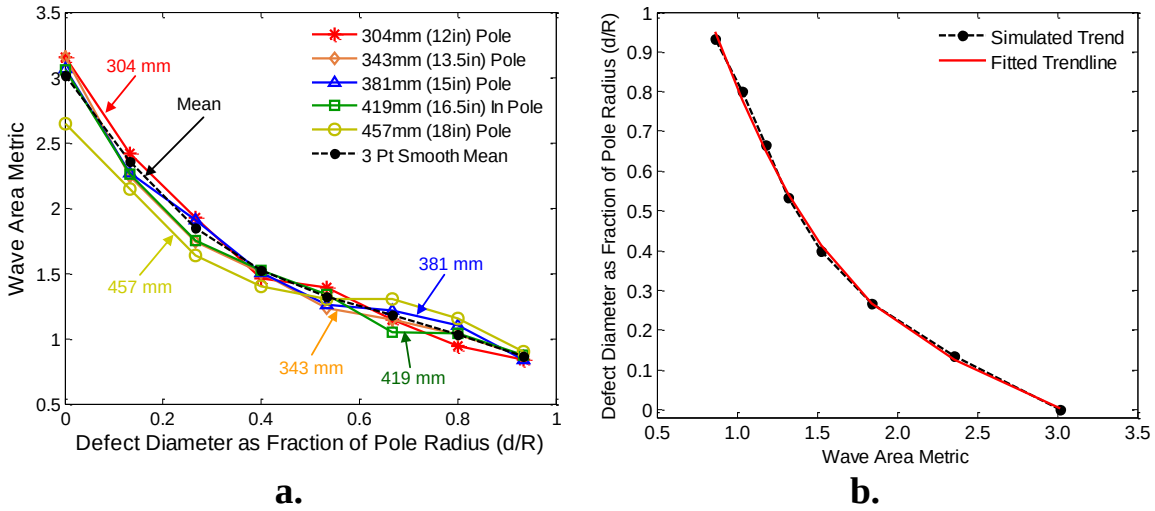


**Figure 85.** Wave area metric versus the defect size. **a.** The wave area metric is defined by Equation 62 and is plotted against the defect diameter, d, expressed as a fraction of the pole radius, R. **b.** Trend line fitted to simulation data (Polynomial in Table 18, $r^2$ 0.9982).

Figure 85a shows the wave area metric, $R_P$, for each of the five cross-sections versus the diameter of the center defect expressed as a fraction of the pole radius. A mean of the values for each defect size is subjected to a three point smoothing routine and is also shown. The value of wave area metric decreases as the diameter of the defect increases. The rate of change of the wave area metric is higher for smaller defects than

larger defects, indicating that this metric may be effective in identifying small internal defects. Figure 85b shows the simulated trend between wave area metric and the defect size. The simulated trend line shown in Figure 85b is the smoothed mean line shown in Figure 85a. The abscissa and ordinate are switched in Figure 85b. The simulated trend line is fitted to a third order polynomial. The polynomial relates the wave area metric to the defect size. The fitted trend line is shown in Figure 85b ($r^2$ 0.9982), and the coefficients of the polynomial are given in Table 18.

#### 4.3.3.2. Time centroid metric

In this section, the defect size is estimated through the use of fractional differences of time centroids. As previously stated, this metric is referred to as the time centroid metric. There are two different time centroids examined in this section, the area time centroid, $T_A$, and the energy time centroid, $T_E$.

The area time centroid represents the time at which most of the signal content has arrived at the receiver. The area moment is the first moment of the rectified acceleration signal with respect to time divided by zeroth moment with respect to time. The formula for the area time centroid was given in Equation 5 (on page 47) and is reproduced here as Equation 63. For clarity, it should be noted that the value calculated in Equations 5 and 63 is typically referred to as simply time centroid; however, since multiple time based centroids are used in this report, the term area time centroid is used here.

$$T_A = \frac{\sum_{i=1}^{N} |A_i| t_i}{\sum_{i=1}^{N} |A_i|} \tag{63}$$

Where:
$T_A$ is the area time centroid
$A_i$ is the amplitude of the acceleration signal at time $t_i$.
t is the time

The energy time centroid represents the time at which most of the signal energy has arrived at the receiver. The energy time centroid is the first moment of the square of the acceleration signal with respect to time divided by the zeroth moment with respect to

time. It is similar to the area time centroid, but gives greater emphasis on large peaks within the signal. The formula for the energy time centroid, $T_E$, is given as Equation 64.

$$T_E = \frac{\sum_{i=1}^{N} A_i^2 t_i}{\sum_{i=1}^{N} A_i^2} \tag{64}$$

As previously mentioned, for any arbitrary time window, the time centroid of that window is dependent upon all of the values contained therein. As a result, it is sensitive to the interference phenomenon. The area time centroid and energy time centroid are calculated using the same data. Interference effects within the signal will affect both time centroids in the same manner, though not necessarily to the same extent as the . By using a difference value between the two time centroids, the effect of interference phenomenon upon the final metric is reduced.

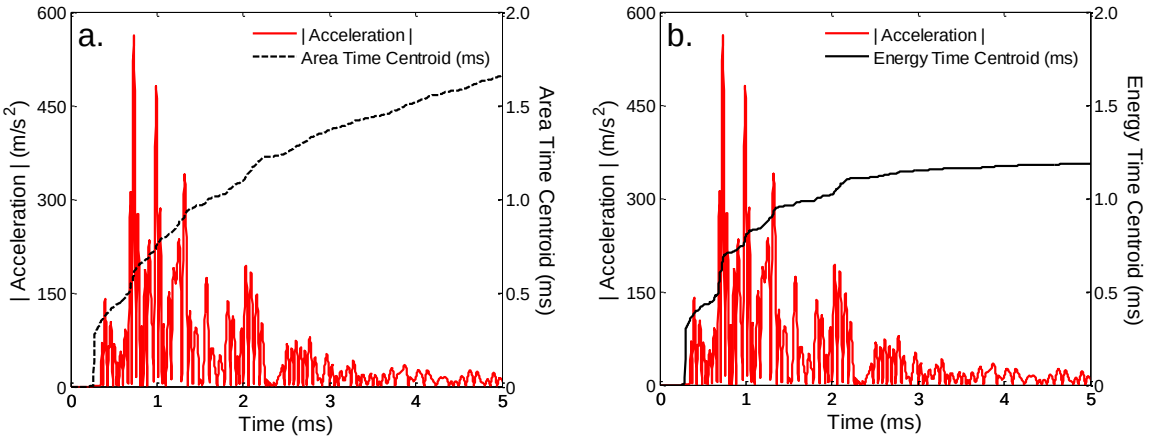


**Figure 86.** Time centroid and rectified acceleration versus time for a 381 mm (15 in) cross-section with no internal defect. In both figures, the rectified acceleration signal in shown in red. The associated time centroid curves shown in black are, **a.** area time centroid, **b.** energy time centroid.

Figure 86 shows the area and energy time centroids for each time step for a cross-section devoid of a defect. The data shown in the examples used in this section are from the simulation of a 381 mm (15 in) cross-section. The acceleration curves shown were recorded at the 180° location. Figure 86a shows the rectified acceleration signal and the area time centroid for each time step. Figure 86b shows the energy time centroid for each time step. At approximately 1.4 ms in Figure 86b, there is a change in the slope of the energy time centroid curve. At that point in time and thereafter, the energy of the signal

observed by the receiver is low compared to the energy of the signal prior to that time. The change is slope is observable in all of the energy time centroid curves. Internal defects cause the change in slope to shift later in time.

Figure 87 shows the area and energy time centroid curves. The metric examined in this section is depends upon the difference between the curves after they diverge. For many curve pairs, the divergence point is distinct and coincides with the last point at which the energy curve surpasses the area curve. However, in some cases, as demonstrated in Figure 87, the two curves remain relatively close in value for a period of time after their final intersection before noticeably diverging. A mean of two times was therefore used to estimate the time of divergence. The first point was the last point in time at which the energy curve surpassed the area curve. This point is the minimum divergence point. The second point located by projecting a line from the end of the energy curve to the area curve. The point of intersection was the maximum divergence point. The mean of the minimum and maximum divergence time is the time of divergence used to develop the time centroid metric.

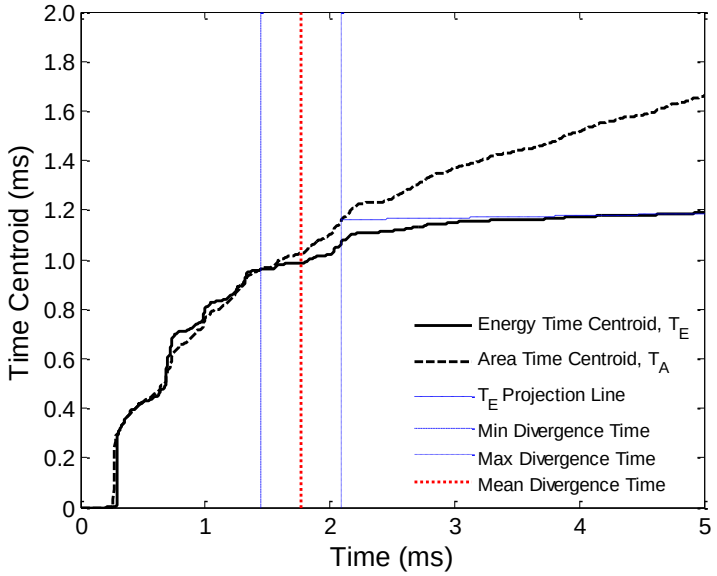


**Figure 87.** Determining point of divergence between time centroid plots. Energy time centroid ($T_E$) is the solid line; the area time centroid ($T_A$) is the dashed line. The mean divergence time is the men of the minimum and maximum divergence times. The data shown is for a 381 mm (15 in) cross-section with no internal defect.

Figure 88a shows the area and energy time centroid plots for no defect (black), a 76 mm (red) defect, and a 152 mm (blue) defect. As the size of the defect increases, the

time at which the value of the energy time centroid permanently falls below the value of the area time centroid increases. Figure 88b shows a close-up view of the plots within the time frame of 2.0 ms to 4.0 ms. Soon after the change in the slope occurs, the individual curves separate and become distinct. At that point, the defect size can be correlated to the difference between the centroid plot. The time chosen to take the difference measurement must be late enough in time such that any defect size likely to be encountered will have a measurable difference between the two curves. However, as the time increases the percentage change between the difference measurements for each defect size decreases and smaller defects become more difficult to identify. From examination of the simulation data, it was found that an appropriate time selection could be made using the time of the divergence as a guide. The time selected to make the difference measurement was 133% of the divergence time of the ±180° receiver. The largest divergence time observed among the simulations of the 381 mm (15 in) cross-sections was 2.831 ms; therefore, the measurement time was 3.774 ms.

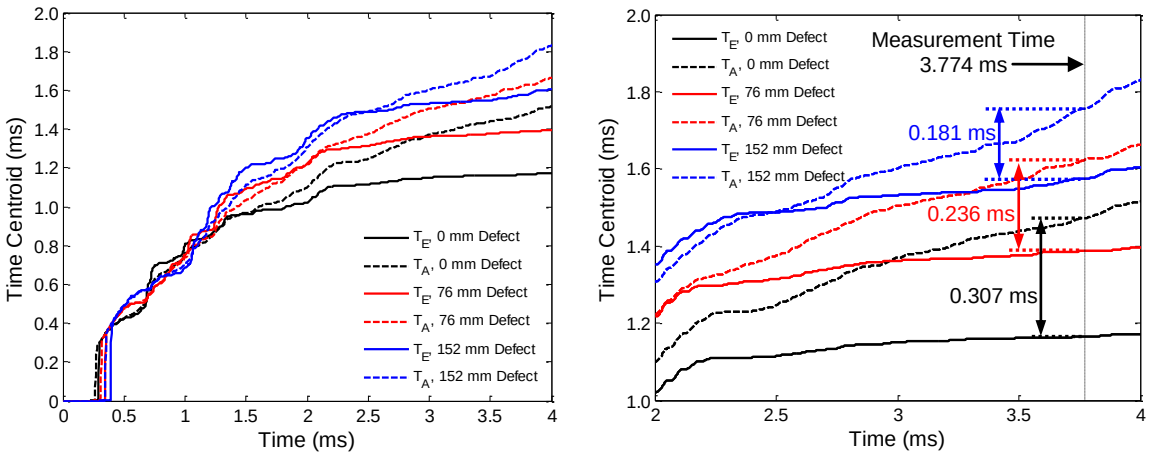


**Figure 88.** Time centroid differences by defect size. **a.** Energy time centroid, $T_E$, (solid) and area time centroid, $T_A$, (dashed) for a cross-section with defects sizes, 0 mm (no defect, black), 76 mm (red), and 152 mm (blue), **b.** close-up view of a. showing the time difference between the curves at time 3.774 ms.

The divergence time and measurement times for each simulated pole diameter is given in Table 13. Table 14 contains the area and energy time centroid values extracted from the simulation data for the 381 mm (15 in) cross-section at the aforementioned measurement time.

**Table 13.** Divergence and measurement times for simulated cross-sections of different diameters

| Simulated Cross Section Diameter | Divergence Time (ms) | Measurement Time (ms) |
|---|---|---|
| 304 mm (12 in) | 1.938 | 2.584 |
| 343 mm (13.5 in) | 2.236 | 2.982 |
| 381 mm (15 in) | 2.830 | 3.774 |
| 419 mm (16.5 in) | 3.144 | 4.192 |
| 457 mm (18 in) | 3.460 | 4.612 |

**Table 14**. Time centroid values from a 381 mm (15 in) cross-section with center defects. Time centroids include energy time centroid, $T_E$, and area time centroid, $T_A$.

| Defect Size | +90°* | | ±180° | |
|---|---|---|---|---|
| | $T_E$ | $T_A$ | $T_E$ | $T_A$ |
| 0 mm | 0.716 | 1.090 | 1.165 | 1.472 |
| 25 mm | 0.742 | 1.114 | 1.121 | 1.485 |
| 51 mm | 0.773 | 1.146 | 1.398 | 1.597 |
| 76 mm | 0.791 | 1.167 | 1.388 | 1.624 |
| 102 mm | 0.813 | 1.207 | 1.498 | 1.696 |
| 127 mm | 0.808 | 1.148 | 1.567 | 1.739 |
| 152 mm | 0.745 | 1.165 | 1.575 | 1.756 |
| 178 mm | 0.795 | 1.169 | 1.604 | 1.762 |

* Simulated cross-sections are symmetric; therefore the values of $T_E$ and $T_A$ at -90° are within 1% of the value at +90°

Table 15 contains the differences between the centroid values. The differences are then divided by the area time centroid values to reduce the effect of velocity variations between different pieces of wood and shown in Equation 65. The value, m, is the fractional difference between centroid and is called centroid fraction. Table 15 also contains the ratio of the time centroid fractions, which is used to estimate the defect size and is the metric referred to as the time centroid metric.

$$m = \frac{T_A - T_E}{T_A} \tag{65}$$

Figure 89a shows the time centroid metrics for the five simulated cross-sections versus the diameter of the center defect expressed as a fraction of the pole radius. At each defect size the mean of the five values obtained from the five cross-sections is taken. The mean values are then smoothed using a three point smoothing routine. The simulated trend line shown in Figure 89b is the smoothed mean line shown in Figure 89a.

The abscissa and ordinate are switched in Figure 89b. The simulated trend line is fitted to a third order polynomial. The polynomial relates the time centroid metric to the defect size. The fitted trend line is shown in Figure 89b ($r^2$ 0.9982), and the coefficients of the polynomial are given in Table 18.

**Table 15**. Centroid fractions and time centroid metrics for a 381 mm (15 in) cross-section.

| Defect Size | +90°* | | ±180° | | $\frac{m_{\pm180}}{m_{+90}}$ |
|---|---|---|---|---|---|
| | $T_A - T_E$ | $m_{+90}$ | $T_A - T_E$ | $m_{\pm180}$ | |
| 0 mm | 0.374 | 0.343 | 0.307 | 0.209 | 0.609 |
| 25 mm | 0.371 | 0.333 | 0.275 | 0.185 | 0.556 |
| 51 mm | 0.372 | 0.325 | 0.199 | 0.125 | 0.383 |
| 76 mm | 0.377 | 0.323 | 0.236 | 0.145 | 0.451 |
| 102 mm | 0.393 | 0.326 | 0.198 | 0.117 | 0.357 |
| 127 mm | 0.340 | 0.296 | 0.173 | 0.099 | 0.335 |
| 152 mm | 0.390 | 0.335 | 0.181 | 0.102 | 0.308 |
| 178 mm | 0.373 | 0.320 | 0.157 | 0.089 | 0.279 |

* Simulated cross-sections are symmetric; therefore the values of $T_E$, $T_A$, and m at -90° are within 1% of the value at +90°
$T_A$ is the area time centroid defined by Equation 63 on page 146
$T_E$ is the energy time centroid defined by Equation 64 on page 147

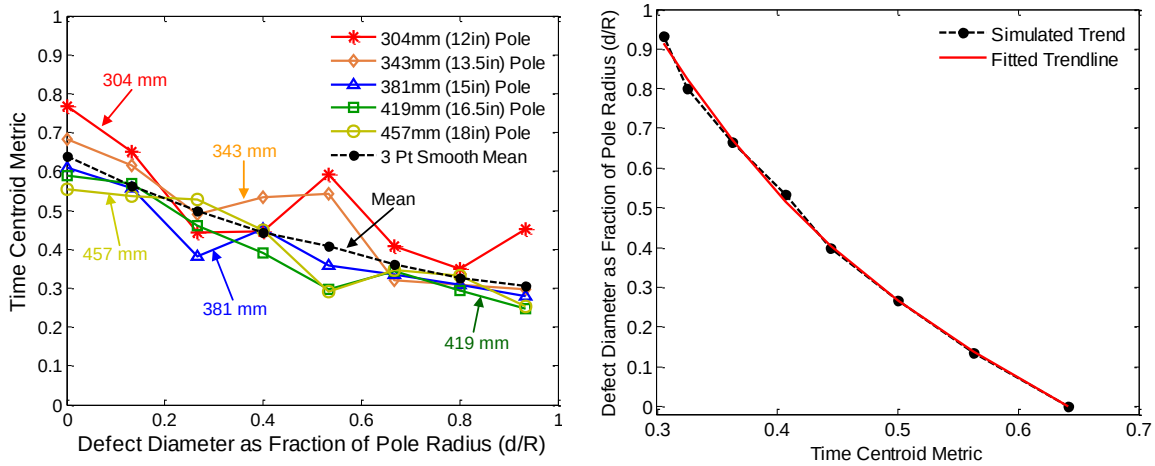


**a.** **b.**

**Figure 89.** Time centroid metric versus the defect size. **a.** The time centroid metric is the ratio of the centroid fractions, m, defined in Equation 65. The time centroid metrics are listed in Table 15, and is plotted against the defect diameter, d, expressed as a fraction of the pole radius, R. **b.** Trend line fitted to simulation data (Polynomial in Table 18, $r^2$ 0.9982).

As the diameter of the center defect increases, the time centroid metric decreases. As expected, the individual curves present some jaggedness as a result of interference phenomenon. Consider, for example, the value for the 304 mm (12 in) cross-section for a

defect diameter that is 53% of the pole radius shown in Figure 89a. There is a large difference between both the value just before (at 40%) and the value just after (at 67%). For that cross-section, the shear wave traveling radially encounters the center defect and begins to travel circumferentially around it. While traveling around the defect, a radial wave is excited through mode conversion at the wood / air boundary of the defect. That excited radial wave arrives at the 90° location just as the tangentially traveling shear wave arrives; however, the radial wave is out of phase with the arriving shear wave and results in destructive interference. The centroid fraction at the 90° location, $m_{90}$, decreases, but the centroid fraction at the 180° location, $m_{180}$, is unchanged. Since the centroid fraction from the 90° location is the denominator of the ratio, the time centroid metric increases. By taking the mean of the values across all of the simulated cross-sections, the overall effect of interference phenomenon on the mean trend line was reduced.

#### 4.3.3.3. Time of flight metric

In this section, the time of flight (ToF) is used to identify the general location of the defect in the cross-section. The predicted wave motion across a wood pole allows an observer to make conclusions regarding the position of a defect by comparing the ToF values around the circumference of the utility pole. A description of the wave motion of the radially and tangentially traveling dilatational waves can be found in Section 4.3.3.1.

The ToF of the waves at 90° or 270° and the 180° locations are used to approximate the tangential and radial velocities, respectively. It is assumed that the relationship between velocity, density, and stiffness obeys Equation 41 (page 112). The ratios of those velocities should approach a nominal ratio that can be obtained from published sources [10]. Note that the ToF ratio of 90° to 270° requires no additional calculations as both wavefronts would be traveling at the tangential velocity and traveling the same (assumed) distance.

Equation 66 is the velocity ratio between the radial and tangential velocities, $R_v$, as a function of the radial and tangential time of flight values, $\tau_r$ and $\tau_t$, respectively. It assumes a circular cross-section of diameter, D. If the calculation were performed on an actual pole, then the radial travel distance, $D_r$, and the tangential travel distance, $D_t$, may

be approximated independently of each other. As a result of taking the ratio of the velocities, the metric becomes independent of the pole diameter.

$$R_v = \frac{v_t}{v_r} = \frac{D_t / \tau_t}{D_r / \tau_r} = \frac{\pi D / 4\tau_t}{D / \tau_r} = \frac{\tau_r}{\tau_t}\frac{\pi}{4} \tag{66}$$

Where:
$R_v$ is the ratio of tangential velocity to radial velocity
$v_t$ and $v_r$ are the tangential and radial velocities, respectively
$D_t$ and $D_r$ are the tangential and radial travel distances, respectively
$\tau_t$ and $\tau_r$ are the tangential and radial times of flight, respectively
D is the diameter of the cross-section

Equation 67 shows the calculation of the nominal velocity ratio based upon published values of the radial and tangential stiffnesses, $E_r$ and $E_t$, respectively. Forest Products Laboratory [10] provides ratios between the longitudinal stiffness, $E_l$, and $E_r$ and $E_t$. The stiffness values used in the simulation are derived from wave velocity values through loblolly pine. The utility poles are Douglas-fir. Both nominal ratios are presented in Table 16.

$$R_v^N = \left[\frac{v_t}{v_r}\right]^N = \sqrt{\frac{\rho v_t^2}{\rho v_r^2}} = \sqrt{\frac{E_t}{E_r}} = \sqrt{\left[\frac{E_t}{E_l}\right]^N \left[\frac{E_l}{E_r}\right]^N} \tag{67}$$

Where:
$^N$ is the nominal values from published sources
ρ is the average cross-sectional density
$E_t$, $E_r$, and $E_l$ are the tangential, radial, and longitudinal elastic moduli, respectively. The ratios of $E_t$ to $E_l$ and $E_r$ to $E_l$ are supplied by Forest Products Laboratory [10]

**Table 16.** Stiffness ratios for loblolly pine and Douglas-fir

| Wood Species | $\frac{E_r}{E_l}$ | $\frac{E_t}{E_l}$ | $\frac{E_t}{E_l}\frac{E_l}{E_r} = \frac{E_t}{E_r}$ | $k_v = \frac{\pi}{4}\sqrt{\frac{E_r}{E_t}}$ |
|---|---|---|---|---|
| Loblolly Pine | 0.113 | 0.078 | 0.690 | 0.946 |
| Douglas-fir | 0.068 | 0.050 | 0.735 | 0.916 |

Equation 68 is the ratio formed by the radial and tangential times of flight normalized by the nominal ratio from published stiffness values. In this form, the value

of $R_{ToF}$ approaches one for a sound piece of wood free of defects. The value of $R_{ToF}$ depends only upon times of flight and is referred to as the time of flight metric.

$$R_{ToF} = \frac{R_v}{R_v^N} = \frac{\tau_r}{\tau_t}\frac{\pi}{4}\sqrt{\frac{E_r}{E_t}} = \frac{\tau_r}{\tau_t}k_v \tag{68}$$

It is well established that the speed of waves traveling through decayed wood is less than the wave speed traveling through sound wood. By comparing the time of flight metric between the three receiver locations, the general region of the defect within the cross-section is identified. Figure 90 shows a schematic of the defect regions based upon a 76 mm (3 in) defect. The defect sizes affect the sizes and shapes of the defect regions. Those effects are discussed later in this section. Table 17 gives the combination of time of flight metrics that indicate a defect in a particular defect region.

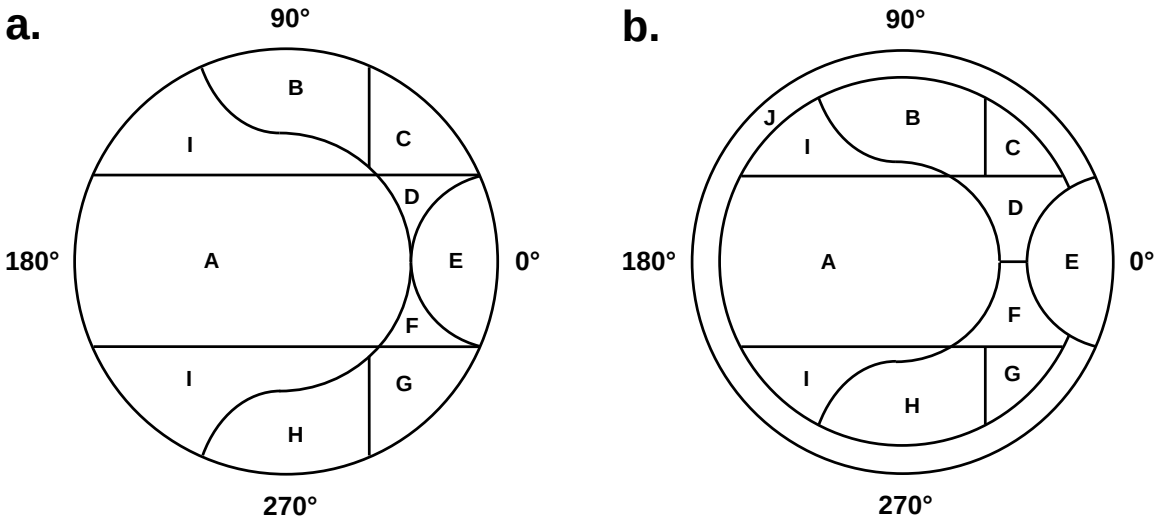


**Figure 90.** Defect regions within the utility pole cross-section. Regions are identified by a letter A through J. The time of flight metric can be used to place the defect within a particular region in accordance with Table 17. The figures assumes a 76.2 mm diameter defect and an input source at 0°. **a.** Regions assuming no surface cracks. **b.** Regions assuming 25 mm surface cracks (region J).

Figure 90a shows the defect regions for a utility pole that has no surface cracks. The configuration of the defect regions as shown in Figure 90 assumes an input source at 0°. If the source were located at 90°, then the figure would need to be rotated counterclockwise by 90°. The figure must be rotated such that region E is at the source location.

**Table 17**. Time of flight metric sets identifying defect regions in Figure 90

| Regions | Time of Flight Metric | | |
|---|---|---|---|
| | $\frac{V_{+90}}{V_{\pm 180}} = \frac{\tau_{\pm 180}}{\tau_{+90}} k_v$ | $\frac{V_{-90}}{V_{\pm 180}} = \frac{\tau_{\pm 180}}{\tau_{-90}} k_v$ | $\frac{V_{+90}}{V_{-90}} = \frac{\tau_{-90}}{\tau_{+90}}$ |
| A | >1 | >1 | ≈1 |
| B | $<k_v$ | ≈1 | <1 |
| C | $\approx k_v$ | ≈1 | $\approx k_v$ |
| D | Unspecified | >1 | <1 |
| E | Unspecified | Unspecified | Unspecified |
| F | >1 | Unspecified | >1 |
| G | ≈1 | $\approx k_v$ | $\approx 1/k_v$ |
| H | ≈1 | $<k_v$ | >1 |
| I or No Rot | ≈1 | ≈1 | ≈1 |
| J* | — | — | — |

*Region J assumes existence of surface cracks. Defects in region J are the least likely to be identified using this technique.

$V_{+90}$, $V_{-90}$, and $V_{\pm 180}$ are wave velocities between the source and the receivers at +90°, -90°, and ±180° from the source.

The general location of the defect is determined by the relationship between the time of flight metrics. For example purposes, assume a defect is in region A. The ToF between 0° and 180° would be increased but the times to 90° and 270° would be unchanged. In that scenario, the time of flight metric 180° to 90° and 180° to 270° would increase above one while the ratio 270° to 90° would remain approximately one. In region F, the defect is blocking both the radial wave from traveling to the 180° location and the tangential wave from traveling to the 270° location. In that scenario, the ratios 180° to 90° and 270° to 90° would increase above a value of one, but the effect upon the ratio 180° to 270° is not defined. In region G, the defect blocks the tangential wave traveling to the 270° location, but the radial wave is unimpeded. In this scenario, the radial wave would travel to the center, excite a radial wave in all directions, and the excited radial wave would be the first wave to arrive at the 270° location. The ratio 180° to 90° would be unchanged, the ratio 180° to 270° would approach the $k_v$ value from Table 16, and the 270° to 90° would approach $1/k_v$. In region H, both the tangential wave and the excited radial wave are blocked from arriving at the 270° location. In this scenario, the ratio 180° to 90° is unchanged, the ratio 180° to 270° is reduced below $k_v$,

and the ratio 270° to 90° is increased. In region E, the source is close to the defect. In this scenario, the effect on the ratios is unknown; however, region E is close to the surface of the pole and likely to be discovered through traditional inspection methods. The pole is symmetric; therefore, the explanations above are true for the regions B, C, and D.

Defects in region I produce no changes in the time of flight metric, as the defect would not interrupt the direct path of travel between source and receivers. All of the ratios would approach a value of one. In a defect free cross-section, the ratios would approach values of one as well. While this metric alone would be unable to identify defects in region I, the presence of the defects should still be identified using the other metrics described here. Also, conducting a second set of tests, where the source is placed at the 90°, 180°, or 270° location would eliminate one or more I regions.

Figure 90b shows the defect regions assuming a 76.2 mm (3 in) defect and 25 mm (1 inch) cracks around the circumference. As mentioned earlier, all of the utility poles possessed numerous shallow surface cracks. In this case, the defect regions are more compactly spaced. Regions F and D grow, and regions A, C, G, and I shrink. A new region, J, is formed. Region J is the area between the surface cracks at or just below the surface of the utility pole. A defect in region J will likely not be identified by any of the metrics presented here unless it happens to fall directly under one of the receivers.

The concern regarding the low probability of sensing defects in region J is mitigated by the fact that region J is composed of the portion of the utility pole that is both most resistant to fungal decay and easiest to inspect with current inspection methods. From CT scans, it was apparent that preservative penetration usually exceeded the length of the majority of the surface cracks, 25 mm. The proximity of region J to the surface make it ideal for defect identification using traditional inspection techniques, such as visual inspection and a pick test.

The shape and size of the defect regions change depending upon the size of the internal defect. As the defect size decreases several changes take place: region A narrows (in the 90° to 270° direction) and elongates (in the 0° to 180° direction), regions E, D, and F shrink, regions B and H shrink and narrow, and regions C, G, and I increase. The defect regions assuming a 50.8 mm (2 in) defect is shown in Figure 91a. As the

defect size increases: region A widens and shortens, regions E, D, and F grow, regions B and H grow and widen, and regions C, G, and I decrease. The defect regions assuming a 101.6 mm (4 in) defect is shown in Figure 91b.

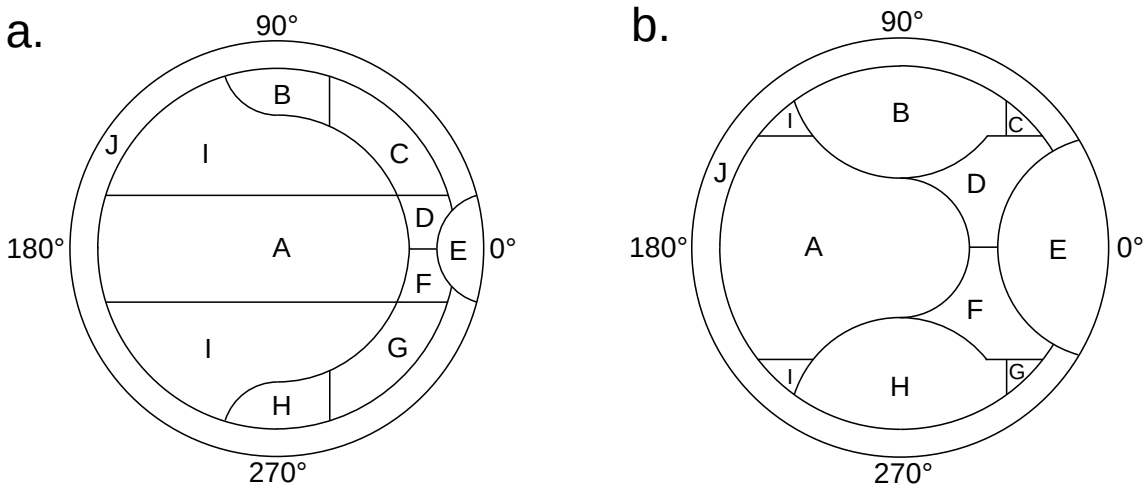


**Figure 91.** Changes in defect regions by size of defect, **a.** defect size of 50.8 mm (2 in), **b.** defect size of 101.6 mm (4 in)

The time of flight metric depends only upon the first arrival of the wavefronts; therefore there should be no interference effects within the curves. The small perturbations within the curves are a result of the sampling rate at which the simulation data is recorded (2 μs). There is a noticeable change in slope between the control cross-sections with no defects, and a cross-section that has a defect that is 0.13 of the pole radius. As shown in Figure 77a (on page 136), the presence of a center void causes a redirection of the wavefront. In the rot model used within the simulation, a dilatational wave traveling through sound wood in the radial direction is approximately 400 m/s faster than a dilatational wave traveling in the tangential direction (about 1400 m/s radial versus 1000 m/s tangential). In addition, the defect regions in the simulation are a voids surrounded by 25 mm (1 in) of rot. The presence of the rot decreases the speed waves traveling through it. For a tangential wave, a decrease from 1000 m/s down to 900 m/s is not uncommon in the simulation. Therefore, the center defect combines several factors that increase the travel time of the wave from the source to the 180° location: increased travel distance, tangential waves are slower than radial waves, and the presence of rot further decreases wave speed. For the smallest simulated defect (defect size 0.13 of the

pole radius), the time of travel within the defect region is approximately 38% of the entire time of flight. For the second smallest simulated defect (defect size of 0.27 of the pole radius), the total travel time within the defect region is approximately 47% of the entire time of flight. Presence of the defect quickly becomes the dominant factor in the wave travel time even though the overall area of the defect is small in comparison to the area of the pole cross-section.

The time of flight metric is also usable to estimate internal defect size. If a center defect exists, then the arrival time of the radial wave at the 180° location is delayed. Figure 92a shows the plot of the time of flight metric versus the defect diameter as a fraction of the pole radius. At each defect fraction size, the mean of all of the values across all of the pole diameters is calculated. The mean values are then smoothed using a three point smoothing routine. The simulated trend line shown in Figure 92b is the smoothed mean line shown in Figure 92a. The abscissa and ordinate are switched in Figure 92b. The simulated trend line is fitted to a third order polynomial. The polynomial relates the time of flight metric to the defect size. The fitted trend line is shown in Figure 92b ($r^2$ 0.9996), and the coefficients of the polynomial are given in Table 18.

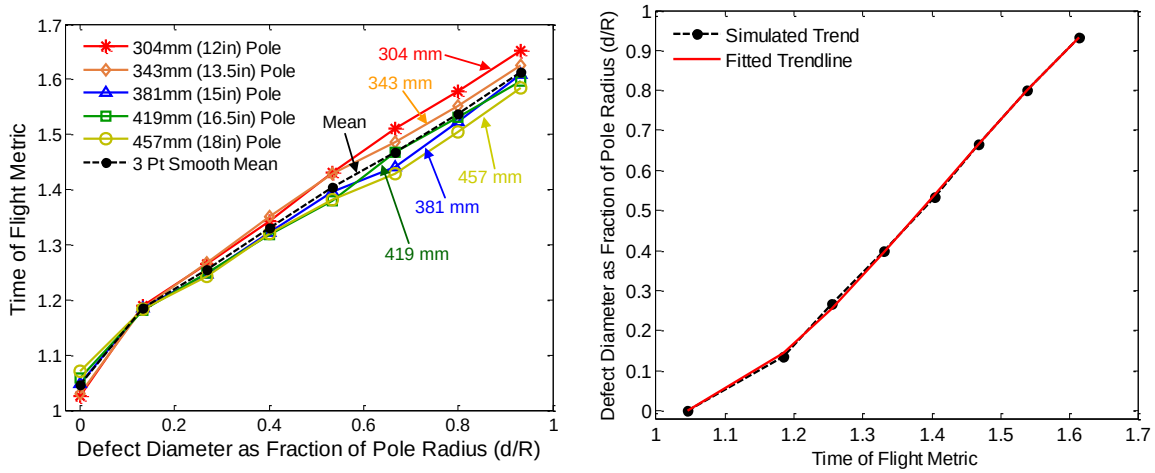


**Figure 92.** Time of flight metric versus size of defect. **a.** The time of flights (ToF) of the arriving wavefront are multiplied by the factor $k_v$ (as shown in Table 16 and described in Equations 68). Defect diameter, d, is expressed as a fraction of the pole radius, R. **b.** Trend line fitted to simulation data (Polynomial in Table 18, $r^2$ 0.9996)

### 4.3.4. Estimating defect size from metrics

The results of the three metrics developed in previous sections were used in combination with each other to estimate the defect size within the cross-section. Two different approaches were attempted to obtain a single estimate. A multivariable regression technique was employed to relate the metrics to the defect size. The other approach was to collect the defect size estimates from the individual metrics and use the root means square (RMS) of those values to obtain a combined estimate for that particular pole test. The mean of the pole test estimates was the final defect size estimate.

An attempt was made to use multivariable regression to create a polynomial that would relate the three metrics to a single defect size. The variability between the utility pole cross-sections and the simulated cross-sections prevented the creation of a unifying polynomial. The relationship between the time of flight metric and the defect size is close to linear for the range shown. For this reason, polynomials created using the simulated relationships place great weight on the time of flight metric. In reality, the ToF metric is very sensitive to the position of the defect within the cross-section. The change in position of the defect from the center of the pole, as it was in the simulations, to other locations in the cross-section, as was the case for the utility pole specimens, caused the time of flight metric to skew the final polynomial value.

An attempt was then made to create a polynomial based upon only the time centroid metric and the wave area metric. First, second, and third order polynomials were examined. It quickly became apparent that the inclusion of terms within the polynomial that depended upon both metrics, at best, had no effect on the accuracy and precision of the final values, and at worst, slightly decreased accuracy and greatly reduced precision. The most accurate and precise polynomials excluded terms any term that depended upon both metrics and were simply weighted sums of monovariable equations. Furthermore, the estimation of the defect in Pole 477 was underestimated regardless of the polynomial examined. Percentage error for the estimate of Pole 477 using multivariable polynomials ranged from just over 33% to over 90%.

A second method of determining a final estimation of the internal defect size from the individual metric estimates was to use the RMS of the values. In this technique, each metric was used to estimate the defect size using the single variable polynomials. All

three metrics were then plotted in a three dimensional space. Values near the origin indicated cross-sections free of internal defects. As the distance from the origin increased, the estimated size of the internal defect increased.

In the previous sections, simulated data was used to extract several metrics which were plotted as functions of the internal defect size. From those plots, trends relating defect sizes to the metrics were developed. The smoothed mean line from each of the metrics was inverted to express defect size as the dependent variable and the metrics as independent variables. The inverted smoothed mean lines were then fitted to a third order polynomial. The coefficients of the polynomials for each metric are shown in Table 18.

**Table 18**. Coefficients of fitted polynomials relating metrics to defect size

$$\frac{d}{R} = a_3 x^3 + a_2 x^2 + a_1 x + a_0$$

| Metric | $a_3$ | $a_2$ | $a_1$ | $a_0$ | $r^2$ |
|---|---|---|---|---|---|
| Wave area | -0.0959 | 0.7666 | -2.2205 | 2.3580 | 0.9982 |
| Time centroid | -9.2417 | 17.6342 | -12.9509 | 34871 | 0.9982 |
| Time of flight | -3.4122 | 14.4954 | -18.5289 | 7.4246 | 0.9996 |

d/R is the defect diameter expressed as a fraction of the pole radius
x is the value of the metric

Each of the 40 simulations (five pole diameters, each with seven defect sizes and a control cross-section) yielded three metrics. Using the polynomials shown in Table 18, each metrics was used to estimate the size of the internal defect. The defect size estimations for each simulation are shown in Figure 93. The location of each data point within the three dimensional space is determined by the three defect estimates. Each axis of Figure 93 is a defect size estimated using a different metric. Figure 94 shows the same three dimensional space; however the data points shown are the simulated trends from Figures 85b, 89b, and 92b. For clarity of explanation, the procedure for combining the defect size results for all three metrics into a single estimate is performed upon the simulated trend data.

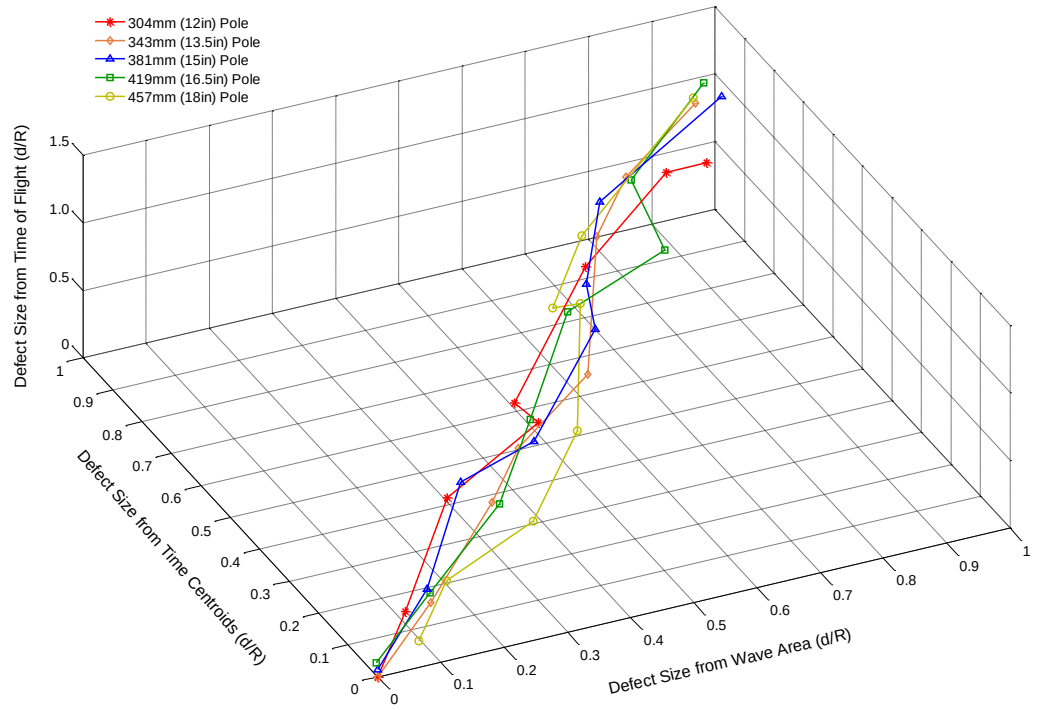


**Figure 93.** Defect estimates from all simulations plotted in three dimensional space. The defect diameter, d, is expressed as a fraction of the pole radius, R.

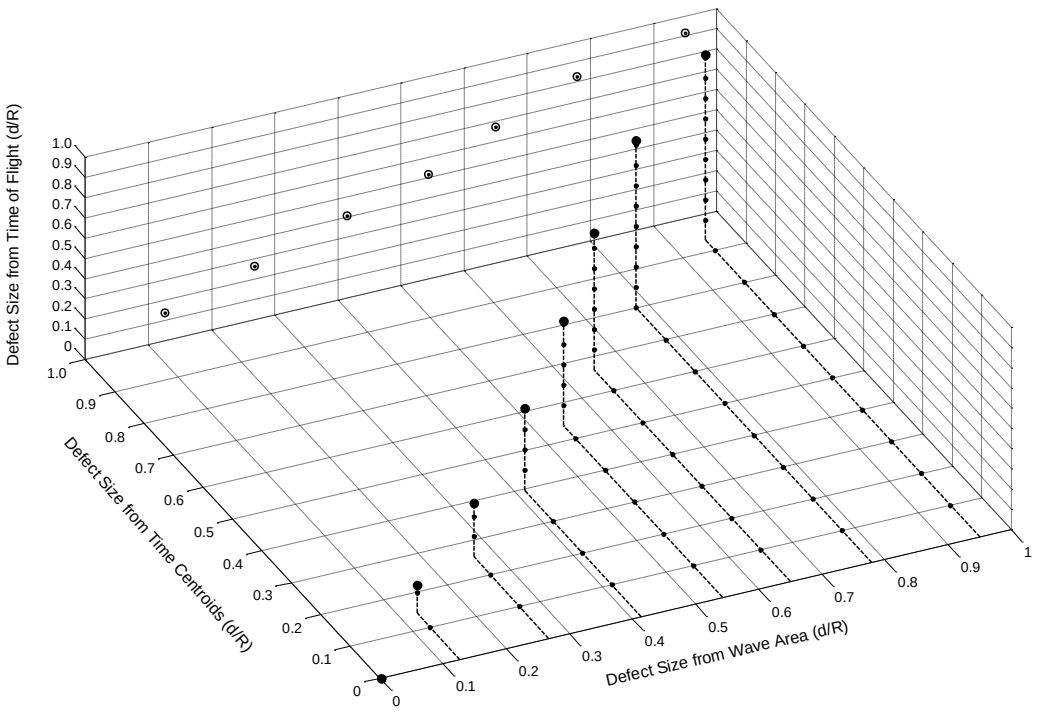


**Figure 94.** Defect estimates for the simulated trend data from Figures 85b, 89b, and 92b plotted in three dimensional space. The defect diameter, d, is expressed as a fraction of the pole radius, R. The dotted circles shown are the projection of the estimates into a two dimensional space and are to aid the viewer in identifying the defect size estimated from the time of flight metric.

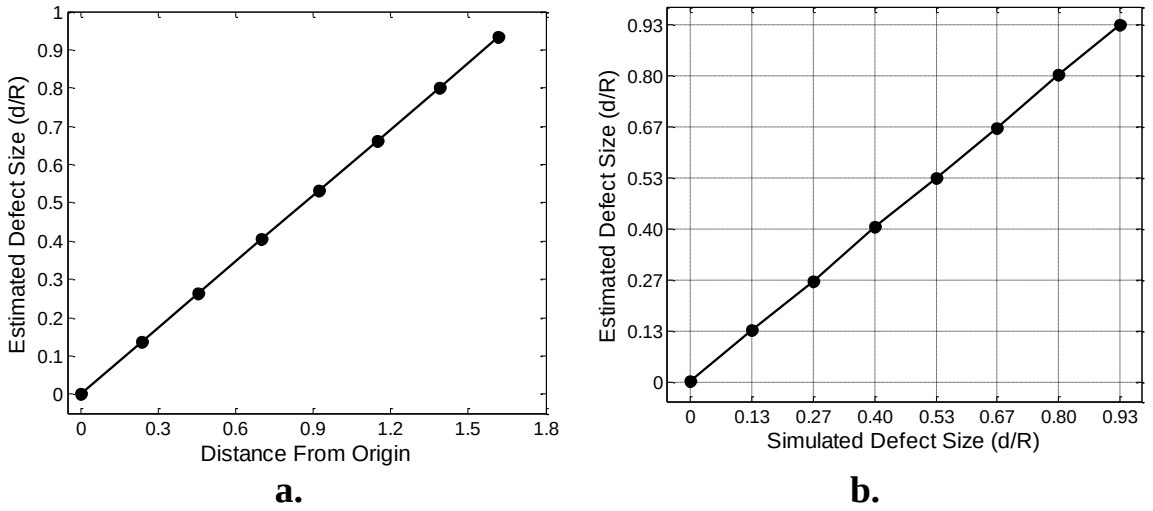


**Figure 95.** Estimated defect sizes of the simulated trend **a.** The estimated defect size is the distance from the origin in Figure 94 divided by the square root of three. **b.** Comparison of the estimated defect size to the simulated defect size. Estimates are accurate to within 4.2%.

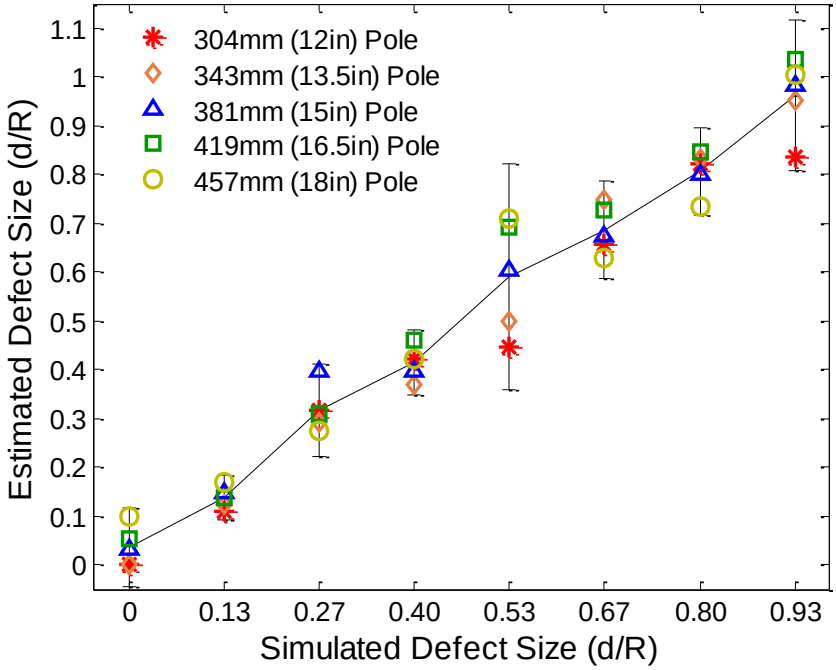


**Figure 96.** Estimated defect sizes of simulated poles. The estimated defect size for each pole test for each defect size is shown. The error bars represent two standard deviations of the estimated defect size for each simulated defect size.

The distance each data point in Figure 95a is from the origin is then used to determine the final defect size estimate. The estimated defect size shown in Figure 95a is the root mean square of the three defect size estimates from the metrics, which is equivalent to the distance from the origin in Figure 94 divided by the square root of three. In Figure 95b, the estimated defect size is then compared to the defect size implemented

within the simulations. The estimated defect sizes are within 4.2% of the simulated defect sizes. In Figure 96, the estimated defect sizes for each simulated pole cross section are shown. The error bars represent two standard deviations of the estimated defect size for each simulated defect size.

### 4.4. Validating Estimates of Defect Size and Location

In this section, data extracted from tests performed upon the utility pole specimens will be examined using the developed metrics and the size of the internal defects will be estimated.

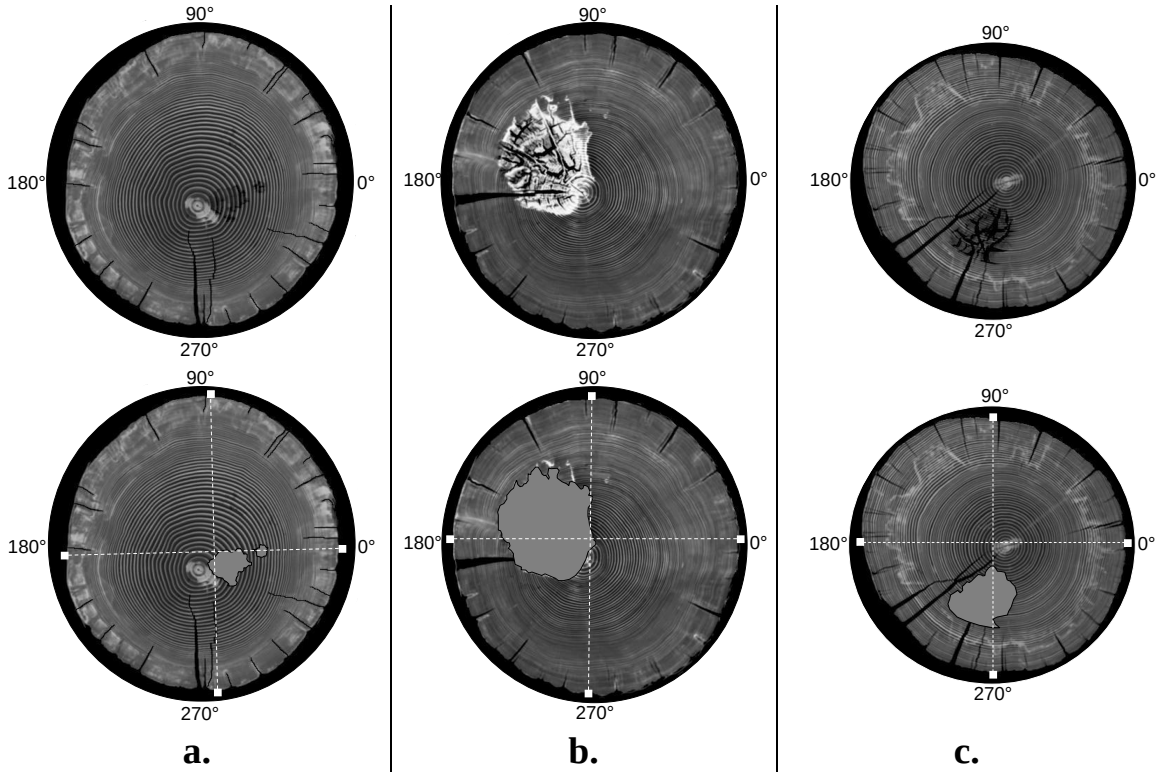


**Figure 97.** Utility pole cross-sections. **a.** Pole 966, **b.** Pole 491, **c.** Pole 477. The top row contains the CT scans. The bottom row shows the decayed regions as hatched areas, and white squares indicate actual positions of the transducers during testing.

Four utility pole specimens were received for testing. Table 7 on page 104 contains the information about the individual poles. Examination of CT scans revealed that Pole 242 had multiple deep cracks extending from the pole surface to the center of the pole. The number and depth of the cracks would cause large portions of the pole cross-section to be isolated from waves traveling from a source location. As a result,

pole 242 was excluded from the test specimens analyzed in this report. Poles 966, 491, and 477 were included in the study.

Each utility pole was identified with either a metal plate with an identifying number or a number written on the end of the pole with a grease pen. The identifying mark was arbitrarily assigned to the 90° location on the pole and the direction of increasing angle was assigned to be counter-clockwise in the CT images. The cross-sections examined and transducer locations are shown in Figure 97.

Seven tests were conducted on the utility pole specimens. Each cross-section was tested twice with the source placed at the 0° location for one test and the 90° location for the other. Pole 966 was tested a third time with the source at the 180° location on the pole. Tests were designated by pole number and a letter representing the source location. The suffix letters Z, N, and R represented sources located at 0°, 90°, and 180°, respectively.

### 4.4.1. Estimating defect sizes and locations in utility pole specimens

The first validation to be performed uses the time of flight metric and identifies the general location of the defect in the cross-section. Using the time of flight metrics sets shown in Table 17, and the regions as defined in Figures 90 and 91, the location of the defect can be approximated. Pole test 966Z has a region of decay that would normally be predicted to be in region A; however, the deep crack at approximately 330° may compact the internal regions and place the defect in region F. In pole test 966N, the defect region diagram in Figure 90 must be rotated counterclockwise such that region E is placed at the source location of 90°. As a result of the relocated source, the decay is predicted to be located in region A. The defect is also predicted to be in region A when the source was placed at 180° for pole test 966R. In pole test 491Z, the defect is clearly predicted to be in region A; however, for pole test 491N, the defect is predicted to be in either region D or B. In pole test 477Z the defect is predicted to be in region A or H. In pole test 477N, the defect region is predicted to be in region A. Table 19 contains the times of flight obtained from each pole and the associated time of flight metric sets and predicted defect regions. The defect locations predicted using the time of flight metric sets agreed with the locations of the defect regions identified in the utility pole CT scans.

**Table 19**. Time of flight metrics from utility poles and predicted defect regions

| Pole Test | Times of Flight (ms) | | | Time of Flight Metrics | | | Defect Region |
|---|---|---|---|---|---|---|---|
| | +90° | ±180° | -90° | $\frac{\tau_{\pm 180}}{\tau_{+90}} k_v$ | $\frac{\tau_{\pm 180}}{\tau_{-90}} k_v$ | $\frac{\tau_{-90}}{\tau_{+90}}$ | |
| 966Z | 0.158 | 0.234 | 0.222 | 1.357 | 0.965 | 1.405 | F |
| 966N | 0.154 | 0.232 | 0.162 | 1.380 | 1.312 | 1.052 | A |
| 966R | 0.168 | 0.220 | 0.172 | 1.199 | 1.172 | 1.024 | A |
| 491Z | 0.150 | 0.216 | 0.162 | 1.319 | 1.221 | 1.080 | A |
| 491N | 0.200 | 0.242 | 0.154 | 1.108 | 1.439 | 0.770 | D |
| 477Z | 0.106 | 0.118 | 0.158 | 1.020 | 0.684 | 1.491 | H |
| 477N | 0.142 | 0.198 | 0.142 | 1.227 | 1.277 | 1.000 | A |

The metric values obtained are made non-dimensional by taking ratios. In some cases, the ratios obtained implied a cross-section with no defect within it. In those cases, the inverse of the ratio was also examined to determine if it fell within the range of values pertinent to the particular metric. Of the 42 metric values obtained from the pole tests, only five values implied a cross-section free of defects. Two of the values were from the time centroid metric, 966R (±180°/-90°) and 477N (±180°/-90°). Three values were from the time of flight metric: 966Z (±180°/-90°), 477Z (±180°/+90°), and 477Z (±180°/-90°). Of the five values, only 477Z (±180°/-90°) had an inverse that fell within the pertinent metric range. The inverse of the other four values still implied a cross-section free of defects; therefore those four values were left unchanged. The value presented for 477Z (±180°/-90°) in Table 23 is the inverted value. The original value for 477Z (±180°/-90°) is presented in Table 19.

Table 20 contains a listing of each pole number and the associated the source location, the pole tests, and symbols of the ratios examined during testing. The values used to develop the ratios are obtained at particular locations around the pole. The locations described within the ratios are relative to the source location. A value obtained from the ±180° location is 180° from the source location. Assuming the source was located at 90°, the +90° location would be at 180°, the ±180° location would be at 270°, and the -90° location would be at 0°. The symbol colors red, blue, and green designate values obtained from poles 966, 491, and 477, respectively.

**Table 20.** Pole Tests, Symbols, and Defect Sizes

| Pole | Source Location | Pole Test | Ratio Symbols* ±180°/+90° | Ratio Symbols* ±180°/-90° | Defect Size From CT Scans (d/R)# Minor Axis | Defect Size From CT Scans (d/R)# Major Axis |
|---|---|---|---|---|---|---|
| 966 | 0° | 966Z | ◀ | ◁ | 0.295 | 0.461 |
| 966 | 90° | 966N | ▼ | ▽ | | |
| 966 | 180° | 966R | ▶ | ▷ | | |
| 491 | 0° | 491Z | ■ | □ | 0.625 | 0.700 |
| 491 | 90° | 491N | ◆ | ◇ | | |
| 477 | 0° | 477Z | ● | ○ | 0.364 | 0.521 |
| 477 | 90° | 477N | ★ | ☆ | | |

Pole Test suffixes Z, N, and R, indicate the source is at the 0°, 90°, 180° locations of the pole, respectively
* Ratio angles are relative to the source location (i.e. ±180° from a 90° source location is the 270° location on the pole)
Colors red, blue, and green designate values from poles 966, 491, and 477, respectively.
# Defects are assumed to have a generally elliptical shape with major and minor axes.

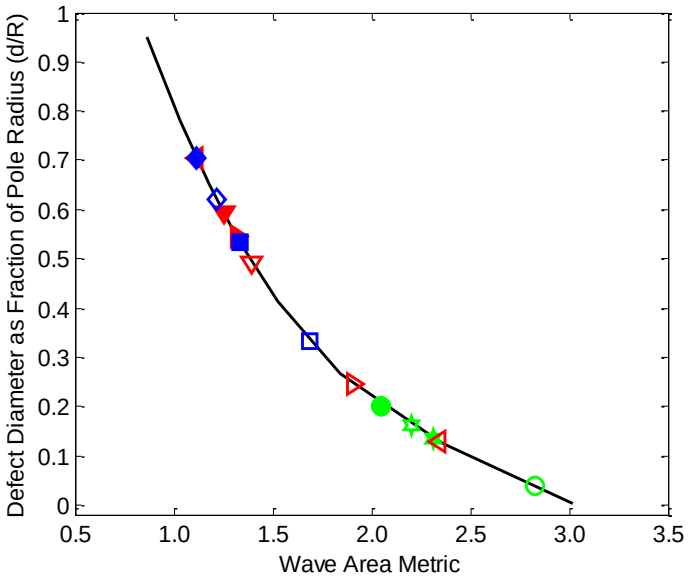


**Figure 98.** Defect size estimated from wave area metric, Values obtained from utility pole specimens. Symbols are defined in Table 20 (Page 166). Values of d/R are given in Table 21.

The wave area metrics and associated defect size estimates for each pole test is shown in Figure 98. The mean and standard deviation for the values for Pole 966 (red symbols) are 0.451 and 0.219, respectively. For the values of Pole 491 (blue symbols), the mean and standard deviation are 0.547 and 0.159, respectively. For the values of Pole 477 (green symbols), the mean and standard deviation are 0.134 and 0.069, respectively.

Individually, the wave area metric correctly estimates the size of the defect in Pole 966 and underestimates the defect sizes in Poles 491 and 477 making it the second most accurate individual metric examined. The standard deviations are the smallest of all three metrics indicating that the wave area metric is the most precise of the examined metrics. The wave area metric values and associated defect size estimates shown in Figure 98 are given in Table 21 alongside the respective symbols.

**Table 21.** Defect sizes estimated from wave area metric

| Pole Test | $\frac{\pm 180^o}{+90^o}$ Ratio | | | $\frac{\pm 180^o}{-90^o}$ Ratio | | |
|---|---|---|---|---|---|---|
| | Symbol | Wave Area Metric | d/R | Symbol | Wave Area Metric | d/R |
| 966Z | ◀ | 1.113 | 0.704 | ◁ | 2.345 | 0.129 |
| 966N | ▼ | 1.251 | 0.592 | ▽ | 1.394 | 0.492 |
| 966R | ▶ | 1.317 | 0.544 | ▷ | 1.912 | 0.244 |
| 491Z | ■ | 1.333 | 0.533 | □ | 1.687 | 0.333 |
| 491N | ◆ | 1.114 | 0.704 | ◇ | 1.215 | 0.620 |
| 477Z | ● | 2.049 | 0.201 | ○ | 2.831 | 0.039 |
| 477N | ★ | 2.315 | 0.136 | ☆ | 2.202 | 0.161 |

Test Designations and Symbols defined in Table 20 (Page 166).
d/R is the defect diameter, d, expressed as a fraction of the pole radius, R

The time centroid metric and associated defect size estimates for each pole test is shown in Figure 99. The mean and standard deviation for the values for Pole 966 (red symbols) are 0.417 and 0.388, respectively. For the values of Pole 491 (blue symbols), the mean and standard deviation are 0.794 and 0.263, respectively. For the values of Pole 477 (green symbols), the mean and standard deviation are 0.407 and 0.288, respectively. The time centroid metric correctly estimates the sizes of the defects in Poles 966 and 477 and overestimates the defect size in Pole 491, making it the most accurate of the examined metrics. The standard deviations are the largest of all three metrics indicating that the time centroid metric is also the least precise of the three metrics. The time centroid metric values and associated defect size estimates shown in Figure 99 are given in Table 22 alongside the respective symbols. Metric values that resulted in d/R values

less than zero were assigned values of zero. The assumption being that a negative defect size has no meaning and a defect size of zero implies a sound pole cross-section free of defects.

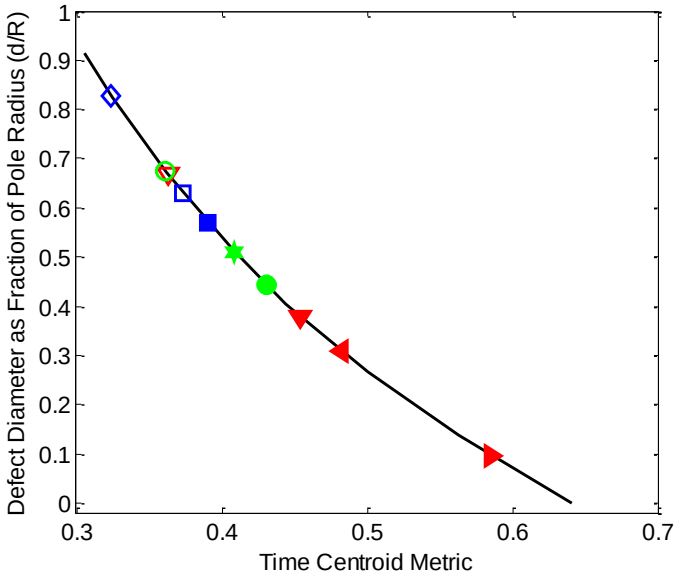


**Figure 99.** Defect size estimated from time centroid metric. Values obtained from utility pole specimens. Symbols are defined in Table 20 (Page 166). Values corresponding to symbols ◆ (d/R = 1.152) and ◁ (d/R = 1.049) are above the range shown. Values corresponding to symbols ▷ and ✡ are below the range shown and have d/R values of zero. Values of d/R are given in Table 22.

**Table 22.** Defect sizes estimated from time centroid metric

| Pole Test | $\frac{\pm 180^o}{+90^o}$ Ratio | | | $\frac{\pm 180^o}{-90^o}$ Ratio | | |
|---|---|---|---|---|---|---|
| | Symbol | Time Centroid Metric | d/R | Symbol | Time Centroid Metric | d/R |
| 966Z | ◀ | 0.482 | 0.308 | ◁ | 0.278 | 1.049 |
| 966N | ▼ | 0.454 | 0.378 | ▽ | 0.363 | 0.669 |
| 966R | ▶ | 0.585 | 0.096 | ▷ | 1.160 | 0* |
| 491Z | ■ | 0.390 | 0.569 | □ | 0.373 | 0.629 |
| 491N | ◆ | 0.260 | 1.152 | ◇ | 0.324 | 0.827 |
| 477Z | ● | 0.430 | 0.443 | ○ | 0.361 | 0.674 |
| 477N | ★ | 0.408 | 0.510 | ✡ | 0.723 | 0* |

Test Designations and Symbols defined in Table 20 (Page 166).
d/R is the defect diameter, d, expressed as a fraction of the pole radius, R
* The values of the defect sizes have a lower bound of zero

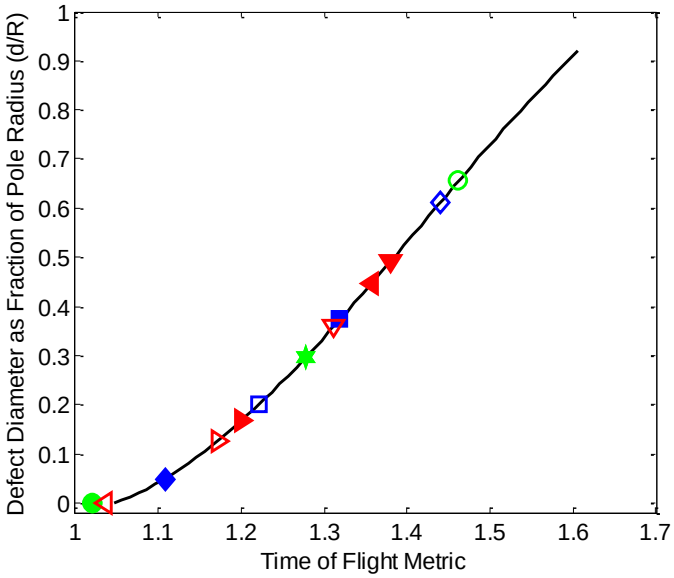


**Figure 100.** Defect size estimated from time of flight metric. Values obtained from utility pole specimens. Symbols are defined in Table 20 (Page 166). Values of d/R are given in Table 23.

**Table 23.** Defect sizes estimated from time of flight metric

| Pole Test | $\frac{\pm 180^o}{+90^o}$ Ratio | | | $\frac{\pm 180^o}{-90^o}$ Ratio | | |
|---|---|---|---|---|---|---|
| | Symbol | Time of Flight Metric | d/R | Symbol | Time of Flight Metric | d/R |
| 966Z | ◀ | 1.357 | 0.446 | ◁ | 1.036 | 0* |
| 966N | ▼ | 1.380 | 0.492 | ▽ | 1.312 | 0.360 |
| 966R | ▶ | 1.200 | 0.166 | ▷ | 1.172 | 0.126 |
| 491Z | ■ | 1.319 | 0.373 | □ | 1.221 | 0.200 |
| 491N | ◆ | 1.108 | 0.049 | ◇ | 1.439 | 0.611 |
| 477Z | ● | 1.020 | 0* | ○ | 1.462 | 0.655 |
| 477N | ★ | 1.277 | 0.296 | ☆ | 1.277 | 0.296 |

Test Designations and Symbols defined in Table 20 (Page 166).
d/R is the defect diameter, d, expressed as a fraction of the pole radius, R
* The values of the defect sizes have a lower bound of zero

The time of flight metric and associated defect size estimates for each pole test is shown in Figure 100. The mean and standard deviation for the values for Pole 966 (red symbols) are 0.265 and 0.196, respectively. For the values of Pole 491 (blue symbols), the mean and standard deviation are 0.308 and 0.241, respectively. For the values of Pole 477 (green symbols), the mean and standard deviation are 0.312 and 0.268, respectively.

The time of flight metric underestimates all of the defect sizes, making it the least accurate of the three metrics. The standard deviations are smaller than those of the time centroid metric and overall greater than those of the wave area metric, making it the second most precise metric. The time of flight metric is sensitive to the position of the defect within the cross-section. As already seen in this section, the time of flight metric is used to identify the general location of the defect within the cross-section. Later in this section, the time of flight will be used to estimate the defect depth within the cross-section. The time of flight metric values and associated defect size estimates shown in Figure 100 are given in Table 23 alongside the respective symbols.

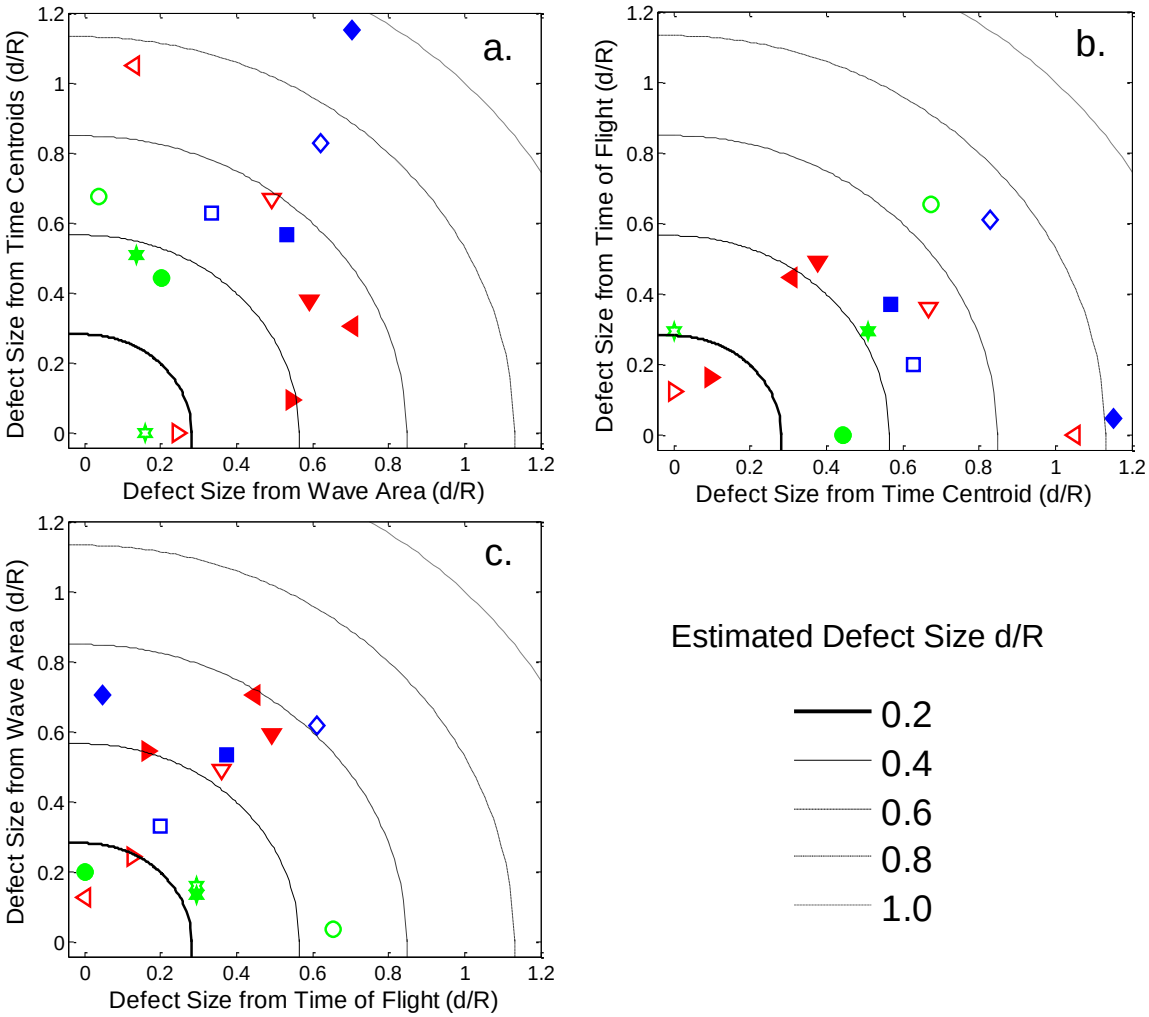


**Figure 101.** Defect estimates by metric plotted versus each other, **a.** wave area metric versus time centroid metric estimates, **b**. time centroid metric versus time of flight metric estimates, **c.** time of flight metric versus wave area metric. The defect diameter, d, is expressed as a fraction of the pole radius, R. Symbols are defined in Table 20 (Page 166).

As described in Section 4.3.4, the final defect size estimation is determined by calculating the RMS of the three defect estimations from the wave area, time centroid, and time of flight metrics. In this technique, each metric was used to estimate the defect size using the single variable polynomials shown in Table 18. All three metrics were then plotted against each other; first in paired groups in Figure 101, and then in a three dimensional space, in Figure 102. Values near the origin indicated cross-sections free of internal defects. As the distance from the origin increased, the estimated size of the internal defect increased.

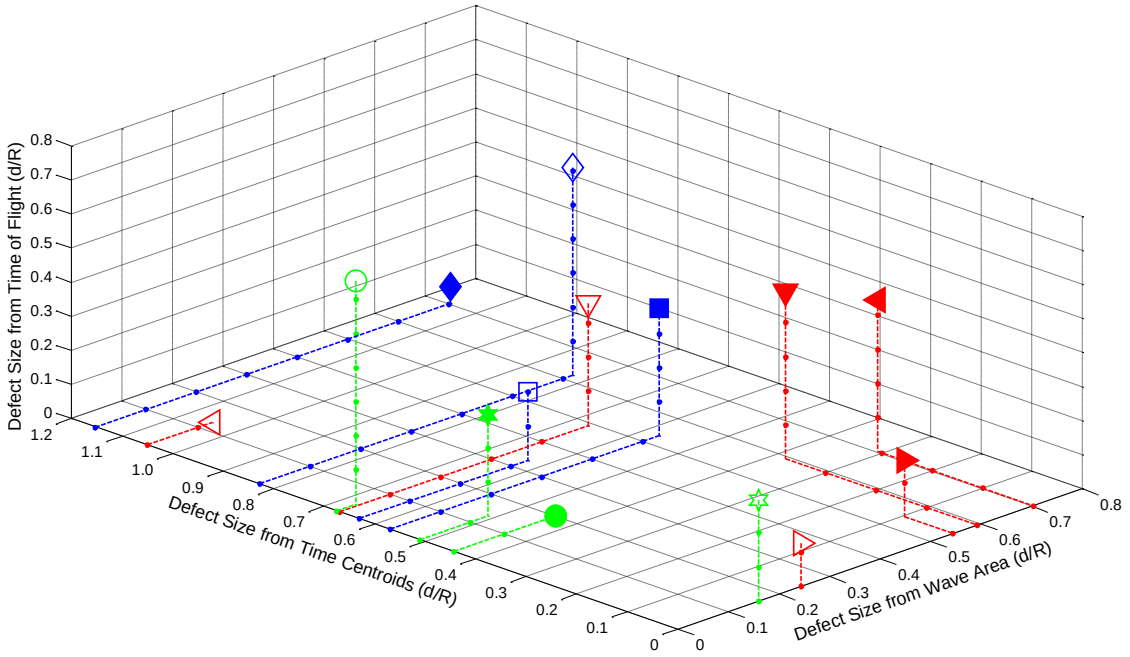


**Figure 102.** All defect estimates plotted in three dimensional space. The defect diameter, d, is expressed as a fraction of the pole radius, R. Symbols are defined in Table 20 (Page 166).

The arcs shown in Figure 101 represent an estimate of the defect size (d/R) obtained by calculating the RMS of the defect estimates of the two metrics. Estimates can be grouped by pole and the general ranges of the values corresponding to each pole can be identified. The majority of the estimates corresponding to Pole 966 are grouped between the arcs corresponding to 0.4 and 0.6 with values skewing lower. In all cases, the lowest values correspond to pole test 966R. Estimates for Pole 491 fall mostly between the arcs corresponding to 0.4 and 0.8. Estimates for Pole 477 fall between the arcs corresponding to 0.2 and 0.4; however, the values tend to be closer to the 0.4 arc.

Figure 102 shows the three dimensional space containing the defect size estimates from all three metrics for each of the individual pole tests.

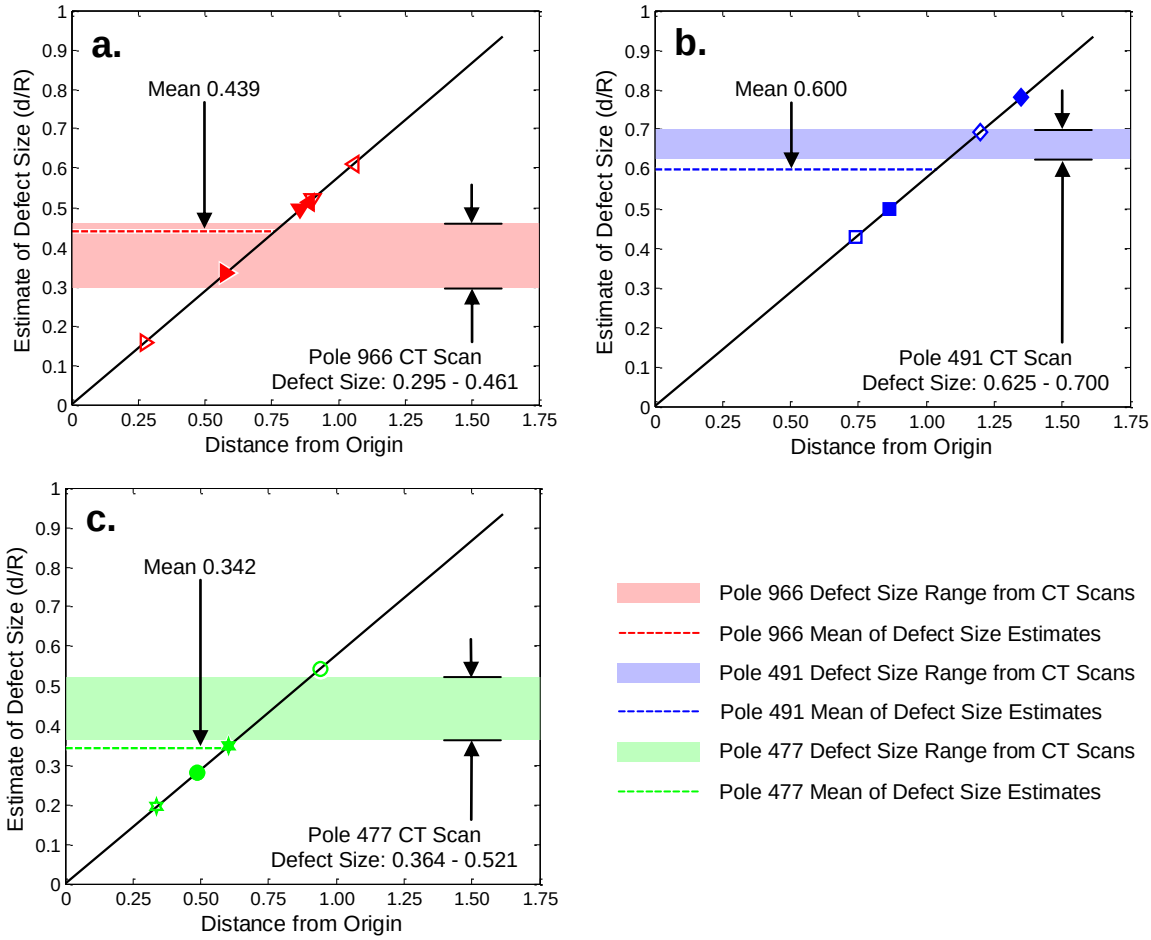


**Figure 103.** Distance from the origin of Figure 102 versus estimate of defect size. Colors red, blue, and green correspond to poles 966, 491, and 477. The mean of the defect size estimates for each pole are shown as colored dashed lines. The colored regions the range of defect values obtained from the CT Scans. Symbols are defined in Table 20 (Page 166) and the values are given in Table 24. **a.** Pole 966, **b.** Pole 491, **c.** Pole 477.

In Figure 102, the coordinates of each data point in the three dimensional metric space corresponds to the defect size estimates from the three metrics associated with that particular pole test. A value located at or near the origin corresponds to a pole test in which all three metrics indicate a small or non-existent defect. A value located at coordinate (1,1,1) would correspond to a pole test in which all three metrics indicate a defect the size of the radius of the pole is present. In Figure 103, the distance of each data point from the origin was plotted against the estimate of the defect size. The estimate of the defect size was the root mean square of the defect estimates from the three

metrics. Each pole has several pole tests: Pole 966 had six, Poles 491 had four, and Pole 477 had four. The mean of the estimates was taken and is shown in Figure 103 as a dashed line. Per the convention already established, the colors red, blue, and green represent values from Poles 966, 491, and 477. The shaded region in each plot is the range of the defect sizes observable from the CT scan. The defect regions are roughly elliptical in shape. The high and low values of the shaded regions represent the approximate major and minor axes of the defect region. The values obtained from for Pole 966 are shown in Figure 103a. The mean of the estimated values, 0.439, falls within the range defect sizes observed from the CT scans (0.295 to 0.461). The values for pole 491 are shown in Figure 103b. The mean of 0.600 underestimates the lower range of the observed defect values (0.625 to 0.700) by 4.0%. The values for Pole 477 are shown in Figure 103c. The mean, 0.342, underestimates the lower range of the observed defect values (0.364 to 0.521) by 6.0%. In all three utility pole specimens, the combined estimate of the defect size accurately predicts the true size internal defect to within 6.0% or less. The major and minor axes of the defect regions are given in Table 24.

**Table 24.** Estimate of defect size (d/R)

| Pole | Test | Distance From Origin | | Estimate of d/R | | Mean d/R |
|---|---|---|---|---|---|---|
| | | $\frac{\pm 180^o}{+90^o}$ | $\frac{\pm 180^o}{-90^o}$ | $\frac{\pm 180^o}{+90^o}$ | $\frac{\pm 180^o}{-90^o}$ | |
| 966 | Z | 0.888 | 1.057 | 0.513 | 0.610 | 0.439 |
| | N | 0.858 | 0.905 | 0.495 | 0.522 | |
| | R | 0.577 | 0.275 | 0.333 | 0.157 | |
| 491 | Z | 0.865 | 0.740 | 0.499 | 0.427 | 0.600 |
| | N | 1.351 | 1.200 | 0.780 | 0.693 | |
| 477 | Z | 0.486 | 0.941 | 0.281 | 0.543 | 0.342 |
| | N | 0.605 | 0.337 | 0.349 | 0.194 | |

The estimated defect size is then used to calculate the area of the defect. Since the defect size is the defect diameter, d, normalized by the pole radius, R, the fraction of the cross-sectional area composed of the defect, $A_d$, is calculated using Equation 69.

$$A_d = \left(\frac{1}{2}\frac{d}{R}\right)^2 \tag{69}$$

The calculated cross-sectional area is then compared to the area of the defect as measured from the CT scans. The defect regions in the cross-sections are assumed to be elliptical and their area is approximated by calculating the area of an ellipse from the major and minor axes as shown in Equation 70. The major and minor axes presented here are normalized by the cross-sectional radius of the respective poles.

$$A_c = \frac{1}{4} \frac{d_a d_b}{R^2} \tag{70}$$

Where:
$A_c$ is the area of the defect based upon measurements taken from the CT scan
$d_a$ is the major axis of the defect region in the CT scan
$d_b$ is the minor axis of the defect region in the Ct scan

Each pole as two values for defect area as a fraction of the cross-sectional area: the value measured from the CT scans and the value estimated from metrics. For Pole 966 the measured and estimated fractional areas are 0.034 and 0.048, respectively, with a difference of 0.014 (1.4% of the cross-sectional area). For Pole 491, the measured and estimated fractional area are 0.110 and 0.090, respectively, with a difference of 0.020 (2.0% of the cross-sectional area). For Pole 477, the measured and estimated fractional areas are 0.047 and 0.029, respectively, with a difference of 0.018 (1.8% of the cross-sectional area). The defect area values are given in Table 25.

**Table 25.** Comparisons of estimated and actual defect sizes by pole

| Pole | RMS d/R | RMS d/R Fraction Cross-sectional Area | Defect Sizes From CT Scans# | | CT Scan Fraction Cross-sectional Area | Difference in Fraction Cross-section Area |
|---|---|---|---|---|---|---|
| | | | Minor | Major | | |
| 966 | 0.439 | 0.048 | 0.295 | 0.461 | 0.034 | 0.014 |
| 491 | 0.600 | 0.090 | 0.625 | 0.700 | 0.110 | 0.020 |
| 477 | 0.342 | 0.029 | 0.364 | 0.521 | 0.047 | 0.018 |

# Defects are assumed to have a generally elliptical shape with major and minor axes.

### 4.4.2. Time of flight and defect depth

Defect depth is the distance from the sending transducer to the center of the defect within the pole. The defect size obtained using the ToF metric is the center projection of the defect, which is size of the defect if it were located at the center of the utility pole.

The defect depth is calculated from a geometric relationship between the defect size, the radius of the pole, and center projection of the defect size obtained from the ToF metric.

The value of the ToF metric is sensitive to the position of the defect within the cross-section. In Section 4.3.3.3, that sensitivity was used to develop predictions of the location of the defect within the cross-section. In Section 4.4.1, those predictions were validated against data collected from the utility poles specimens. The ToF metric is now used to more accurately calculate the center location of the defect.

Each pole test yields two ToF metrics. The value that is farthest from unity is the ratio most influenced by the presence of the defect. The defect size predicted by the greater ToF metric is the size of the center projection of the defect. As previously mentioned in Section 4.3.3.3, the value for Pole test 477Z (-90°) was inverted to obtain a pertinent value within the ToF range. Table 26 contains the selected list of selected ToF metrics, associated center projection defect sizes, and symbols. The selected ToF values and their respective defect sizes are shown in Figure 104. The curve presented in Figure 104 was previously presented in Figure 100.

**Table 26**. Time of flight metrics most influenced by defects

| Pole Test | Time of Flight Metrics | | Metric Most Influenced by Internal Defect | | Center Projected Defect Size ($d_c$/R) |
|---|---|---|---|---|---|
| | $\frac{\tau_{\pm 180}}{\tau_{+90}} k_v$ | $\frac{\tau_{\pm 180}}{\tau_{-90}} k_v$ | Symbol | Selected Value | |
| 966Z | 1.357 | 0.965 | ◀ | 1.357 | 0.446 |
| 966N | 1.380 | 1.312 | ▼ | 1.380 | 0.492 |
| 966R | 1.199 | 1.172 | ▶ | 1.199 | 0.166 |
| 491Z | 1.319 | 1.221 | ■ | 1.319 | 0.373 |
| 491N | 1.108 | 1.439 | ◇ | 1.439 | 0.611 |
| 477Z | 1.020 | 1.462 | ○ | 1.462 | 0.655 |
| 477N | 1.227 | 1.277 | ★, ✡ | 1.277 | 0.296 |

Highlighted values are the values greatest than one and correspond to the metric most affected by the defect.

Defect depth is determined using geometric relationships described in Figure 105. The depth of the defect, $R_d$, is calculated using Equation 71. Table 27 shows the estimated center projected defect size, the estimated defect size, and radius of each of the

utility poles, and the defect depth of each defect. It should be noted that the cross-section of Pole 966 is elliptical and therefore the radius from changes at various locations around the circumference. Poles 491 and 477 have cross-sections that are close to circular; therefore those poles each have a single radius value. Since both defect diameter estimates are ratios normalize by the pole radius, the ratio of the defect diameters causes the common pole radius value to cancel.

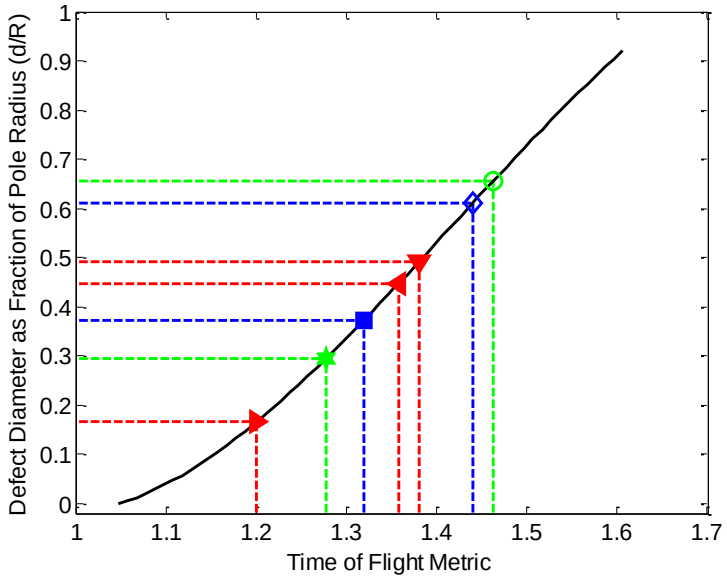


**Figure 104.** Time of flight metric versus the size of the defect. The colored symbols are the metric selected from Table 26. Values for Poles 966, 491, and 477 are represented by the colors red, blue, and green, respectively.

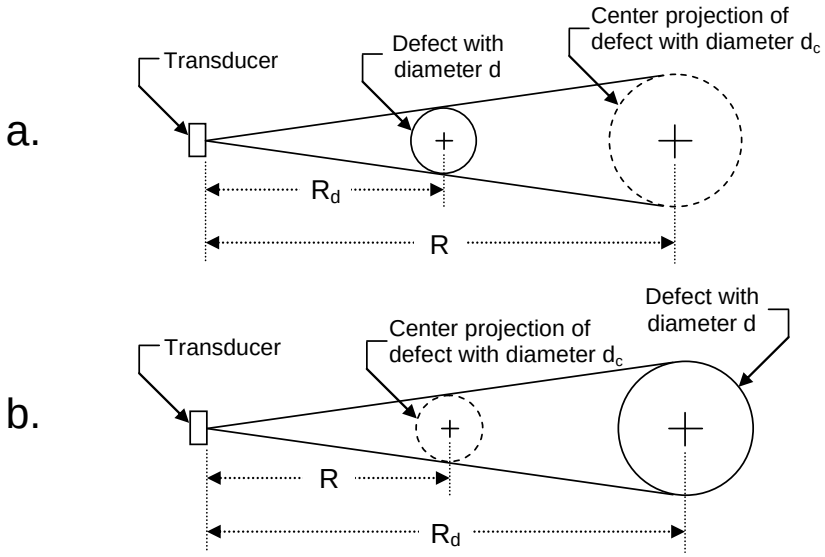


**Figure 105.** Center projection of defects. **a.** Defect between transducer and center of utility pole. **b.** Center between defect and transducer. The radius of the utility pole is R. The depth of the defect is $R_d$.

$$R_d = \left( \frac{d}{R} \frac{R}{d_c} \right) R = \frac{d}{d_c} R \tag{71}$$

**Table 27.** Estimated defect depth within utility pole

| Pole Test | Center Projected Defect Size ($d_c/R$) | Size of Defect (d/R) | Pole Radius (R) (mm) | $d_c$ (mm) | d (mm) | Defect Depth (mm) |
|---|---|---|---|---|---|---|
| 966Z | 0.446 | 0.439 | 184* | 82 | 81 | 181 |
| 966N | 0.492 | 0.439 | 197* | 97 | 86 | 176 |
| 966R | 0.166 | 0.439 | 184* | 31 | 81 | 486 |
| 491Z | 0.373 | 0.600 | 191 | 71 | 115 | 307 |
| 491N | 0.611 | 0.600 | 191 | 117 | 115 | 188 |
| 477Z | 0.655 | 0.342 | 178 | 117 | 61 | 93 |
| 477N | 0.296 | 0.342 | 178 | 53 | 61 | 206 |

* Pole 966 is oval shaped. The 0° and 180° sensors were placed along the minor diameter of 368 mm while the 90° and 270° sensors were placed along the major diameter of 394. For poles 491 and 477, the distances between oppositely placed sensors were approximately equal within each respective pole.
**$d_c$** is the center projected defect diameter, **d** is the predicted defect size, **R** is the pole radius

It should be noted that Pole 966 is oval shaped. The distance between the 0° and 180° locations is 368 mm (radius 184) while the distance between the 90° and 270° locations is 394 mm (radius 197). The cross-sections of Poles 491 and 477 were approximately circular and each has a single radius value (191 mm for Pole 491, and 178 mm for pole 477).

### 4.4.3. Predicted defects within pole cross-sections

In this section, the estimated defect sizes and locations are compared against the visible defects from the CT scans. The data for poles 491 and 477 are presented first. Data from pole 966 is presented last as additional analysis was required. The decay region within each pole is hatched for greater visibility. A solid circle is used to depict the predicted defect. The diameter of the predicted defect is the product of the size of defect and pole radius values given in Table 27. The dashed circle is the center projected defect. The "center" used in the center projection calculation is based upon half of the measured diameter and may not necessarily correspond to the pith center of the pole.

Figure 106 shows the results of pole test 491Z. The defect is predicted to be within defect region A (according to Figure 90 on page 154). The defect is not composed

of brown rot and is higher in density than the surrounding wood. Nevertheless, the predicted defect size and position give good agreement with the actual defect. The actual defect region is roughly elliptical with major and minor diameters of 133 and 119 mm, respectively. The predicted defect (solid circle) has a diameter of 115 mm. The center projected defect (dashed circle) has a diameter of 71 mm. The center of the estimated defect is approximately 51 mm from the center of the actual defect region.

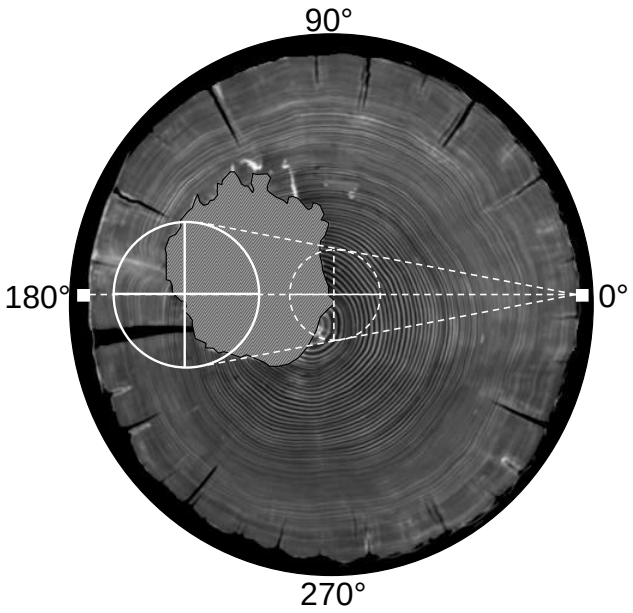


**Figure 106.** Predicted defect within pole 491 with source at 0°. Values associated with pole test 491Z. Hatching shows the actual defect region, which is roughly elliptical (major and minor axes of 133 and 119 mm, respectively) and is in defect region A (Figure 90 on page 154). The dashed circle is the center projected defect area with a diameter of 71 mm. The solid circle is the predicted defect area with a diameter of 115 mm. The predicted defect depth is 307 mm. The center offset of the predicted defect region from the actual defect region is 51 mm.

Figure 107 shows the results from pole test 491N. The defect is predicted to be within defect region D. The center projected defect (dashed circle) has a diameter of 117 mm. The center of the estimated defect (solid circle) is approximately 14 mm from the center of the actual defect region. The estimated defect shown in Figure 108 was placed midway between the locations predicted from figures 491Z (Figure 106) and 491N (Figure 107). The center of the predicted defect is approximately 31 mm from the center of the actual defect region, which is 16.2% of the radius of the pole.

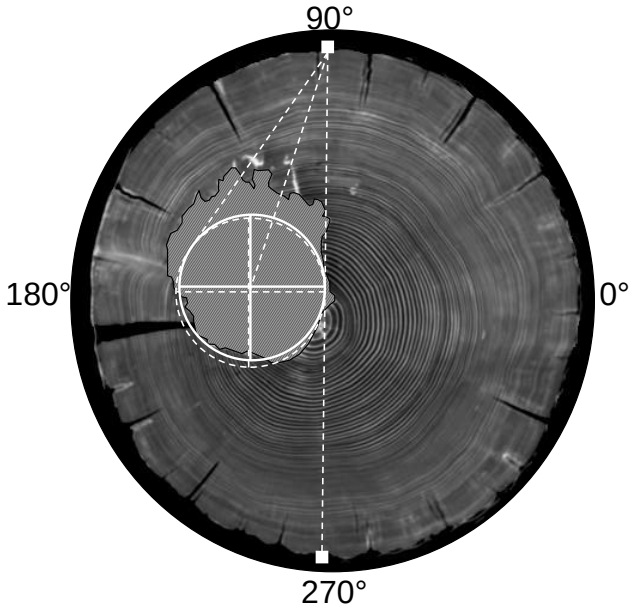


**Figure 107.** Predicted defect within pole 491 with source at 90°. Values associated with pole test 491N. Hatching shows the actual defect region, which is roroughly elliptical (major and minor axes of 133 and 119 mm, respectively) and is in defect region D (Figure 90 on page 154). The dashed circle is the center projected defect area with a diameter of 117 mm. The solid circle is the predicted defect area with diameter of 115 mm. The predicted defect depth is 188 mm. The center offset of the predicted defect area from the actual defect region is 14 mm.

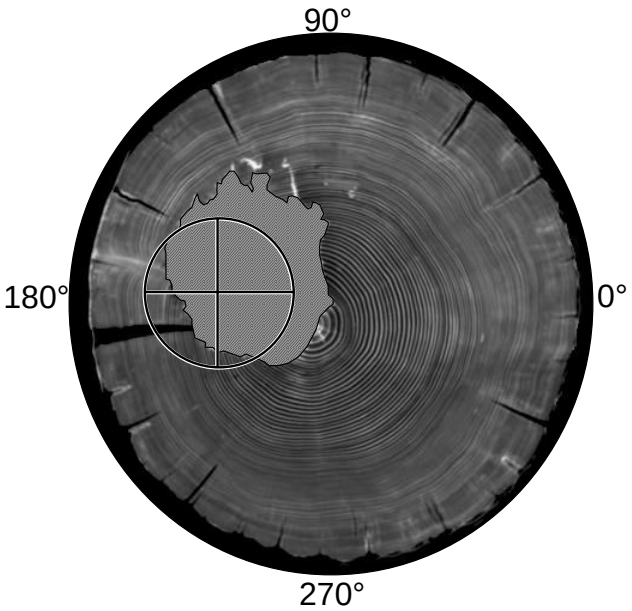


**Figure 108.** Actual and predicted defect for pole 491. Hatching shows the actual defect region, which is roughly elliptical (major and minor axes of 133 and 119 mm, respectively). The solid black circle is the predicted defect area with a diameter of 115 mm, and is positioned midway between the positions of the defects predicted for Pole tests 491Z (Figure 106) and 491N (Figure 107). The center offset of the predicted defect region from the actual defect region is 31 mm.

Figure 109 shows the results of pole test 477Z. The defect is predicted to be within defect region H. It was necessary to invert the time of flight ratio in order to obtain a value greater than one and estimate the center projection of the defect size. For this reason, the receiver at the 270° location is used to estimate the defect location from the center projection. The defect is roughly elliptical with a major diameter of 93 mm and a minor diameter of 65 mm. The predicted defect (solid circle) has a diameter of 61 mm. The center projected defect (dashed circle) has a diameter of 117 mm. The center of the estimated defect is approximately 16 mm from the center of the actual defect region.

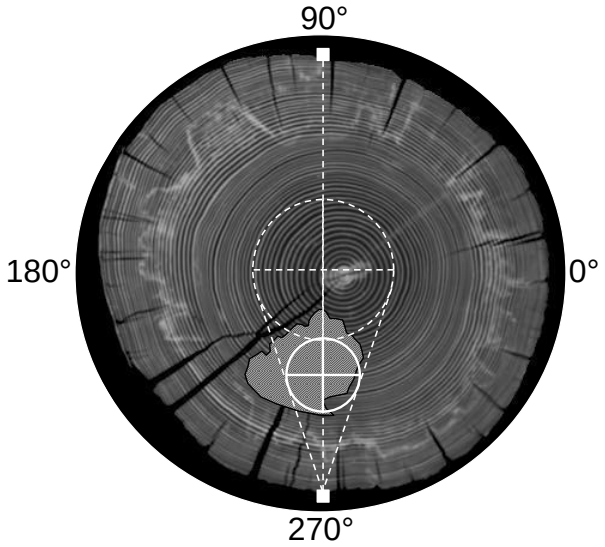


**Figure 109.** Predicted defect within pole 477 with source at 0°. Values associated with pole test 477Z. Hatching shows the actual defect region, which is roughly elliptical (major and minor axes of 93 and 65 mm, respectively) and is in defect region H. The dashed circle is the center projected defect area with a diameter of 117 mm. The solid circle is the predicted defect area with a diameter of 61 mm. The predicted defect depth is 93 mm. The center offset of the predicted defect region from the actual defect region is 16 mm. The time of flight metric between 180° and 270° required inversion in order to obtain a center projection; therefore, the receiver at 270° is used to estimate the defect location from the center projection.

Figure 110 shows the results from pole test 477N. The defect is predicted to be within defect region A. The center projected defect (dashed circle) has a diameter of 53 mm. The center of the estimated defect (solid circle) is approximately 48 mm from the center of the actual defect region. The estimated defect shown in Figure 111 was placed midway between the locations predicted from figures 477Z (Figure 109) and 477N (Figure 110). The center of the predicted defect shown in Figure 111 is approximately 23 mm from the center of the actual defect region, which is 12.9% of the radius of the pole.

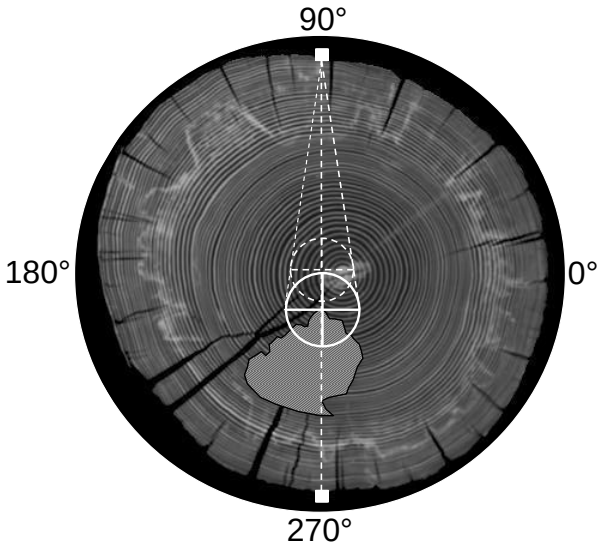


**Figure 110.** Predicted defect within pole 477 with source at 90°. Values associated with pole test 477N. Hatching shows the actual defect region, which is roughly elliptical (major and minor axes of 93 and 65 mm, respectively) and is in defect region A. The dashed circle is the center projected defect area with a diameter of 53 mm. The solid circle is the predicted defect area with diameter of 61 mm. The predicted defect depth is 206 mm. The center offset of the predicted defect area from the actual defect region is 48 mm.

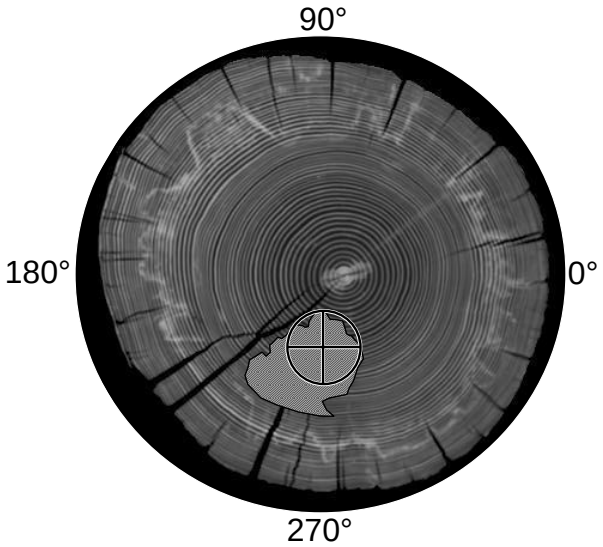


**Figure 111.** Actual and predicted defects for pole 477. Hatching shows the actual defect region, which is roughly elliptical (major and minor axes of 93 and 65 mm, respectively). The solid black circle is the predicted defect area with a diameter of 61 mm, and is positioned midway between the positions of the defects predicted for Pole tests 477Z (Figure 109) and 491N (Figure 110). The center offset of the predicted defect region from the actual defect region is 23 mm.

Figure 112 shows the results of test 966Z. The defect is predicted to be within decay region F. The decayed wood is split into two separate areas which can be encircled

with an ellipse with a major diameter of 85 mm and a minor dimension of 54 mm. Whether or not the area between the two regions is also rotten cannot be determined from the CT scans. The predicted defect area (solid circle) has a diameter of 81 mm. The center projected defect area (dashed circle) has a diameter of 82 mm. The center of the estimated defect region is approximately 47 mm from the center of the actual defect region.

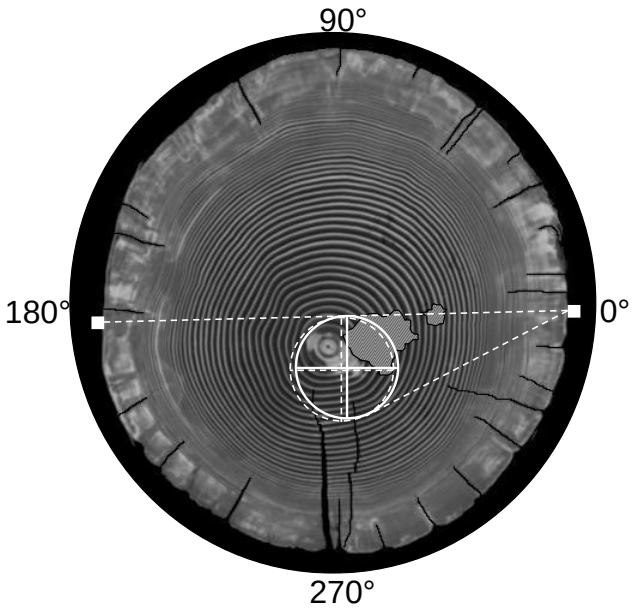


**Figure 112.** Predicted defect within pole 966 with source at 0°. Values associated with pole test 966Z. Hatching shows the actual defect region, which is roughly elliptical (major and minor axes of 85 and 54 mm, respectively) and is in defect region F. The dashed circle is the center projected defect area with a diameter of 82 mm. The solid circle is the predicted defect area with a diameter of 81 mm. The predicted defect depth is 181 mm. The center offset of the predicted defect region from the actual defect region is 47 mm.

The results from the first 966N test yielded an obviously invalid estimate of the defect size. The signal observed by the receiver at ±180° had an abnormally low attenuation. Signals persisted abnormally long and the amplitudes observed remained relatively high when compared with the signals observed at ±90°. As a result, those results were not used in the analysis. Figure 113a shows the receiver locations used for 966Z and the first attempt of pole test 966N. The receiver at 270° (which is -90° for the 966Z test and ±180° for the attempted 966N) is positioned on a relatively narrow strip between two cracks. One of the two cracks has a length greater than 60% of the pole radius. It is believed that a combination of mode conversion and resonance within the narrow space contributed to the persistence of the signal. The ±180° receiver was moved

to the opposite side of the major crack in order to perform the 966N test, as shown in Figure 113b.

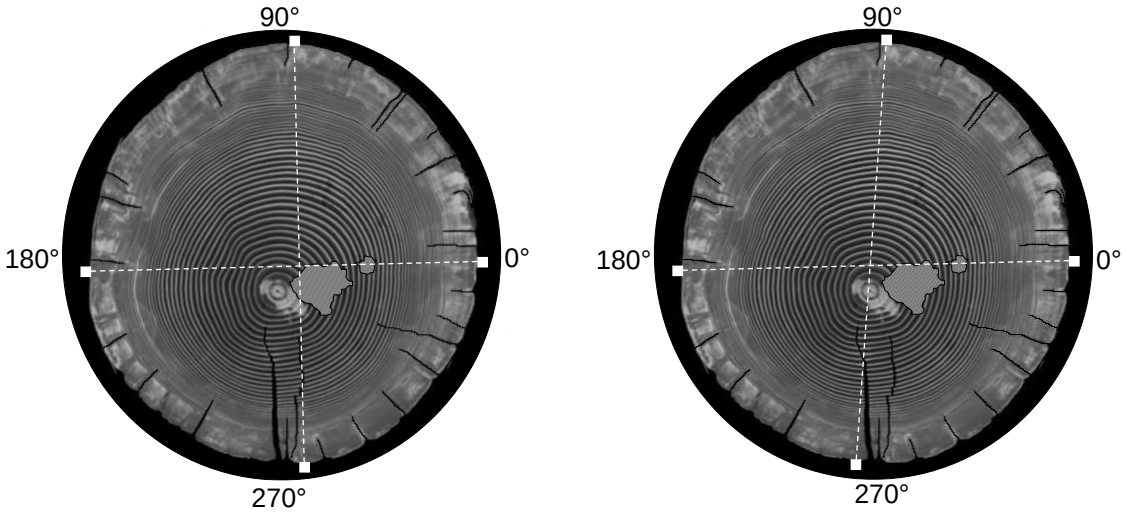


**Figure 113.** Sensor locations for testing of pole 966. **a.** Sensor locations for pole test 966Z with source located at 0° **b.** Sensor locations for pole tests 966N and 966R, with sources at 90° and 180°, respectively.

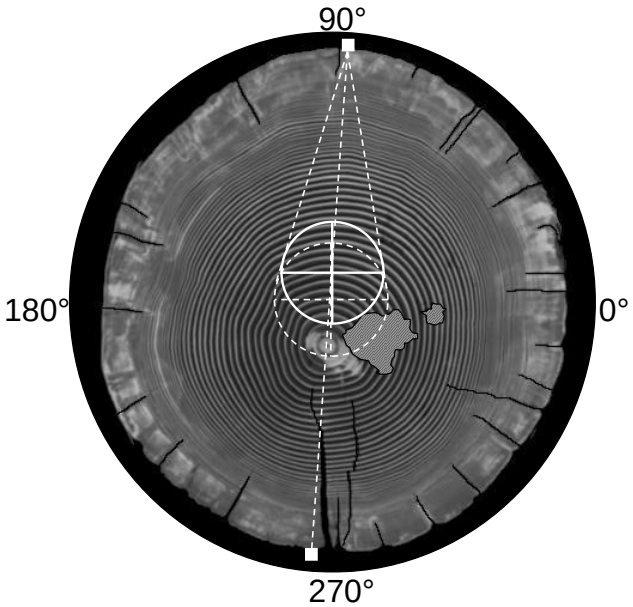


**Figure 114.** Predicted defect within pole 966 with source at 90°. Values associated with pole test 966N. Hatching shows the actual defect region, which is roughly elliptical (major and minor axes of 85 and 54 mm, respectively) and is in defect region A. The dashed circle is the center projected defect area with a diameter of 97 mm. The solid circle is the predicted defect area with a diameter of 86 mm. The predicted defect depth is 176 mm. The center offset of the predicted defect region from the actual defect region is 69 mm.

Figure 114 shows the results from pole test 966N. The defect is predicted to be within defect region A. The center projected defect (dashed circle) has a diameter of 97 mm. The center of the estimated defect (solid circle) is approximately 69 mm from the center of the actual defect region.

For pole test 966R, the defect is predicted to be within defect region A. The center projected defect has a diameter of 31 mm. The calculated defect depth using a center projected defect diameter of 31 mm was 486 mm, which is a distance greater than the diameter of the pole (for this reason, no figure is provided). The defect depth estimate for pole test 966R is the largest of all of the pole tests. The second largest is pole test 966N. The defect depth calculations placed the defects such that there was no overlap between the predicted defects and the actual defect location. The defect depth calculations for Poles 491 and 477 yielded value that had some overlap between the predicted defect location and the actual defect region. This discrepancy led to the belief that additional factors may be affecting the defect depth calculations. The placement of the defects is affected by the times of flight measured during the testing. The cross-section was examined for features that could affect the time of flight of the waves.

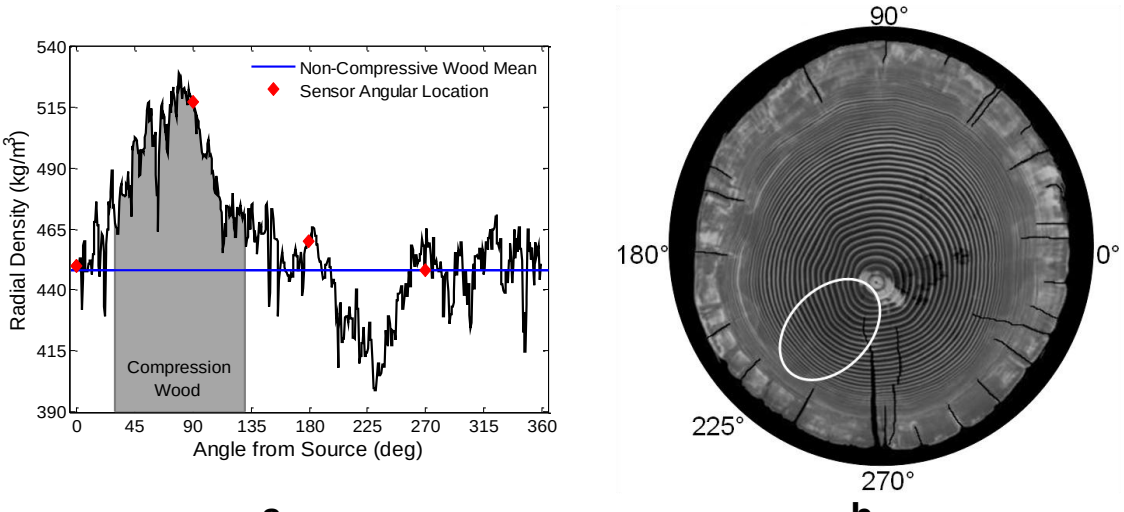


**Figure 115.** Radial density of pole 966. **a.** Radial density angle (Reprint of Figure 74a on page 127). **b.** Cross-section of pole 966 showing region of diminished density as indicated in Figure 115a.

The presence of rot in wood slows wave speed through it. Loss of density is often an indicator of the presence of rot in wood. The hatched areas of the cross-sections show

regions of advanced decay that were clearly visible in the CT scans. During the compression wood analysis, the radial density of the pole was examined; the radial density figure is reproduced in Figure 115a. Excluding the region of compression wood, there is a region of the pole between approximately 190° and 260° that has noticeably lower density that the other portions of the pole. The pole region is shown in Figure 115b. On average, the density in that region is approximately 12% lower than the density of the other, non-compression wood portions of the pole. However, lower density alone is not necessarily indicative of rot.

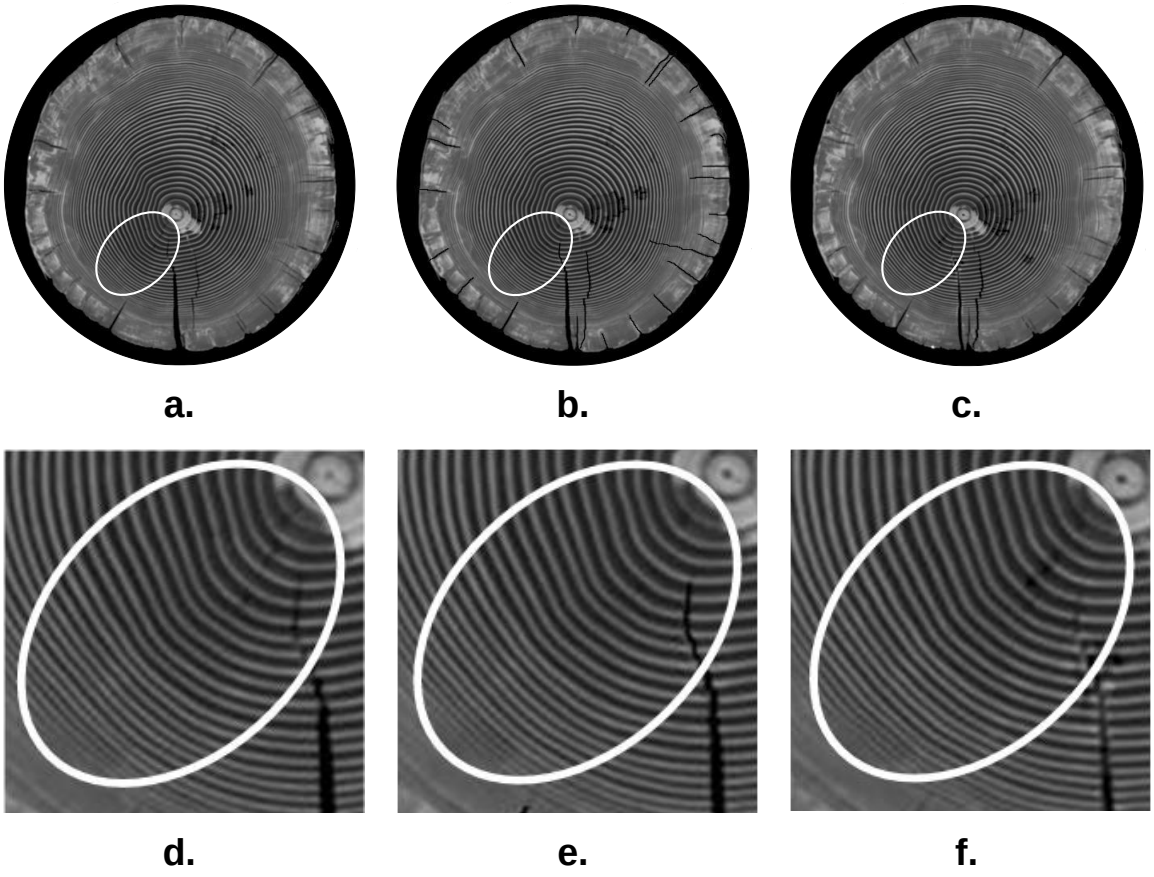


**Figure 116.** Decay region within pole 966. **a.** cross-section -30 mm below the examined cross-section, **b.** examined cross-section, **c.** cross-section at +30 mm above examined cross-section, **d.** close-up view of decayed region for -30 mm cross-section (note the split in the upper right of the oval), **e.** close of view of decayed region for examined cross-section, **f.** close-up view of decayed region for +30 mm cross-section (note the split in the upper right of the oval)

The CT scans of nearby slices were examined for areas of rot in the vicinity. CT scans of pole 966 were taken every 10 mm. At +30 mm and -30 mm, splitting became

visible. The ±30 mm cross-sections are shown in Figure 116. Close-up views of the decay region are also shown. Splitting is apparent in the upper right of the oval. Splitting in conjunction with mass loss in a region is indicative of advanced decay. Therefore, based upon combination of low density and proximity to splitting, it is likely that the area shown between 190° and 260° of the cross-section has incipient to intermediate decay.

Correcting times of flight due to the presence of rot may improve estimation of the defect location within the cross-section. McGovern's [125] polynomials were used to estimate the speed reduction caused by rot. A center frequency of 8 kHz was assumed for the calculations. For mass loss of 12% and a center frequency of 8 kHz, the radial velocity is reduced by 12% and the tangential velocity is reduced by 4.9% with respect to zero percent mass loss. It is assumed that the entire distance between the 180° sensor and the 270° sensor for pole test 966R is rotten wood. It is also assumed that half of the travel distance from the 90° to the 270° sensor in pole test 966N is rotten wood. The correction for the travel times for pole tests 966R and 966N are shown in Equations 72a and 72b, respectively. Table 28 contains the updated time of flight ratio and center projected defect size. Table 29 contains the updated defect depth. Pole tests with corrected time of flight values are given the suffix letter C.

$$\tau^{*}_{+90} = (1-0.049)\,\tau_{+90} = (1-0.049)(168\mu s) = 160\mu s \tag{72a}$$

$$\begin{aligned} &\frac{\tau^{*}_{+180}}{2} + \frac{(1+0.12)\,\tau^{*}_{+180}}{2} = \tau^{*}_{+180}\left(\frac{2.12}{2}\right) = \tau_{+180} \\ &\tau^{*}_{+180} = \left(\frac{2}{2.12}\right)\tau_{+180} = \left(\frac{2}{2.12}\right)(232\mu s) = 219\mu s \end{aligned} \tag{72b}$$

**Table 28.** Corrected center projected defect size for 966N and 966R

| Pole Test | Times of Flight (ms) | | Time of Flight Ratio | Center Projected Defect Size ($d_c$/R) |
|---|---|---|---|---|
| | +90° | ±180° | $(\tau_{\pm 180}/\tau_{+90})k_v$ | |
| 966NC | 0.154 | 0.219 | 1.297 | 0.332 |
| 966RC | 0.160 | 0.220 | 1.260 | 0.265 |

Where suffix C denotes a pole test with a corrected time of flight.

**Table 29.** Corrected defect depth for 966N and 966R

| Pole Test | Center Projected Defect Size ($d_c$/R) | Size of Defect (d/R) | Pole Radius (R) (mm) | $d_c$ (mm) | d (mm) | Defect Depth (mm) |
|---|---|---|---|---|---|---|
| 966NC | 0.332 | 0.439 | 197* | 65 | 86 | 260 |
| 966RC | 0.265 | 0.439 | 184* | 49 | 81 | 305 |

* Pole 966 is oval shaped. The 0° and 180° sensors were placed along the minor diameter of 368 mm while the 90° and 270° sensors were placed along the major diameter of 394. For poles 491 and 477, the distances between oppositely placed sensors were approximately equal within each respective pole.
**$d_c$** is the center projected defect diameter, **d** is the predicted defect size, **R** is the pole radius

Figure 117 shows the results from pole test 966N using the corrected time of flight defect placement. The corrected pole test will hereafter be referred to as 966NC. The defect is still within defect region A. The new diameter of the center projected defect (dashed circle) is 65 mm (reduced from 97 mm), and the new defect depth is 260 mm (raised from 176 mm). The center of the predicted defect area is 67 mm from center of the actual defect region, which is only a slight (2 mm) improvement over the uncorrected value.

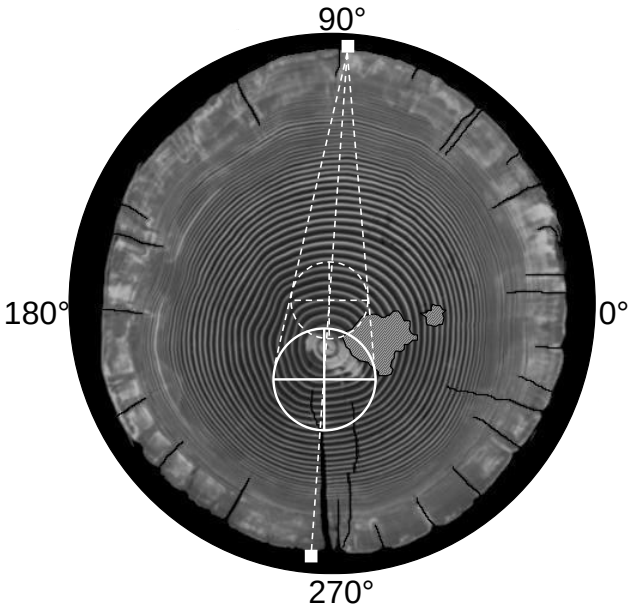


**Figure 117.** Corrected predicted defect for pole 966 with source at 90°. Values associated with pole test 966NC. Hatching shows the actual defect region, which is roughly elliptical (major and minor axes of 85 and 54 mm, respectively) and is in defect region A. The dashed circle is the center projected defect area with a diameter of 65 mm. The solid circle is the predicted defect area with a diameter of 86 mm. The predicted defect depth is 260 mm. The center offset of the predicted defect region from the actual defect region is 67 mm.

Figure 118 shows the results from pole test 966R using the time of flight corrected defect placement. The corrected pole test will hereafter be referred to as 966RC. The defect is still within defect region A. The new diameter of the center projected defect (dashed circle) is 49 mm (increased from 31 mm) and the new defect depth is 305mm (decreased from 486 mm). The center of the predicted defect area is 76 mm from center of the actual defect region, which is 181 mm closer than uncorrected value.

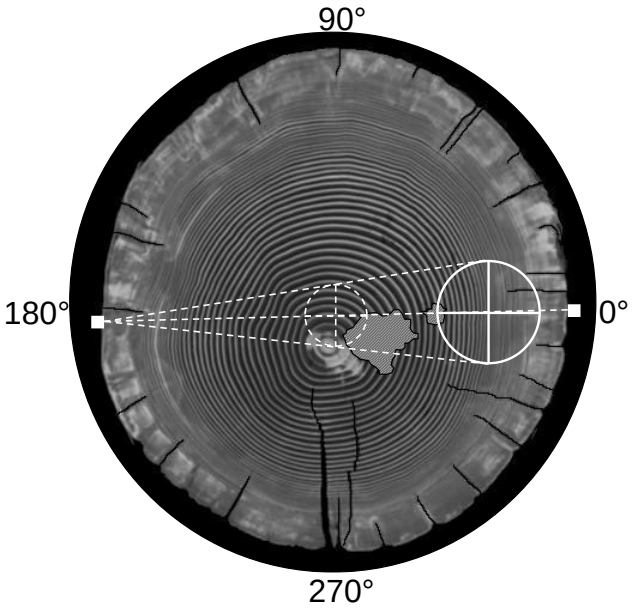


**Figure 118.** Corrected predicted defect for pole 966 with source at 180°. Values associated with pole test 966RC. Hatching shows the actual defect region, which is roughly elliptical (major and minor axes of 85 and 54 mm, respectively) and is in defect region A. The dashed circle is the center projected defect area with a diameter of 49 mm. The solid circle is the predicted defect area with a diameter of 81 mm. The predicted defect depth is 305 mm. The center offset of the predicted defect region from the actual defect region is 76 mm.

The three pole tests for Pole 966 yield three different estimates of the location of the predicted defect. The estimated defect shown in Figure 119 was placed at the centroid of the triangle formed by the three predicted locations from pole tests 966Z (Figure 112), 966NC (Figure 117), and 966RC (Figure 118). The center of the predicted defect is approximately 19 mm from the center of the actual defect region, which is 10.3% of radius of the pole. Pole 966 is oval shaped and has a major and minor radii. The minor radius of 184 mm was used in the calculations to give the largest and most conservative percentile value.

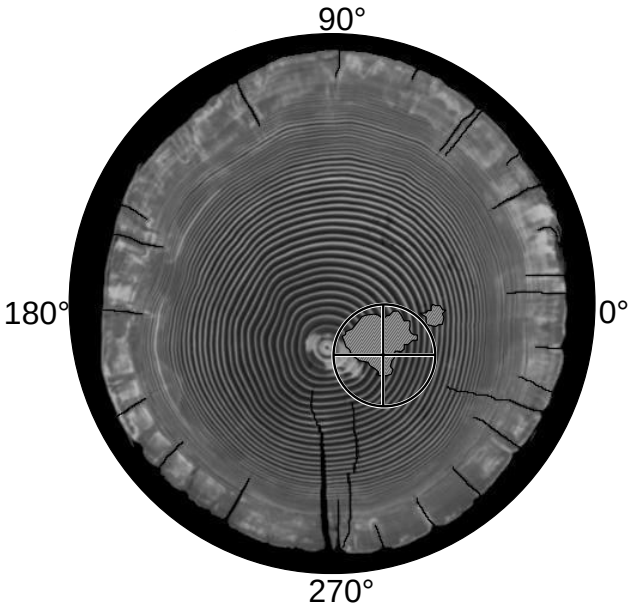


**Figure 119.** Actual and predicted defects with correction for pole 966. Hatching shows the actual defect region, which is roughly elliptical (major and minor axes of 85 and 54 mm, respectively)). The solid black circle is the predicted defect area with a diameter of 81 mm, and is positioned at the centroid of the triangle formed by positions of the defects predicted for Pole tests 966Z (Figure 112), 966NC (Figure 117), and 966RC (Figure 118). The center offset of the predicted defect region from the actual defect region is 19 mm.

**Table 30.** Comparison of predicted and actual defects

| Pole | Defect Area as a Percentage Cross Sectional Area of the Pole | | | Offset Distance of Predicted Defect from Actual Defect | |
|---|---|---|---|---|---|
| | Predicted | CT Scan | Difference | Distance (mm) | Percentage of Pole Radius |
| 966 | 4.8 | 3.4 | 1.4 | 19 | 10.3 |
| 491 | 9.0 | 11.0 | 2.0 | 31 | 16.2 |
| 477 | 2.9 | 4.7 | 1.8 | 23 | 12.9 |

In Table 30, the areas of the actual defects and the predicted defects are compared for each pole. The defect areas (originally expressed in Table 25 as fraction of the pole cross-section) are within 2.0% of the actual defect areas obtained from the CT Scans of the cross-sections. The locations of the predicted defects are within 17% of the pole radius for Poles 491 and 477. For Pole 966, the location based upon the time of flight values was clearly inaccurate and placed the defect outside the pole diameter; however, the inaccuracy was traced to a second area of decay within the cross-section that skewed the time of flight values for pole tests 966N and 966R. Corrections were made to the wave velocity and time of flight values based upon mass loss estimated from the CT

scans. When those corrections were applied, the resulting location of the predicted defect was within 10.3% of the pole radius.

The correction procedure highlights one shortfall of the current defect estimation method. The method accurately predicts the size and location of a defect within a cross-section that contains a single defect. When a cross-section contains multiple defects that are not collocated, accuracy of the estimation method suffers. In the case of Pole 966, the estimation method accurately estimated the size of the region of advanced decay, but the defect depth was inaccurate for two of the three pole tests.

### 4.5. Focused Inspection by Placing Source Adjacent to Surface Cracks

In all of the utility poles specimens received, there was a single large surface crack that extended deep within the pole. In previous studies, Lemaster [134] found that decay often occurred near these cracks. Preservative agents can penetrate several centimeters (3 to 7 cm (1 to 3 inches) is not uncommon) below the surface of a pole. Large cracks can have lengths that extend beyond the preservative penetration depth giving agents of decay access to unpreserved portions of the pole. Placing signal sources near these cracks has two advantages: ray paths are likely oriented such that pole rot near the crack will be found, and the received signals appear to have greater magnitude. The greater magnitude of the received signals when tested near a crack is likely a result of wave energy confined and / or redirected within the pole cross-section.

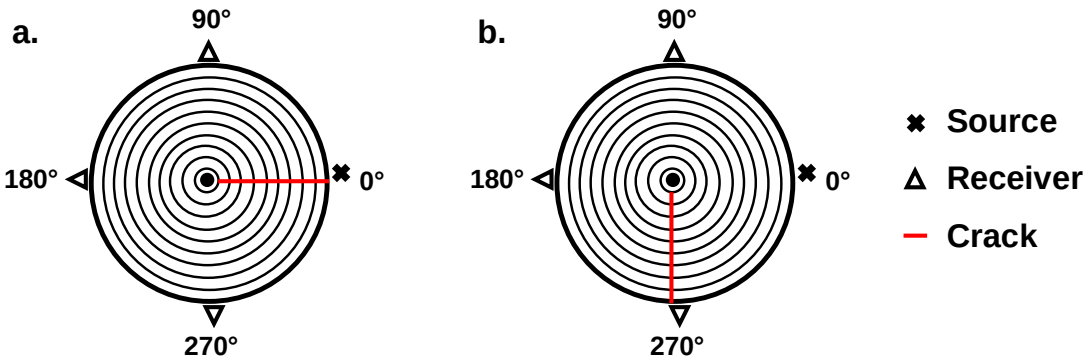


**Figure 120.** Simulated pole cross-sections with cracks, **a.** Crack next to source at 0°, **b.** Crack at 270°

Figure 120a shows the input source next to a crack at 0°. Figure 120b shows the crack at 270°. The cross-sections had radii of 191 mm (7.5 inches), and the cracks extended radially towards the centers to a depth of 185 mm (7.3 inches). A third cross-section without a defect was used as a control simulation. The same input was used for all three simulations with the source at 0° and receivers at 90°, 180°, and 270°. The energy observed at the receivers was compared against two sets of tests performed on Pole 966. The experimental setup shown in Figure 72 (page 124) corresponds to the simulated cross-section shown in Figure 120b. Another set of measurements were taken on Pole 966 with the source located at the 270° (on the bottom of Figure 72, on the side of the crack facing the 0° location). That test setup corresponded to the simulated cross-section shown in Figure 120a, with a coordinate system rotated 90° clockwise (the 270°, 0°, 90°, and 180° locations shown in Figure 72 correspond to the 0°, 90°, and 180°, and 270° locations of Figure 120a). The energy values presented are normalized against the energy of the control cross-section.

In a perfect cross-section, any input signal will spread in all directions. When a crack is next to the input source, as in Figure 120a, some of the energy from the input is redirected. The impedance mismatch between air and wood is significant. Waves traveling through wood to a wood / air boundary are almost entirely reflected back into the wood. A crack near the source will redirect incident wave energy. Some areas of the cross-section will have diminished energy content while other portions have increased energy content. Waves that would normally travel from the input at 0° to the receiver at 270° are reflected and travel towards the 90° receiver. As a result, the wave energy observed at 90° is increased. If the crack is located at the 270° location, then the change in energy between the control and the 90° receiver should be minimal. The majority of the energy observed at the 90° location comes during the passage of the first primary and shear waves. Wave energy that travels circumferentially around the pole from the 0° to the 90° location via the 270° and 180° locations is highly attenuated and comparably small. As a result, the wave energy observed at 90° should be similar to the control.

Figure 121 shows the relative signal energy versus time at the 90° receiver. The observed energy when the crack is located next to the source at 0° for both pole 966 and the simulated data is greater than the control energy. Compression wood in the area of

the 90° receiver likely diminishes the magnitude of the pole 966 test data resulting in a lower energy level than the simulated data. When the crack is at the 270° location, the observed energy for the simulated data closely matches the control; however, the energy from testing pole 966 is less. There is an area of rot between the 270° and 0° locations in pole 966. The rot area increases signal attenuation and energy loss.

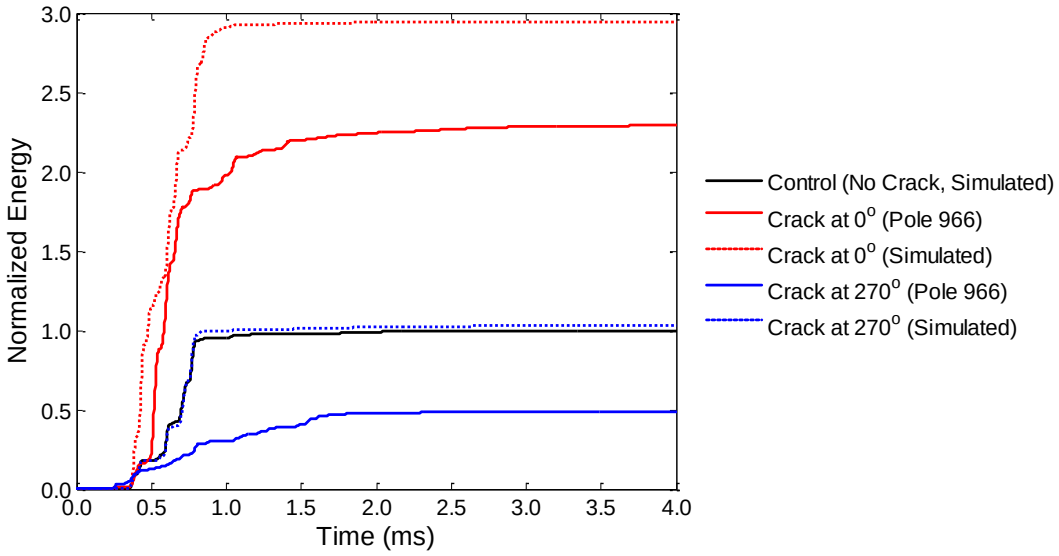


**Figure 121.** Normalized wave energy versus time for 90° receiver. Energy values are normalized against the control energy. Black is the control cross-section with no rot. Red is the cross-section with the crack next to the source at 0°. Blue is the crack located at 270°. A solid line represents data from testing Pole 966. A dashed line represents simulated data.

The control energy observed at the 180° receiver is greater than any of the cross-sections contain a crack. If the crack is located at 270°, then half of the signal is blocked from traveling around the circumference of the pole to the 180° receiver. In that case, it is expected that the energy would be quartered (signal energy is the square of the signal voltage). If the crack is located at 0°, then there will be little effect on the waves energy observed at 180° from waves traveling tangentially around the circumference. In a control cross-section, the tangential waves travel circumferentially in both directions from the source at 0° to the receiver at 180°. As both waves pass the 180° receiver, constructive interference doubles the signal magnitude. If a crack were located at the 0° location, then all of the tangential wave energy would travel circumferentially in one direction; however, from the point of observation at the 180° receiver, there is little

difference between two waves constructively interfering resulting in a doubling of magnitude and a single passing wave with twice the magnitude of the individual waves. The presence of the crack at 0° will disrupt the radial waves that travel across the cross-section from 0° to 180°. The radial dilatational and shear waves carry less energy than the tangentially traveling wave. As a result, the presence of a crack at 0° should result in a reduction of signal energy at the 180° receiver no greater than 50%; therefore, the signal energy at 180° should be between 50% and 100% of the control energy.

Figure 122 shows the wave energy observed at the 180° receiver. As predicted, the control energy is the highest. Both of the data sets with the crack at 0° (simulated and pole 966) have energy levels reduced approximately 20% (80% of the control energy), which is within the predicted range of 50% to 100%. As predicted, the energy observed from the simulated cross-section with the crack at 270° is approximately one quarter of the control energy. The energy from pole 966 with the crack at 270° is approximately 67% of the control energy. The crack length in Pole 966 is shorter than the simulated crack and allows greater signal energy to pass from the source to the receiver. Also, with the presence of compression wood near the 90° reflecting waves from that area, the energy density for the non-compression wood portions of the pole are likely increased causing the pole energy to exceed the simulated energy.

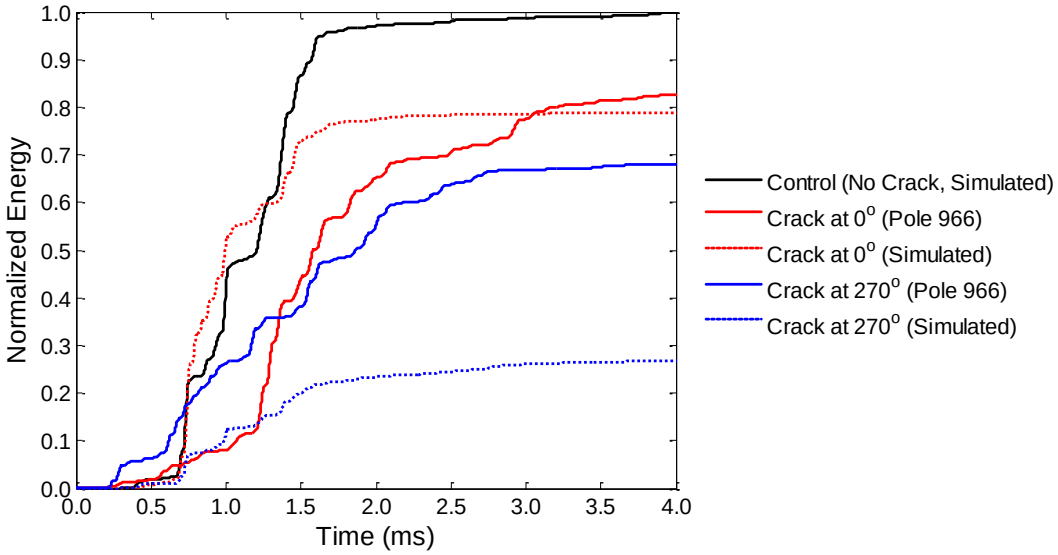


**Figure 122.** Normalized wave energy versus time for 180° receiver. Energy values are normalized against the control energy. Black is the control cross-section with no rot. Red is the cross-section with the crack next to the source at 0°. Blue is the crack located at 270°. A solid line represents data from testing pole 966. A dashed line represents simulated data.

The variation in wave energy is greatest at the 270° receiver. If the crack is located at 270°, then a significant portion of the wave energy in the cross-section is directed towards the receiver. As a result, the observed energy will be greater than the control energy. If the crack is located at 0°, there is no direct path between the input and the receiver at 270°. Waves must either travel tangentially around the pole or must travel from the source to the center then from the center to the receiver. Either path results in significant energy loss when compared with the control.

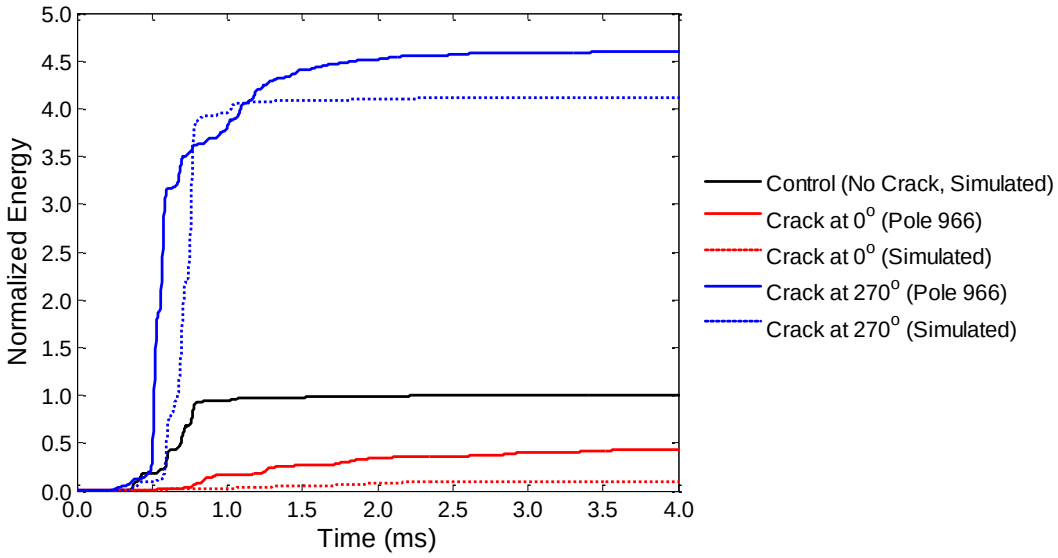


**Figure 123.** Normalized wave energy versus time for 270° receiver. Energy values are normalized against the control energy. Black is the control cross-section with no rot. Red is the cross-section with the crack next to the source at 0°. Blue is the crack located at 270°. A solid line represents data from testing Pole 966. A dashed line represents simulated data.

Figure 123 shows the wave energy observed at the 270° receiver. If the crack is located at 270°, the signal energy is over four times greater than the control energy. The fact that the energy level is above the control energy matches predicted behavior. There is good agreement between the simulated data and data collected from pole 966. The energy from the pole test exceeds the simulated energy. Again, this is likely a result of the compression wood near the 90° sensor causing the energy density of the non-compression portions of the pole to increase. Also, differences in energy can be attributed to the degree of constructive interference at the receiver. Slight changes in the

270° receiver position during the testing of pole 966 could decrease the signal energy at or below the level observed in the simulation. If the crack is located at 0°, then the signal energy is decreased below the control level, and matches predicted behavior. The pole 966 test data is greater than the simulated data. The difference can be attributed to differences in the crack lengths between the simulation and the actual pole. Since the actual crack length is smaller than the simulated crack length, waves pass more easily from the source to the receiver. As a result, the observed energy for the actual cross-section will be higher than the simulated cross-section.

Figure 124a shows the combined energy of the three receivers. It is clear that the presence of a crack increased the observable energy in the cross-section above that of the control. The highest total observed energy within the cross-sections was observed when the crack was at 270°; however, in that case, most of the observed energy was at the 270° receiver. If the energy contribution from the 270° receiver is removed, then the total energy level drops below that of the control, as shown in Figure 124b. When the crack is at 0°, the observed energy at 90° is increased above the control and the energy at 180° is decreased slightly below the control. The energy at both the 90° and the 180° locations was greater when the crack was next to the source at 0° rather than at 270°.

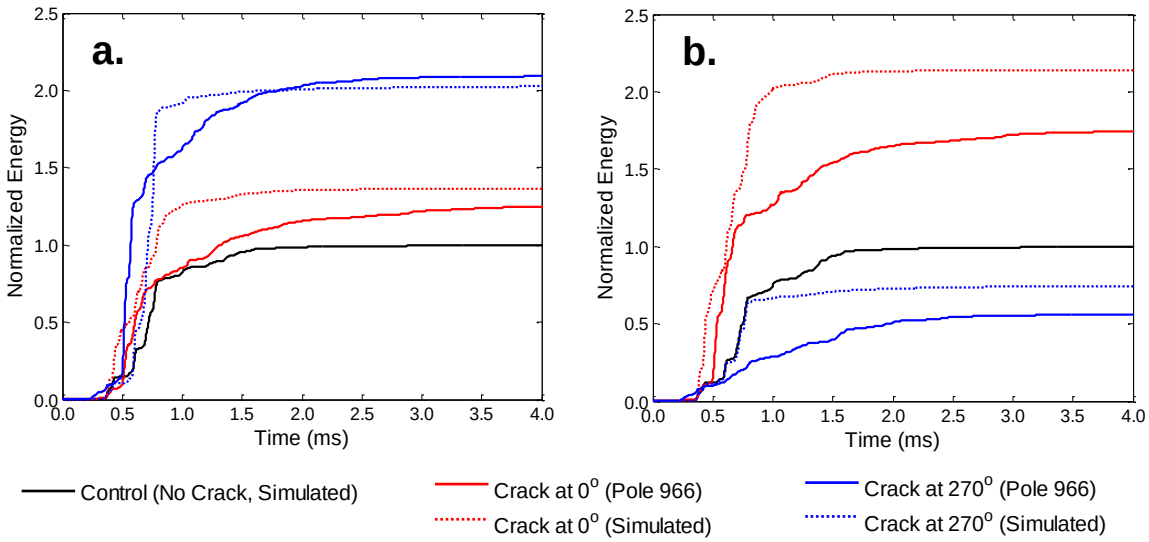


**Figure 124.** Total normalized wave energy for multiple receivers. **a.** total energy for all receivers, **b.** total energy for 90° and 180° receivers. Black is the control cross-section with no rot. Red is the cross-section with the crack next to the source at 0°. Blue is the crack located at 270°. A solid line represents data from testing Pole 966. A dashed line represents simulated data.

The metric presented in this report is capable of examining an area of the pole that encompasses ±90° of the source location as well as path along the diameter of the pole between the source and 180° of the source. Deep cracks within ±90° of the source can potentially limit the inspection area and increase the number of required tests. Placing the source at either +90° or -90° from the crack maximizes the inspection area of the metrics presented. If it is desirable to focus the inspection in the area surrounding the crack, then the source should be placed next to the crack as doing so will increase the signal energy collected at 180° and at 90° from the source (on the same side of the crack as the source).

### 4.6. Conclusions of Utility Pole Analysis

The utility pole analysis began with the construction of a finite difference, time domain (FDTD) model. The model constructed in this report has several unique characteristics that have not previously been implemented. First, the model uses density data collected directly from CT scans of specimens. The CT scans allowed accurate placement of defect and exact specimen geometry. Second, the model implements dispersive wave behavior through wood. In the model implemented here, both velocity and attenuation are dependent upon frequency and amount of mass loss due to decay. Third, this model uses the concept of perfect matched layers (PML) in order to allow wave attenuation to change throughout the cross-section without the presence of spurious reflections that are not present in real world testing. Other FDTD models have used PML to create reflectionless boundaries at the edge of the simulation space. In this model, it is used internally, within the analysis region of the simulation space. Lastly, this model uses a center point calculation that allows waves to travel through the center point.

Wave behavior through an ideal utility pole cross-section was simulated. The wave motion of dilatational and shear waves was recorded and validated against theoretical wave motion predicted by an analytical model. Good agreement was found between the two models.

Geometric and density data was then collected from an actual utility pole cross-section using X-ray computer tomography. The cross-section was then subjected to an

input modeled from the input of an impact test performed upon the actual specimen. The simulation output was then compared against the system output from the actual specimen. Agreement was found between both magnitude and frequency range. Frequency discrepancies were explained as differences between the wave speed of the particular piece of wood in the actual test and the assumed wave velocity within the simulation model. The magnitude discrepancy was partially explained as differences between the actual attenuation of the particular piece of wood and the assumed attenuation within the model. The largest magnitude discrepancy occurred at a single location within the cross-section and was attributable to the presence of compression wood. The behavior of the system output at that location matches the expected behavior of a wave traveling through compression wood.

A series of 40 simulations were run to observe the effects of defects on system output. Five different cross-sectional radii were examined: 305 mm (12 inch), 343 mm (13.5 in), 381 mm (15 in), 419 mm (16.5 in), and 457 mm (18 in). Internal defects of varying sizes were simulated in each cross-section and the system output was recorded. "Rules of thumb" metrics were then developed based upon the observed changes in the output. Three metrics were developed: a time of flight metric comparing the time of flight of the radially and tangentially traveling dilatational waves, a wave area metric which compared the area under the signal for the radial and tangential waves, and a time centroid metric which compared the area and energy time centroids. A method of estimating the defect size was constructed by combining the estimates of the three different metrics. In addition, the time of flight metric identified the general location of the defect within the cross-section and determined the defect depth.

A cross-section was then taken from each of three different utility poles to validate the method. Use of different poles was necessary as each pole has its own unique wave speed and attenuation characteristics. The predicted defect sizes were accurate to within 2.0% of the cross-sectional area of the utility pole. The predicted defect locations were accurate to within 17% of the utility pole radii.

The method developed required that the output be recorded at four locations around the circumference of the pole. In reality, only three were needed, but a fourth was taken near the input source to provide a start time for time of flight measurements. The

developed method accurately predicts the location, size, and depth of the defect within ±90° of the source and along a line 180° of the source. Defects located outside of those regions will be identified, but the location of the defect will not be known. Defects within those two regions can be identified by performing another set of tests with the source positioned 90°, 180°, or 270° from the original source and no changes to the receiver locations. It is recommended that a second set of measurements be performed with the source at a location different than the first set of tests. The second test provides confirmation of the first test results and/or may provide information regarding multiple decay locations within a single cross-section.

The model accurately simulates waves through cross-sections containing rot and / or voids. There are several other potential wood characteristics that can be implemented. Moisture content, compression wood, and knots all have specific behaviors that have the potential to be modeled and added to the simulation. The effects of cracks, both in radial and tangential directions, can be examined in terms of both depth and position around the circumference. The simulation can be extended into three dimensions to see the likely range over which a single impact test could effectively identify an internal defect. However, even in its current form, the model constructed in this report provides a powerful and unique tool that can be used to develop additional "rules of thumb" for a myriad of cross-sectional defects. This knowledge would be invaluable to inspectors in their efforts to maintain the utility pole infrastructure.

### 4.7. Recommendations for Future Work in Utility Pole Analysis

There are several avenues along which this analysis may be expanded. With further analysis of the existing data, it may be possible to determine additional metrics useful in identifying the presence of decay in utility poles. Also, any number of internal defects can be created and their output characteristics examined.

There are many potential additions that would expand the utility of the FDTD model. The existing model can be expanded into three dimensions. Reaction wood is a common defect in pole cross-sections, and modifying the simulation to account for the presence of reaction wood would increase the accuracy of the simulation outputs. This modification would require characterizing wave behavior through reaction wood. The

modification which would likely yield the greatest utility would be the inclusion of moisture content. In the current model, wave velocity and wave attenuation are expressed only as functions of frequency and mass loss. In order to include moisture content in the simulation, the functions would need to be expressed in terms of frequency, mass loss, and moisture content.

Streamlining the testing process and simplifying the testing apparatus has the potential to lead to the development of a field testing unit. In its current form, the testing setup used to examine the utility poles is work-intensive for the operator. Each sensor must be individually placed by hand. Also, the data analysis is performed on a computer separate from the data collecting system. The author envisions a belt of several sensors that can be wrapped around a utility pole. Data recording can begin when any of the sensors observe a voltage above a user defined threshold voltage. This would allow the location of the input source to be arbitrarily chosen by the inspector. The data analysis would be performed by the data collecting computer on site allowing near instant evaluation of the examined pole.

## CHAPTER 5. FINAL CONCLUSIONS AND RECOMMENDATIONS

In this study, both glulam beams and wooden utility poles were examined with the purpose of developing nondestructive methods to detect and assess internal decay. The conclusions and recommendations from the study are given in this section.

One Douglas-fir glulam beam with a cross-section of 19.1 cm by 12.7 cm (7.5 in by 5 in) was salvaged from a construction site. The glulam beam was made from five 12.7 cm by 3.8 cm (5 in by 1.5 in) boards. Visual inspection of the original beam did not show any indications of decay on the entire beam. A segment 114 cm (45 in) long of this beam was then cut for this study. In this beam segment, the only observed indication of decay was at the end of the beam in Lamina 2 where a small interior hole was observed. However, the level of decay for the beam segment could not be assessed using visual inspection. A small (millimeter-wide) longitudinal split on the top surface of Lamina 1 was also observed. Using X-ray computer tomography, severe decay, i.e., mass loss, was detected in the Lamina 2. It was observed that significant decay had also progressed to the adjacent laminae, i.e., Laminae 1 and 3. In addition, it was observed that Laminae 4 and 5 were made of sound wood, and that Lamina 3 had a region of severe decay, a region of sound wood, and a region with varying degrees of decay.

In the glulam beams, the loss of density was identified as a characteristic of rot. However, low density itself could not be used as a metric. The density variations between wood beam laminae beam were on the same order of magnitude as the rot within a beam. Laminae 1 and 3 contained areas of rot; however, the density of those laminae were greater than Lamina 4, which was sound along its entire length.

The glulam beam was first inspected using ultrasonic transducers in a through-transmission setup to excite a frequency of 100 kHz and monitor a frequency range of 85 kHz to 120 kHz. Within that frequency range, good correlation was found between the frequency of highest magnitude and the presence of rot within the glulam beam. As the presence of rot increased, the frequency of highest magnitude shifted lower towards 80 kHz. The sound wood / decayed wood boundary did not show distinct reflections. Good correlation was found between the area under the power spectral density (PSD) curve and the presence of rot. As rot increased in severity, the area under the PSD decreased. Time of flight of propagating waves was also strongly correlated to the presence of rot. As rot

increased, the time of flight increased. Access to both sides of the beam was necessary for this technique. In some locations, gains as high as 140 dB were necessary to obtain results. It is likely higher gains would be necessary in order to use a pulse echo technique, limiting its field potential.

Further analysis was performed using a modified impact-echo setup. A steel sphere was dropped onto the surface of the glulam beam and the dynamic response was monitored using an accelerometer. The frequency range examined using this technique was 500 Hz to 20 kHz. Growth rings within individual lamina cause wave guide effects that can influence the observed output signal. Within the same frequency range, good correlation was found between the presence of decayed wood and the mean attenuation rate. A mean attenuation rate of 1.17 Nepers per millisecond or higher was an indication of the likely presence of rot. The impulse-echo decay rate approach leads to a 5.7% probability of false negative calls (i.e., decayed wood assumed to be sound wood) and to a 3.5% probability of false positive calls (i.e., sound wood assumed to be decayed), with an overall rate of false calls of 7.2%. This approach has the advantage of only requiring access to one lateral side of the beam. Considering the variability that exists in wood including the presence of splits, different orientation and thickness of growth rings, etc., this relatively low rate of false calls makes this approach very attractive.

In many in situ situations, access can only be gained to one side of a glulam beam. In that case, an input source other than a dropped metal sphere must be used. Designing a test setup such that allows the examined beam to be at any orientation would greatly expand the applicability of the modified pulse echo technique. Such a test set up would necessarily include a means of coupling the sensor to the surface of the glulam beam in a manner that does not alter the condition of the beam. Also, modifying the input source to excite frequencies higher than 20 kHz would be advantageous. Wave attenuation through decayed wood increases, and wave velocity through decayed wood decreases with increasing frequency; therefore, higher frequency input signals will have increased likelihood of detecting decay. There may exist a frequency range in which all three parameters: mean decay rate, the area under the power spectrum, and the frequency of highest magnitude are reliable indicators of the presence of rot. Identifying such a range would greatly increase the likelihood that internal rot would be identified.

The utility pole analysis began with the construction of a finite difference, time domain (FDTD) model. The model constructed in this report has several unique characteristics that have not previously been implemented. First, the model uses density data collected directly from CT scans of specimens. The CT scans allowed accurate placement of defect and exact specimen geometry. Second, the model implements dispersive wave behavior through wood. In the model implemented here, both velocity and attenuation are dependent upon frequency and amount of mass loss due to decay. Third, this model uses the concept of perfect matched layers (PML) in order to allow wave attenuation to change throughout the cross-section without the presence of spurious reflections that are not present in real world testing. Other FDTD models have used PML to create reflectionless boundaries at the edge of the simulation space. In this model, it is used internally, within the analysis region of the simulation space. Lastly, this model uses a center point calculation that allows waves to travel through the center point.

Wave behavior through an ideal utility pole cross-section was simulated. The wave motion of dilatational and shear waves was recorded and validated against theoretical wave motion predicted by an analytical model. Good agreement was found between the two models.

Geometric and density data was then collected from an actual utility pole cross-section using X-ray computer tomography. The cross-section was then subjected to an input modeled from the input of an impact test performed upon the actual specimen. The simulation output was then compared against the system output from the actual specimen. Agreement was found between both magnitude and frequency range. Frequency discrepancies were explained as differences between the wave speed of the particular piece of wood in the actual test and the assumed wave velocity within the simulation model. The magnitude discrepancy was partially explained as differences between the actual attenuation of the particular piece of wood and the assumed attenuation within the model. The largest magnitude discrepancy occurred at a single location within the cross-section and was attributable to the presence of compression wood. The behavior of the system output at that location matches the expected behavior of a wave traveling through compression wood.

A series of 40 simulations were run to observe the effects of defects on system output. Five different cross-sectional radii were examined: 305 mm (12 inch), 343 mm (13.5 in), 381 mm (15 in), 419 mm (16.5 in), and 457 mm (18 in). Internal defects of varying sizes were simulated in each cross-section and the system output was recorded. "Rules of thumb" metrics were then developed based upon the observed changes in the output. Three metrics were developed: a time of flight metric comparing the time of flight of the radially and tangentially traveling dilatational waves, a wave area metric which compared the area under the signal for the radial and tangential waves, and a time centroid metric which compared the area and energy time centroids. A method of estimating the defect size was constructed by combining the estimates of the three different metrics. In addition, the time of flight metric identified the general location of the defect within the cross-section and determined the defect depth.

A cross-section was then taken from each of three different utility poles to validate the method. Use of different poles was necessary as each pole has its own unique wave speed and attenuation characteristics. The predicted defect sizes were accurate to within 2.0% of the cross-sectional area of the utility pole. The predicted defect locations were accurate to within 17% of the utility pole radii.

The method developed required that the output be recorded at four locations around the circumference of the pole. In reality, only three were needed, but a fourth was taken near the input source to provide a start time for time of flight measurements. The developed method accurately predicts the location, size, and depth of the defect within ±90° of the source and along a line 180° of the source. Defects located outside of those regions will be identified, but the location of the defect will not be known. Defects within those two regions can be identified by performing another set of tests with the source positioned 90°, 180°, or 270° from the original source and no changes to the receiver locations. It is recommended that a second set of measurements be performed with the source at a location different than the first set of tests. The second test provides confirmation of the first test results and/or may provide information regarding multiple decay locations within a single cross-section.

Streamlining the testing process and simplifying the testing apparatus has the potential lead to the development of a field testing unit. In its current form, the testing

setup used to examine the utility poles is work-intensive for the operator. Each sensor must be individually placed by hand. Also, the data analysis is performed on a computer separate from the data collecting system. The author envisions a belt of several sensors that can be wrapped around a utility pole. Data recording can begin when any of the sensors observe a voltage above a user defined threshold voltage. This would allow the location of the input source to be arbitrarily chosen by the inspector. The data analysis would be performed by the data collecting computer on site allowing near instant evaluation of the examined pole.

There are several avenues along which the analysis using the FDTD model may be expanded without modifying the model. With further analysis of the existing data, it may be possible to determine additional metrics useful in identifying the presence of decay in utility poles. Also, internal defects of any size, shape, and severity can be created and their effects upon output signal characteristics can be examined.

There are many potential additions that would expand the utility of the FDTD model. The existing model can be expanded into three dimensions to see the likely volume over which a single impact test could effectively identify an internal defect. Moisture content, reaction wood (which includes compression wood), and knots all have specific behaviors that have the potential to be modeled and added to the simulation. Reaction wood is a common defect in pole cross-sections, and modifying the simulation to account for the presence of reaction wood would increase the accuracy of the simulation outputs. This modification would require characterizing wave behavior through reaction wood. The modification which would likely yield the greatest utility would be the inclusion of moisture content. In the current model, wave velocity and wave attenuation are expressed only as functions of frequency and mass loss. In order to include moisture content in the simulation, the functions would need to be expressed in terms of frequency, mass loss, and moisture content. However, even in its current form, the model constructed in this report provides a powerful and unique tool that can be used to develop additional “rules of thumb” for a myriad of cross-sectional defects. This knowledge would be invaluable to inspectors in their efforts to maintain the utility pole infrastructure.

## REFERENCES


1. Stewart, A.H. and J.R. Goodman, "Life Cycle Economics of Wood Pole Utility Structures," IEEE Transactions on Power Delivery, Vol. 5, No. 2, pp. 1040-1046, 1990.
2. Morrell, J., "Estimated service life of wood poles," North American Wood Pole Council: Technical Bulletin, 2008.
3. Szymani, R., and K.A. McDonald, "Defect Detection in Lumber: State-of-the-Art," Forest Products Journal, Vol. 31, No. 11, pp. 34-44, 1981.
4. Bauer, C., G. Kilbertus, and V. Bucur, "Ultrasonic Technique for Determining the Extent of Fungus Attack of Beech and Pine Wood," Holzforschung, Vol. 45, No. 1, pp. 41-46, 1991.
5. Beall, F.C., and W.W. Wilcox, "Relationships of Acoustic Emission During Radial Compression to Mass Loss from Decay," Forest Products Journal, Vol. 37, No. 4, pp. 38-42, 1987.
6. Wilcox, W.W., "Detection of Early Stages of Wood Decay with Ultrasonic Pulse Velocity," Forest Products Journal, Vol. 38, No. 5, pp. 68-73, 1988.
7. Patton-Mallory, M., and R.C. DeGroot, "Detecting Brown-Rot Decay in Southern Pine by Acousto-Ultrasonics," Proceedings of the Seventh NDT of Wood Symposium, Pullman, WA, pp. 29-44, 1990.
8. Zabel, R.A., and J.J. Morrel, Wood Microbiology: Decay and its Prevention, Academic Press, NY, 1992.
9. Madsen, B., "Radiological Density Scanning – A Portable Gamma Camera Based on Backscatter Tomography," Ninth NDT of Wood Symposium, Pullman, WA, 1994.
10. Forest Products Laboratory, "Wood Handbook: Wood as an Engineering Material", General Technical Report FPL-GTR-113, United States Department of Agriculture, Forest Service, Forest Products Laboratory, Madison, Wisconsin, 1999.
11. Haygreen, J. and J. Bowyer, Forest Products and Wood Science: An Introduction – Third Edition, Iowa State University Press, Ames, Iowa, 1996.
12. Bodig, J. and B. Jayne, Mechanics of Wood and Wood Composites, Van Nostrand Reinhold Company, New York, New York, 1982.
13. Bucur, V., Acoustics of Wood. Institute National de la Recherche Agronomique Centre de Recherches Forestieres. Nancy, France. CRC Press, Inc. Boca Rotan, Florida, 1995.
14. Foulger, A. "Classroom Demonstrations of Wood Properties", U.S. Department of Agriculture, Forest Service, Forest Products Laboratory, PA-900, April 1969.
15. Sehlstedt-Persson, M., and O. Karlsson, "Natural durability and phenolic content in dried Scots pine heartwood," BioResources, Vol. 5, No. 2, pp. 1126-1142,

2010.

16. Gierlinger, N., D. Jacques, M. Schwanninger, R. Wimmer, and L. Pâques, "Heartwood extractives and lignin content of different larch species (Larix sp.) and relationships to brown-rot decay-resistance," Trees Vol. 18, pp 230-236, 2004.

17. Venäläinen, M., A. Harju, P. Saranpää, P. Kainulainen, M. Tiitta, and P. Velling, "The concentration of phenolics in brown-rot decay resistant and susceptible Scots pines heartwood," Wood Science Technology, Vol. 38, pp 109-118, 2004.

18. Eaton, R.A. and M.C.D. Hale, Wood: Decay, pests, and protection, New York, Chapman and Hall, 1993.

19. Green III, F. and T. Highley, "Mechanism of Brown-Rot Decay: Paradigm or Paradox," International Biodeterioration and Biodegradation, Vol. 39, No. 2-3, pp. 113-124, 1997.

20. Goodell, B., "Brown-Rot Fungal Degradation of Wood: Our Evolving View," Wood Deterioration and Preservation, ACS Symposium Series, Washington D.C., American Chemical Society, pp. 97-118, 2003.

21. McGovern, M., A. Senalik, H. Reis, G. Chen, and F. Beall, "Effect of decay on ultrasonic velocity and attenuation measurements," Proc. SPIE 7981, 79810N, 2011.

22. Wilcox, W.W., "Changes in Wood Microstructure through Progressive Stages of Decay," U.S. Dept. Agri., Forest Service, Forest Product Laboratory, Research Paper, FPL-70, Madison, WI, 1968.

23. Winandy, J. and J. Morrell, "Relationship Between Incipient Decay, Strength, and Chemical Composition of Douglas-fir Heartwood," Wood and Fiber Science, Vol. 25, No. 3, pp. 278-288, 1993.

24. Curling, S., C. Clausen, and J. Winandy, "Relationships Between Mechanical Properties, Weight Loss, and Chemical Composition of Wood During Incipient Brown-Rot Decay," Forest Products Journal, Vol. 52, No. 7/8, pp.34-39, July/August, 2002.

25. Howell, C., A. Hastrup, B. Goodell, and J. Jellison, "Temporal changes in wood crystalline cellulose during degradation by brown rot fungi," International Biodeterioration & Biodegradation, Vol. 63, pp. 414-419, 2009.

26. Xu, G., and B. Goodell, "Mechanisms of wood degradation by brown-rot fungi: chelator-mediated cellulose degradation and binding of iron by cellulose," Journal of Biotechnology, Vol. 87, pp. 43-57, 2001.

27. Michael Hughes of http://michaelmhughes.com/wordpress/?tag=mushroom

28. Filley, T., R. Blanchette, E. Simpson, and M. Fogel, "Nitrogen cycling by wood decomposing soft-rot fungi in the "King Midas tomb," Gordion, Turkey," Proceedings of the National Academy of Sciences of the United States of America, Vol. 98, No. 23, pp. 13346-13350, November 6th, 2001.

29. Morrell, J., Wood Pole Maintenance Manual, 1996 Edition, Oregon State University, College of Forestry, Forest Research Laboratory, Corvallis, OR, October 1996.

30. Gravito, F., "Inspection and maintenance of wooden pole structure," Global ESMO 2003, March 17-21, 2003 – Orlando, Florida.

31. Galligan, W.L., "A Status Report—Nondestructive Testing of Wood," Forest Products Journal, Vol. 14, pp. 221-227, 1964.

32. Wilcox, W., "Review of Literature on the Effects of Early Stages of Decay on Wood Strength," Wood and Fiber, Vol. 9, No. 4, pp. 252-257, 1978.

33. Gerhards, C.C. "Longitudinal Stress Waves for Lumber Stress Grading: Factors Affecting Applications: State-Of-The-Art," Forest Products Journal, Vol. 32, No. 2, pp. 20-25, 1982.

34. Falk, R.H., M. Patton-Mallory, and K.A. McDonald, "Nondestructive testing of wood products and structures: State-of-the-art and research," USDA Forest Service, Forest Products Laboratory. In Nondestructive Testing and Evaluation for Manufacturing and Construction: Proceedings of Conference, Ed. Reis, H., Champaign, IL, August 9-12, 1988.

35. Ross, R., and R. Pellerin, "Nondestructive testing for assessing wood members in structures: A review," Forest Products Laboratory, General Technical Report, FPL-GTR-70, May 1994.

36. Beall, F.C., "Subsurface Sensing of Properties and Defects in Wood and Wood Products," Subsurface Sensing Technologies and Applications, Vol. 1, No. 2, pp. 181-204, 2000.

37. Beall, F., "Overview of the use of ultrasonic technologies in research on wood properties," Wood Science and Technology, Vol. 36, pp 197-212, 2002.

38. Kawamoto, S., and R.S. Williams, "Acoustic Emission and Acousto-Ultrasonic Techniques for Wood and Wood Based Composites: A Review," United States Department of Agriculture, Forest Service, Forest Products Laboratory, General Technical Report, FLP-GTR-134, 2002.

39. Bucur, V., "Techniques for high resolution imaging of wood structure: a review," Measurement Science Technology, Vol. 14, No. 12, pp. 91-98, 2003.

40. Stoker, R., "X-Ray Pole Inspection," Proc. 44th Annual Meeting of American Wood Preservation Association, Vol. 44, pp. 298-313, 1948.

41. Eslyn, W.E., "Radiographical Determination of Decay in Living Trees by Means of Thulium X-ray Unit," Forest Science Journal, Vol. 5, No. 1, pp. 37-47, 1959.

42. Miller, W., "Design and Implementation of a Portable Computerized Axial Tomography System for Field Use," Nuclear Instruments and Methods in Physics Research Section A: Accelerators, Spectrometers, Detectors and Associated Equipment, Vol. 270, No. 2-3, pp. 590-597, 1988.

43. Davis, J., R. Davies, P. Wells, and N. Benci, "A Field Transportable

Computerized Tomography Scanner for the NDT of Wooden Power Poles," Materials Evaluation, Vol. 51, No. 3, pp. 332-337, 1993.

44. Schmoldt, D., Z. Dongping, R. Conners, "Nondestructive evaluation of hardwood logs using automated interpretation of CT images," Review of Progress in Quantitative Nondestructive Evaluation, Vol. 12, pp. 2257-2264, 1993.

45. Eslyn, W.E., "Utility Pole Decay – Part II: Basidiomycetes Associated with Decay in Poles," Wood Science and Technology, Vol. 4, No. 2, pp. 97-103, 1970.

46. Eslyn, W.E., "Utility Pole Decay – Part III: Detection in Pine by Color Indicators," Wood Science and Technology, Vol. 13, No. 2, pp. 117-126, 1979.

47. Wyckhuyse, A., and X. Maldague, "A Study of Wood Inspection by Infrared Thermography, Part I: Wood Pole Inspection by Infrared Thermography," Research in Nondestructive Evaluation, Vol. 13, No. 1, pp. 1-12, 2001.

48. Wyckhuyse, A., and X. Maldague, "A Study of Wood Inspection by Infrared Thermography, Part II: Thermography for Wood Defects Detection," Research in Nondestructive Evaluation, Vol. 13, No. 1, pp. 13-21, 2001.

49. Shortle, W.C., A.L. Shigo, and J. Ochrymowych, "Patterns of Resistance to a Pulsed Electric Current in Sound and Decayed Utility Poles," Forest Products Journal, Vol. 28, No. 1, pp. 48-51, 1978.

50. Sandoz, J.L., and O. Vanackere, "Wood Poles Ageing and Non Destructive Testing Tool," CIRED 97, 2-5 June 1997, Conference Publication No. 438, IEE, pp. 3.26.1-3.26.6, 1997.

51. Nicolotti, G., L. Socco, R. Martinis, A. Godio, and L. Sambuelli, "Application and comparison of three tomographic techniques for detection of decay in trees," Journal of Arboriculture, Vol. 29, No. 2, pp. 66-78, March 2003.

52. DeGroot, R., R. Ross, and W. Nelson, "Non-destructive assessment of wood decay and termite attack in southern pine sapwood," Wood Protection, Vol. 3, pp. 25-34, 1998.

53. Sakai, H., A. Minimisawa, and K. Takagi, "Effect of Moisture Content on Ultrasonic Velocity and Attenuation in Woods," Ultrasonics, Vol. 28, No. 6, pp. 382-385, 1990.

54. Fukada, E., "The Vibrational Properties of Wood II," Journal of the Physical Society of Japan, Vol. 6, No. 6, pp. 417-421, 1951.

55. Miller, B.D., F.L. Tayler, and R.A. Popeck, "A Sonic Method for Detecting Decay in Wood Poles," Proc. American of Wood Preservation Association, Vol. 61, pp. 109-115, 1965.

56. James, W.L., "Effects of Transverse Moisture Content Gradients on the Longitudinal Propagation of Sound in Wood," Research Report 466, USDA Forestry Service, Madison, WI, 1986.

57. Wielandt, E., “On the validity of the ray approximation for interpreting delay times,” in Seismic Tomography, pp. 85-98, ed. Nolet, G., Reidel, Dordrecht, 1987.

58. Quarles, S.L., “The Effect of Moisture Content and Ring Angle on the Propagation of Acoustic Signals in Wood,” Journal of Acoustic Emission, Vol. 9, No. 3, pp. 189-195, 1990.

59. Ross, R., R. Pellerin, N. Volny, W. Salsig, and R. Falk, “Inspection of timber bridges using stress wave timing nondestructive evaluation tools: A guide for use and interpretation,” Gen. Tech. Rep. FPL-GTR_114, Madison, WI: US Dept. Agri., Forest Service, Forest Products Laboratory, 1991.

60. Mishiro, A., “Ultrasonic Velocity and Moisture Content in Wood II,” Mokuzai Gakkaishi, Vol. 42, No.6, pp. 612-617, 1996.

61. Olivito, R.S., 1996, “Ultrasonic Measurements in Wood,” Materials Evaluation, Vol. 54, No. 4, pp. 514-517.

62. Simpson, W., “Equilibrium moisture content of wood in outdoor locations in the United States and worldwide,” U.S. Dept. of Agri., Forest Service, Forest Products Laboratory, Research Note, FPL-RN-0268, 1998.

63. Fukada, E., “The Vibrational Properties of Wood I,” Journal of the Physical Society of Japan, Vol. 5, No. 5, pp. 321-327, 1950.

64. Dunlop, J., “Damping loss in wood at mid kilohertz frequencies,” Wood Science Technology, Vol. 12, pp 49-62, 1978.

65. Bucur, V., “An Ultrasonic Method for Measuring the Elastic Constants of Wood Increment Cores Bored From Living Trees,” Ultrasonics, Vol. 21, No.3, pp. 116-126, 1983.

66. Bucur, V., and R.R. Archer, “Elastic Constants for Wood by an Ultrasonic Method,” Wood Science Technology, Vol. 18, pp. 255-265, 1984.

67. Suzuki, H., and E. Sasaki, “Effect of Grain Angle on the Ultrasonic Velocity of Wood,” Mokuzai Gakkaishi, Vol. 36, No. 2, pp. 103-107, 1990.

68. Bucur, V., and F. Feeney, “Attenuation of ultrasound in solid wood,” Ultrasonics, Vol. 30, No. 2, 1992.

69. Bucur, V. and I. Böhnke, “Factors affecting ultrasonic measurements in solid wood,” Ultrasonics, Vol. 32, No. 5, pp. 385-390, 1994.

70. Mishiro, A., “Effect of Density on Ultrasonic Velocity in Wood,” Mokuzai Gakkaishi, Vol. 42, No. 9, pp. 887-894, 1996.

71. Mishiro, A., “Effects of Grain and Ring Angles on Ultrasonic Velocity in Wood,” Mokuzai Gakkaishi, Vol. 42, No. 6, pp. 211-215, 1996.

72. Berndt, H., A. Schniewind, and G. Johnson, “High-resolution ultrasonic imaging of wood,” Wood Science and Technology, Vol. 33, pp. 185-198, 1999.

73. Lemaster, R.L., and D.A. Dormfield, “Preliminary Investigation of the Feasibility of Using Acousto-Ultrasonics to Measure Defects in Lumber,”

Journal Acoustic Emission, Vol. 6, No. 3, pp.157-165, 1987.

74. Sandoz, J.L., "Grading of Construction Lumber by Ultrasound," Wood Science Technology, Vol. 23, No. 1, pp. 95-108, 1989.

75. Sandoz, J., Y. Benoit, and L. Demay, "Wood testing using acousto-ultrasonics," Wood Conference on Timber Engineering, Session 7.5-5, Advanced Grading of Lumber, Whistler Resort, British Columbia, Canada, July 31 – August 3, 2000.

76. Lord, W., R. Ludwig, and Z. You, "Finite Element Modeling of Ultrasonic Wave Propagation in Materials," New Direction in NDE of Advanced Materials, Winter Annual Meeting of Mech. Eng., Chicago, IL, 1988.

77. Lord, W., R. Ludwig, and Z. You, "Developments in Ultrasonic Modeling with Finite Element Analysis," Journal of Nondestructive Evaluation, Vol. 9, No. 2/3, pp.129-143, 1990.

78. Biernacki, J. and F. Beall, "Development of an acousto-ultrasonic scanning system for nondestructive evaluation of wood and wood laminates," Wood and Fiber Science, Vol. 25, No. 3, pp. 289-297, 1993.

79. Dickens, J.R., D.A. Bender, and D.E. Bray, "A Critical Angle Ultrasonic Technique for the Inspection of Wood Parallel-To-Grain," Wood Fiber Science, Vol. 28, No. 3, pp. 380-388, 1996.

80. Ross, R., R. DeGroot, and W. Nelson, "Nondestructive evaluation of biologically degraded wood," Nondestructive Characterization of Materials IV, Plenum Press, New York, 1994.

81. Ross, R., R. DeGroot, W. Nelson, and P. Lebow, "The relationship between stress wave transmission characteristics and compressive strength of biologically degraded wood," Forest Products Journal, Vol. 47, No. 5, pp. 89-93, 1997.

82. Ross, R., and R. DeGroot, "Scanning technique to identify biologically degraded wood," Experimental Techniques, pp. 32-33, May / June 1998.

83. Tiitta, M., F. Beall, and J. Biernacki, "Acousto-ultrasonic assessment of internal decay in glulam beams," Wood and Fiber Science, Vol. 30, No. 3, pp. 259-272, 1998.

84. Tiitta, Markku, "Non-destructive methods for characterization of Wood Materials," Doctoral Dissertation, University of Kuopio, Department of Physics, Finland, November, 2006.

85. Im, K., D. Hsu, S. Song, H. Cho, J. Park, J. Sim, and I. Yang, "A study of ultrasonic evaluation of material homogeneity in wood," Review of Progress in Quantitative Nondestructive Evaluation, AIP Conf. Proc. 760, pp. 1515-1522, Golden, Colorado (USA), 25-30 July 2004.

86. Yang, Y., I. Kwang, D. Hsu, S. Kim, S. Soug, H. Cho, J. Park, and Y. Kim, "On nondestructive evaluation of wood materials using ultrasonic techniques," Trans Tech Publications, Key Engineering Materials, Vol. 297-300, pp. 1973-1978, Switzerland, Nov. 2005.

87. Lee, J. and M. Bae, "Determination of ratio of wood deterioration using NDT technique," Mokchae Konghak, Vol. 32, No. 3, pp. 33-44, 2004.

88. Schubert. S., D. Gsell, J. Dual, M. Motavalli, and P. Niemz, "Resonant ultrasound spectroscopy applied to wood: Comparison of shear modulus $G_{RT}$ of wood before and after exposure to fungal pathogens," 14th Int. Symp. Of NDT of Wood, Hannover, 2005.

89. Shaw, D.A., "Sonic Vibration Technique for Rot Detection in Wood Poles," IEEE Transactions on Instrumentation and Measurement, Vol. IM-23, No. 3, Sept. 1974.

90. Dunlop, J., "Testing of poles by using acoustic pulse method," Wood Science Technology, Vol. 15, pp 301-310, 1981.

91. McCracken, F.I., and S.R. Vann, "Sound Can Detect Decay in Standing Hardwood Trees," Research Paper SO-195, USDA Forest Service, Southern Forest Experiment Station, New Orleans, LA, pp. 6, 1983.

92. Bulleit, W., "Modeling stress wave passage times in wood utility poles," Wood Science Technology, Vol. 19, No. 2, pp. 183-191, 1985.

93. Aggour, M., A. Hachichi, and M. Mayer, "Nondestructive evaluation of timber bridge piles," Evaluation and upgrading of wood structures: case studies: Proceedings of Structures Congress '86, Hyatt Regency Hotel, New Orleans, Louisiana, September 15-18, 1986.

94. Falk, R., and R. Ross, "Methods for assessing wood structures in place," Serviceability and Durability of Construction Materials – Proceedings of the First Materials Engineering Congress, Part 1 (of 2), Aug 13-15, Denver, CO, pp 324-330, ISBN: 0-8726-7772, 1990.

95. Han, W., and R. Birkeland, "Ultrasonic scanning of logs," Industrial Metrology, Vol. 2, No. 3–4, pp. 253-281, ISSN 0921-5956, 1992.

96. Beall, F., J. Biernacki, and R. Lemaster, "The use of acousto-ultrasonics to detect biodeterioration in utility poles," Journal of Acoustic Emission, Vol. 12, No. 1/2, pp. 55-64, 1994.

97. Holt, J., S. Chen, and R. Douglas, "Determining lengths of installed timber piles by dispersive wave propagation," Transportation Research Record: Journal of the Transportation Research Board, Vol. 1546 / 1996, pp 112-120, ISSN: 0361-1981, 1999.

98. Schwarze, S., C. Rabe, D. Ferner, and S. Fink, "Detection of decay in trees with stress waves and interpretation of acoustic tomograms," Arboricult. J. Vol. 28, pp. 3-19, 2004.

99. Socco, L., L. Sambuelli, R. Marinis, E. Comino, and G. Nicolotti, "Feasibility of ultrasonic tomography for nondestructive testing of decay on living trees," American Society for Nondestructive Testing, Research in Nondestructive Evaluation, Vol. 15, pp 31-54, 2004.

100. Kim, K., J. Lee, S. Lee, and H. Yo, "Improvement of wood CT images by consideration of skewing of ultrasound caused by grown ring angle," Wood and Fiber Science, Vol. 40, No. 4, pp 572-579, 2008.

101. Kim, K., S. Lee, and J. Lee, "Cross-sectional image reconstruction of wooden members by considering variation of wave velocities," Mokchae Konghak, Vol. 35, No. 5, pp 16-23, 2007.

102. Kim, K., and J. Lee, "CT image reconstruction of wood using ultrasonic velocities I," Mokchae Konghak, Vol. 33, No. 5, pp 21-28, 2005.

103. Kim, K. and J. Lee, "NDE of decayed wood with ultrasonic CT," Key Engineering Materials, Vol. 321-323, pp. 1182-1185, 2006.

104. Kim, K., and J. Lee, "CT Image reconstruction of wood using ultrasound velocities II," Mokchae Konghak, Vol. 33, No. 5, pp. 29-37, 2005.

105. Lee, S., K. Kim, and J. Lee, "Improvement of ultrasonic and X-ray CT techniques for field application," 9th World Conference on Timber Engineering, Portland, Oregon, USA, August 6-10, 2006.

106. Yanagida, H., Y. Tamura, K. Kim, and J. Lee, "Development of ultrasonic time-of-flight computed tomography for hard wood with anisotropic acoustic property," Japanese Journal of Applied Physics, Vol. 46, No. 8A, pp. 5321-5325, 2007.

107. Payton, R.G., "Wavefronts in wood," The Quarterly Journal of Mechanics and Applied Mathematics 56(4), 527-546, 2003.

108. Wang, X., R.B. Allison, L. Wang, and R.J. Ross, "Acoustic Tomography for Decay Detection in Red Oak Trees," U.S. Dept. of Agri., Forest Service, Forest Products Laboratory, Research Paper FPL-RP-642, 2007.

109. Schubert, S., D. Gsell, J. Dual, M. Motavialli, and P. Niemz, "Acoustic wood tomography on trees and the challenge of wood heterogeneity," Holzforschung, Vol. 63, pp. 107-112, 2009.

110. McGovern, M., C.A. Senalik, G. Chen, F.C. Beall, and H. Reis, "Detection and assessment of wood decay using X-ray computer tomography," Proc. of SPIE, 7647, 76474B-1-12, 2010.

111. American Society for Testing and Materials, "Standard test method for wood preservatives by laboratory soil-block cultures." D-1413-99. Annual Book of ASTM Standards 4.10, 2003.

112. Ting, T.C.T., "Pressuring, shearing, torsion and extension of a cylindrical tube or bar of cylindrically anisotropic material," The Royal Society, Proceedings: Mathematical, Physical and Engineering Sciences 452, No. 1954, 2397-2421, 1996.

113. Ting, T.C.T., Anisotropic Elasticity: Theory and Applications, Oxford Science Publications, New York, 1996.

114. Martin, P.A., and J.R. Berger, "Waves in wood: Free vibrations of a wooden

pole," Journal of Mechanics and Physics of Solids 49, 1155-1178, 2001.

115. Yee, K.S., "Numerical solution of initial boundary value problems involving Maxwell's equations in isotropic media," IEEE Transactions on Antennas and Propagation 14(3), 302-307, 1966.

116. Gsell, D., T. Leuteneggar, and J. Dual, "Modeling three-dimensional elastic wave propagation in circular cylindrical structures using a finite difference approach," Journal of the Acoustical Society of America 116, 3284-3293, 2004.

117. Schubert, S., D. Gsell, M. Motavalli, J. Dual, and P. Niemz, "Non-destructive testing of trunks: Studying elastic wave propagation by numerical simulation," Wood Research 51(3), 11-24, 2006

118. Senalik, C.A., F.C. Beall, and H. Reis, "Detection and assessment of wood decay in glulam beams using a decay rate approach," British Institute of Non-Destructive Testing, Insight, Vol 52, No. 10, October 2010.

119. Proud, J., P. Tamarkin, and W. Meecham, "Reflection of sound from a surface of sawtooth profile," Journal of Applied Physics, Vol. 28, No. 11, pp. 1298-1301, 1957.

120. Berenger, J., "A perfectly matched layer for absorption of electromagnetic waves," Journal of Computational Physics 114, 185-200, 1994.

121. Chew, W.C., and Q.H. Liu, "Perfectly matched layers for elastodynamics: A new absorbing boundary condition," Journal of Computational Acoustics 4, 341-359 1996.

122. Graff, K.F., Wave Motion in Elastic Solids, Oxford University Press, London, 1975.

123. Liu, Q.H., and J. Tao, "The perfectly matched layer for acoustic waves in absorptive media," Journal of the Acoustical Society of America 102, 2072-2082 1997.

124. Liu, Q.H., "Perfectly matched layers for elastic waves in cylindrical and spherical coordinates," Journal of the Acoustical Society of America 105, 2075-2084, 1999.

125. McGovern, M., "Assessment of Brown-Rot Decay Using X-Ray Computer Tomography and Ultrasonic Measurements," M.S. Thesis, University of Illinois at Urbana-Champaign, Urbana, IL, 2011.

126. Chen, Y.H., W.C. Chew, and Q.H. Liu, "A three-dimensional finite difference code for modeling sonic logging tools," Journal of the Acoustical Society of America 103, 702-712, 1998.

127. Gedney, S., "An Anisotropic Perfectly Matched Layer-Absorbing Medium for the Truncation of FDTD Lattices," IEEE Transactions on Antennas and Propagation, Vol. 44, No. 12, pp. 1630-1639, December 1996.

128. Hu, F., "A Stable, Perfectly Matched Layer for Linearized Euler Equations in Unsplit Physical Variable," Journal of Computational Physics, Vol. 173, pp. 455-

480, 2001.

129. Gindl, W., "Comparing Mechanical Properties of Normal and Compression Wood in Norway Spruce: The Role of Lignin in Compression Parallel to the Grain," Holzforschung, Vol. 56, pp. 395-401, 2002.

130. Maurer, H., S. Schubert, F. Bächle, S. Clauss, D. Gsell, J. Dual, and P. Niemz, "A simple anisotropy correction procedure for acoustic wood tomography," Holzforschung, Vol. 60, pp. 567-573, 2006.

131. Mavko, G., T. Mukerji, and J. Dvorkin, The Rock Physics Handbook, Second Edition: Tools for Seismic Analysis of Porous Media, Cambridge University Press, New York, 2009.

132. Hagrey, S., "Geophysical imaging of root-zone, trunk, and moisture heterogeneity," Journal of Experimental Botany, Vol. 58, No. 4, pp 839-854, 2007.

133. Liang, S., X. Wang, J. Wiedenbeck, Z. Cai, and F. Fu, "Evaluation of acoustic tomography for tree decay detection," Proceedings of the 15th International Symposium on Nondestructive Testing of Wood, Duluth Minnesota, USA, Sept. 10-12, 2007.

134. Lemaster, R.L., and F.C. Beall, "The Use of Acousto-Ultrasonics to Detect Advanced Decay in Round Wood," NDE Center Report No. 35.02.01, Univ. of California, Forest Products Laboratory, Richmond, CA, 1989.

## ADDITIONAL REFERENCES

The references below were reviewed, but not cited in the thesis.


135. Bodig, J., R.W. Anthony, and J.R. Goodman, "NDE of wood poles – current status," Vol. 1, Report EL-5063, EPRI, Paulo Alto, CA, 1987.

136. Courant, R. and D. Hilbert, Methods of Mathematical Physics, Vol II. Interscience Publishers, a division of John Wiley & Sons, New York, 1966.

137. Drossaert, F., and A. Giannopoulos, "Complex frequency shifted convolution PML for FDTD modeling of elastic waves," Wave Motion, Vol. 44, pp. 593-604, 2007.

138. Dunlop, J.I., 1983, "Testing of Poles by Acoustic Resonance," Wood Science Technology, Vol. 17, pp. 31-38.

139. Eaton, R.A., and R.S. Johnstone, "A Novel Device for Detecting Internal Defects in Wooden Poles," The Intern. Research Group in Wood Preservation, Working Group II, Sub-Group 5, NDT for Defects in Wooden Structures, 20th Annual Meeting, Lappenranta, Finland, Document No. IRG/WP/2329, May 22-26, 14 pp, 1989.

140. Emmerich, H., and M. Korn, "Incorporation of attenuation into time-domain computations of seismic wave fields," Geophysics, Vol. 52, No. 9, pp 1252-1264, 1987.

141. Eslyn, W.E., 1968, "Utility Pole Decay – Part I: Appraisal of a Device for Nondestructive Detection of Decay," Forest Science Journal, Vol. 2, pp. 128-137.

142. Godunov, S.K., and V.S. Ryabenkii, Difference Schemes: An Introduction to the Underlying Theory, Studies in Mathematics and Its Applications, Vol. 19., Elsevier Science Publishers B.V., 1987.

143. Green, A.T., 1991, "Ultrasonic Waves in Anisotropic Materials: Past, Present and Future," Proceedings of ASNT Fall Conference and Quality Testing Show, Boston, MA, pp. 42-46.

144. Hildebrand, F.B., Finite Difference Equations and Simulations, Prentice-Hall, Inc. Englewood Cliffs, New Jersey, 1968.

145. Katz, J.L., et al. "On the anisotropic elastic properties of wood," Journal of Materials Science 43, 139-145, 2008.

146. Kline, M., and I. Kay, Electromagnetic Theory and Geometrical Optics, John Wiley & Sons, Inc., New York, 1965.

147. Lemaster, R.L., and W.W. Wilcox, "The Use of Acousto-Ultrasonics to Detect Decay in Wood–Based Products," Second International Conference on Acousto-Ultrasonics, Atlanta, GA, pp.188-190, 1993.

148. Martín, S., "Air-coupled ultrasonic propagation and novel non-destructive bonding quality assessment of timber composites," Doctoral Thesis, Swiss Federal Institute of Technology, Zurich, Switzerland 2012.

149. Minamizawa, A., and A. Ozawa, "Measurement of Moisture Diffusivity in Woods Using Ultrasound," Mokuzai Gakkaishi, Vol. 40, No. 10, pp. 1052-1058, 1994.

150. Noack, D., and W. von Roth, "On the theory of elasticity of orthotropic material wood," Wood Science and Technology 10, 97-110, 1976.

151. Pellerin, R.F., R. C. DeGroot, and G.R. Esenther, "Nondestructive Stress Wave Measurements of Decay and Termite Attack in Experimental Wood Units," Fifth NDT of Wood Symposium. Pullman, WA, pp. 319-352, 1985.

152. Reis, H., A.K. Habboub, and S.H. Carpenter, "Noise Abatement In Asphalt Concrete Pavements: Part I -- Nondestructive Estimation of Characteristic Lengths Using an Impulse-Echo Approach", INSIGHT -- Non-Destructive Testing and Condition Monitoring, Vol. 42, No. 7, pp. 458-464, 2000.

153. Reis, H., A.K. Habboub, and S.H. Carpenter, "Noise Abatement In Asphalt Concrete Pavements: Part II -- Estimation of Acoustic Properties", INSIGHT -- Non-Destructive Testing and Condition Monitoring, Vol. 42, No. 8, pp. 534-541, 2000.

154. Reis, H., and A.K. Habboub, "Nondestructive Evaluation of Dimension Stone Using Impulse Generated Stress Waves: Part 1 – Theoretical Aspects and Experimental Prospects," in **"**Dimension Stone Cladding: Design, Construction, Evaluation, and Repair," ASTM 1394, K. R. Hoigard, Ed., American Society for Testing and Materials, West Conshohocken, PA, pp. 3-23, 2000.

155. Reis, H., and A.K. Habboub, "Nondestructive Evaluation of Dimension Stone Using Impulse Generated Stress Waves: Part 2 – Estimation of Complex Moduli," in **"**Dimension Stone Cladding: Design, Construction, Evaluation, and Repair," ASTM 1394, K. R. Hoigard, Ed., American Society for Testing and Materials, West Conshohocken, PA, pp. 24-38, 2000.

156. Reis, H., and A.K. Habboub, "Nondestructive Evaluation of Dimension Stone Using Impulse Generated Stress Waves: Part 3 -- Microstructure Characterization," in **"**Dimension Stone Cladding: Design, Construction, Evaluation, and Repair," ASTM 1394, K. R. Hoigard, Ed., American Society for Testing and Materials, West Conshohocken, PA, pp. 39-54, 2000.

157. Rose, J.L., Ultrasonic Waves in Solid Media, Cambridge University Press, 1999.

158. Sansalone, M., "Impact-Echo: The Complete Story," American Concrete Institute-Structural Journal, V. 94, No. 6, pp.777-786, 1997.

159. Schneider, J.B., C.L. Wagner, and S.L. Broschat, "Implementation of transparent sources embedded in acoustic finite-difference time-domain grids," Journal of the Acoustical Society of America 103, 136-142, 1998.

160. Senalik, A., F. Beall, K. O'Dell, and H. Reis, "Detection and assessment of wood

decay in glulam beams using a through-transmission ultrasonic approach," SPIE Smart Structures/NDE/Sensors and Smart Structures Technologies for Civil, Mechanical, and Aerospace Systems Conference, San Diego, CA, Vol. 6932, pp. W1-12, 2008.

161. Senalik, A., F. Beall, and H. Reis, "Wood decay detection and assessment in glulam beams using a modified impulse-echo approach," SPIE Smart Structures/NDE/Sensors and Smart Structures Technologies for Civil, San Diego, CA, Vol. 7292, pp. Y1-12, 2009.

162. Shashkov, M., Conservative Finite-Difference Methods on General Grids, CRC Press, 1996.

163. Zheng, F., and Z. Chen, "Numerical dispersion analysis of the unconditionally stable 3-D ADI-FDTD method," IEEE Transactions on Microwave Theory and Techniques 49, No. 5, 1006-1009, 2001.

164. Levy, H., and F. Lessman, Finite Difference Equations, Sir Isaac Pitman & Sons, LTD, London, 1959.

165. Davis, J., Finite Difference Methods in Dynamics of Continuous Media, MacMillan Publishing Company, New York, 1986.

## APPENDIX: OTHER EXAMINED METRICS

One of the goals of the utility pole study was to develop metrics that could be correlated to the size of the internal defect. Using the simulation data, eight potential metrics were developed. The metrics were then applied to data extracted from the utility pole specimens. The variations in the cross-sections of the utility pole specimens caused several of the metric values obtained from the pole tests to exhibit a range of values much larger than the simulated values. Of the group of eight metrics, only three were capable of estimating the defect size despite significant variations in the utility pole cross-sectional geometrics. Those three metrics were described in the body of this report in Section 4.3.3 and were called: the wave area metric, the time of flight metric, and the time centroid metric. The other five metrics proved to be too sensitive to the cross-sectional geometry of the utility poles and were not used in the final defect size estimation method. For completeness of the dissertation, this appendix contains a description of the other five metrics examined.

Simulations were run for cross-sections of five different diameters: 305 mm (12 inch), 343 mm (13.5), 381 mm (15 in), 419 mm (16.5 in), and 457 mm (18 in). A control free of internal defects was run for each cross-section. After the control simulation was complete, cross-sections with center holes were simulated. The diameters of the center holes were varied in proportion to the pole radii with fractional values of: 0.133, 0.267, 0.400, 0.533, 0.667, 0.800, and 0.933. For a 381 mm (15 in) pole, the fractional values correspond to a center hole diameters ranging from 25 mm (1 in) to 178 mm (7 in) in 25 mm (1 in) increments. A simulation was run for each pole diameter and each center hole for a total of 40 simulations (five pole sizes, seven center hole sizes and a control). Four acceleration signals were recorded from each simulation at four fixed locations around the circumference of the poles. The first was next to the source and is referred to as the 0° location. The other three locations were +90°, 180°, and -90° (270°). The angles refer to the angle constructed by drawing lines from the source to the center of the pole and then from the pole to the location of the receiver.

Three metrics were used in the final defect size estimation, and five were discarded. A brief description of each discarded metric is given here, and a full description is given later in this Appendix. The first discarded metric was a comparison

of the root mean square of the recorded signals at the 180° and 90° locations. The second was a comparison between the maximum amplitude within the frequency domain for the radial wave at the 180° location and the tangential wave at the 90° location. The third was a comparison of the area under the first cycle of the rectified acceleration signals at the 180° and 90° locations. The fourth is a comparison of the areas under the rectified acceleration signal at the 180° and 90° locations when the tangential wave passed the 180° location. The fifth is a comparison of the time necessary for the area under the rectified curve to increase from 11% of the total area to 22% of the total area. The comparison is made between the 180° and 90° locations.

### A.1. Root Mean Square Metric

The first discarded metric is the root mean square (RMS) of the signal. The root mean square is a measure of the mean energy in the signal. The root mean square of the signal is given by Equation 73.

$$R_{RMS} = \frac{RMS_{180}}{RMS_{90}} = \frac{\sqrt{\frac{1}{N}\sum_{i=1}^{N}\left[A_{180}(t_i)\right]^2}}{\sqrt{\frac{1}{N}\sum_{i=1}^{N}\left[A_{90}(t_i)\right]^2}} \tag{73}$$

Where:
$R_{RMS}$ is the root mean square metric
$RMS_{\angle}$ is the root mean square taken at a location corresponding to angle $\angle$
$A_{\angle}(t_i)$ is the acceleration recorded at location corresponding to angle $\angle$ at time, $t_i$
N number of points in the data set.

In order to non-dimensionalize the metric, the RMS calculated for the signal collected at the 180° location ($RMS_{180}$) is normalized by the RMS of the 90° location signal ($RMS_{90}$). Figure 125 shows the RMS ratios for each of the five cross-sections versus the diameter of the center defect expressed as a fraction of the pole radius. Since the root mean square depends upon all of the points within the signal, it is affected by interference effects. The interference effects lead to variability in the RMS values that cause the metrics line seen in Figure 125 to exhibit jaggedness. The effects of interference upon the RMS values are described in Section 4.3.3. A mean of the values is

taken and a subjected to a three point moving average. As the defect diameter increases, the mean ratio of the RMS values decreases in a nearly linear manner. The decrease is due to the fact that the signal energy traveling from the source to the receiver at 180° must travel a greater distance. Also, as described in Section 4.1.5, the defect is surrounded by an inch of rotten wood. The rotten wood has greater attenuation than sound wood; therefore, as the defect size increases, the percentage of the cross-section composed of rotten wood also increases. As a result, an increase in the size of the defect causes the signals within to the cross-section to travel greater distances through wood that is likely highly attenuative relative to sound wood.

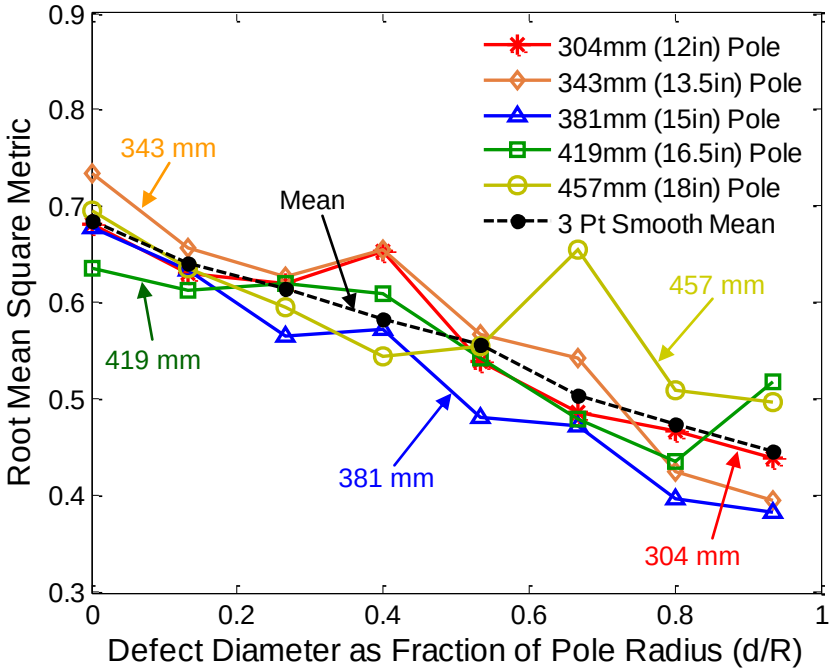


**Figure 125.** Root mean squared metric versus defect size. The defect diameter, d, is expressed as a fraction of the pole radius, R.

The root mean square (RMS) metric was then applied to the utility pole specimens. The mean trend line of the RMS metrics (black dashed with dots) has a range of values between 0.685 for a cross-section free of defects down to a value of 0.447 for a cross-section with a defect size (d/R) of 0.933. Eleven of the fourteen pole tests fell outside the range of the RMS metric. For this reason, the RMS metric was not used in the defect size estimate analysis. The disparate ranges of values were caused by differences in the geometries between the simulated cross-sections and the utility pole

specimens. The simulated cross-sections were circular, symmetric, and had defects positioned at their centers. All three of the utility pole specimens had a deep surface crack that extended nearly to the center of the pole. The deep cracks block or divert nearly half of the wave energy of tangentially traveling wave from traveling from the source to the receiver 180° location. As a result, the RMS value at the 180° location of the utility pole diverges significantly from the range of metric values obtained from the simulated results. The values of the RMS metric obtained from the pole tests are presented in Table 31.

It should be noted that the sensitivity of the RMS metric to cracks within the cross-section may indicate that it is suited for the estimation of crack depth. In such a study, the center defect would be removed and a surface crack would be added. A series of simulations with varying sized surface cracks would be performed and the system output would be collected. The RMS metric could then be applied to system outputs to determine if a noticeable trend exists.

**Table 31.** Defect sizes estimated from root mean square metric

| Pole Test | $\frac{\pm 180^o}{+90^o}$ Ratio | | | $\frac{\pm 180^o}{-90^o}$ Ratio | | |
|---|---|---|---|---|---|---|
| | Symbol | RMS Metric | d/R | Symbol | RMS Metric | d/R |
| 966Z | ◀ | 0.891 | 0* | ◁ | 0.310 | 1+ |
| 966N | ▼ | 1.401 | 0* | ▽ | 2.778 | 0* |
| 966R | ▶ | 0.064 | 1+ | ▷ | 0.304 | 1+ |
| 491Z | ■ | 0.278 | 1+ | □ | 0.161 | 1+ |
| 491N | ◆ | 0.585 | 0.394 | ◇ | 0.232 | 1+ |
| 477Z | ● | 0.483 | 0.758 | ○ | 0.193 | 1+ |
| 477N | ★ | 0.346 | 1+ | ☆ | 0.581 | 0.412 |

Test Designations and Symbols defined in Table 20 (Page 166).
d/R is the defect diameter, d, expressed as a fraction of the pole radius, R
* The values of the defect sizes have a lower bound of zero

## A.2. Maximum Magnitude Metric

The frequency content of the partitioned signals shown in Figure 83c and 83d (on page 144) was then examined. The time partitioned signals were normalized by the RMS of the partition window and a Fourier transform was taken of the signal to construct a

power spectral density (PSD) curve. The maximum acceleration amplitude was extracted from each PSD curve. Figure 126a and 126b show the PSD curves for the 90° and 180° locations, respectively. The maximum amplitudes at the 90° and 180° locations are designated $f_{max,90}$ and $f_{max,180}$, respectively. The metric examined is the ratio of $f_{max,180}$ to $f_{max,90}$, and is referred to as the maximum magnitude metric, $R_M$. This metric quantifies the relative strength of the strongest signal within the time partition. Figure 127 shows the maximum magnitude metric for each of the five cross-sections versus the diameter of the center defect expressed as a fraction of the pole radius. As in Figure 125, a mean of the values at each defect size is calculated, and the series of mean values undergo a three point moving average. The value of $R_M$ decreases as the diameter of the defect increases. The reason for this decrease is the same as those given in the description of the RMS metric (Figure 125). The rate of change in $R_M$ is higher for smaller defects than larger defects, indicating that this metric, like the wave area metric, may be effective in identifying small internal defects.

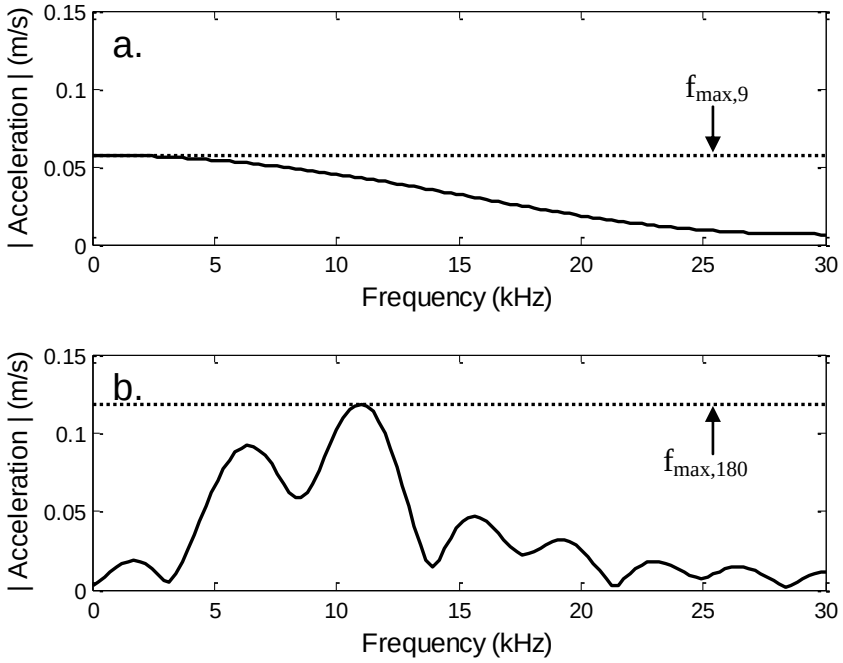


**Figure 126:** Power spectral density curves of the time partition signals shown in Figure 83c and Figure 83d. **a.** The maximum magnitude of the spectra is $f_{max,90}$. **b.** The maximum magnitude of the spectra is $f_{max,180}$.

**Table 32.** Defect sizes estimated from maximum magnitude metric

| Pole Test | $\frac{\pm 180^o}{+90^o}$ Ratio | | | $\frac{\pm 180^o}{-90^o}$ Ratio | | |
|---|---|---|---|---|---|---|
| | Symbol | Maximum Magnitude Metric | d/R | Symbol | Maximum Magnitude Metric | d/R |
| 966Z | ◀ | 1.202 | 0.671 | ◁ | 2.519 | 0* |
| 966N | ▼ | 1.246 | 0.634 | ▽ | 1.495 | 0.410 |
| 966R | ▶ | 1.685 | 0.303 | ▷ | 1.850 | 0.211 |
| 491Z | ■ | 1.347 | 0.521 | □ | 1.672 | 0.310 |
| 491N | ◆ | 1.362 | 0.510 | ◇ | 0.955 | 0.923 |
| 477Z | ● | 1.864 | 0.204 | ○ | 2.425 | 0* |
| 477N | ★ | 1.923 | 0.171 | ☆ | 1.978 | 0.140 |

Test Designations and Symbols defined in Table 20 (Page 166).
d/R is the defect diameter, d, expressed as a fraction of the pole radius, R
* The values of the defect sizes have a lower bound of zero

The maximum magnitude metric is not independent of the wave area metric. Trends in the values of the wave area metric appeared within the maximum magnitude metric in both the simulated and pole test values. Values of $R_M$ obtained from the pole tests are given in Table 32. While this metric is insensitive to interference phenomenon, variability exists in the maximum value of the spectrum between simulations. This variability leads to the jagged plots seen in Figure 127. Values of $R_M$ are given in Table 32. Inclusion of the maximum magnitude metric in the defect size estimation was equivalent to placing greater weight upon the wave area metric in the defect estimation method. The maximum magnitude metric has undesirable characteristics when compared with the wave area metric: greater processing requirements and greater variability resulting in jaggedness in the trends. Also, it is not independent of the wave area metric. These characteristics led to the decision to exclude the maximum magnitude metric from the defect size estimation.

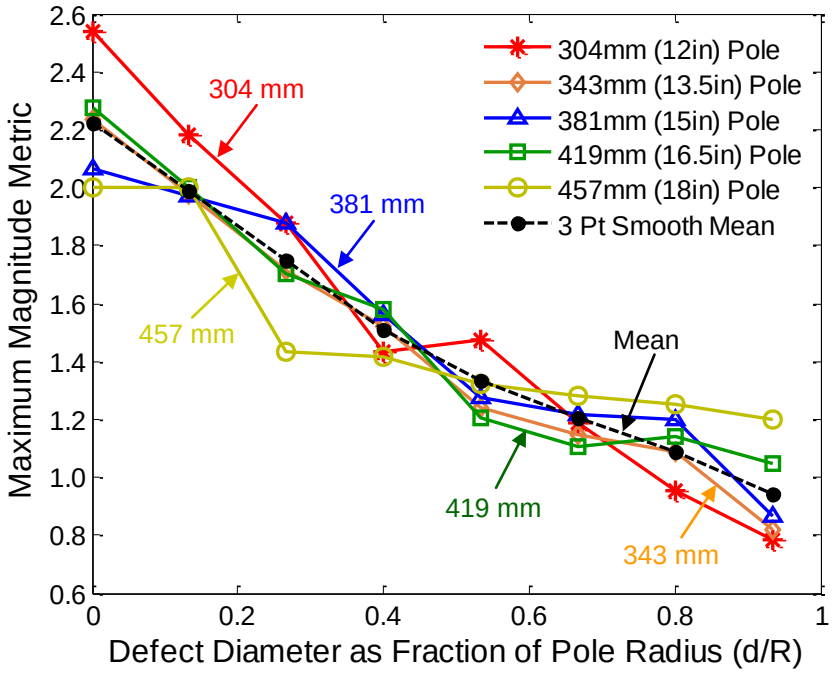


**Figure 127.** Maximum magnitude metric versus defect size. The defect diameter, d, is expressed as a fraction of the pole radius, R.

### A.3. First Cycle Metric

The third metric was the rectified area under the first cycle of the arriving wave. The first cycle is composed of the fastest traveling frequencies. Higher frequencies travel faster through wood and have higher attenuation. Any increase in attenuation, such as in the presence of rot, should have a greater impact upon higher frequencies than lower frequencies. This metric was selected to examine a portion of the wave that should be composed of the highest frequencies contained within the acceleration signals, and which should be sensitive to the presence of rot. The first cycle of the signals collected at the 90° and 180° locations are shown in Figures 128a and 128b, respectively. The rectified area of the first cycle of the signals is shown in Figures 128c and 128d, respectively.

Figure 129 shows the ratio of the areas under the first cycle. The area of the first cycle from the 180° location is normalized by the area of the 90° location. The ratio is referred to as the first cycle metric and is designated $R_C$. As the size of the defect increases, the first cycle of the 180° location becomes composed of lower frequencies. As the frequencies lower, the first curve arrives later and it is wider. The wider first

cycle possess greater area than the first curve composed of high frequencies. The first cycle of the 90° location, while affected, is not as sensitive to the presence of rot as the 180° location. As a result, the ratio of the area of the first cycle increases with increasing defect size.

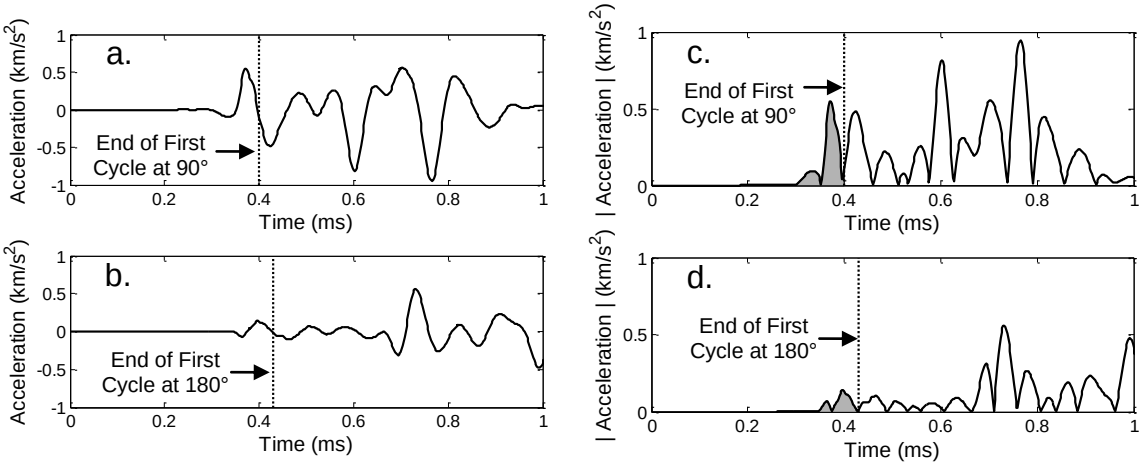


**Figure 128.** Area of the first full cycle after the wave arrival. The end of the first cycle is shown for waves arriving at locations **a.** 90° and **b.** 180°. The first cycle of the rectified area is shown as the shaded region for locations **c.** 90° and **d.** 180°.

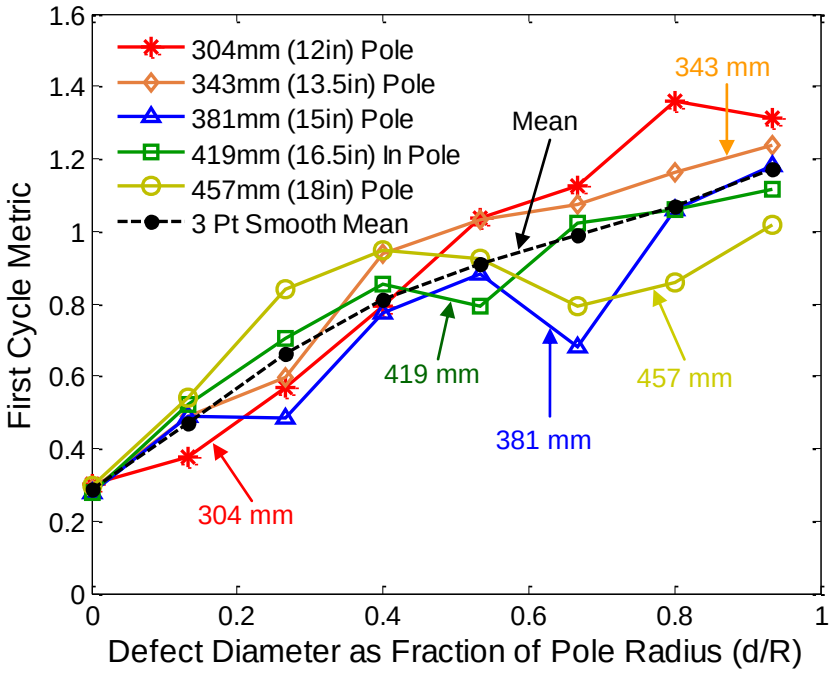


**Figure 129.** First cycle metric versus defect size. The defect diameter, d, is expressed as a fraction of the pole radius, R.

Examination of Figure 129 reveals some features that require explanation. The values for the 381 mm (15 in) pole for defect size 0.267 falls sharply. Dispersion effects

at the 90° location cause the first cycle to be abnormally wide, increasing its area significantly. Since the area at the 90° is in the denominator, the metric value decreases. A similar effect occurs in the defect size 0.667, however the dispersion occurs at the 180° location and causes the magnitude of the wave to be diminished resulting in a lower metric value. The first cycle metric also has an additional consideration in that wave traveling through larger cross-sections experience greater attenuation. Since the attenuation is frequency dependent, the first cycle arriving at the receivers for larger diameter cross-sections with (relatively) large inner defects will contain lower frequencies than the first cycle observed at smaller diameter cross-sections with the same relative sized inner defects. This phenomenon is visible in all curves within the d/R range of 0.400 to 0.933. The 304 mm (12 in) curve has the highest slope above 0.400 and the 457 mm (18 in) curve has the lowest. The higher frequencies of the larger poles with large inner defects are more attenuated than the smaller poles with defects of the same fractional size d/R. As a result, this metric was not truly non-dimensional and larger poles would inherently yield lower values. The sensitivity of this metric to the pole size led to the decision to exclude it from the defect size estimation. For completeness, Table 33 is presented with the first cycle metrics from the pole tests.

**Table 33.** Defect sizes estimated from first cycle metric

| Pole Test | $\frac{\pm 180^o}{+90^o}$ Ratio | | | $\frac{\pm 180^o}{-90^o}$ Ratio | | |
|---|---|---|---|---|---|---|
| | Symbol | First Cycle Metric | d/R | Symbol | First Cycle Metric | d/R |
| 966Z | ◀ | 3.269 | 1+ | ◁ | 0.637 | 0.250 |
| 966N | ▼ | 0.859 | 0.465 | ▽ | 3.502 | 1+ |
| 966R | ▶ | 0.218 | 0* | ▷ | 0.634 | 0.248 |
| 491Z | ■ | 0.507 | 0.159 | □ | 0.109 | 0* |
| 491N | ◆ | 0.797 | 0.388 | ◇ | 0.035 | 0* |
| 477Z | ● | 0.714 | 0.313 | ○ | 0.695 | 0.298 |
| 477N | ★ | 0.019 | 0* | ☆ | 0.348 | 0.044 |

Test Designations and Symbols defined in Table **20** (Page 166).
d/R is the defect diameter, d, expressed as a fraction of the pole radius, R
* The values of the defect sizes have a lower bound of zero

## A.4. Tangential Area Metric

The fourth metric examined the recorded acceleration signals at a time when the tangentially traveling dilatational wave traveled from the source and passed the 180° location. The time when the tangential wave passes at the 180° location is shown in Figure 130b. At that time, both the radially traveling and tangentially traveling dilatational waves had passed at the 180° location. The area under the rectified signal at that time was 22% of the total signal area. The time was designated as $\tau_{180,22}$. The area under the curve at the 90° location was calculate for the same time, as shown in Figure 130a. The signal at the 90° includes the radially and tangentially traveling dilatational waves, and some portion of the tangentially traveling shear wave. The metric examined the amount of signal content that was traveling to the 180° location via the 90° location. The ratio is referred to as the tangential area metric and is designated $R_A$.

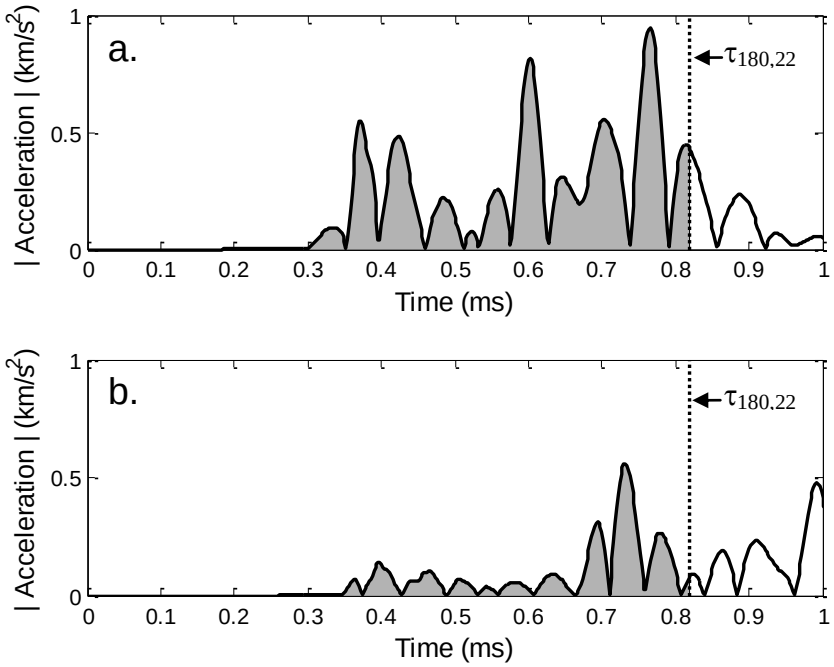


**Figure 130.** Signal areas as the tangential wave passes the 180° location. The regions of comparison are shaded. **a.** The area of the signal at the 90° location when the tangential wave passes the 180° location. **b.** The area of the signal at the 180° when the tangential wave passes that location. The area at the passage of the tangential wave is 22% of the total signal area.

The tangential area metric, $R_A$, is plotted against the defect size in Figure 131. As the diameter of the defect increased, the radially and tangentially traveling dilatational

waves were subjected to greater attenuation. The magnitude of the waves measured at the 180° location were less than the magnitude of the waves measured at the 90° location. In addition, the signal at the 90° location contained additional shear wave information that had not yet arrived at the 180° location. As a result, the area of the rectified signal for the window of time examined decreased more rapidly at the 180° location than the 90° location, and the tangential area metric decreased with increasing defect diameter. The time window for this metric was the third largest among the metrics (the root mean squared metric and time centroid metric used the largest windows) and was susceptible to interference phenomena. The area of the signal recorded from the 90° was large relative to the area recorded at the 180° location, and, as a result, the metric did not appear overly sensitive to interference effects.

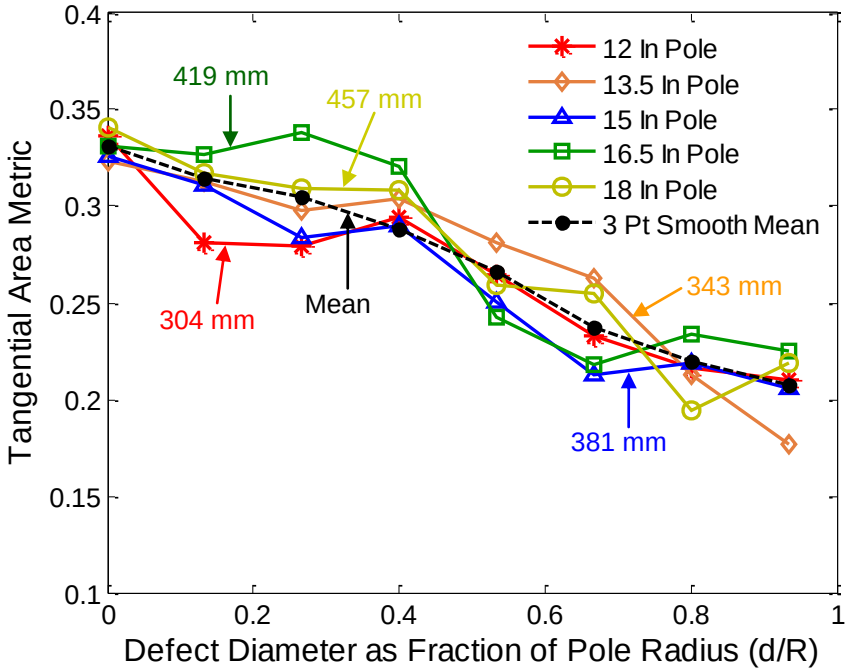


**Figure 131.** Tangential area metric versus defect size. The defect diameter, d, is expressed as a fraction of the pole radius, R.

The tangential area metric proved to be extremely sensitive to variations in the cross-section when applied to the utility pole specimens. The deep cracks mentioned in the description of the RMS metric and the common surface cracks caused the signals arriving at the receivers to vary greatly from the simulated signals. The time of arrival of the tangential wave at the 180° location was difficult to know with certainty. In addition,

the presence of the deep cracks blocked half of the tangentially traveling dilatational waves from arriving at the 180° location. As a result, most metric values obtained from the pole tests were outside the range of values predicted by the simulated trend. Of the fourteen pole tests, twelve had values outside the simulated range. The tangential metric values obtained from the poles test are given in Table 34.

**Table 34.** Defect sizes estimated from tangential area metric

| Pole Test | $\frac{\pm 180^o}{+90^o}$ Ratio | | | $\frac{\pm 180^o}{-90^o}$ Ratio | | |
|---|---|---|---|---|---|---|
| | Symbol | Tangential Area Metric | d/R | Symbol | Tangential Area Metric | d/R |
| 966Z | ◀ | 0.675 | 1+ | ◁ | 0.2329 | 0.699 |
| 966N | ▼ | 0.496 | 1+ | ▽ | 0.933 | 1+ |
| 966R | ▶ | 0.082 | 0* | ▷ | 0.366 | 1+ |
| 491Z | ■ | 0.173 | 0* | □ | 0.090 | 0* |
| 491N | ◆ | 0.369 | 1+ | ◇ | 0.122 | 0* |
| 477Z | ● | 0.265 | 0.540 | ○ | 0.097 | 0* |
| 477N | ★ | 0.162 | 0* | ☆ | 0.379 | 1+ |

Test Designations and Symbols defined in Table **20** (Page 166).
d/R is the defect diameter, d, expressed as a fraction of the pole radius, R
* The values of the defect sizes have a lower bound of zero

## A.5. Time Span Metric

The fifth metric was the time between 11% and 22% of the total rectified signal area arriving at each sensor. This metric is referred to as the time span metric and is shown in Equation 74.

$$R_S = \frac{\tau_{180,22} - \tau_{180,11}}{\tau_{90,22} - \tau_{90,11}} \tag{74}$$

Where:
$R_S$ is the time span metric
$\tau_{\angle,\%}$ is the time at which the percentage of the rectified signal area corresponding to % has passed the location corresponding to angle $\angle$

As previously mentioned, 22% of the area at the 180° corresponded to passage of the tangentially traveling dilatational wave. Near the arrival of the wave, the area was

approximately 11%. For a sound cross-section free of defects, the time at which 11% of the signal area had arrived at the 90° location was just as the tangentially traveling dilatational wave passed. The time at which 22% of the area had passed the 90° location was just as the tangentially traveling shear wave had arrived. These times are shown in Figure 132.

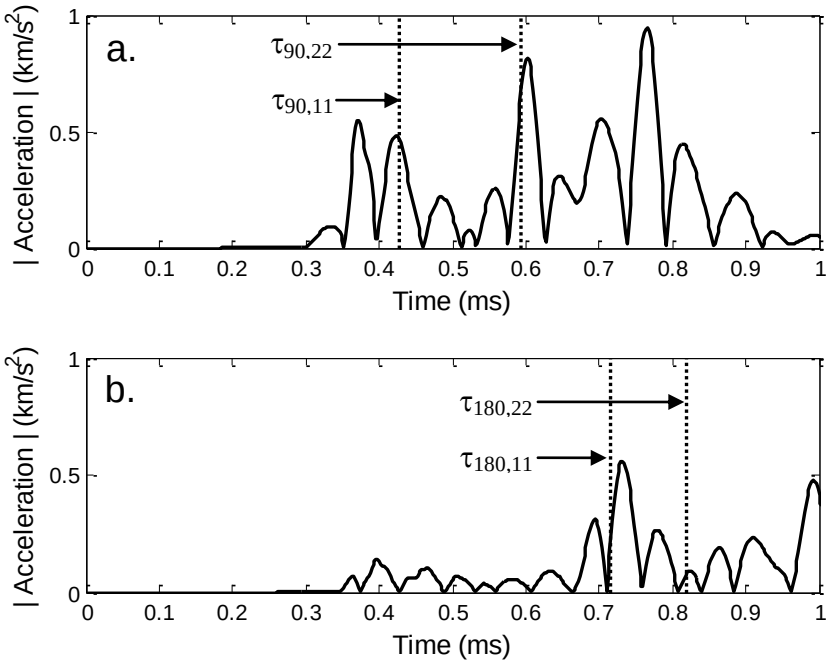


**Figure 132.** Time window between signal area of 11% and 22%. The signal area times are the times at which the area of the signal is 11% or 22% of the total signal area **a.** At 90°, the times for 11% and 22% are $\tau_{90,11}$, and $\tau_{90,22}$, respectively. **b.** At 180°, the times are $\tau_{180,11}$, and $\tau_{180,22}$, respectively.

As the size of the center defect increases, the time window at the 90° remained relatively constant (the denominator of Equation 74 was unchanged). The time span at the 180° location increased with increasing defect size. For all defect sizes, the time at which 11% of the signal area passed the 180° location was at or near the arrival of the tangentially traveling dilatational wave. The increased attenuation associated with the larger defects caused the moment at which 22% of the signal area passed the 180° location to shift later in time. As a result, the time span at the 180° location increased (the numerator of Equation 74 increased). As the defect size increased, the time span metric increased. The time span metric is shown in Figure 133.

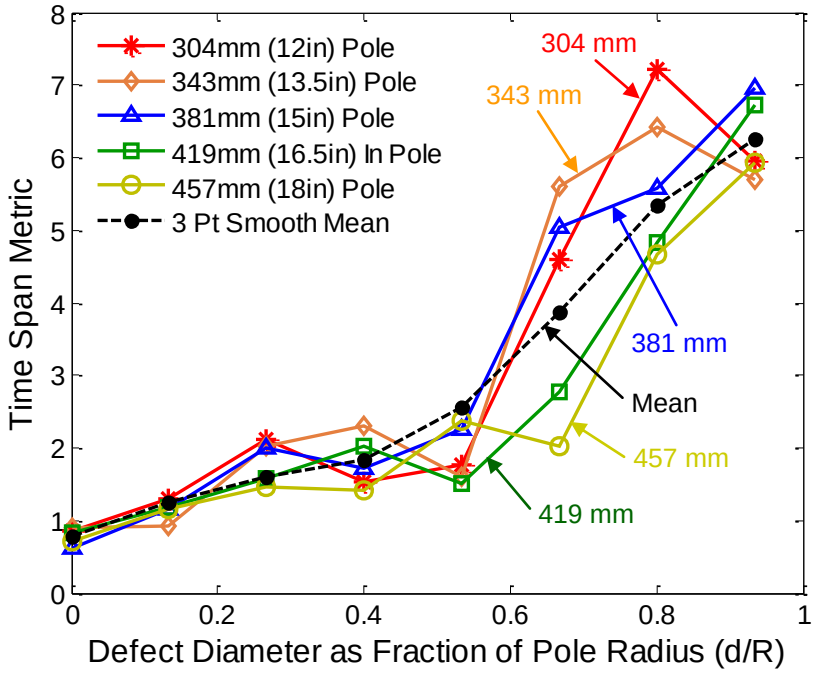


**Figure 133.** Time span metric versus defect size. The defect diameter, d, is expressed as a fraction of the pole radius, R.

The time span metric covers a relatively narrow time window of the signal; however, the window occurs while multiple waves have passed, and noticeable interference effects are likely to be present. The interference effects manifest as jaggedness within the metric value curves. The most noticeable example of interference effects within the metric values is the precipitous drop of the point corresponding to a defect size of 0.933 for the 304 mm (12 in) curve. In this case, constructive interference causes a peak early in time within the signal to increase. As a result, the time at which 22% of the signal area passes the 180° location is earlier than in signals corresponding to smaller center defects.

The meaning of the time span metric as it relates to the defect size was not as clear when the metric was applied to the pole test data. Within the simulated signals individual waves (shear versus dilatational) were easily identified. Within the pole test data, differentiating between individual wave types was not a certain process. Without the ability to clearly identify particular wave types, the physical foundation of the time span metric was called into question. The values produced by the time span metric were relatively accurate when compared with the other independent metrics presented in this

Appendix. A greater sample set of specimens are necessary in order to validate or invalidate the time span metric. The time span metric values are given in Table 35.

**Table 35.** Defect sizes estimated from time span metric

| Pole Test | $\frac{\pm 180^o}{+90^o}$ Ratio | | | $\frac{\pm 180^o}{-90^o}$ Ratio | | |
|---|---|---|---|---|---|---|
| | Symbol | Time Span Metric | d/R | Symbol | Time Span Metric | d/R |
| 966Z | ◀ | 1.000 | 0.061 | ◁ | 3.308 | 0.608 |
| 966N | ▼ | 1.656 | 0.300 | ▽ | 1.447 | 0.209 |
| 966R | ▶ | 3.833 | 0.662 | ▷ | 1.548 | 0.249 |
| 491Z | ■ | 1.905 | 0.411 | □ | 1.409 | 0.194 |
| 491N | ◆ | 2.152 | 0.457 | ◇ | 1.283 | 0.144 |
| 477Z | ● | 1.670 | 0.307 | ○ | 2.867 | 0.564 |
| 477N | ★ | 0.699 | 0*[a] | ☆ | 0.513 | 0*[a] |

Test Designations and Symbols defined in Table **20** (Page 166).
d/R is the defect diameter, d, expressed as a fraction of the pole radius, R
* The values of the defect sizes have a lower bound of zero
[a] As ratios, the value of ★ and ☆ can be inverted to obtain pertinent values within the range. If inverted the metric values obtained for ★ and ☆ are 1.430 and 1.950 with corresponding d/R values of 0.202 and 0.419, respectively.

As already described in Section 4.3.3, metrics based upon phase and / or frequency were extremely sensitive to the cross-sectional geometry and interference effects. Amplitude fluctuations within the frequency domain caused by interference regularly exceeded the changes attributable to internal decay. As a result, those metrics are not considered reliable decay detectors. It has been observed that the ratio of high frequency signal energy to low frequency signal energy decreases as internal rot increases [7]; however, the positions of surface cracks relative to the receiving sensor can skew the frequency content through resonance and mode conversion. Surface cracks on wood poles are common and may not be easily identified by surface examination. Several of the surface cracks on the wood pole specimens used in this analysis can only be identified from CT scans. As a result, the high to low frequency energy ratio may be skewed under conditions commonly encountered and difficult to identify. The sensitivity of phase and / or frequency based metrics to cross-sectional geometry and interference effects caused those metrics to be inaccurate or less accurate than metrics based upon area, energy, and / or time.